Ultra-Wideband Pulse Doppler Radar for Short-Range Targets

by

Nicola Jean Kinzie

B.S., Kansas State University, 2006

M.S., University of Colorado, 2008

A thesis submitted to the

Faculty of the Graduate School of the

University of Colorado in partial fulfillment

of the requirements for the degree of

Doctor of Philosophy

Department of Electrical, Computer, and Energy Engineering

2010

This thesis entitled:

Ultra-Wideband Pulse Doppler Radar for Short-Range Targets

written by Nicola Jean Kinzie

has been approved for the Department of Electrical, Computer, and Energy Engineering

_____

Zoya Popović

_____

Dejan Filipović

Date _____

The final copy of this thesis has been examined by the signatories, and we Find that both the content and the form meet acceptable presentation standards Of scholarly work in the above mentioned discipline.

Kinzie, Nicola Jean (Ph.D., Electrical Engineering)

Ultra-Wideband Pulse Doppler Radar for Short-Range Targets

Thesis directed by Professor Zoya Popović

Abstract

This thesis addresses the design and characterization of a pulse Doppler radar designed to detect targets at short range ($R \leq 7\,\text{m}$). To minimize the shortest detectable range, a subnanosecond transmitted pulsewidth is desired. UWB design techniques were combined with a pulse Doppler radar architecture to demonstrate a full radar, including the transmitter, receiver, simulated channel, and post processor.

The transmitted pulse train has a 2.5 GHz carrier frequency, a 730 ps pulsewidth, and a 1 GHz 10 dB-bandwidth. The PRF of the radar is 20 MHz, which allows unambiguous range and Doppler detection with a single PRF. The peak transmitted power is 1.2 W. The characteristics of the transmitted waveform provide fine range accuracy ($\delta R = \pm 0.03\,\text{m}$), facilitate a short minimum range, and allow for an efficient transmitter design. The receiver was designed to complement the transmitter; it has a homodyne architecture and is pulsed to isolate a specific detectable range.

A closed-loop channel model was designed to simulate the range delay, Doppler shift, and channel attenuation of a moving target; the model is connected to the transmitter and receiver with coaxial cable, facilitating bench-top characterization of the radar and eliminating some effects of wireless transmission, such as multipath. Extensive closed-loop radar testing was performed, and the following radar characteristics were determined: (1) The minimum detectable SNR, assuming a 36.5 μs integration time, is 0 dB. (2) Assuming a

transmitter-to-receiver isolation of 80 dB, the minimum range of the radar is $R_{min} = 1.3\,\text{m} + R_{lk}$, where R_{lk} is the apparent leakage range between the transmitter and receiver. Depending on the antenna system design, the radar can detect targets from $1.5\,\text{m} \lesssim R \leq 7\,\text{m}$, meeting the original goal of this work. These results support the supposition that a UWB pulse Doppler radar architecture can be employed for short-range, moving target detection.

Dedication

To Matthew and waiting for two cookies [1].

Personal Acknowledgments

I have been fortunate to share the last four and a half years with some fantastic people, both in and out of the electromagnetics group. While many people have contributed to my experience at CU, I would like to thank a few people in particular: Evan Cullens for bringing a little bit of Kansas to the mountains; Negar Ehsan and Mabel Ramiŕez for some great girl talk; Kendra Kumley for much needed coffee breaks; Erez Falkenstein, Mike Roberg, and Rob Scheeler for bringing some...humor to the lab; Dr. Mike Elsbury, Dr. John Hoversten, Dr. Luke Sankey, and Rebecca Sankey for making me feel welcome and included from the very beginning; Joseph Mruk for always making me smile; Dr. Randy Direen for enthusiastic lunch breaks; Dr. Charles Dietlein for teaching me the ropes; Jonathan Chisum for many great conversations about science fiction, fantasy, engineering, and life. I would like to thank Dan Kuester for helping me through my toughest semester at CU and being a fantastic friend ever since. Finally, I would like to thank Kirsten Farnsworth and Evan Sheehan for bringing some music, entertainment, and fun into my life.

I would like to thank my parents who have always been supportive. Who bought me new books when I begged on every shopping trip. Who logged hours on the road driving me to music lessons, concerts, and camps. Who barely flinched when I announced I was going to attend that "other" university in Kansas and even put a purple tag on the front of my pickup. Who drove the

Macksville–Boulder–Albuquerque triangle many, many times helping me move to and from Albuquerque each summer. My parents taught me to always do work I was proud of and to choose a career that I would enjoy doing. I would not be who I am without their love and guidance. Thanks, Mom and Dad.

I would like to thank my little sister, Paige, for always being there to listen, to share a good book with, or to shop for black sheep. In many ways, no one understands me better than Paige. Many times graduate school left me wanting to scream, "That's not fair!", and Paige knows that the correct response is "Fair as chocolate cake and elephant's knees." Thanks, Paige, for always being there and for being such a great friend.

Finally, I would like to thank Matthew Martin. Seven years ago we started dating and assumed the relationship would end when he left our alma mater for Cornell University; little did we know that we would be dating long distance for over six years. Despite the distance and the accompanying hardships, Matt has been incredibly supportive, both emotionally and professionally, throughout my tenure at CU. He's encouraged me to challenge myself and helped me cope when I've taken on challenges that seemed too big. He's my best friend, and I can't wait to start the next chapter of my life with him. Thank you, Matt. The best is yet to come.

Professional Acknowledgments

I would like to thank my advisor, Dr. Zoya Popović, for the opportunity to be a part of her research group. She has brought together an excellent group of students and put together a fantastic microwave lab. I would especially like to thank her for taking a chance on a new student who came in with a potential project in mind. Prior to starting graduate school, I spent eight months interning in a radar group at Sandia National Laboratories. From day one I was hooked and knew I wanted to work there upon graduation, so when I learned they were interested in funding a graduate student to research ultra-wideband radar, I jumped at the opportunity. After hearing the details of the project, Zoya graciously agreed to advise me. Through the course of the project, I have had to the opportunity to spend my summers at Sandia, working on my thesis project. Had Zoya not been willing to take a chance on something new, I would not have had the opportunity to stay actively involved in the company I wanted to work for.

I would also like to thank my other committee members: Dr. Tom DeGrand, Dr. Dejan Filipović, Dr. Ed Kuester, and Dr. Chris Rodenbeck. I appreciate the time they have invested during these last months of my studies, reading and evaluating my thesis and making suggestions regarding my work. I also

appreciate the time they have invested in my education, both in and out of the classroom. They have taught me invaluable technical skills and have fostered my desire to continually pursue new knowledge.

I would like to thank Sandia National Laboratories for funding my thesis project.[1] I would like to specifically thank a few individuals: John Dye for opening the door to a young engineer; Dr. Luke Feldner for introducing me to microwave engineering and helping me find my path; Tedd Rohwer and Dr. Chris Rodenbeck for having faith in me and supporting me throughout my graduate career; Clint Haslett, Ray Ortiz, and Dennis Wilder for technical support in the lab; and Brian Duverneay, Adam Ferguson, Rick Heintzleman, Rick Knudson, Jesse Lai, and Jeff Pankonin for mentoring me and providing excellent technical advice and support.

I would like to thank the administrative staff at CU for their time and assistance, especially Jarka Hladisova and Adam Sadoff. I would like to thank the U.S. Department of Education for funding Prof. Popović's Graduate Assistance In Areas of National Need (GAANN) fellowship proposal, which funded my first year of graduate research. Finally, I would like to thank Lincoln Laboratory for providing additional funding through their graduate fellowship.

[1] Sandia National Laboratories is a multi-program laboratory managed and operated by Sandia Corporation, a wholly owned subsidiary of Lockheed Martin Corporation, for the U.S. Department of Energy's National Nuclear Security Administration under contract DE-AC04-94AL85000.

Contents

List of Tables

List of Figures

Chapter 1

Introduction

This thesis presents a pulse Doppler radar that utilizes ultra-wideband (UWB) techniques to facilitate short-range target detection. To better present the requirements that drive the design, we begin with an overview of radar.

1.1 Radar Systems

Radar, which was originally an acronym for RAdio Detection And Ranging, has a rich history dating back to Heinrich Hertz's classical experiments in the 1880's [2]. Today, radar systems exist for a variety of applications from weather observation to guidance systems and law enforcement. In its simplest form, a radar system consists of three subsystems: a transmitter, a receiver, and an antenna system, as illustrated in Figure 1.1[1] . The transmitter generates an electrical signal that is radiated by the antenna system. If the signal is incident on a target, such as an airplane, rain, or a bird, it will be partially reflected back to the radar system and incident on the antenna system. The received signal will be routed by the antenna system to the receiver. The receiver processes the signal to determine the

[1] The nomenclature TX and RX will be used in this thesis for the transmitter and receiver subsystems, respectively.

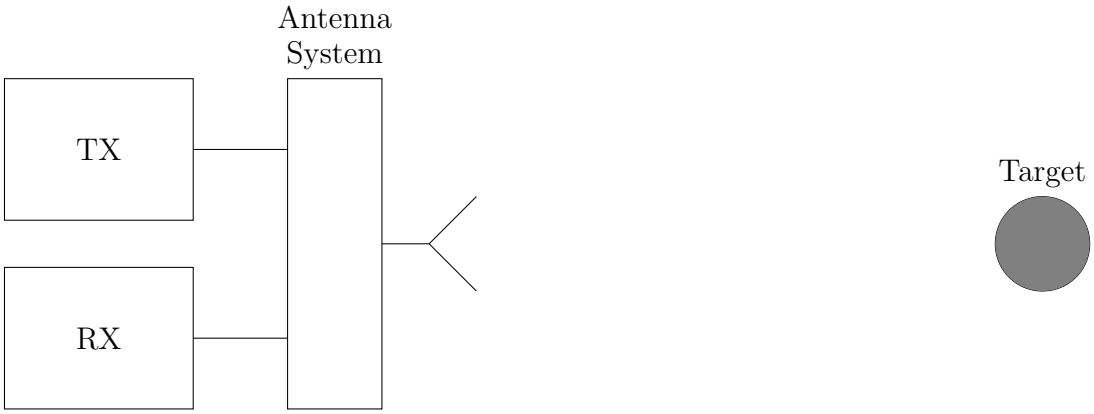

Figure 1.1: *Radar Subsystem Diagram.* A radar system consists of three subsystems: a transmitter, a receiver, and an antenna system. The radar system is used to detect the presence of a target, as well as characteristics of the target.

presence of a target, as well as target characteristics, such as range and velocity. A variety of design choices exist for each subsystem, and the primary subsystem characteristics are summarized in the following sections.

1.1.1 Transmitter

The transmitter's purpose is to generate an electrical signal that in transmitted by the antenna system, reflected from a target, and received by the antenna system. It can then be processed by the receiver to determine target characteristics, such as range and velocity. As such, the transmitter specifications focus on the desired transmitted waveform, and the transmitter hardware is designed to generate the specified waveform. Waveform characteristics and transmitter technologies are presented in the following sections.

Transmitted Waveform: Frequency Domain

Radar systems operate over a wide range of frequencies in the microwave regime, often considered to be between 300 MHz and 300 GHz [3]. In the past, most

Table 1.1: IEEE Standard RF Letter-Band Nomenclature. (Adapted from [2])

Band Designation	Nominal Frequency Range
HF	3–30 MHz
VHF	30–300 MHz
UHF	300–1000 MHz
L	1–2 GHz
S	2–4 GHz
C	4–8 GHz
X	8–12 GHz
K_u	12–18 GHz
K	18–27 GHz
K_a	27–40 GHz
V	40–75 GHz
W	75–110 GHz
mm	110-300 GHz

operational systems were designed in the 100 MHz to 36 GHz range; however, systems exist that operate at frequencies as low as a few megahertz and up to the millimeter-wave regime, where wavelengths are on the order of a millimeter [2]. Impulse, or carrier-free, radars operate down to frequencies on the order of 1 MHz [4] and light detection and ranging (LIDAR) systems operate in the optical regime [5].

The microwave spectrum is subdivided into bands, as noted in Table 1.1. Transmission in the electromagnetic (EM) spectrum is regulated by government bodies, such as the Federal Communications Commission (FCC) in the United States. A radio license is required to operate a microwave system in most of the EM spectrum; notable exceptions are the industrial, scientific, and medical (ISM) bands, which are 902–928 MHz, 2.400–2.484 GHz, and 5.725–5.850 GHz in the United States, and the UWB band, which is 3.1-10.6 GHz in the United States [3]. While a licence is not required, it is important to note that explicit rules exist for transmission in the ISM and UWB bands, especially related to the allowed power densities.

Microwave signals can be characterized by their carrier, or center, frequency and bandwidth. The carrier frequency is often defined as the frequency in the middle of the transmission band. For example, the carrier frequency could be 1.5 GHz for a radar operating in the 1–2 GHz L-band. The bandwidth describes the range of frequencies covered by the microwave signal and can be defined in a variety of ways:

- *3-dB Bandwidth.* The 3-dB bandwidth of a bandpass signal is defined by the half-power points of the signal spectrum. If f_h is the upper half-power corner frequency and f_l is the lower half-power corner frequency of the spectrum, then the 3-dB bandwidth is $\beta_{3dB} = f_h - f_l$, as illustrated in Figure 1.2a. In this thesis, the 3-dB bandwidth of a low-pass signal will be given based on the double-sided signal spectrum or the full-width half-maximum (FWHM) bandwidth. In other words, if the half-power corner frequency is f_l, then $\beta_{3dB} = 2f_l$, as illustrated in Figure 1.2b.

- *10-dB Bandwidth.* The 10-dB bandwidth is defined like the 3-dB bandwidth, except the corner frequencies are taken at the -10 dB points of the normalized signal power spectrum.

- *Fractional Bandwidth.* The fractional bandwidth of a bandpass signal is defined as $(f_h - f_l)/f_c$, where f_c is the center frequency of the signal and is defined as $(f_h + f_l)/2$. The corner frequencies can be selected as desired. In this thesis, the 3-dB and 10-dB fractional bandwidths will be used, where the corner frequencies are selected as the -3 dB and -10 dB points, respectively.

- *Bandwidth Ratio.* The bandwidth of a bandpass signal can be defined as the ratio of the upper to lower corner frequency, or $f_h/f_l : 1$. A bandwidth

ratio of 2:1 corresponds to an octave; a bandwidth of 10:1 corresponds to a decade.

- *Effective Bandwidth.* The effective bandwidth, or the root mean square (rms) bandwidth, is defined as

$$\beta_{eff}^2 = \frac{\int_{-\infty}^{\infty}(2\pi f)^2|S(f)|^2 df}{\int_{-\infty}^{\infty}|S(f)|^2 df} \tag{1.1}$$

  where β_{eff} is the effective bandwidth, f is frequency, and $S(f)$ is the double-sided, baseband signal spectrum [6]. It is used when calculating radar accuracies, as in Section 2.1.1.

Transmitted signals are classified as narrowband, wideband, or UWB based the signal bandwidth. A narrowband signal has up to 1% 10-dB fractional bandwidth; a wideband signal has between 1% and 20% 10-dB fractional bandwidth [7]; and a UWB signal has greater than 20% fraction bandwidth [8]. Most conventional radar systems are narrowband [9].

Transmitted Waveform: Time Domain

It is also important to consider the time-domain characteristics of the transmitted radar signal. The radar signal can be a continuous-wave (CW) waveform or a pulsed waveform. A CW transmitter broadcasts a continuous radio frequency or radar frequency (RF) signal, while a pulsed transmitter broadcasts a train of RF pulses with a system-specific carrier frequency, pulse repetition frequency (PRF), and duty cycle. The PRF is the frequency at which the RF pulses are transmitted and is equal to $1/T$, where T is the time between transmitted pulses, as shown in Figure 1.3. The duty cycle is defined as the ratio τ:T, where τ is the transmitted pulsewidth.

CW radar systems are generally simpler than pulsed radars in terms of hardware and signal control since they are always on. However, the design of

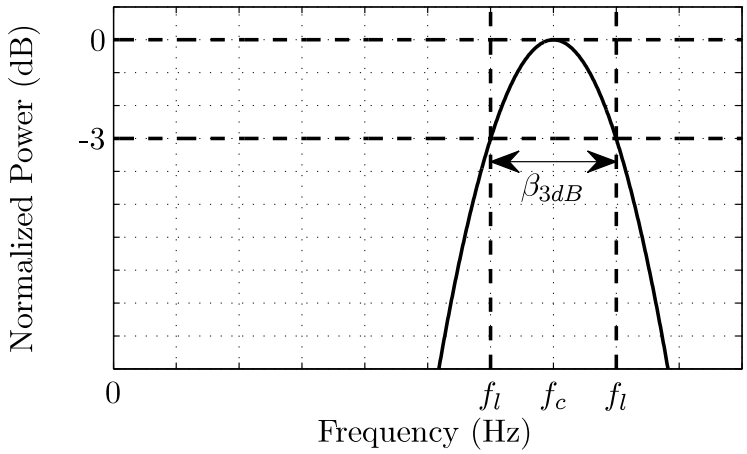

(a)

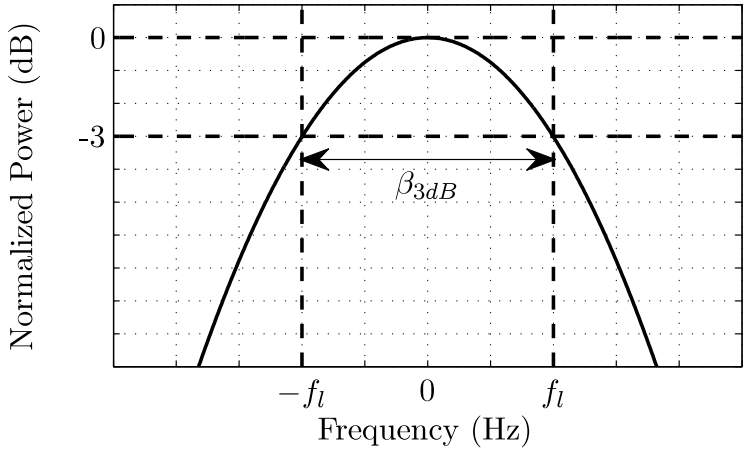

(b)

Figure 1.2: *Bandwidth Definitions.* The 3-dB bandwidth of a bandpass and low-pass signal are illustrated in (a) and (b), respectively.

CW radars is complicated due to significant disparity between the transmitted and received power levels; the power ratio can be can be on the order of $P_{TX} : P_{RX} = 10^9$, making detection difficult. In a pulsed system, the transmitter and receiver are never on simultaneously, making it easier to detect a target return at the expense of increased hardware and signal complexity.

A pulsed radar signal can be incoherent or coherent. To be coherent there must be a deterministic phase relationship for the carrier from pulse to pulse.

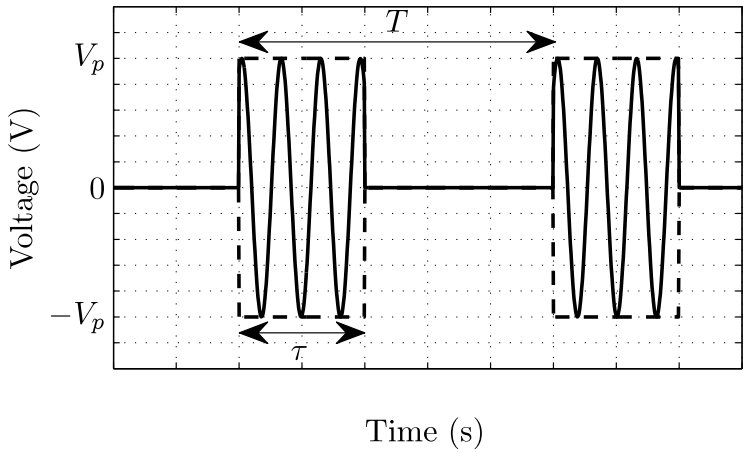

Figure 1.3: *Pulsed Signal.* A pulsed signal is defined by its carrier frequency, PRF, and duty cycle, where the PRF equals $1/T$ and the duty cycle equals τ/T.

This can be accomplished by switching a CW carrier on and off.

Transmitted Waveform: Power

The transmitted power level is application dependant. The required power level will depend on a variety of criteria including: the selected duty cycle, the range to the target, the radar cross section (RCS) of the target, the antenna system, the receiver characteristics, and the transmission environment. The relationship between the transmitted power level and these criteria will be discussed in Section 1.2 in the context of the radar range equation.

Transmitted Waveform: Modulation

Both CW and pulsed transmitters can include waveform modulation, which can be phase modulation, frequency modulation, amplitude modulation, or a combination of modulation types. For pulsed systems, the modulation can be applied within each pulse over the time period τ, so the modulation varies throughout the pulse. Alternately, the modulation can be constant over each

individual pulse; in this case, the modulation is often referred to as pulse tagging. Waveform modulation will be discussed in more detail in Chapter 2 as it relates to the radar described in this work.

Transmitter Technologies

Transmitter architectures can be divided into two categories: power oscillator transmitters and power amplifier transmitters [10]. Power oscillator transmitters typically employ a magnetron, or similar device, to generate the transmitted signal directly. A power amplifier transmitter generates the RF signal at low power using an oscillator and amplifies the signal with a power amplifier or a set of power amplifiers. Power amplifier transmitters can be constructed using vacuum tubes or solid-state devices.

Power amplifier transmitters exhibit advantages over power oscillator transmitters in terms of stability, since a lower-power LO combined with a power amplifier (PA) can be designed with better stability than a high power oscillator. As such, power amplifier transmitters are better suited for coherent radar systems [11]. A power amplifier transmitter will be used in this thesis work.

The component technology also impacts the capabilities of the transmitter. Tube-based devices are often used for high power applications, as they can produce 1 kW to 1 MW average power. Solid-state devices, such as transistors, are typically used for lower power applications. Single transistors can achieve up to few hundred watts at S-band, and transistor amplifier arrays have been demonstrated at kilowatt power levels. Solid state devices are of particular interest in radar transmitters because the devices have a long mean time between failure, leading to higher system reliability. In addition, solid-state design lends itself to modular construction, simplifying the initial system design and allowing for easy system maintenance. Finally, solid state devices operate at lower voltages

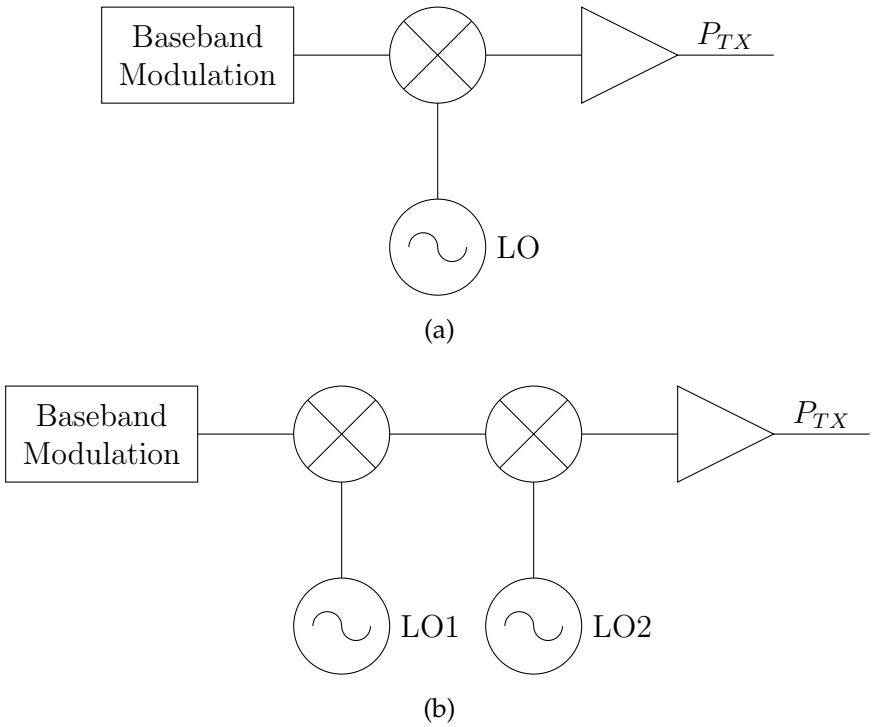

Figure 1.4: *Power Amplifier Transmitter.* A homodyne transmitter is shown in (a), and a heterodyne transmitter is shown in (b).

than tube-based devices and have low noise and good stability [10]. This thesis work focuses on a low-power design ($P_p^{TX} \simeq 1\,\mathrm{W}$), so solid-state devices will be used.

Two examples of simple power amplifier transmitter architectures are illustrated in Figure 1.4. Part (a) illustrates a homodyne architecture where a baseband signal modulates the RF LO signal through a mixing stage. The prefix "homo-" indicates that a single upconversion stage is utilized. Part (b) illustrates a heterodyne architecture where the baseband signal undergoes two stages of upconversion, with two different LOs, resulting in an RF carrier equal to the sum of the LO frequencies. The prefix "hetero-" indicates that two or more upconversion stages are utilized.

1.1.2 Antenna System

There is a great deal of variety in antenna system design, and the antenna system specifications depend on the application. Here we will focus on following variables: the antenna pattern, the number of antennas, and the antenna locations.

Antennas can be directional or omnidirectional. Directional antennas radiate energy more effectively in some directions than in others [12]; examples include horn antennas, tapered slot antennas, spiral antennas, and Yagi-Uda antennas. Omnidirectional antennas radiate energy uniformly in one plane and are directional in perpendicular planes [12]; the doughnut-shaped pattern of a dipole antenna is an excellent example. Directional and omnidirectional antennas are often specified relative to isotropic antennas. An isotropic antenna is a hypothetical antenna which radiates equally in all directions [12].

Radar antenna systems can consist of a single TX/RX antenna, a pair of antennas for transmission and reception, or an array of antennas. A single TX/RX antenna can be used for pulsed systems, but is normally avoided in CW configurations [13]; a single antenna system is illustrated in Figure 1.5a. When a single antenna is employed, a circulator is used to connect the transmitter, antenna system, and receiver. Assuming an ideal circulator, the transmitted signal passes from port 1 to 2 of the circulator, but not port 3; as such, the transmitted signal does not reach the receiver. If a target is present, the reflected signal is received by the antenna system and passed from port 2 to 3 of the circulator, but not port 1; as such, the received signal is passed to the receiver but not the transmitter. Realistically, there will be finite isolation between the circulator ports, leading to finite isolation between the transmitter and receiver. The ratio of the transmitted to received power is normally several orders of magnitude, so it is vital that the circulator provide sufficient isolation between ports 1 and 3 to allow the receiver to detect the received signal without being

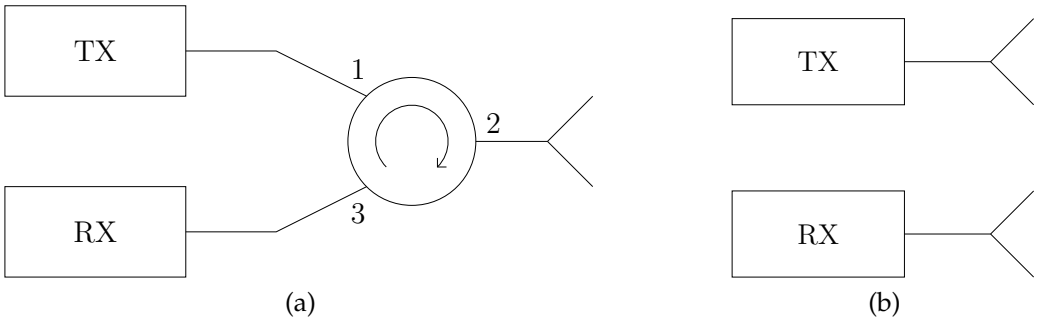

Figure 1.5: *Antenna Systems.* Antenna systems can include one or two antennas or an array of antennas. A single antenna system design is illustrated in (a); a two-antenna system is illustrated in (b).

jammed by the transmitted signal that leaks through the circulator.

If separate transmit and receive antennas are used, the circulator of Figure 1.5a can be eliminated in favor of the setup in Figure 1.5b. In this case two antennas are used, and the intrinsic isolation between the antennas is leveraged to minimize the leakage from the transmitter to the receiver through the antenna system [13].

Finally, the antenna system can be comprised of an array of antennas. The transmitter and receiver can share an antenna array or use separate arrays. Antenna arrays are often used to achieve high directivity and are used extensively in radio astronomy and synthetic aperture radar (SAR) applications [14].

If separate transmit and receive antennas are used, the antenna system can use either a monostatic or bistatic setup. In a monostatic setup, the transmit and receive antennas are close together. For first order approximations, monostatic antennas are assumed to be colocated. In a bistatic setup, the transmit and receive antennas are far apart, allowing for increased isolation between the transmitter and receiver through the antenna system. However, the separation distance must be accounted for when processing received target returns to ensure correct calculation of range or other target characteristics.

1.1.3 Receiver

The radar receiver must amplify, filter, and downconvert the received target echo in such a way that the resulting intermediate frequency (IF) or baseband signal can be processed to discriminate between the desired echo and any interferers, including noise, clutter, etc. [15]. The functionality of the receiver is accomplished by two receiver subsections, the RF front-end and the IF block, as shown in Figure 1.6. The RF front-end is comprised of an low noise amplifier (LNA), a bandpass filter, and a downconverter. As the first stage in the receiver, the LNA should exhibit high gain and a low noise figure to maintain a low noise figure for the overall receiver. The bandpass filter sets the RF bandwidth of the receiver and limits the receiver noise. The downconverter converts the received signal frequency to the IF band by mixing the received signal with the LO. In a coherent radar system, the receiver's LO is synchronized with the transmitter's LO; coherent systems are common in modern radar systems. In a heterodyne architecture, the downconverted signal is centered around the first LO frequency; in a homodyne architecture, the downconverted signal is centered at DC. Upon downconversion to the IF band, the signal is filtered and amplified. The IF filter sets the final noise bandwidth of the receiver. The output of the receiver is then digitized, and digital signal processing is applied.

The signal processing can be facilitated by including I/Q channels. I/Q channels can be set up in multiple ways. The downconverter can be replaced by an I/Q demodulator, resulting in I and Q IF channels. Alternatively, in a heterodyne setup, an I/Q demodulator can be added at the output of the IF block, and the baseband I and Q channels can be digitized separately. Finally, it is possible to perform the I/Q demodulation after the digitizer, as discussed in [15].

In addition to the stated components, the RF front-end or IF block can include a variable gain or attenuation stage or a limiter [15]. A variable gain or attenuation

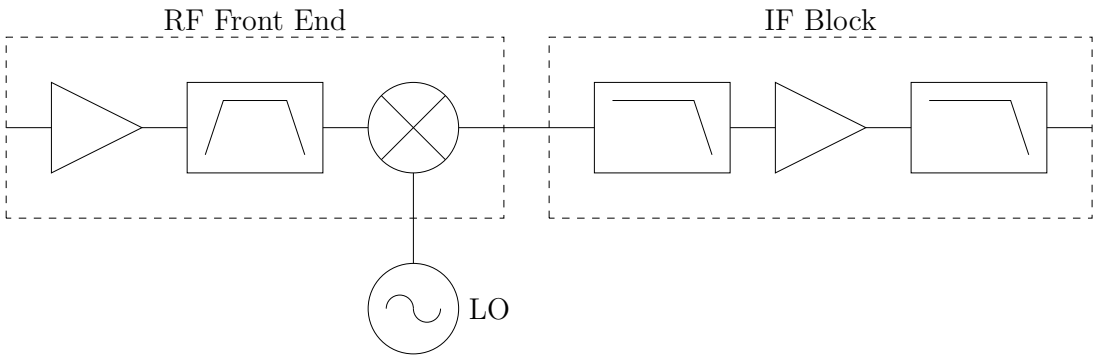

Figure 1.6: *Basic Receiver Architecture.* A basic receiver consists of two subsections– the RF front-end and the IF block.

stage can be used to improve the sensitivity or dynamic range of the receiver. One example of a variable attenuation stage is a range gate, which will be presented in Section 3.2. A limiter can be used to protect the receiver from large amplitude signals and to improve the dynamic range of the receiver.

1.2 Radar Range Equation

The radar channel includes the environment surrounding the radar, including the target and any interfering reflectors. The radar channel impacts the transmitter and receiver requirements and can be represented by the radar equation:

$$P_{in}^{RX} = \frac{P_{TX} G_{A,TX} G_{A,RX} \lambda^2 \sigma}{(4\pi)^3 R^4} \tag{1.2}$$

where P_{in}^{RX} is the power at the input of the receiver, P_{TX} is the power at the output the transmitter, $G_{A,TX}$ is the transmit antenna gain, $G_{A,RX}$ is the receive antenna gain, λ is the wavelength of the carrier frequency, σ is the RCS of the target, and R is the range to the target [16]. The radar equation is often modified to suit a particular application, but the form will be similar to Eqn. (1.2) [17].

Additional channel loss mechanisms, such as atmospheric attenuation due to oxygen or water vapor, and system loss mechanisms, such as sampling loss,

can also be included in the radar range equation as follows:

$$P_{in}^{RX} = \frac{P_{TX} G_{A,TX} G_{A,RX} \lambda^2 \sigma}{(4\pi)^3 R^4 L_A^{ch} L_A^{sys}} \tag{1.3}$$

where L_A^{ch} is the additional channel loss and L_A^{sys} is the additional system loss.

1.2.1 Maximum Range, Receiver Sensitivity, and Dynamic Range

The maximum range of a radar is:

$$R_{max} = \left(\frac{P_{TX} G_{A,TX} G_{A,RX} \lambda^2 \sigma}{(4\pi)^3 S_{min}^{in}} \right)^{\frac{1}{4}} \tag{1.4}$$

where R_{max} is the maximum target range and S_{min}^{in} is the minimum detectable power at the input of the receiver. The expression demonstrates the relationship between the target range, transmitted power, and minimum detectable received power. Increasing the transmitted power and/or decreasing the minimum detectable received power increases the maximum range of the radar. A 2-fold increase in R_{max} requires a 16-fold increase in P_{TX} or a 16-fold decrease in S_{min}^{in}.

The minimum detectable received power is often related to the receiver voltage sensitivity through the following expression:

$$V_{min}^{in} = \sqrt{2 Z_o S_{min}^{in}} \tag{1.5}$$

where V_{min}^{in} is the voltage sensitivity and Z_o is the receiver characteristic impedance [18]. The voltage sensitivity describes how small the received radar signal can be before it is overcome by noise.

Another standard receiver specification is the dynamic range, which is defined as:

$$\text{DR} = \frac{S_{max}^{in}}{S_{min}^{in}} \tag{1.6}$$

where DR is the dynamic range and S_{max}^{in} is the maximum allowable power at the input of the receiver [18]. S_{max}^{in} can be defined based on any number of distortion specifications such as the 1-dB compression point of the receiver [17]. The dynamic range describes the range of powers that can be processed by the receiver. There is normally a trade-off between sensitivity and dynamic range, and it is important to consider which is more important in the initial design stages [18].

1.2.2 Receiver SNR

One common receiver specification is the minimum single-pulse SNR at the output of the receiver. It can be related to S_{min}^{in} as follows:

$$\mathrm{SNR}_{1,min}^{out} = \frac{\mathrm{SNR}_{1,min}^{in}}{F_{RX}} = \frac{S_{min}^{in}}{k_B T_{ant} \beta_N F_{RX}} \tag{1.7}$$

where $\mathrm{SNR}_{1,min}^{out}$ is the minimum detectable SNR at the output of the receiver, $\mathrm{SNR}_{1,min}^{in}$ is the minimum detectable SNR at the input of the receiver, F_{RX} is the noise figure of the receiver, k_B is the Boltzmann constant (1.38e-23 J/K), T_{ant} is the antenna temperature, and β_N is the noise bandwidth of the receiver [19]. By substituting Eqn. (1.2) into Eqn. (1.7), SNR_1^{out} can be written in terms of the transmitted power.

$$\mathrm{SNR}_1^{out} = \frac{P_{TX} G_{A,TX} G_{A,RX} \lambda^2 \sigma}{(4\pi)^3 R^4 k_B T_{ant} \beta_N F_{RX}} \tag{1.8}$$

1.2.3 Radar Cross Section

The RCS of an object is the projected area of a metal sphere that would return the same echo signal as the object [20]. For all but the simplest targets, a sphere is an overly simplistic model; however, RCS remains a standard measure to characterize radar targets. Target behavior can be divided into three regimes

based on the size of the target's equivalent sphere. The regimes are the Rayleigh region, optics region, and resonance or Mie region [20], [16]:

- The Rayleigh region includes targets that are small compared to the transmitted wavelength ($2\pi a \ll \lambda$, where a is the radius of the equivalent sphere); the targets are not resolvable and behave roughly as point targets. The reflection from a point target is based on diffraction, which is discussed below. The RCS is proportional to f^4 in the Rayleigh region, where f is frequency.

- The optics region includes targets that are large compared to a wavelength ($2\pi a \gg \lambda$). Specular reflections are the primary scattering mechanism in the optics region. The RCS of a sphere in the optics region is comparable to its physical area ($\sigma \simeq \pi a^2$).

- The resonance region includes targets whose size is comparable to a wavelength ($2\pi a \simeq \lambda$). These targets exhibit a superposition of specular reflections and creeping waves, which are discussed below. The RCS of a sphere in the resonance region oscillates as a function of frequency about its value in the optics region; the maximum value is 5.6 dB higher and the minimum value is 5.5 dB lower than the value in the optics region.

While some targets can be adequately represented by a single, spherical, scattering center or another well-defined target shape like a cylinder or a cone-sphere, many are too complex for such a simple representation and must be modeled as a set of discrete scattering points and mechanisms. There are seven basic scattering mechanisms, as illustrated in Figure 1.7 [20]:

(1) *Reentrant Structures.* Reentrant structures include cavities in a target, such as intake ducts, exhaust ducts, and cockpits on airplanes. Reentrant structures tend to be metallic and produce large echoes.

(2) *Specular Scatterers.* Specular reflections result from surfaces that are perpendicular to the radar's line-of-sight. The echo in the specular direction tends to be large but falls off quickly as the angle-of-incidence varies from 90°.

(3) *Traveling-Wave Echoes.* It is common for a surface wave to develop on a target if the angle of incidence is small (i.e. the line-of-sight is nearly parallel to the target). The surface wave will travel along the surface of the target and can be reflected from discontinuities toward the rear of the target. The resulting echo is called a traveling-wave echo and is common on targets such as airplanes and missiles. Traveling-wave echoes can be nearly as large as specular echoes.

(4) *Diffraction.* Tips, edges, and corners tend to diffract the radar signal but normally result in less significant echoes than specular reflections.

(5) *Surface Discontinuities.* Discontinuities such as seams, rivets, and gaps can result in diffractive echoes; the effects of surface discontinuities tend to be small.

(6) *Creeping Waves.* Creeping waves are the result of surface waves that follow the curvature of the target and are launched back toward the radar.

(7) *Interactions.* Interaction echoes result when the radar signal is reflected back toward the radar after bouncing off two or more target surfaces.

Target modeling is a challenging field and is normally approached using statistical techniques, as discussed in [16], [20], [21], and [22]. Oftentimes it is advantageous to simplify the problem and begin with a point-target model. This is particularly useful for proof-of-concept designs for a general set of applications; this is the approach taken in this thesis.

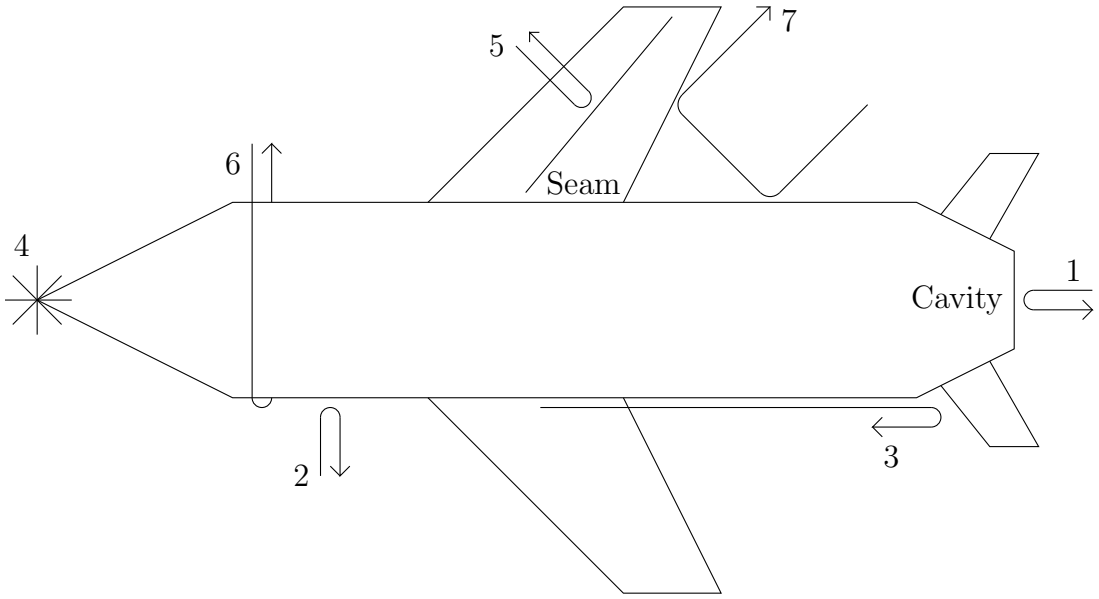

Figure 1.7: *Scattering Mechanisms.* A distributed scatterer, such as an airplane, can sometimes be modeled as a discrete set of point scatterers using various scattering mechanisms (Adapted from [20]).

1.2.4 Noise Figure

The noise figure of a device is a measure of the noise produced by the device [23]. It is defined as a the ratio of SNR at the input of the device to the SNR at the output of the device:

$$F = \frac{\text{SNR}_1^{in}}{\text{SNR}_1^{out}} \geq 1 \tag{1.9}$$

Eqn. (1.9) can be rewritten in terms of noise and device characteristics as follows:

$$F = \frac{P_{out,N}^{RX}}{k_B T_o \beta_N G} \tag{1.10}$$

where $P_{out,N}^{RX}$ is the noise power at the output of the device, k_B is Boltzman's constant, T_o is the temperature of the device, β_N is the noise bandwidth of the device, and G is the gain of the device.

The noise figure of a chain of devices, such as a receiver, can be calculated

using the following expression:

$$F = F_1 + \frac{F_2 - 1}{G_1} + \frac{F_3 - 1}{G_1 G_2} + ... + \frac{F_N - 1}{G_1 G_2 ... G_{N-1}} \tag{1.11}$$

where F_n is the noise figure and G_n is the gain of the n^{th} device. As can be ascertained from the expression, the noise figure and gain of the first device in the receiver have a significant impact on the overall noise figure of the receiver. The noise figure of a lossy element, such as an attenuator or a section of cable, is approximately equal to the loss of the component [24]. As such, it is beneficial to limit the loss between the receive antenna and the first LNA. In addition, it is desirable to select an RF LNA with a low noise figure and high gain in order to limit the noise figure of the receiver [24]. The noise figure of a good, narrowband microwave LNA can vary from several tenths of a dB to 1 dB, depending on the technology and frequency of the device [25]; a wideband LNA will typically have a larger noise figure. The gain of a single stage amplifier is practically limited to about 20–30 dB to ensure adequate device stability [26], [27].

1.3 Radar Applications

Radar is employed for a variety of applications, including the following short list:

(1) *Weather Radar.* Radar is used extensively to help understand and predict the weather and weather phenomena [2], as with the NEXRAD radar employed in the United States. Meteorological radar is discussed in [28].

(2) *Space Applications.* Radar has been used to observe meteors, the moon, the earth, and other planets [2]. Radar has also been employed in the guidance systems in rovers and other space vehicles [2]. Several examples are discussed in [29].

(3) *Imaging Radar.* High resolution imaging radars, such as interferometric synthetic aperture radar (ISAR) and SAR , have been used to create detailed maps of cities and terrain as well as for reconnaissance [30]. SAR images are available through several institutions, including Jet Propulsion Laboratory (JPL) (http://www.jpl.nasa.gov/radar/sircxsar/), Sandia National Laboratories (SNL) (http://www.sandia.gov/radar/sar-data.html), and Lincoln Laboratory.

(4) *Material Penetration and Characterization.* Low carrier frequency ($< 1\,\text{GHz}$) and carrier-free radar has been used extensively to penetrate and characterize materials, such as the ground, concrete, walls, and foliage. The low frequency content of the signals can penetrate further into these materials than higher frequency signals [31].

(5) *Military Applications.* Radar is used for offensive and defensive weapons systems [2]. It can be used for target detection, target recognition, weapon guidance, and weapon fuzing, to name a few applications [2].

(6) *Ranging Radar.* One of the original radar applications was ranging; in fact, ranging was such an important application that it is part of the original acronym: RAdio Detection And Ranging [2]. Radars are still employed extensively to determine the range to a target, as in this thesis.

(7) *Moving Target Indicators and Velocity Detection Radars.* Many radars employ the Doppler shift to detect targets and/or determine the target's velocity [13]. Both moving target indicator (MTI) and pulse Doppler radars employ the Doppler shift; pulse Doppler radar will be discussed in Section 2.2.2.

(8) *Localization Radar.* Similar to ranging radars, localization radars observe the distance to a target. However, rather than observing the range using

a single source, multiple sources are employed in order to determine the target position in three dimensions.

(9) *Air-Traffic Control.* Radars are used throughout the world to support safe air travel; they are used to monitor air traffic and weather systems in the vicinity of airports [2].

The radar target varies between applications and is important to consider when specifying a radar system. It can be advantageous to assume a point-like target for an initial radar design, as it allows additional flexibility; this is useful for this thesis as the radar under study is a generic prototype that can be augmented for use in a variety of applications.

Other target parameters, such as the target range and velocity, can also be used to specify the radar. This thesis will focus on short-range ranging applications, as discussed in Chapter 2.

Chapter 2

Short-Range Radar

Short-range radar is a challenging design task because of the limited time frame associated with a moving target in close proximity to the radar. This work defines short range to be less than 7 m. This chapter presents important considerations for short-range radar, as well as specific architectures that can be employed.

2.1 Short-Range Radar Parameters

Range accuracy, range resolution, Doppler accuracy, and Doppler resolution are important radar parameters for short-range applications and are defined in the following sections.

2.1.1 Range Accuracy and Resolution

Range accuracy, δR, is a metric that illustrates how accurately the radar can determine the range to a target. The rms range error, or range accuracy, is defined

as:

$$\delta R = \frac{c_o}{2\beta_{eff}\sqrt{2P_s/P_N}} \tag{2.1}$$

$$\beta_{eff}^2 = \frac{\int_{-\infty}^{\infty}(2\pi f)^2|S(f)|^2 df}{\int_{-\infty}^{\infty}|S(f)|^2 df} \tag{2.2}$$

where c_o is the speed of light, β_{eff} is the effective bandwidth of the radar signal (see Eqn. (1.1)), P_s is the signal power, and P_N is the noise power [6]; the range accuracy for rectangular and Gaussian pulse envelopes is given in Table 2.1. Based on the expression, the radar signal must be wideband or have a high SNR to achieve high range accuracy. This work uses a wide bandwidth to reduce the transmitted power requirements.

The range resolution defines how far apart two targets must be in range for the radar to resolve them. The range resolution of a radar can be determined by considering returns from two targets; for simplicity consider a Gaussian pulse envelope, as shown in Figure 2.1. If the targets are spaced too closely, the returns will superimpose, and the radar will register a single target return, as in Figure 2.1a. If the target returns are spaced such that their FWHM points align, as in Figure 2.1b, the targets will be just resolvable, and the time delay between the peaks defines the range resolution:

$$\Delta R = \frac{\tau c_o}{2} \tag{2.3}$$

where τ is the FWHM pulsewidth [6]. Based on the expression, fine range resolution results from narrow pulses (for a pulsed system). Narrow pulses correspond to wide bandwidths, which are required for accurate ranging. It is important to note, however, that a highly accurate radar does not necessarily ensure fine range resolution [6].

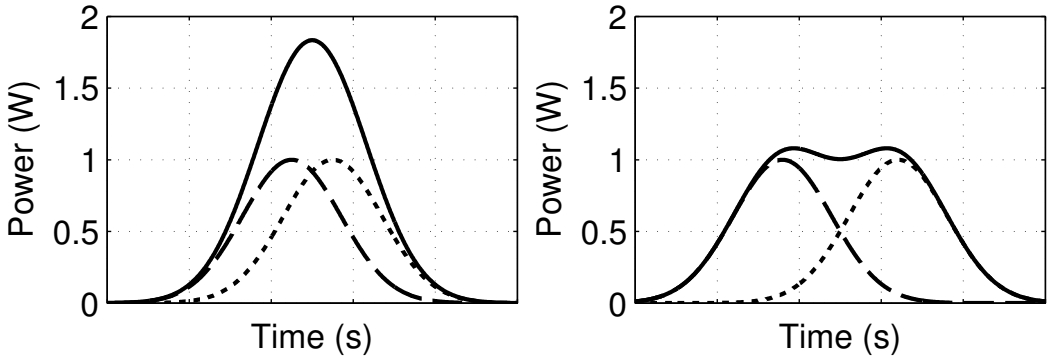

(a) (b)

Figure 2.1: *Range Resolution.* Range resolution is a measure of how far apart two targets must be in order for a radar to resolve them and is dependant on the transient signal characteristics. The dashed and dotted waveforms represent independent target returns, and the solid waveform represents the composite waveform. In (a), the returns are not resolvable. In (b), the peaks of the returns are separated in time by their FWHM pulsewidth and are just resolvable.

2.1.2 Doppler Accuracy and Resolution

Doppler accuracy is a measure of how accurately a radar can determine the Doppler shift of a target and, thus, its velocity. The rms error in a Doppler frequency measurement is:

$$\delta f_D = \frac{1}{\alpha \sqrt{2P_s/P_N}} \tag{2.4}$$

$$\alpha^2 = \frac{\int_{-\infty}^{\infty} (2\pi t)^2 s^2(t) dt}{\int_{-\infty}^{\infty} s^2(t) dt} \tag{2.5}$$

where $s(t)$ is the received time domain signal, which peaks at $t = 0$, and α is the effective time duration of the signal [6]. The Doppler accuracy for rectangular and Gaussian pulse envelopes is given in Table 2.1. As can be seen, wide pulsewidths lead to high Doppler accuracy; this is in contention with the short pulsewidths that lead to high range accuracy and resolution. The trade-off between range accuracy/resolution and Doppler accuracy, as well as techniques to resolve the trade-off, are discussed in Section 2.1.3.

Table 2.1: Doppler Accuracy [6]

Pulse Envelope Shape	δR	δf_D
Rectangular	$\sim \frac{c_o \tau}{4.2\sqrt{2P_s/P_N}}$	$\frac{\sqrt{3}}{\pi\tau\sqrt{2P_s/P_N}}$
Gaussian	$\frac{c_o \tau}{2.36\sqrt{2P_s/P_N}}$	$\frac{1.18}{\pi\tau\sqrt{2P_s/P_N}}$

Doppler resolution refers to the radar's ability to distinguish between two targets with different velocities. Like frequency accuracy, the frequency resolution improves as the effective time duration of the signal increases.

2.1.3 Radar Uncertainty Principle

For a simple radar system, there is a trade-off between range and Doppler accuracy, which is related to the radar uncertainty principle [6]:

$$\beta_{eff}\alpha \geq \pi \tag{2.6}$$

By multiplying Eqns. (**??**) and (2.4), and substituting Eqn. (2.6), we obtain:

$$\delta R \delta f_D \leq \frac{c_o}{2\pi(2P_s/P_N)} \tag{2.7}$$

It is evident that the product of the range and Doppler accuracies is limited by the radar uncertainty principle. In order to reduce the uncertainty product, both the effective bandwidth, β_{eff}, and the signal duration, α, should be large. This can not be achieved with a single pulse, as discussed. However, by integrating multiple pulses, the effective signal duration can be increased, while the effective bandwidth is maintained. As such, pulsed radars often employ pulse integration at the output of the receiver to improve the Doppler accuracy, as well as the overall radar accuracy.

2.2 Short-Range Radar Architectures

A variety of architectures can be employed to implement a short-range radar. The primary architectures are frequency-modulated continuous-wave (FMCW) radar, pulse Doppler radar, and pulse compression radar.

2.2.1 Frequency-Modulated Continuous-Wave Radar

CW radars transmit an uninterrupted RF sinusoid. If the transmitted signal is reflected by a moving target, then the sinusoid is Doppler shifted by an amount $f_D = 2f_c v/c_o$. The reflected signal is detected by the receiver, and the velocity of the target is determined based on the Doppler shift. A standard CW radar cannot determine the range to the target; however, the range can be determined by employing frequency modulation. A common topology for an FMCW radar is shown in Figure 2.2a. The voltage controlled oscillator (VCO) is swept from f_l to f_h, resulting in a full-scale frequency change of Δf. A linear, triangular frequency modulation is common for FMCW and is illustrated in Figure 2.2b. The transmitter transmits a signal at frequency f_1. The signal propagates until it reaches a target at range R, where it is reflected and reaches the receiver after a delay of $t_R = 2R/c_o$. The signal is mixed with the current transmitted signal, resulting in a frequency change f_r:

$$f_r = \frac{4Rf_m\Delta f}{c_o} \tag{2.8}$$

where f_m is the modulation frequency, as illustrated in Figure 2.2b [13]. Assuming zero-crossing processing, the range accuracy is:

$$\delta R = \frac{Af_r c_o}{4f_m\Delta f} \tag{2.9}$$

where A is a constant [32]. Based on the expression, a wide bandwidth is needed for fine range accuracy. In order to achieve a wide bandwidth, the VCO must

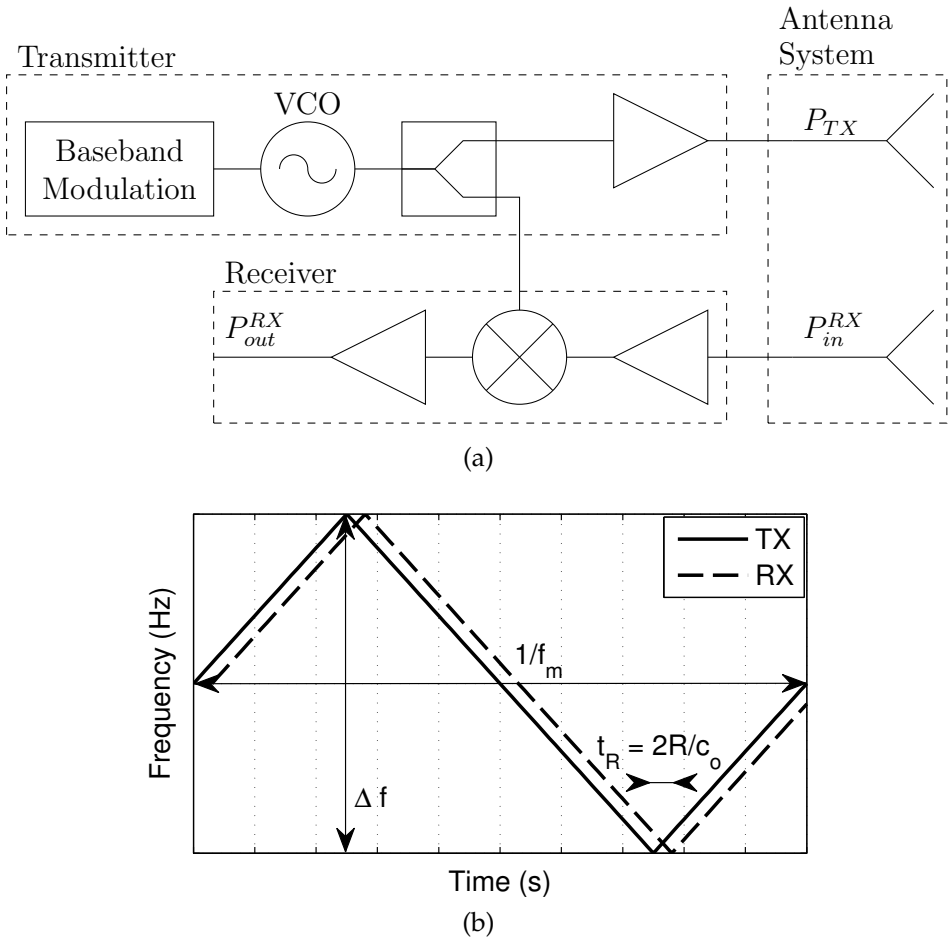

Figure 2.2: *Basic FMCW Architecture.* A basic FMCW radar sweeps the frequency of an RF VCO over a pre-determined bandwidth from f_l to f_h in order to allow target range and Doppler determination ((b) adapted from [13]).

operate with a large fractional bandwidth; this is a challenging design criteria, as discussed in [33].

For short-range radar, the minimum detectable range is also important. For FMCW radar, the minimum range is not limited by the radar signal. The minimum detectable range is ultimately limited by the TX-RX isolation, but for comparison to other architectures, we assume the minimum detectable range is not limited for FMCW radar.

Range accuracy, hardware constraints, and minimum range are not the only considerations for a short-range radar; the peak transmitted power, the ability to

resolve multiple targets, the ability to reject clutter, and the TX-RX isolation are also important. Since FMCW radars transmit a continuous signal, the average power is equal to the rms power of the signal. As a result, the peak power of the signal is low compared to pulsed signals [13]. FMCW radar does not provide a simple means to resolve targets, and it does not have the natural clutter rejection capabilities of a pulsed radar since the receiver is always on [13]. Since the transmitter and receiver are both on continuously, TX-RX isolation is a significant design challenge. Often, FMCW radars use separate transmit and receive antennas to achieve the desired TX-RX isolation, whereas other architectures, such as pulsed radars, can use a single antenna to accomplish both transmission and reception [13]. Sometimes, modulation techniques can be employed so a single antenna can be used for an FMCW radar, as discussed in [34], at the cost of increased signal processing and hardware complexity. The characteristics of FMCW radar are summarized in Table 2.2.

2.2.2 Pulse Doppler Radar

A pulsed radar architecture is illustrated in Figure 2.3. A baseband pulse envelope is generated and applied to the IF port of the upconverter. The RF signal is generated using a stable oscillator and applied to the RF port of the upconverter. The resulting upconverted signal occupies a bandwidth of approximately $\beta \simeq 1/\tau$, where τ is the pulsewidth of the envelope; the precise bandwidth will depend on the shape of the baseband envelope [6]. It is common to illustrate the baseband envelope as a series of rectangular pulses, but the envelope shape can be selected to suit the radar requirements.

As with FMCW radar, if the pulsed transmitted signal is reflected by a moving target, then the reflected signal is Doppler shifted. The reflected signal can be detected by the receiver, and the velocity of the target is determined based on the

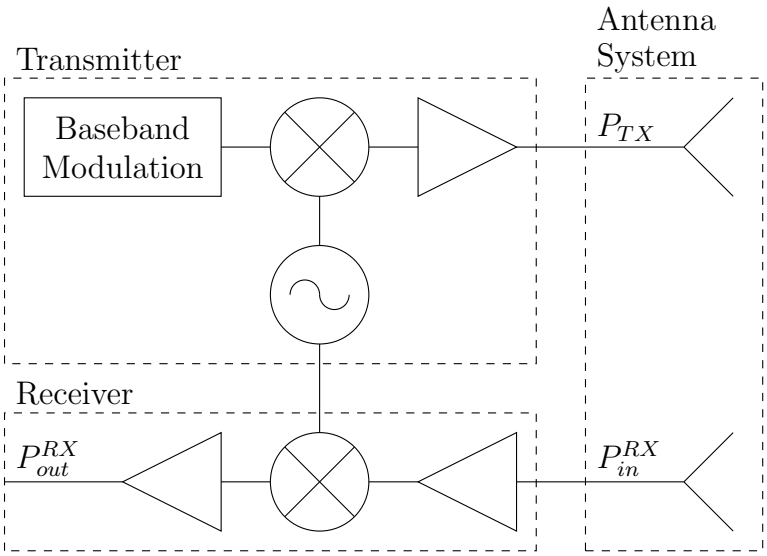

Figure 2.3: *Basic Pulse Doppler Architecture.* A basic pulse Doppler radar transmits a pulse of RF energy in order to allow target range and Doppler determination.

Doppler shift. The receiver often employs a range gate in the RF front-end. Range gating allows the radar user to select a single target range to observe. When open, the range gate allows normal signal detection; when closed, it attenuates the received signal so that it is not detectable. The range-gate pulsewidth is normally matched to the transmitted pulsewidth, and the leading edge is delayed by an amount t_R^{obs}, relative to the transmitted pulse. The observable range to the target can then be established as $R_{obs} = c_o t_R^{obs}/2$.

The range accuracy for a rectangular and Gaussian pulse envelope is given in Table 2.1. As discussed in Section 2.1.1, a wide bandwidth leads to fine range accuracy; a narrow pulsewidth corresponds to wide bandwidth and is one way to achieve fine range accuracy, as seen from the table. As such, a pulsed transmitter for short range detection must include a short-pulse generator. However, unlike an FMCW radar, it only requires a single frequency LO.

The minimum detectable range of a pulse Doppler radar is limited by the transmitted pulsewidth. The transmitter and receiver are never on simultaneously,

and the receiver cannot be turned on until after the transmitter completes its transmission, leading to a minimum range of $R_{min} = c_o\tau/2$. As with the FMCW architecture, the minimum detectable range of a pulse Doppler system will be limited by nonidealities, including finite TX-RX isolation and clutter. However, the fundamental limit is a result of the transmitted pulsewidth.

Unlike FMCW radars, a pulsed radar does not transmit a continuous signal, and, assuming a rectangular pulse envelope, the average power is equal to $P_p\tau/T$, where P_p is the peak power of the signal. Assuming a given average power, the required peak power of a short-pulse signal is high compared to other radar signals, due to its low duty cycle (τ/T). However, for short-range radar, the power requirements are relatively low, so a "high" peak power may not be a concern.

Pulsed radars provide natural target resolution and clutter rejection due to range gating; the pulsed nature of the transmitter simplifies target resolution, and the pulsed nature of the receiver simplifies clutter rejection. Since both the transmitter and receiver are pulsed, TX-RX isolation requirements are also simpler to meet than with a CW system. The characteristics of pulse Doppler radar are summarized in Table 2.2.

2.2.3 Pulse Compression Radar

Pulse compression radars transmit a relatively long pulse that is frequency or phase modulated within each transmitted pulse; the modulation bandwidth is considerably wider than the pulse bandwidth [35]. For example, to achieve a 1 ns compressed pulsewidth, a 1 GHz modulation bandwidth with any pulsewidth could be employed. The received pulse is processed using a pulse compression filter, which compresses the pulse in time so that the processed pulse has a bandwidth roughly equal to the modulation bandwidth. Pulse compression radars exhibit the same fine range resolution and accuracy as short-pulse radars;

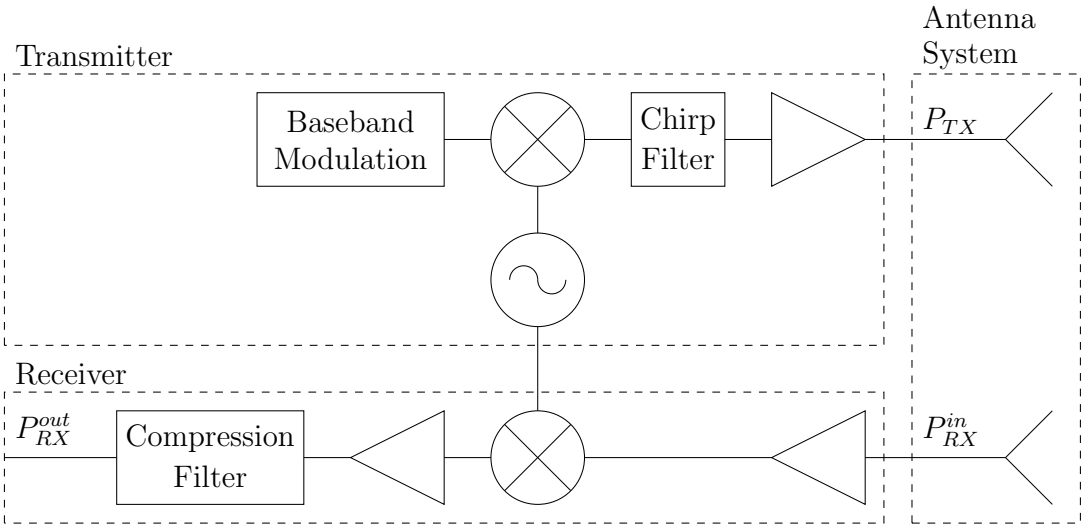

Figure 2.4: *Basic Pulse Compression Radar Architectures.* A passive pulse compression radar architecture is illustrated

however, the wide transmission pulsewidth reduces the peak power requirement and facilitates simpler pulse generation.

The pulse modulation, often a linear frequency chirp, can be generated using a passive or active circuit [36]. For passive generation, a narrow pulse of RF energy is time-expanded using a chirp filter. For an active implementation, a VCO with a linear control circuit can generate a chirp by sweeping the control voltage. A passive pulse compression radar architecture is illustrated in Figure 2.4; an active pulse compression radar architecture resembles the pulse Doppler architecture of Figure 2.3, except a baseband modulation is applied to the VCO.

The range accuracy for a pulse compression radar is based on the compressed pulsewidth, or equivalently, the modulation bandwidth. The expressions in Section 2.1.1 apply. As noted, a wide bandwidth leads to fine range accuracy.

The minimum detectable range of a pulse compression radar is limited by the transmitted pulsewidth. Since the transmitter and receiver are never on simultaneously, the minimum range is $R_{min} = c_o\tau/2$. The minimum range of a

pulse compression radar will be larger than an equivalently designed short-pulse Doppler radar because the pulse compression radar transmits a time-expanded pulse. The minimum detectable range will be limited by nonidealities, including finite TX-RX isolation and clutter.

For a given average power, a pulse compression radar can transmit a lower peak power than an equivalently designed short-pulse Doppler radar because the transmitted pulsewidth is wider. As the signal is pulsed, the peak power will be higher than for an FMCW radar with the same average power.

Like pulse Doppler radars, pulse compression radars provide natural target resolution and clutter rejection due to range gating, and the TX-RX isolation requirements are simpler to meet than with an FMCW system. The characteristics of pulse compression radar are summarized in Table 2.2.

2.2.4 Short-Range Radar Architecture Trade-Offs

It is useful to examine the trade-offs between the three proposed architectures as they are relevant to the goals of this work. Each architecture requires a set of broadband components to implement the transmitter source. FMCW and active, linear FM pulse compression radar both require a wideband VCO and control circuitry to linearly adjust the VCO's amplitude and frequency. A pulse generator is also required for the pulsed implementation. A single frequency LO and a short-pulse generator are required for the passive, linear-frequency modulated (FM) pulse compression radar and the short-pulse Doppler radar. In addition, the pulse compression radar requires a chirp filter to implement the frequency modulation. In summary, both implementations of transmitters for pulse compression radar require more source components than either the

FMCW or the short-pulse Doppler radar implementations.

In order to attain a constant average power for each architecture, the peak transmitted power requirement increases as the length of the transmitted pulse decreases; however, due to the short range requirement and wide bandwidth in this work, the peak transmitted power is about 1 W even for a short-pulse system. As such, peak power is not a primary factor in choosing an architecture.

Another trade-off is the required transmitter-to-receiver isolation. Pulsed systems, by nature, have high levels of isolation since the transmitter and receiver are never on simultaneously; the transmitter and receiver in a CW system, on the other hand, are always on, leading to spillover which must be mitigated [13].

Table 2.2: Short-Range Radar Trade-Offs

ARCHITECTURE	MINIMUM RANGE	TX SOURCE	PEAK POWER	MULTIPLE TARGETS	CLUTTER	TX-RX ISOLATION
FMCW Radar	No limit	Wideband VCO and control circuitry	Low	Difficult to resolve	Difficult to reject	Difficult challenge
Short-Pulse Doppler Radar	Short, limited by transmitted pulsewidth	LO and short-pulse generator	High	Resolvable	Limited by windowing	Moderate challenge
Active Linear FM Pulse Compression Radar	Moderate, limited by expanded pulsewidth	Wideband VCO, control circuitry, and wide-pulse generator	Moderate	Resolvable	Limited by windowing	Moderate challenge
Passive Linear FM Pulse Compression Radar	Moderate, limited by expanded pulsewidth	LO, short-pulse generator, and chirp filter	Moderate	Resolvable	Limited by windowing	Moderate challenge

Finally, the radar architecture impacts the minimum detectable range. An FMCW system theoretically does not have a minimum range, while both pulsed systems have a minimum detectable range. The minimum range of a pulsed system depends on the transmitted pulsewidth and will be shorter for the short-pulse Doppler radar than for the pulse compression radar.

Based on the trade-offs between the various architectures, a short-pulse Doppler architecture was selected for this work in order to: reduce the complexity of the source hardware, minimize the transmitter-to-receiver isolation requirement, and minimize the shortest detection range.

2.3 Short-Pulse Doppler Radar Parameters

The short-pulse Doppler radar design parameters can be broken into the following three categories, as illustrated in Figure 2.5:

(1) Frequency Domain Parameters:

- *Frequency Band of Operation.*
- *Carrier Frequency.* The carrier frequency, f_c, is the RF signal frequency.
- *PRF.* The PRF defines the rate at which pulses are transmitted.
- *Transmitted Envelope Bandwidth.* The envelope bandwidth, β_{3dB}, is related to the envelope pulsewidth, τ, as $\beta_{3dB} \simeq 1/\tau$. It is often expressed as the 10-dB bandwidth for radar systems, rather than the 3-dB bandwidth.
- *Anticipated Doppler Shifts.* The range of anticipated Doppler shifts is application specific and based on the expected target velocities. In this

work, the range will be defined as $0\,\text{Hz} < f_D \leq f_{max}^D = 50\,\text{kHz}$, making it applicable to a wide range of applications.

(2) Time Domain Parameters:

- *Pulse Repetition Interval.* The pulse repetition interval (PRI), T, defines the period of time between transmitted pulses and is related to the PRF as follows: $T = 1/\text{PRF}$.
- *Transmitted Envelope Pulsewidth.* The envelope pulsewidth, τ, defines the length of time during each PRI that the transmitter is "on". It is approximately inversely proportional to the envelope bandwidth.
- *Range Delay.* The range delay, t_R, refers to the length of time it takes the transmitted signal to reach the target and return to the receiver. It is defined by the range to the target, R, as $t_R = 2R/c_o$.
- *Range-Gate Pulsewidth.* The range-gate pulsewidth, τ_{RG}, defines the length of time the receiver is "on" and can receive signals. It can be set to match the transmitted pulsewidth ($\tau_{RG} = \tau$) or the desired range accuracy, δR ($\tau_{RG} = 2\delta R/c_o$).

(3) Range Parameters:

- *Target Range.* The expected range to the target, R, helps define radar parameters such as the range delay at which the range gate is opened.
- *Range Accuracy.* The range accuracy, δR, of a radar system can be calculated using Eqn. **??**.

The operation band is generally defined by the application; in this thesis, the operation band will be S-band. The carrier frequency is limited to the selected operation band, and is further constrained by the envelope bandwidth.

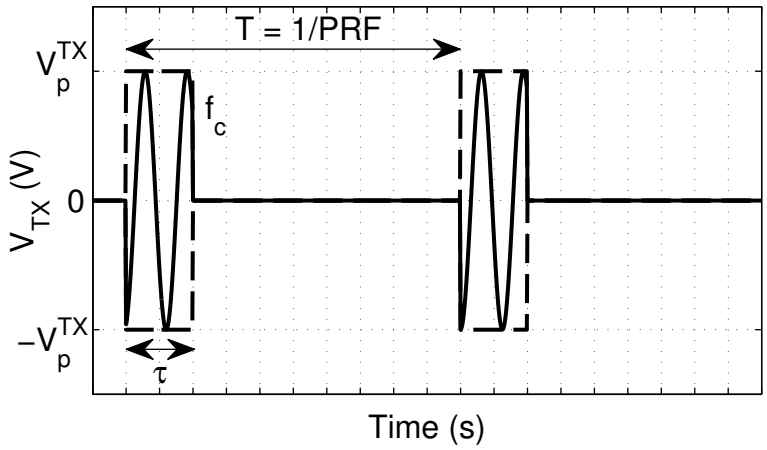

(a)

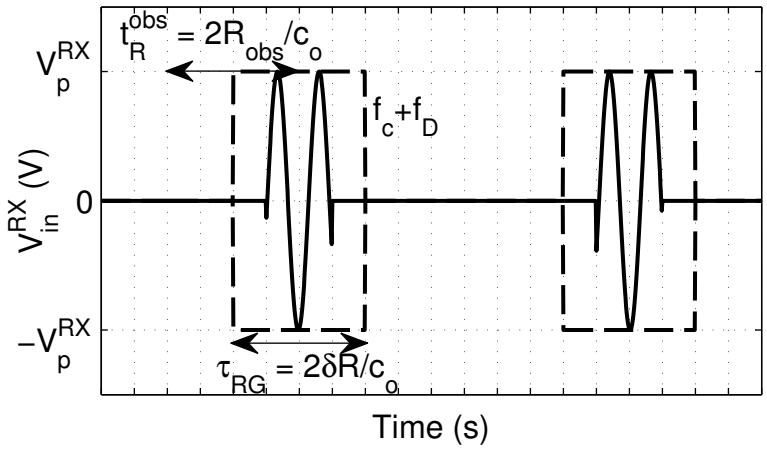

(b)

Figure 2.5: *Pulse Doppler Radar Design Parameters.* The various frequency domain, time domain, and range parameters associated with pulse Doppler radar are illustrated on the transmitted (a) and received (b) waveforms.

The PRF is often selected as a compromise between range and Doppler ambiguities. Range ambiguities arise when the target delay is longer than the PRI; in other words, it is assumed that the reflected signal is received before the next pulse is transmitted. The maximum unambiguous range is:

$$R_{max} = \frac{c_o T}{2} \tag{2.10}$$

Doppler ambiguities are also related to the PRF of the radar. The maximum unambiguous Doppler frequency is:

$$f_{max}^{D} = \frac{\text{PRF}}{2} \tag{2.11}$$

The limit can be understood in terms of Nyquist's sampling rate, $f_N = 2B$, where f_N is the Nyquist rate and B is the highest frequency of interest. The transmitted pulse train is effectively sampling the velocity of the target at a sampling rate of PRF; as such, the PRF can be related to the Nyquist sampling rate. The Doppler shift is the signal of interest and can be equated to B, providing a direct link between the Nyquist rate and the maximum unambiguous Doppler shift.

Eqns. (2.10) and (2.11) can be rewritten to establish criteria for selecting the PRF:

$$\text{PRF} \leq \frac{c_o}{2R_{max}} \tag{2.12}$$

$$\text{PRF} \geq 2f_{max}^{D} \tag{2.13}$$

Oftentimes, these criteria are in contention with one another. As a result, most pulsed radars fall into one of the following categories:

- *Unambiguous in Range, Ambiguous in Doppler.* These radars are traditionally referred to as MTI and have a low PRF; the definition of low is application specific.

- *Ambiguous in Range, Ambiguous in Doppler.* These radars are typically referred to as medium PRF radars.

- *Ambiguous in Range, Unambiguous in Doppler.* These radars are typically referred to as pulse Doppler radars and have a high PRF; the definition of high is application specific.

A variety of techniques exist to resolve range and/or Doppler ambiguities, as discussed in [37].

A special case arises if:

$$R_{max} f_{max}^{D} \leq \frac{c_o}{4} \tag{2.14}$$

If this condition is met, it is possible to unambiguously determine both the target range and velocity by selecting a PRF from the range $2f_{max}^{D} \leq \text{PRF} \leq c_o/2R_{max}$; for a short range radar, it is plausible to meet the condition and, thus, minimize the hardware and signal processing complexity of the radar. Given this range of PRFs, it is advantageous to select a PRF near the upper limit for two reasons: to increase the average transmitted power for a given pulse envelope and to increase the number of pulse returns in a given integration interval, both of which improve the radar detection probability.

As discussed, the transmitter and receiver of a pulsed radar are never on simultaneously, so blind zones exist whenever the transmitter is transmitting, as illustrated in Figure 2.6. For a pulsed radar designed for unambiguous range detection, a single blind zone exists for targets within the maximum range, and it limits the minimum detectable range. A narrow pulse envelope can be utilized to limit the impact of the blind zone and reduce the minimum detectable range. To achieve a blind zone of 1 m, the pulse envelope must decay to a prescribed level, P_{off}^{TX}, within nanoseconds, so it is advantageous to transmit a sub-nanosecond FWHM pulse. Unfortunately, in a realistic radar system, there is a finite TX-RX isolation, and some transmitted energy will leak directly from the transmit antenna to the receive antenna, resulting in an attenuated, delayed leakage signal incident on the receiver. It is evident that the leakage signal, which is illustrated in Figure 2.6, imposes a further limitation on the minimum detectable range. However, minimizing the envelope pulsewidth will still help minimize the shortest detectable range. In this thesis, a subnanosecond pulse envelope is

pursued.

A subnanosecond short-pulse Doppler radar system is a challenging design. This thesis utilizes UWB design techniques to generate a short pulse envelope and design transmitter, antenna system, and receiver components that can manipulate a subnanosecond pulse without distorting the pulse shape.

2.3.1 Ultra-Wideband Systems

Based on the FCC's definition, UWB systems have at least a 20% 10-dB fractional bandwidth or a 500 MHz 10-dB bandwidth [8]. The bandwidth can be used instantaneously or frequency hopping can be employed [38]. Systems that employ instantaneous UWB bandwidths typically use short pulses on the order of a nanosecond; this is directly related to the Fourier relationship between the time and frequency domains where a narrow time-domain pulse corresponds to a wide frequency-domain spectrum and vice-versa. Many of the UWB examples in the literature specifically utilize the FCC's UWB band, which is defined in Table 1.1. The UWB band is an unlicensed band, so systems designed in the band must conform to a spectral mask defined in [8]. This thesis does not assume operation in the UWB band.

UWB techniques have been used for a variety of applications including:

- *Ground Penetrating Radar.* ground-penetrating radars (GPRs) are typically carrier-free or employ a low frequency carrier (~500 MHz); the low frequency content of the transmitted signal allows it to penetrate materials such as concrete and soil more readily than a higher frequency signal. GPRs typically operate in the near-field [39] in order to map changes in the dielectric constant of the material under study. Consider a metallic object buried in the ground. The transmitted signal will be reflected from the

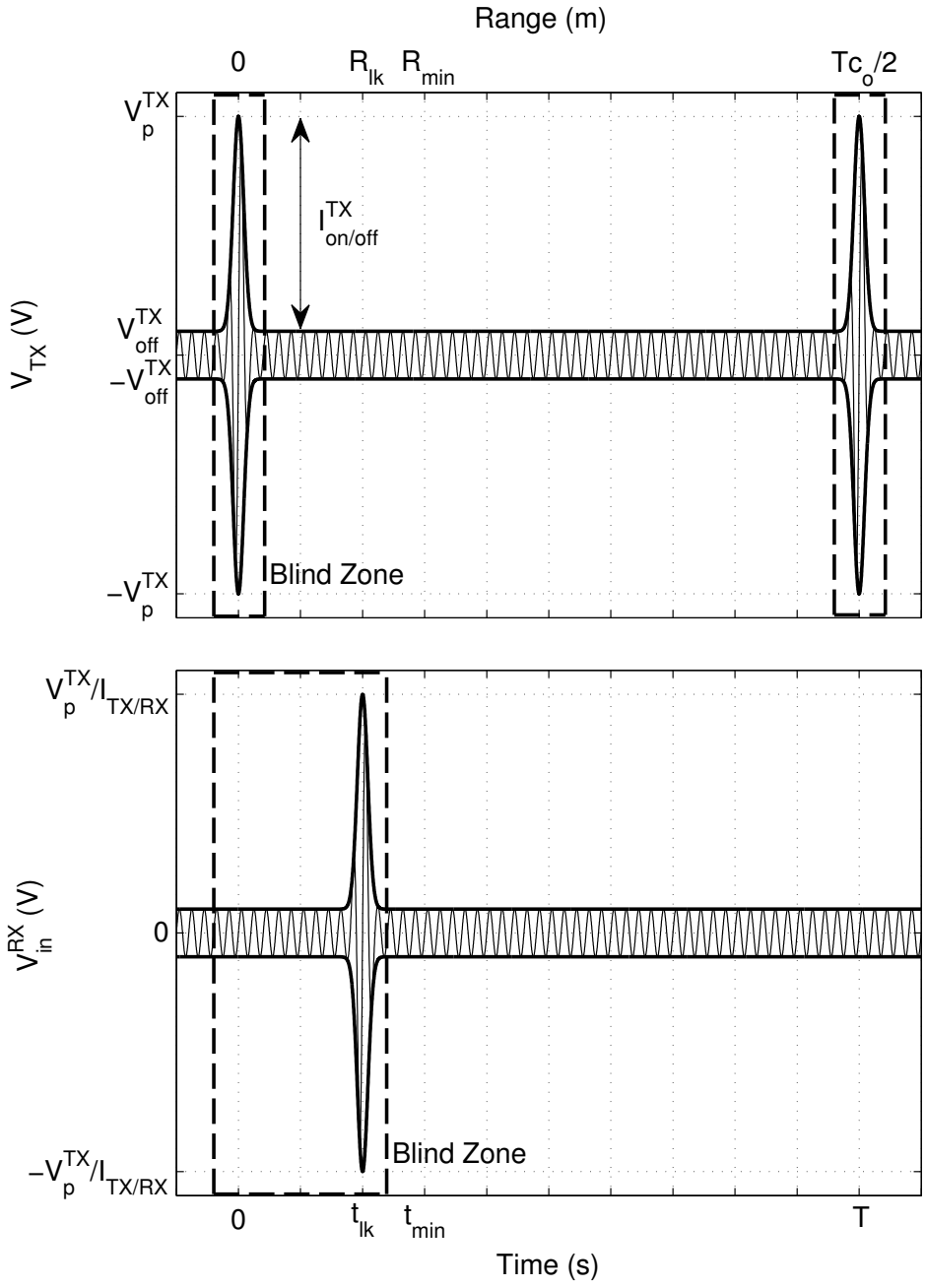

Figure 2.6: *Pulse Doppler Radar Blind Zone.* For a pulsed radar designed for unambiguous range detection, a blind zone exists for short ranges, as indicated by the dashed boxes. The minimum range, R_{min}, defined by the blind zone is extended due to finite TX-RX isolation, $I_{TX/RX}$, which results in a leakage signal with a delay, t_{lk}. The transmitted signal is illustrated in the upper waveform, and the leakage signal is illustrated in the lower waveform.

object and, after some time delay, the reflected signal will be incident on the receive antenna. The distance to the buried object can be determined based on the time delay; in other words, GPR employs time-domain techniques to locate any discontinuities in the otherwise opaque target. GPR has been demonstrated for the detection of buried items, such as mines [40], [41] and fossils [42]; nondestructive evaluation of pavement [43]; and geological surveys [44], [45], [46]. A variety of system implementations have been presented: [40] and [41] utilize wideband SAR techniques, [43] and [45] use short-pulse architectures, [44] uses a pulse-compression architecture, and [46] and [39] use step-frequency implementations.

- *Foliage Penetration.* Similar to GPR, foliage-penetrating radars utilize low frequency, wideband transmitted signals to "see" through a solid material, in this case trees. [40] presents a SAR-based foliage-penetrating radar used to detect vehicles hidden in a wooded area.

- *Through-Wall Imaging.* UWB through-wall imaging has been presented for both observing the inanimate contents of a room [47], [48], [49], [50] and detecting the life-signs of animate inhabitants of a room [51], [52], [53] from a position outside the room. Similar to GPR, [47] and [48] employ real-time SAR techniques to identify inanimate objects and their movements; the objects are separated from the radar by a wall. [49] presents a fixed-aperture approach as an alternative to a SAR-based through-wall imaging system. [50] presents techniques when the wall is reinforced with rebar. [51] and [52] employ pulse Doppler techniques to detect respiration and/or heart rate of animate targets; a pulsed signal is transmitted and, if incident on a human or animal, the reflected signal is Doppler modulated at a frequency matching a combination of the target's heart rate and respiration rate. [53]

also uses Doppler processing to detect life-signs but utilizes a noise-based transmission signal, rather than a pulsed signal, to reduce the probability of intercept for the radar system. Consistent with a pulse Doppler architecture, [51], [52], and [53] are coherent radars. Assuming the targets remain mostly still, long integration periods can be utilized for life-sign detection radars. For example, the results in [51] are based on a 10 s integration time, the results in [53] are based on a 20 s sample set, and the results in [52] are based on a 2.4 ms/frame integration time. In contrast, a short integration time is considered in this work, as will be discussed in Chapter 3.

- *Collision Avoidance Systems.* In addition to the 3.1–10.6 GHz unlicensed UWB band, the FCC opened a UWB from 22–29 GHz for vehicular radar applications [8]. A variety of pulsed, coherent UWB radar systems have been designed in this frequency band for short-range vehicular collision avoidance systems [54], [55], [56].

- *Localization.* Fine resolution UWB localization systems have been explored for medical applications [57], [58] and warehouse management [59]. The systems employ an RF tag which can be located by triangulating its position using a set of base-stations. [57] demonstrates a coherent, pulsed localization system; for the experimental setup, the base-stations are synchronized. [58] demonstrates a similar pulsed localization system; however, the base-stations are independent, and the system is noncoherent. [59] and [60] present an FMCW approach to the UWB localization application; [60] presents a similar target range requirement as is used in this thesis.

- *Short-Range Communications.* The FCC 3.1–10.6 GHz UWB band is being explored for short-range communications applications, as discussed in [61]. [62] presents a 3–5 GHz transceiver that employs binary phase-shift

keying (BPSK) modulation and pulse position modulation at a high PRF (500 MHz) for short-range communications.

- *Other Applications.* A variety of other UWB applications exist. For example, [63] presents a multi-functional UWB communications and radar system; the system employs pulsed up- and down-chirps to generate orthogonal radar and communications signals. An overview of additional applications is available in [38] and [61].

Although life-sign detection radars employ the Doppler shift to locate individuals, to the author's knowledge, a UWB pulse Doppler radar has not been investigated to meet the challenge of short-range, moving target detection. However, the aforementioned applications share similarities to the desired system characteristics and offer a great body of work to draw upon for the radar design.

To fully characterize most UWB systems, it is important to consider both the time- and frequency-domain characteristics of the system. It is important to maintain sufficient bandwidth for the devices, antennas, and interconnections in the radar to avoid distorting the frequency-domain characteristics by filtering the spectrum. Both dispersion, or group delay, and reflections can distort a UWB time-domain waveform. Preventing time-domain distortion is particularly important for short-pulse Doppler radar. If the pulse envelope is broadened or warped as it passes through the radar components, the minimum range of the radar will be degraded. Based on this knowledge, a variety of parameters must be considered when defining the bandwidth of a UWB component, including the gain, gain flatness, group-delay flatness, and return loss. For an antenna system, the criteria expand to include consistent beamwidth, front-to-back ratio, and phase center over the UWB operating band. The topic of UWB component design and its application to short-pulse Doppler radar will be discussed in

more detail throughout this thesis.

2.4 A Note On Units

Both linear and log values are used extensively in RF and radar literature to express power, gain, noise figure, etc. In this thesis, linear equations are assumed. If an expression utilizes log values, "[dB]" will be included at the end of the equation to indicate that log values should be used. As an example, the expressions for linear and log noise figure would be expressed as:

$$\begin{aligned} F &= \frac{\mathrm{SNR}_1^{in}}{\mathrm{SNR}_1^{out}} \\ F &= \mathrm{SNR}_1^{in} - \mathrm{SNR}_1^{out}[\mathrm{dB}] \end{aligned}$$

If a gain or loss is provided in an equation, it corresponds to voltage or power gain as appropriate to the equation. Gains and losses quoted in dB are power gains or losses.

Chapter 3

UWB Pulse Doppler Radar Architecture

The UWB pulse Doppler radar system is designed to detect targets at a maximum target range of 7 m and a ±0.75 m worst-case range accuracy for a single-pulse SNR of -13.5 dB. The radar operates in the S-band. The system-level block diagram of the UWB pulse Doppler radar is shown in Figure 3.1. The system can be broken into six subsystems: the transmitter, receiver, antenna system, digital control, post processor, and channel. The subsystem characteristics are described in the subsequent sections.

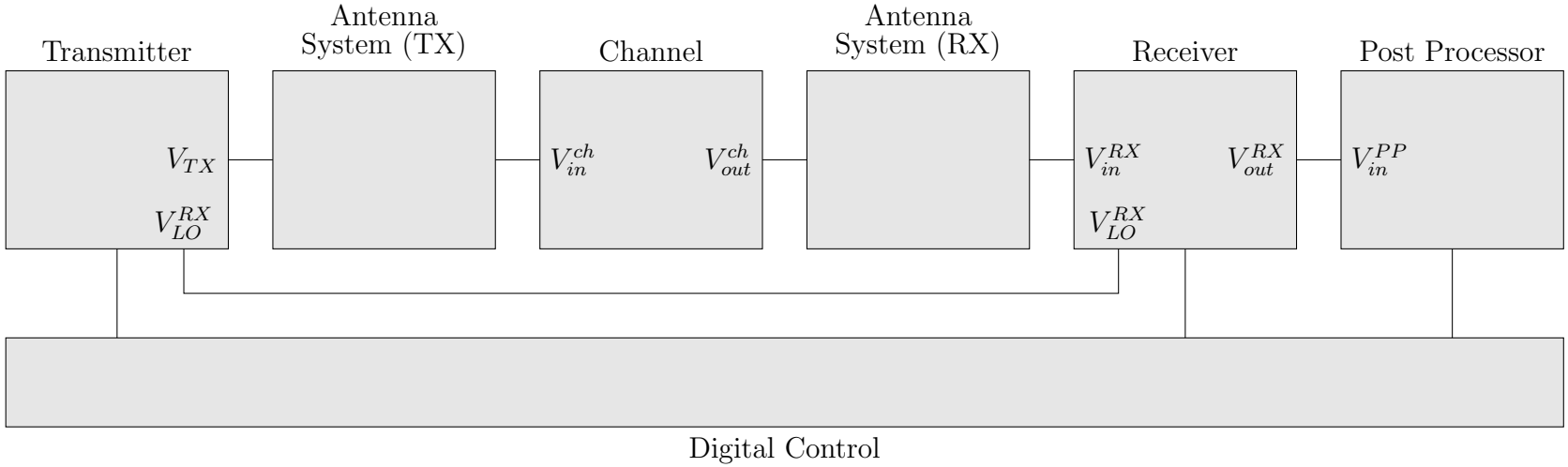

Figure 3.1: *System-Level Block Diagram.* The short-pulse Doppler radar can be broken into six primary subsystems: the transmitter, receiver, antenna system, digital control, post processor, and channel.

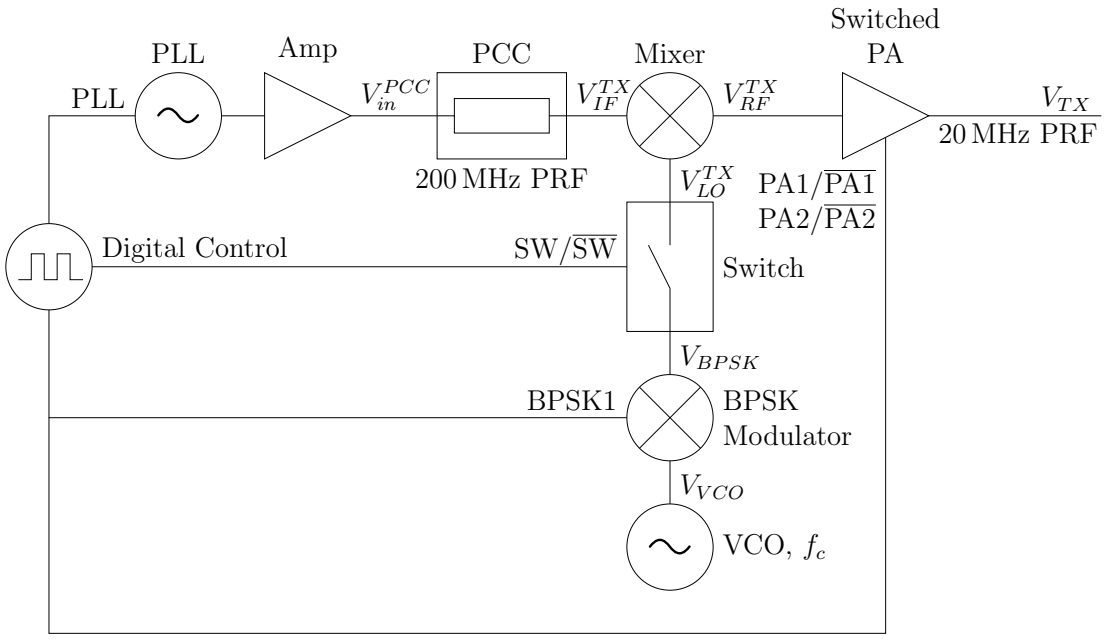

Figure 3.2: *Transmitter Block Diagram.* The IF branch of the transmitter generates a subnanosecond FWHM Gaussian-like pulse envelope. The LO branch of the transmitter generates a phase-coded LO signal that is switched at a rate of 20 MHz with a 10% duty cycle to set the PRF of the transmitter. The RF branch of the transmitter provides amplification and increases the on-off isolation of the transmitted signal.

3.1 Transmitter Architecture

The top-level block diagram of the UWB transmitter is shown in Figure 3.2 and is a coherent, pulsed topology. A variety of free parameters exist for the transmitter design, including the: PRF, transmitted pulsewidth (τ), carrier frequency (f_c), minimum on-state transmitted power ($P_{on,min}^{TX}$), and maximum off-state transmitted power ($P_{off,max}^{TX}$). In addition, a pulse tagging scheme must be selected to allow out-of-range target rejection.

Based on Eqn. (2.14), this system can be designed to achieve unambiguous range and Doppler resolution since $R_{max} f_{max}^{D} = 560\,\text{km/s} < c_o/4$ ($f_{max}^{D} = 80\,\text{kHz}$, assuming the maximum carrier frequency, $f_c = 4\,\text{GHz}$). To meet this criterion, the PRF can be selected in the range $160\,\text{kHz} \leq \text{PRF} \leq 21.4\,\text{MHz}$. A 20 MHz

PRF was selected for this work to maximize the number of samples for a given integration interval; the results can be extended to other PRFs.

As noted in Section 2.3, the desired FWHM pulsewidth is $\tau \leq 1\,\text{ns}$, so the pulse compression circuit (PCC) must generate subnanosecond pulses at a rate of PRF $= 20\,\text{MHz}$ or at a rate that can be down-sampled to match the desired transmitted PRF. A variety of pulse envelopes can be used, including rectangular, triangular, Gaussian, and higher-order Gaussian pulses. For this work, a Gaussian pulse envelope was selected because it falls off smoothly in both the time and frequency domains, simplifying the antenna system and UWB component designs [6]. The designed output of the PCC, which will serve as the envelope of the transmitted signal, is a train of Gaussian-like 730 ps FWHM pulses with a PRF of 200 MHz. The pulse generator, comprised of the phase-locked loop (PLL), amplification stage, and PCC, will be discussed in detail in Chapters 4 and 5.

The 3-dB and 10-dB bandwidths of the radar system are set by the pulsewidth of the envelope to $\beta_{3dB} = 605\,\text{MHz}$ and $\beta_{10dB} \simeq 1\,\text{GHz}$ and dictate the minimum bandwidth for the upconverter and the RF branch of the transmitter. The components must provide a flat response in gain, return loss, and group delay over the pulse bandwidth to avoid distorting the pulse envelope. The 10-dB bandwidth also limits the range of carrier frequencies to $2.5\,\text{GHz} \leq f_c \leq 3.5\,\text{GHz}$. A 2.5 GHz carrier frequency was selected for this work to take advantage of commercially available components that operate in the 2–3 GHz half-octave band.

The peak transmitted power must be high enough to achieve a minimum SNR at the input of the receiver, given a predetermined channel attenuation. The desired minimum detectable SNR for this work is $\text{SNR}^{out}_{1,min} = -13.5\,\text{dB}$ at the output of the receiver, and the maximum channel attenuation is $L^{ch}_{max} = 110\,\text{dB}$.

The minimum peak signal power can be calculated as:

$$P_{on,min}^{TX} = \text{SNR}_{1,min}^{out} - G_{A,TX} - G_{A,RX} + L_{max}^{ch} + P_N + F_{pulsed}^{RX}[\text{dB}] \tag{3.1}$$

Assuming a receiver noise figure of 15 dB, a receiver noise bandwidth of 520 dB, and antenna gains of 0 dB, the minimum peak signal power should be $P_{on,min}^{TX} = 0.6\,\text{W}$. The maximum off-state transmitted power, $P_{off,max}^{TX}$, is selected to prevent false alarms due to finite TX-RX isolation, $I_{TX/RX}$. The radar design in this thesis assumes a two-antenna system, so the TX-RX isolation is defined as the isolation between the transmit and receive antennas. Since the TX-RX isolation is not infinite, an attenuated and delayed replica of the transmitted signal will be incident on the receive antenna. The transmitter will exhibit a finite on-off isolation, $I_{on/off}^{TX} = P_{on}^{TX}/P_{off}^{TX}$, so its off-state power level must be low enough to prevent a false alarm when the receiver is in its on-state and the transmitter is in its off-state. The maximum off-state power can be calculated as follows:

$$P_{off,max}^{TX} = \text{SNR}_{1,max}^{out,rej} - G_{A,TX} - G_{A,RX} + I_{TX/RX} + P_N + F_{pulsed}^{RX}[\text{dB}] \tag{3.2}$$

where $P_{off,max}^{TX}$ is the maximum off-state transmitted power and $\text{SNR}_{1,max}^{out,rej}$ is the maximum rejectable single-pulse SNR at the output of the receiver. Assuming $\text{SNR}_{1,max}^{out,rej} = -30\,\text{dB}$, $I_{TX/RX} = 80\,\text{dB}$, and $G_{A,TX} = G_{A,RX} = 0\,dB$, the maximum off-state transmitted power is $P_{off,max}^{TX} = 12\,\mu\text{W}$. This corresponds to a transmitter on-off isolation of $I_{on/off}^{TX} \geq 46.5\,\text{dB}$.

The primary transmitter parameters have been defined, and a proof-of-concept transmitter was designed primarily using off-the-shelf components. The transmitter design is presented in detail in Chapters 4 and 5. An overview of the transmitter operation, following Figure 3.2, is provided here:

- As noted, the desired transmitted PRF is 20 MHz, and the output PRF of the PCC is 200 MHz. As a result, the PCC PRF must be reduced by

a factor of 10. The LO branch of the transmitter, which includes a VCO, BPSK modulator, and RF switch, implements the PRF reduction, as will be discussed in Section 5.1.2.

- In addition to down-sampling the IF signal, the LO branch generates the carrier and implements BPSK pulse tagging to enable discrimination between in- and out-of-range targets. The modulator is triggered at a rate of 20 MHz to phase code the LO signal at the same rate as the transmitted PRF. The design and functionality of the LO branch is discussed in more detail in Chapter 5.

- The upconverter operates as a double sideband (DSB) mixer. As a result, the radar will not be capable of distinguishing between closing and opening targets, so it is not necessary to employ an image-reject mixer in the receiver.

- The RF branch of the transmitter centers on a switched PA which amplifies the upconverted signal to achieve a minimum peak output power of $P^{TX}_{on,min} = 0.6\,\text{W}$. The switched PA also increases the transmitter on-off isolation to meet the desired $I^{TX}_{on/off} \geq 46.4\,\text{dB}$ specification. The details of the RF branch will be presented in Chapter 5.

- The digital control in Figure 3.2 provides control signals for several transmitter components, as well as other radar components. It will be discussed in Section 3.4 and throughout the remainder of this thesis.

3.2 Receiver Architecture

A coherent, homodyne receiver architecture was selected for this work, consistent with a pulse Doppler radar architecture. Coherent UWB receivers are presented in [52], [63], and [54].

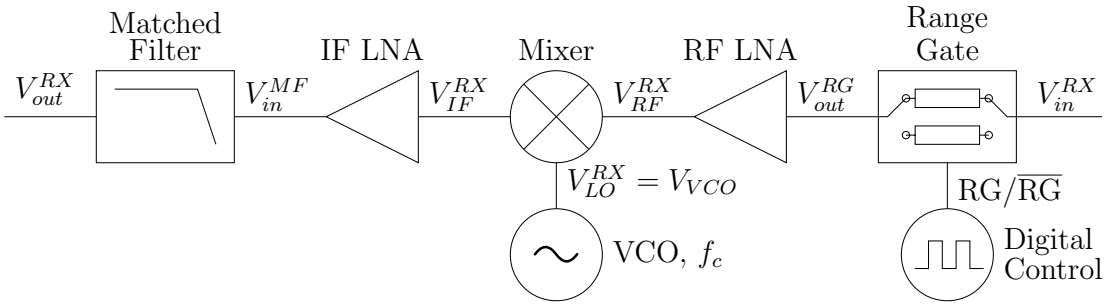

Figure 3.3: *Receiver Block Diagram.* The receiver employs a homodyne architecture.

The top-level block diagram of the UWB receiver is shown in Figure 3.3. The gain of the receiver is split between the RF and IF stages; the total gain is $G_{RX} = 55 \pm 2$dB under static conditions and $G_{pulsed}^{RX} = 52 \pm 2$dB under pulsed conditions. The static receiver noise figure is 11.8 dB and is primarily limited by the range gate; the noise figure is 14.8 dB under pulsed conditions. The receiver utilizes a homodyne architecture, so the output of the receiver should match the UWB pulse envelope at the output of the transmitter, except for a potential Doppler modulation if a moving target is present. A DSB downconverter is used, so the noise bandwidth equals the 520 MHz noise bandwidth of the receiver, due to frequency folding. The IF filter was designed as a quasi-matched filter based on the 605 MHz FWHM Gaussian-like output spectrum of the PCC.

The receiver employs a switched attenuator at its input to implement the receiver range gate. The range gate operates at a rate of PRF = 20 MHz to match the PRF of the transmitted signal with a duty cycle of τ_{RG}/T, where τ_{RG} is the pulsewidth of the range gate and defines the "on" time of the receiver. The range-gate pulsewidth was selected to match the desired range accuracy of the system: $\tau_{RG} = 2\delta R/c_o = 10$ ns. The on-off isolation of the switched attenuator sets the receiver on-off isolation; for this work, it is $I_{on/off}^{RX} = 49$ dB.

3.3 Antenna System

A pair of separate transmit and receive antennas was selected for this work. The antennas must display flat gain and group delay over the 2–3 GHz bandwidth of the transmitted signal. Tapered-slot antennas were selected to take advantage of the inherent isolation between two directional antennas placed side-by-side. The antenna system is discussed in detail in Chapter 7.

3.4 Digital Control

A Xilinx Virtex-5 field-programmable gate array (FPGA) with a 20 MHz external clock provides the digital control signals for this work. The FPGA serves as a common clock for the radar system, ensuring that all control signals are synchronous, as is required in a practical system [64]. The outputs of the FPGA are level-shifted and amplified on a daughter board using a combination of Fairchild Semiconductor FIN1002 drivers and a custom buffer circuit designed at Sandia National Laboratories. The outputs are summarized in Table 3.1

3.5 Post Processor

The post-processor is implemented as a digitizer, and the signal processing is performed in MATLAB for the proof-of-concept design. An Acqiris DP240 (Agilent U1069A) 8-bit, 2 GSa/s PCI digitizer was selected; it provides $\beta_{3dB}^{dig} =$ 1 GHz analog bandwidth, which is sufficient to cover the IF output of the receiver. The output of the receiver, V_{out}^{RX}, is sampled at a rate of $f_s = 20$ MHz. The 3-dB IF bandwidth of the matched filter (and receiver) is $\beta_{3dB} = 540$ MHz. Since $f_s < \beta_{3dB}$, the signal is subsampled. As such, the sampled time-domain signal, V_{in}^{pp}, will not be the same as the output of the receiver, V_{out}^{RX}. Rather, a single sample will be

taken per pulse, preferably at the peak of the signal. The output will be aliased in the frequency domain. The sample rate is not sufficient to reconstruct the received pulse envelope; however, the sample rate is high enough to determine the Doppler shift, which is significantly less than f_s. The BPSK phase code, generated by the FPGA, is also sampled at a sample rate of f_s. The receiver output can be correlated with the phase code to allow in- and out-of-range target discrimination.

Table 3.1: FPGA Outputs

Signal Name	**Subsystem**	**Description**
PLL	TX	A single-ended, 20 MHz low-voltage transistor-transistor logic (LVTTL) clock signal applied to the input of the PLL.
BPSK1	TX	A single-ended, 20 MHz LVTTL pseudo-random bi-phase code generated using a 27-bit linear feedback shift register (LFSR). It serves as the control signal for the BPSK modulator.
SW/$\overline{\text{SW}}$	TX	A differential, 20 MHz, 10% duty cycle control signal applied to the switch. The signal levels are 0/-5 V.
PA1/$\overline{\text{PA1}}$	TX	A differential, 20 MHz, 10% duty cycle control signal applied to the switched PA. The signal levels are 0/-5 V.
PA2/$\overline{\text{PA2}}$	TX	A differential, 20 MHz, 10% duty cycle control signal applied to the switched PA. The signal levels are 0/-5 V.
RG/$\overline{\text{RG}}$	RX	A differential, 20 MHz, 20% duty cycle control signal applied to the switched attenuator. The signal levels are 0/-1 V.
CLK	Post Processor	A single-ended, 20 MHz LVTTL clock signal used as the digitizer's external clock.
BPSK2	Post Processor	A replica of the differential, 20 MHz LVTTL pseudo-random bi-phase code applied to the BPSK modulator. It is sampled by the digitizer.

A variety of the digitizer settings can be varied, including the full-scale voltage range, V_{fs}. It can be varied from 100 mV to 5 V in 1-2-5 steps; for this work, the full-scale range is centered around 0 V. There are two considerations when selecting the full-scale voltage range: the maximum signal voltage and quantization noise. The full-scale voltage range should be large enough to avoid saturating the analog-to-digital converter (ADC) in order to prevent signal distortion. The full-scale voltage range determines the least significant bit (LSB); it is equal to $V_{fs}/(2^b)$, where b is the number of bits. Quantization noise is related to the LSB. The input signal, V_{in}^{pp}, is quantized by the digitizer, and there will be an error associated with the digitization process [65]. The amount of error can be reduced by ensuring the noise voltage associated with V_{in}^{pp} is large enough to toggle at least the LSB [65]. The receiver can be designed to ensure the criterion is met by careful selection of the gain and noise figure combination.

The digitizer can collect over 8.3 million samples per collection period. The full data set is saved, and signal processing is performed after the data set is retrieved by the digitizer. The signal processing script is detailed in Appendix A and can be summarized as follows:

(1) Process the BPSK phase code.

- The BPSK phase code is further digitized by setting all positive samples equal to 1 and all negative samples equal to -1.
- The output is V_{pr}^{BPSK}.

(2) Subtract the DC component from V_{in}^{pp}.

- The digitizer will contribute a DC offset to the sampled data set. To account for this error, the mean of V_{in}^{pp} is subtracted from each sample point.

- The output is $V_{in}^{pp'}$.

(3) Correlate V_{pr}^{BPSK} signal and $V_{in}^{pp'}$.

- The two signals are correlated by multiplying them element by element.
- The output is V_{corr}^{pp}.

(4) Calculate the power spectral density (PSD) of V_{corr}^{pp}.

- The PSD is computed using a periodogram.[1]
- A Hamming window is applied to the sampled data.
- Both the number of samples and the amount of zero-padding are adjustable.
- A single, continuous sample set can be used, or a few sample sets can be processed independently and averaged.
- The output is $P_{pp}(f)$.

(5) Calculate the signal power.

- The signal power is determined by integrating around the desired signal frequency with a specified bandwidth.
- The integration bandwidth is selected based on the 10, 20, 30, or 40 dB Hamming main-lobe bandwidth. It is equal to $\beta_{int} = Af_s/N$, where N is the number of samples and A is 2.3, 3.1, 3.6, or 4.0 for 10, 20, 30, or 40 dB Hamming main-lobe bandwidth.
- The output is P_S^{pp}.

[1] A periodogram is a technique for calculating the PSD. First, the FFT of the data set is calculated. Next the power spectrum is calculated as $S(f) = |X(f)|^2/N$, where $S(f)$ is the PSD, N is the number of samples, and $X(f)$ is the FFT result [66].

(6) Calculate the noise power.

- The noise power is determined by integrating the full PSD, $P_{pp}(f)$, and subtracting the signal power, P_S^{pp}.
- The output is P_N^{pp}.

(7) Calculate the SNR.

- The desired metric is the single-pulse SNR. It is calculated as the ratio of P_S^{pp} to P_N^{pp}.
- The output is SNR_1^{pp}.

The signal processing script requires a set of input parameters, which are summarized in Table 3.2. There are some trade-offs to consider when selecting values for the various parameters, as discussed in the following sections.

3.5.1 Number of Samples

The number of samples, N, impacts a variety of parameters, including the frequency resolution of $P_{pp}(f)$ and the integration gain for the SNR. The frequency resolution for a fast Fourier transform (FFT) process can be related to the number of samples as $\Delta f = f_s/N$, where f_s is the sample rate; therefore, increasing N improves the frequency resolution of the output spectrum. This goes hand-in-hand with the improvement in frequency resolution due to integration. The longer the integration period is, or the more samples that are integrated, the finer the frequency resolution [66]. In addition, there is a SNR processing gain due to integration. For a coherent signal, the processing gain is $10\log(N)$. For a noncoherent signal, the processing gain is between $10\log\left(\sqrt{N}\right)$ and $10\log(N)$ [68]. The received noise is random and tends to add destructively as it is integrated, resulting in a reduction to the noise power variance. The desired signal, on the

Table 3.2: Signal Processing Variables

Variable	**Description**
Number of Samples	The number of samples can be selected to simulate different integration periods.
Zero Padding	The amount of zero padding can be adjusted to interpolate the PSD, increase the PSD calculation speed, or to set the desired number of frequency bins in the PSD. Note that while zero padding increases the number of frequency bins and smooths the PSD, it does not provide additional frequency resolution [67].
Number of Sample Sets	The number of sample sets can be set to one for standard processing, or it can be increased to allow for averaging of several sample sets.
Signal Frequency	The signal frequency can either be initialized to a specific value, or it can be automatically assigned to correspond to the frequency at which $P_{pp}(f)$ is largest.
Integration Bandwidth	The integration bandwidth can be selected as the 10, 20, 30, or 40 dB bandwidth of the Hamming main lobe.
Range Shift Offset	The range shift offset indicates the number of sample shifts to assume when correlating V_{pr}^{BPSK} and $V_{in}^{pp'}$. The delay can be used to account for time delays inherent in the measurement setup or to observe the out-of-range ambiguity rejection.
System Impedance	The system impedance is used to calculate P_S^{pp} and P_N^{pp}. The MATLAB script verifies that the stated system impedance matches the digitizer settings.
LPF Setup	A digital low-pass filter (LPF) can be applied to the data set before calculating the PSD. If a LPF is selected, the cutoff frequency, filter order, and filter method must be specified.

other hand, will integrate constructively. Since the integrated signal strength remains nearly constant, the reduction in noise variance makes it easier to identify the signal [66].

3.5.2 Number of Samples and Integration Bandwidth

The number of samples and the integration bandwidth impact the minimum calculable single-pulse SNR. To illustrate, consider a white-noise spectrum ($S(f) = N_o$), and assume a predefined integration bandwidth, β_{int}. For any given "signal" frequency, f_{sig}, the signal power is:

$$P_S^{pp} = \int_{f_{sig}-\beta_{int}/2}^{f_{sig}+\beta_{int}/2} S(f)df + \int_{-f_{sig}-\beta_{int}/2}^{-f_{sig}+\beta_{int}/2} S(f)df = 2\beta_{int}N_o \tag{3.3}$$

The noise power is equal to the signal power subtracted from the total power:

$$P_N^{pp} = \int_{-f_s/2}^{f_s/2} S(f)df - P_S^{pp} = N_o(f_s - 2\beta_{int}) \tag{3.4}$$

The minimum calculable single-pulse SNR is approximately:

$$\mathrm{SNR}_{1,min}^{floor} \simeq \frac{P_{sig}}{P_N} = \frac{2\beta_{int}}{f_s - 2\beta_{int}} \tag{3.5}$$

If the 30 dB Hamming main-lobe bandwidth is used to the define the integration bandwidth, then $\beta_{int} = 3.6f_s/N$. Eqn. 3.5 can be rewritten for this case as:

$$\mathrm{SNR}_{1,min}^{floor} \simeq \frac{7.2}{N - 7.2} \tag{3.6}$$

Based on the equation, if the desired SNR floor is $\mathrm{SNR}_{1,min}^{floor} = -40\,\mathrm{dB}$, then at least seventy-two thousand pulses should be integrated.

3.5.3 Integration Bandwidth

The integration bandwidth limits not only the minimum calculable SNR; it determines the maximum calculable SNR, $\mathrm{SNR}_{1,max}^{calc}$. In this thesis, the integration

bandwidth is set as the 30 dB Hamming main-lobe bandwidth. As a result, the maximum calculable SNR is limited to $\text{SNR}_{1,max}^{calc} \simeq 30\,\text{dB}$.

3.5.4 Number of Samples and Signal Frequency

The relationship between the number of samples and the signal frequency can also impact the PSD calculation. Consider a sinusoidal input signal, and assume that no windowing is applied during the periodogram calculation. If the data set includes an integer number of signal cycles, then the PSD will have two spectral components, located at $\pm f_{sig}$, as shown in Figures 3.4a and 3.4b. If a fractional number of signal cycles is employed, then the periodogram calculation will result in spectral smearing due to the overlapping aliasing effect [66], as shown in Figures 3.4c and 3.4d.

There are two solutions to this problem. First, an integer number of signal cycles can be sampled. Unfortunately, this is not a realistic option unless the signal frequency is always known ahead of time. The second option is to apply a window function to the sampled data before the periodogram calculation [66]. The windowing function weights the samples to minimize the impact of the finite number of samples; a Hamming window is used in the periodogram calculation in this thesis.

3.5.5 Number of Sample Sets

SNR gains can also be achieved by averaging several data sets [66], so the number of sample sets will impact the final SNR result. Consider several data sets with N samples. The PSD can be calculated for each data set, and the PSDs can then be averaged, bin-by-bin, to reduce the noise variance. This is an especially helpful technique for coherent systems. Every coherent system has a finite coherent

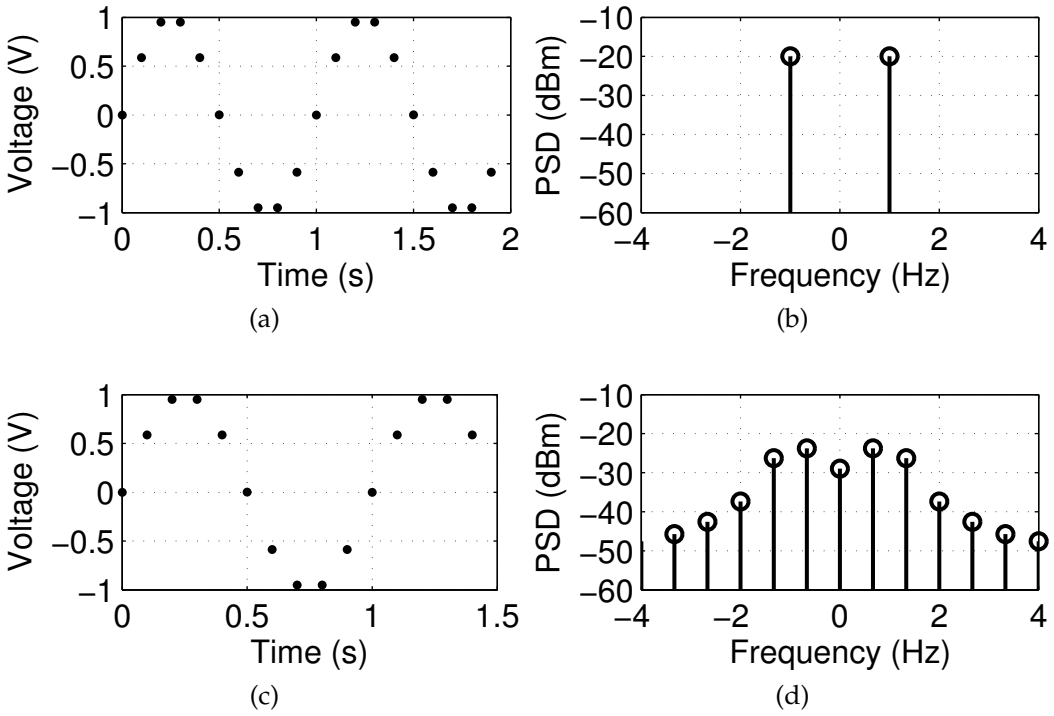

Figure 3.4: *Impact of Number of Cycles on PSD Calculation.* If the number of samples corresponds to an integer number of cycles of a sinusoid, the PSD will have two impulse-like spectral components at $\pm f_{sig}$ (see (a) and (b)). If a non-integer number of cycles is sampled, the spectrum will be spread about $\pm f_{sig}$ (see (c) and (d)).

integration interval, which is limited by short-time stability characteristics like jitter, phase noise, etc [69]. If integration is performed only over the coherent integration interval, a coherent integration gain can be assumed. However, if the integration is performed for a longer period of time, the integration gain will be reduced, as the signal is no longer coherent. An alternative technique is to integrate several short data sets over their coherent integration intervals and average the resulting PSDs to increase the SNR processing gain [66]. One side-effect of averaging is decreased frequency resolution, so the decision to average or not should be based on the system specifications [66].

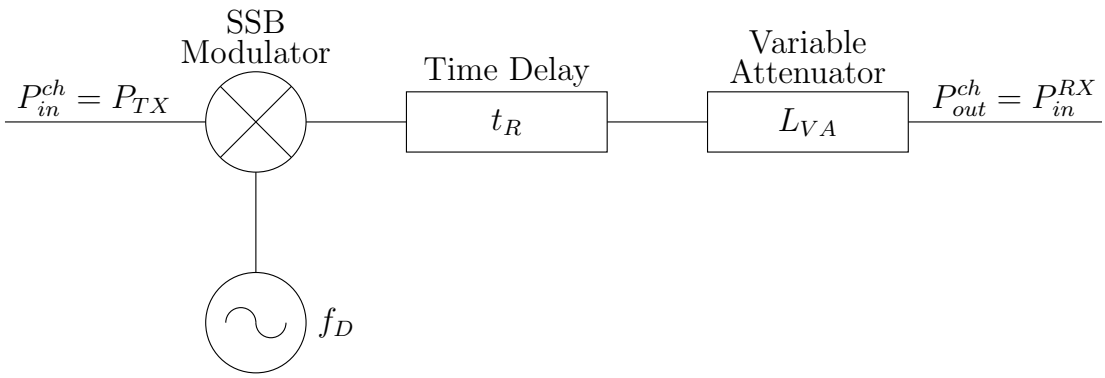

Figure 3.5: *Closed-Loop Channel Model.* A closed-loop channel model is used to characterize the radar system. It is comprised of a SSB modulator, a Doppler shift generator, a variable attenuator, and a variable time delay.

3.6 Channel

Radar testing can be performed using a variety of techniques. One option is closed-loop radar testing, which models the channel as a hard-wired system [70], as shown in Figure 3.5. The Doppler shift, channel attenuation, and range delay are simulated in hardware using a single-sideband (SSB) modulator, a variable attenuator, and a variable time delay. A closed-loop model helps verify the ideal expected behavior of the radar system by eliminating degradations that are present in a wireless channel with an actual moving target. The degradations can include leakage from the transmit to receive antenna due to finite TX-RX isolation, multipath, clutter, fading, and target fluctuations, to name a few. By removing the nonidealities, it is simpler to characterize the receiver's sensitivity and dynamic range and to measure the radar's out-of-range ambiguity rejection capability and the time-domain SNR response of the radar system. Closed-loop radar testing can be performed on a bench-top and will be covered in more depth in Chapter 8.

Another radar testing option is open-loop radar testing, which includes the antenna system [70]. Open-loop radar testing can be performed as shown in

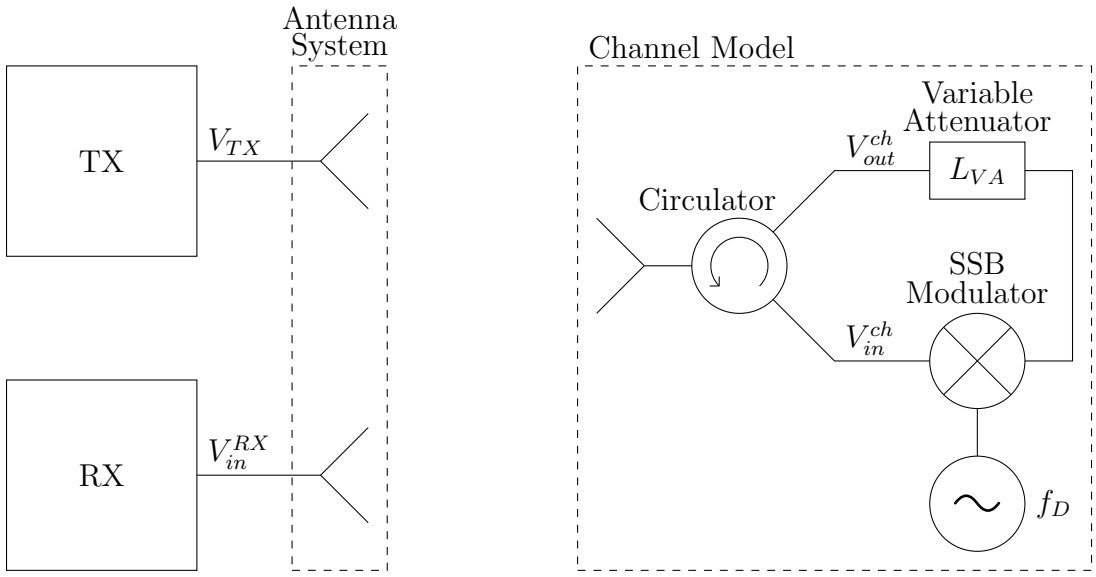

Figure 3.6: *Open-Loop Channel Model.* An open-loop channel model is used to characterize the radar system. It is comprised of an antenna, a circulator, a SSB modulator, a Doppler shift generator, and a variable attenuator.

Figure 3.6. Rather than hard-wiring the input and output of the channel model to the transmitter and receiver, a wireless link is employed. An antenna and a circulator serve as the input and output of the open-loop channel model, like in a single-antenna system, to transmit and receive with a single antenna. In holding with the closed-loop channel model, the received signal is Doppler shifted and attenuated using a SSB modulator and a variable attenuator. The modulated signal is re-emitted and acts as the reflected radar signal. As with the closed-loop channel model, the open-loop channel model eliminates many nonidealities associated with wireless transmission; however, it allows the tester to introduce nonidealities, such as multipath, as desired. Open-loop testing can be performed in a controlled environment such as an anechoic chamber.

Finally, radar testing can be performed in the field using a realistic target. Field testing was not performed as part of this thesis work.

3.6.1 Limitations of Closed- and Open-Loop Radar Testing

Closed- and open-loop channel models provide a simple means to characterize a radar system. They simulate the Doppler effect of a moving target, while allowing the test to be performed on a bench-top, in an anechoic chamber, or in an otherwise controlled laboratory environment. Unfortunately, the models presented in Figures 3.5 and 3.6 lack one important feature of a moving target– they do not simulate the time-domain motion of the target. The position of a moving target changes over time, but the simulated target appears stationary in the time domain. There are two techniques that can be used to account for this nonideality in the model. First, the time delay of the channel could be swept over time to simulate the target's motion. While plausible, this technique complicates the channel model hardware. The second technique is applied during signal processing. The integration interval, T_{int}, is limited based on the time required for the target to move through the range gate. The interval is determined based on the transmitted pulsewidth. Recall the expression relating the time delay between the transmission and reception of a radar signal, assuming a target at range R:

$$t_R = \frac{2R}{c_o} \tag{3.7}$$

Now consider a small change in the time delay due to a small change in the range:

$$t_{R2} - t_{R1} = \frac{2(R_2 - R_1)}{c_o} \tag{3.8}$$

Assume that the post processor takes a single sample per PRI at a constant sample rate at one range. In this case, if $(t_{R2} - t_{R1})$ exceeds τ, some of the samples will only include noise; in other words, to ensure that all (or most) samples in

the integration interval include signal, $(t_{R2} - t_{R1}) \leq \tau$, or:

$$\tau \geq \frac{2(R_2 - R_1)}{c_o} \tag{3.9}$$

The time that is takes the target to move a distance $(R_2 - R_1)$ is related to its velocity:

$$t' = \frac{R_2 - R_1}{v} \tag{3.10}$$

where t' is the time of flight. During the time of flight, N pulses, spaced with period T, are incident on the target, so the Eqn. (3.10) can be rewritten as:

$$NT = \frac{R_2 - R_1}{v} \tag{3.11}$$

Solving Eqn. (3.11) for the change in range and substituting it into Eqn. (3.9) results in the maximum number of pulses that can be integrated:

$$\begin{aligned} \tau &\geq \frac{2NTv}{c_o} \\ N &\leq \frac{c_o \tau}{2vT} \end{aligned} \tag{3.12}$$

A similar limit is defined and discussed in [71]. When the closed- and open-loop channel models are used with the radar system described in this chapter, the number of integrated samples should be limited as indicated in Eqn. (3.12) to more accurately simulate the effect of a moving target. The integration interval limit can be particularly challenging for coherent, short-pulse radars [72]. In this thesis, we assume the maximum integration time for the maximum Doppler shift to provide the worst case scenario for the link budget.

3.7 Theoretical Radar Characteristics

The characteristics for each of the subsystems are summarized in Tables 3.3–3.7. The transmitter design and its measured and simulated characteristics

are presented in Chapters 4 and 5. The receiver design and its measured and simulated characteristics are presented in Chapter 6. A UWB antenna system, which is used for open-loop radar testing, is presented in Chapter 7.

The system level characteristics, or the radar performance, are also important. The primary radar performance metrics, including the sensitivity, minimum range, and out-of-range ambiguity rejection, are detailed in the following sections, and the system measurements are presented in Chapter 8.

3.7.1 Sensitivity

As discussed in Sections 1.2.1 and 1.2.2, the sensitivity of the radar system can be described using the voltage sensitivity or the minimum single-pulse SNR at the output of the receiver. This thesis uses the minimum SNR metric. The minimum SNR is typically selected to meet some minimum criteria for the probability of false alarm and the probability of detection [16]. The probability of false alarm is the probability that the envelope of the noise voltage will exceed the detection threshold of the radar when only noise is present. Alternatively, some texts quote the mean time between false alarms. The probability of detection is the probability that the envelope of the total signal, including both signal and noise, will exceed the detection threshold of the radar. Both probabilities can be expressed in terms of the signal-to-noise ratio of the received signal. A simple empirical formula for the relationship between the probability of false alarm, probability of detection, and signal-to-noise ratio is:

$$\mathrm{SNR}_1^{out} = \ln\left(\frac{0.62}{p_{fa}}\right) + 0.12\ln\left(\frac{0.62}{p_{fa}}\right)\ln\left(\frac{p_{det}}{1-p_{det}}\right) + 1.7\ln\left(\frac{p_{det}}{1-p_{det}}\right) \tag{3.13}$$

where SNR_1^{out} is the single-pulse SNR ratio at the output of the receiver, p_{fa} is the probability of false alarm, and p_{det} is the probability of detection [73], [16]. The expression assumes a single pulse is used to calculate the SNR; in other words,

Table 3.3: Desired UWB Pulse Doppler Radar Parameters

Specification Type	**Parameter**	**Symbol**	**Value**
Target	Maximum Target Range	R_{max}	7 m
	Maximum Doppler Shift	f^D_{max}	50 kHz
Channel	Maximum Attenuation	L^{ch}_{max}	110 dB
System	Operating Band	—	S-band
	Minimum Range Accuracy	δR_{min}	±0.75 m
	Probability of False Alarm	p_{fa}	1E-7
	Probability of Detection	p_{det}	0.99
	Minimum Detectable SNR	SNR_{pr}	15 dB
	Maximum Rejectable SNR	$\text{SNR}^{out,rej}_{1,max}$	-30 dB
TX	Pulse Repetition Frequency	PRF	20 MHz
	FWHM Pulsewidth	τ	≤ 1 ns
	Carrier Frequency	f_c	2.5 GHz
	Minimum Peak TX Power, on-state	$P^{TX}_{on,min}$	0.6 W
	Maximum Peak TX Power, off-state	$P^{TX}_{off,max}$	12 μW
	TX on-off Isolation	$I^{TX}_{on/off}$	≥ 46.5 dB
Digitizer	Analog Bandwidth	β^{dig}_{3dB}	1 GHz
	Sample Rate	f_s	20 MHz

Table 3.4: Measured UWB Transmitter Parameters

Parameter	Symbol	Value
FWHM Pulsewidth	τ	730 ps
3-dB Bandwidth	β_{3dB}	605 MHz
10-dB Bandwidth	β_{10dB}	1 GHz
Effective Bandwidth	β_{eff}	1.6 GHz
Range Accuracy ($SNR_1^{out} = -13.5$ dB)	δR	±0.16 m
Range Accuracy ($SNR_1^{out} = 0$ dB)	δR	±0.03 m
Peak TX Power, on-state	P_{on}^{TX}	1.2 W
Peak TX Power, off-state	P_{off}^{TX}	4.5 μW
TX On-Off Isolation	$I_{on/off}^{TX}$	54 dB
TX Turn-Off Time ($I_{on/off}^{TX} = 40$ dB)	t_{to}^{TX}	5.4 ns
TX Turn-Off Rate ($I_{on/off}^{TX} \leq 30$ dB)	R_{to}^{TX}	10.0 dB/ns
TX Turn-Off Rate (30 dB $< I_{on/off}^{TX} \leq 45$ dB)	R_{to}^{TX}	2.9 dB/ns
TX Turn-Off Rate (45dB $< I_{on/off}^{TX} \leq 55$ dB)	R_{to}^{TX}	0.7 dB/ns

Table 3.5: Measured UWB Receiver Parameters

Parameter	Symbol	Value
Static Receiver Gain	G_{RX}	55 dB
Static Receiver Noise Figure	F_{RX}	11.8 dB
Pulsed Receiver Gain	G_{pulsed}^{RX}	52 dB
Pulsed Receiver Noise Figure	F_{pulsed}^{RX}	14.8 dB
Range-Gate Pulsewidth	τ_{RG}	10 ns
Receiver On-Off Isolation	$I_{on/off}^{RX}$	49 dB
Noise Bandwidth	β_N	520 MHz
Noise Power (Input)	P_N	-87 dBm
Dynamic Range ($SNR_1^{out} = -13.5$ dB, RX only)	DR	57.5 dB
Dynamic Range ($SNR_1^{out} = -13.5$ dB, RX and ADC)	DR	51.5 dB
Dynamic Range ($SNR_1^{out} = 0$ dB, RX only)	DR	44.0 dB
Dynamic Range ($SNR_1^{out} = 0$ dB, RX and ADC)	DR	38.0 dB

Table 3.6: Expected UWB Pulse Doppler Radar Parameters, Based on TX & RX Measurements: C = Coherent, NC = Noncoherent

Parameter	Symbol	Value
Number of Samples	N	730
Minimum Detectable SNR (C)	$\mathrm{SNR}_{1,min}^{out}$	-13.6 dB
Maximum Channel Attenuation (C)	L_{max}^{ch}	113 dB
Minimum Detectable SNR (NC)	$\mathrm{SNR}_{1,min}^{out}$	0.7 dB
Maximum Channel Attenuation (NC)	L_{max}^{ch}	99 dB

Table 3.7: Measured UWB Pulse Doppler Radar Parameters

Parameter	Symbol	Value
Minimum Detectable SNR	$\mathrm{SNR}_{1,min}^{out}$	0 dB
Maximum Channel Attenuation	L_{max}^{ch}	100–105 dB
Sampling Loss	—	1–3 dB
Total Radar Losses	—	4–5 dB
Minimum Noise and Leakage Power (Output)	—	-16 dBm
Coherent Processing Interval	—	5 ms
Radar Turn-Off Time ($I_{TX/RX} = 90$ dB)	t_{to}	2.8 ns
Radar Turn-Off Rate ($I_{TX/RX} = 90$ dB)	R_{to}	10.7 dB/ns
Radar Turn-Off Time ($I_{TX/RX} = 80$ dB)	t_{to}	3.5 ns
Radar Turn-Off Rate ($I_{TX/RX} = 80$ dB)	R_{to}	11.1 dB/ns
Minimum TX-RX Isolation	$I_{min}^{TX/RX}$	80 dB
Minimum Range ($I_{TX/RX} = 80$ dB)	R_{min}	1.3 m + R_{lk}

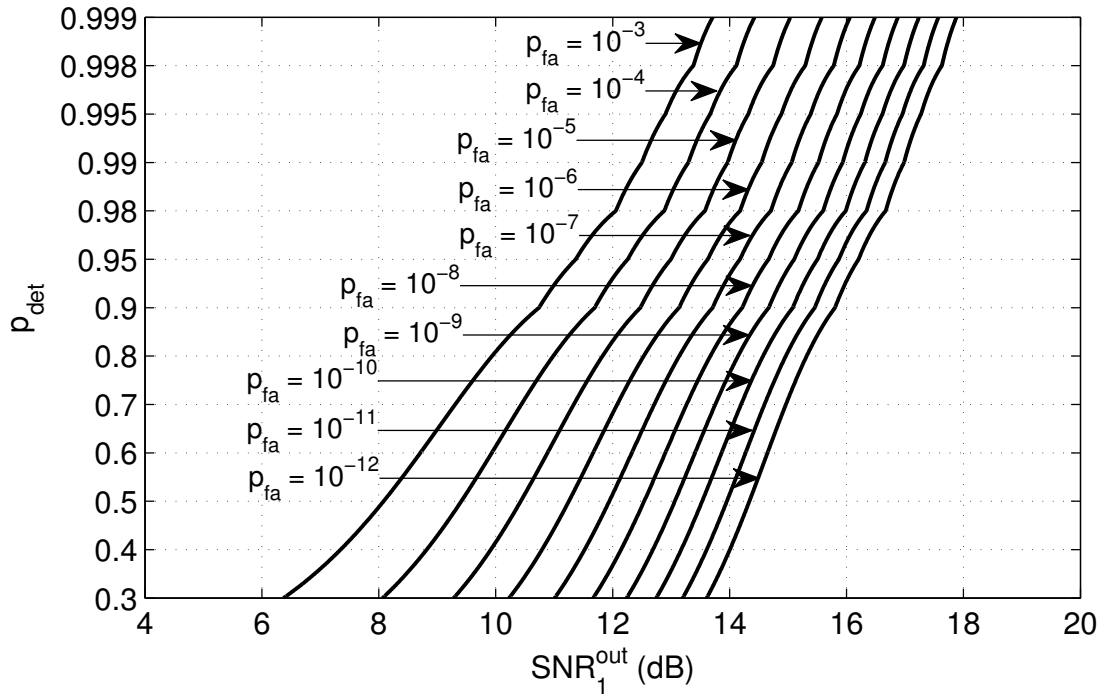

Figure 3.7: *Single-Pulse SNR, Probability of False Alarm, and Probability of Detection.* An empirical relationship between the three parameters is given in Eqn. (3.13) and plotted.

it neglects integration gain. Some results from the equation are plotted in Figure 3.7.

For this work, the desired probability of false alarm is 1E-7 and the desired probability of detection is 0.99. The corresponds to a minimum detectable processed SNR of 15 dB. Based on Eqn. 3.12 and the maximum considered Doppler shift, about 730 pulses can be integrated for the radar in this work. This corresponds to the worst case integration time, and the measurement results can be extended to smaller Doppler shifts and longer integration times as per the application. The minimum detectable single-pulse SNR can be calculated as:

$$\mathrm{SNR}_1^{out} = \mathrm{SNR}_{pr} - G_{int}[\mathrm{dB}] \tag{3.14}$$

where G_{int} is the SNR gain due to integration. The processed SNR gain for a coherent radar is $10\log(N)$; assuming coherent integration of 730 pulses, the min-

imum detectable single-pulse SNR is -13.6 dB for this work. This corresponding maximum channel attenuation is calculated as:

$$L_{ch} = P_{TX} + G_{A,TX} + G_{A,RX} - P_N - F_{pulsed}^{RX} - \text{SNR}_{1,min}^{out}[\text{dB}] \tag{3.15}$$

Assuming $G_{A,TX} = G_{A,RX} = 0$ dB and coherent integration of 730 pulses, the maximum channel attenuation is 113 dB. The processed SNR gain for a noncoherent radar is at least $10\log(\sqrt{N})$. For a noncoherent radar, the minimum detectable single-pulse SNR is 0.7 dB, and the maximum channel attenuation is 99 dB. The sensitivity, or alternatively the minimum detectable SNR, of the radar described in this work will be presented in Chapter 8.

To achieve coherent processing gain, two things are required. First, the radar must be coherent, which is achieved by maintaining the phase relationship between the transmitter and receiver's LOs. In this work, the output of a single VCO is divided to provide the LO signal for both the transmitter and receiver. Second, the post processor must sample the received signal using a trigger that is synchronous with the pulse envelope [74]. In this work, the FPGA generates the synchronous 20 MHz signals that: (1) trigger the input to the PCC, which forms the transmitted pulse envelope, (2) sets the transmitted PRF, and (3) triggers the digitizer. Since the radar in this thesis is coherent, the coherent sensitivity specifications will be assumed. The coherent integration characteristics align well with the desired radar specifications for maximum channel loss and minimum detectable SNR.

As noted in Section 3.5.5, nonidealities, such as jitter and phase noise, limit the coherent processing interval (CPI) of the radar. If the integration time is less than the CPI, the integration gain will follow the expected $10\log(N)$ curve; if the integration time exceeds the CPI, the integration gain will be reduced. Coherent integration gain and the CPI for this radar in this work will be discussed in Chapter 8.

As part of the radar performance characterization, the single-pulse SNR will be calculated for various channel attenuation states for comparison to the theoretical SNR values. As discussed in Section 3.5, the number of pulses that are integrated limits the minimum calculable SNR. In order to ensure the accurate calculation of the single-pulse SNR, one million pulses will be integrated and the integration bandwidth will be set to match the 30 dB Hamming window, resulting in an SNR floor on the order of -50 dB. This is significantly more pulses than would be integrated in the field but allows accurate radar characterization.

3.7.2 Minimum Range and Minimum TX-RX Isolation

The main driver for this thesis work is to minimize the closest detectable range of a pulse Doppler radar by employing UWB techniques to minimize the transmitted pulsewidth. In an ideal system, the minimum range would be limited by the "on" time of the transmitter; however, finite TX-RX isolation increases the minimum detectable range (see Section 2.3). The minimum range is increased to account for the delay of the leakage path between, for example, the transmit and receive antennas. Fortunately, a short transmitted pulsewidth still helps minimize the shortest detectable range, even when a leakage signal is present. If the receiver and antenna system had infinite bandwidth, the minimum range will be limited by the turn-off rate of the transmitter:

$$R_{min}^{TX} = c_o \left(\frac{t_{lk}}{2} + \frac{t_{to}^{TX}}{2} + \frac{\tau_{RG}}{4} \right) \tag{3.16}$$

where t_{lk} is the time delay associated with the leakage signal, t_{to}^{TX} is the turn-off time of the transmitted signal, and τ_{RG} is the range-gate pulsewidth. The apparent leakage range is $R_{lk} = c_o t_{lk}/2$. As will be discussed in Section 5.3, the turn-off characteristics of the transmitted signal depend on the desired transmitter on-off

isolation. For example, for $I^{TX}_{on/off} = 40\,\text{dB}$, the turn-off time is 5.4 ns, leading to a minimum range of $R^{TX}_{min} = 1.6\,\text{m} + R_{lk}$. Realistically, the receiver and antenna system do not have infinite bandwidth and can store energy that dissipates or radiates according to a system-specific time-constant(s) [75]. As such, it is necessary to measure the time-domain SNR response of the full radar system.

The time-domain SNR response is a characterization of the system behavior when the receiver is on and the transmitter is off. As discussed, the post processor only takes a single sample per PRI, so it cannot reconstruct the received pulse envelope with a single data set. However, the time-domain SNR response measurement can be used to reconstruct the received pulse enveloped similar to a sampling oscilloscope. It is performed by changing the time delay of the channel in small increments over the range $0 \leq t_R \leq T$ and recording the output of the receiver as the signal moves through a fixed range gate. The single-pulse SNR is calculated for each data point and is plotted versus t_R. For an ideal radar, the waveform should match the envelope of the transmitted signal. However, due to the finite bandwidth of the receiver, the waveform will likely turn off more slowly than the transmitted waveform. The turn-off time of the measured output of the radar can be used to calculate the minimum detectable range:

$$R_{min} = c_o \left(\frac{t_{lk}}{2} + \frac{t_{to}}{2} + \frac{\tau_{RG}}{4} \right) \tag{3.17}$$

where t_{to} is the turn-off time of the full radar. A metric must be selected to determine the turn-off time. For this thesis, the turn-off time will be based on a maximum, rejectable single-pulse SNR at the output of the receiver; it is $\text{SNR}^{out,rej}_{1,max} = -30\,\text{dB}$ for this work. This turn-off time is defined as the time delay between the peak SNR value due to the leakage signal and the point at which the SNR is less than or equal to the maximum, rejectable SNR. This criterion leads to a trade-off between the minimum range and minimum TX-RX isolation of the radar. For high TX-RX isolation values, the leakage signal reduces to a

-30 dB SNR quickly. A limiting case occurs for infinite TX-RX isolation. In this scenario, the minimum range is only limited by the "on" time of the transmitter. On the other hand, if the TX-RX isolation is low, the leakage signal reduces to a -30 dB SNR slowly. In the worst case, it does not reach the required SNR level before the next pulse is transmitted. The trade-off between minimum range and minimum TX-RX isolation can be explored through closed-loop testing and will be discussed in detail in Chapter 8.

3.7.3 Minimum TX-RX Isolation

The minimum TX-RX isolation specification not only depends on the scenario where the receiver is "on" and the transmitter is "off", but also on the case where the receiver is "off" and the transmitter is "on". In this case, the peak of the leakage signal should be sufficiently attenuated to ensure the maximum rejectable single-pulse SNR of -30 dB is not exceeded. The minimum TX-RX isolation through the antenna system for this case can be calculated as follows:

$$I_{min}^{TX/RX} = P_{TX} - I_{RG} - P_N - F_{pulsed}^{RX} - \mathrm{SNR}_{1,max}^{out,rej}[\mathrm{dB}] \tag{3.18}$$

where I_{RG} is the on-off isolation of the range gate and $\mathrm{SNR}_{1,max}^{out,rej}$ is the maximum rejectable single-pulse SNR at the output of the receiver. $I_{min}^{TX/RX} = 81\,\mathrm{dB}$ for the radar in this work. The actual TX-RX isolation specification may be more stringent, depending on the desired trade-off between the minimum range and minimum TX-RX isolation, as discussed in the previous section.

3.7.4 Out-of-Range Ambiguity Resolution

As discussed, BPSK pseudo-random pulse tagging is applied to the transmitted signal to resolve out-of-range ambiguities. The sampled BPSK signal is correlated with the sampled output of the receiver. The autocorrelation of a pseudo-random

code is similar to white noise, making it an excellent choice to distinguish between in- and out-of-range targets [76], [77]. For in-range targets, the phase code is aligned with the phase-coded received signal, and the target return can be detected. For out-of-range targets, the phase code is misaligned with the phase-coded received signal, and the PSD of the target return will be similar to white noise. In this thesis, the out-of-range ambiguity rejection ratio is defined as the ratio of the SNR for an in-range target to the SNR of an out-of-range target. The rejection ratio will depend on the specific segment of the maximal length pseudo-random phase code that is analyzed, as well as the number of samples that are considered. For example, the rejection ratio will be limited by the minimum calculable SNR, which was discussed in Section 3.5.2.

Chapter 4

UWB Pulse Generator

A varactor-diode based PCC serves as the pulse generator for the UWB transmitter. Its design, analysis, nonlinear simulations, and characterization are covered in this chapter. In addition, the properties of the PCC, as they pertain to the UWB short-pulse Doppler radar, are discussed.

4.1 Pulse Generator Requirements

The pulse generator has a significant impact on the behavior of the UWB short-pulse Doppler radar, and a variety of factors contribute to the selection of the pulse generator topology. The selection criteria are discussed in the following sections.

4.1.1 Output Pulse Shapes

A variety of UWB pulse shapes can be utilized, including square, Gaussian, monocycle, and triangular pulses. The derivatives of a Gaussian pulse are also used in UWB systems. The n^{th} derivative of a Gaussian pulse is referred to as an n^{th}-order Gaussian; the 1^{st}-order Gaussian is often referred to as a Gaussian

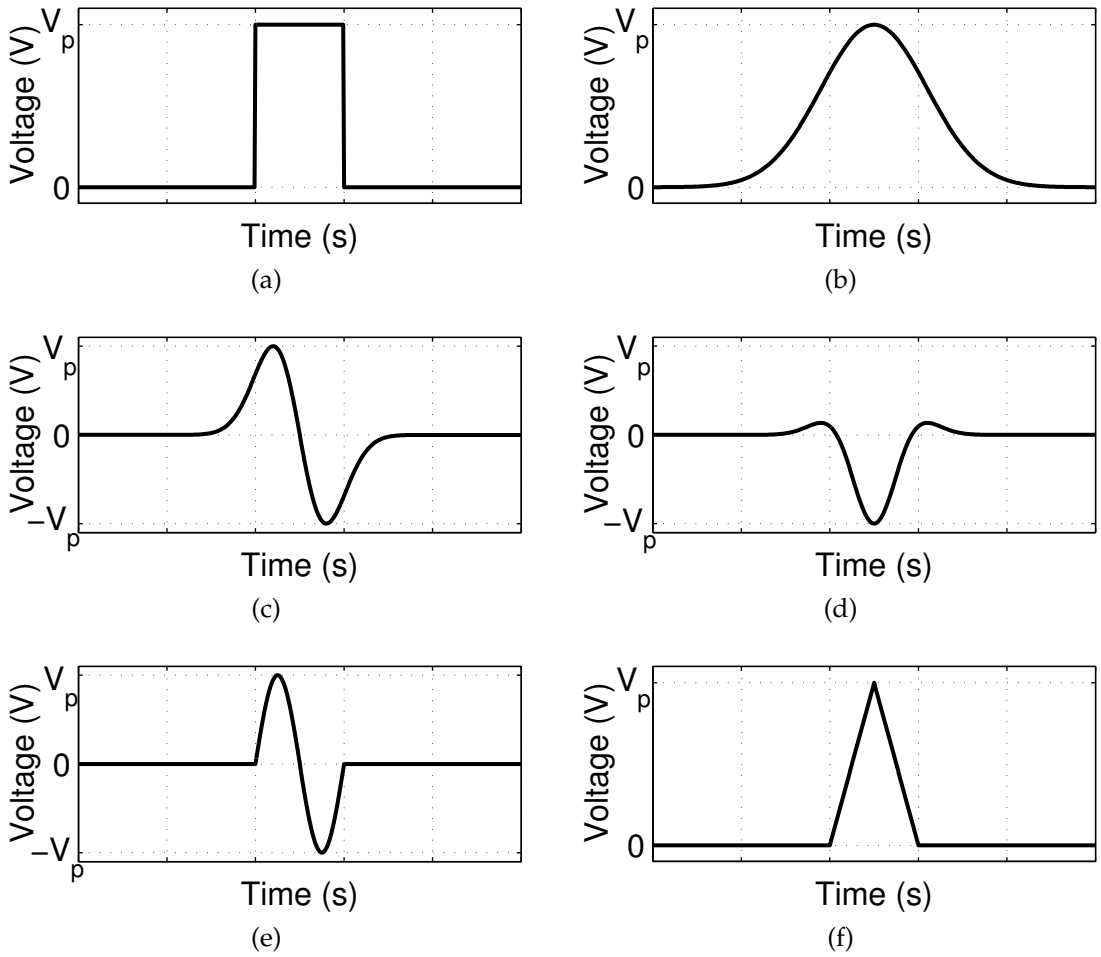

Figure 4.1: *Pulse Shapes.* (a) Square, (b) Gaussian, (c) 1st-order Gaussian (also called a Gaussian monocycle), (d) 2nd-order Gaussian, (e) monocycle, and (f) triangular pulses are illustrated.

monocycle. Several pulse shapes are illustrated in Figure 4.1.

The UWB pulse often serves as the envelope for a carrier-based radar, and it is important to consider the time-domain characteristics of the pulse. As seen in the figure, monocycles and derivatives of Gaussian pulses introduce a phase inversion within the pulse. As noted, BPSK pulse tagging will be employed in the transmitter. As such, introducing a phase inversion via the pulse envelope could complicate the correlation step applied in the post processor. Only single polarity pulse envelopes were considered for this work.

Another important time-domain characteristic of the pulse envelope is the pulsewidth. The pulse should be narrow to minimize the shortest detectable range; however, a very short pulse corresponds to a very short integration period (see Section 3.6.1). In addition, if the pulsewidth is comparable to the period of the carrier, the pulse envelope will be differentiated and distorted upon transmission through the antenna system, as will be discussed in Chapter 7. In other words, there are trade-offs when selecting the pulsewidth, and it should be selected to suit the specific radar application.

The frequency-domain characteristics of the pulse envelope are also important. Square and triangular envelopes result in sinc and sinc^2 frequency spectra, respectively. A Gaussian pulse envelope has a Gaussian frequency spectrum, which falls off without the side lobes exhibited with a square or triangular envelope. A Gaussian spectrum eases the requirements for the transmitter components, antenna system, and receiver components, making it a desirable option; it was, therefore, selected for this work.

4.1.2 Pulse Doppler Radar Requirements

A pulse Doppler topology was selected for this work. As such, the pulse generator must lend itself to a coherent radar design. An important requirement for coherent operation is that the transmitter and receiver share an LO or a pair LOs that are phase coherent. To conform with this hardware constraint, the pulse generator should produce a baseband pulse train which can be applied to the LO signal through a mixing or switching process. As coherency is vital in a pulse Doppler design, it is also important to minimize the added phase noise due to the pulse generator.

4.1.3 Circuit Technology

The prototype radar described in this thesis was designed using commercial off-the-shelf (COTS) components. It is desirable to integrate future iterations of the radar in a monolithic microwave integrated circuit (MMIC) technology, so it is advantageous to select a pulse generator topology that lends itself to both hybrid and MMIC designs. By selecting a topology that can be designed in both technologies, the prototype radar components can be replaced one at a time with MMIC components without significantly changing the overall radar performance; a similar approach was taken in [78].

4.2 UWB Pulse Generator Technologies

UWB pulse generators are used extensively for pulsed UWB systems, and a variety of subnanosecond pulse generator topologies have been demonstrated in the literature. Although optical short-pulse generators exist, we are interested in a microwave solution. Common microwave pulse generator implementations include step recovery diode (SRD) circuits, passive pulse generators and pulse-shaping circuits, digital pulse generators, transistor circuits, and nonlinear transmission lines (NLTLs).

4.2.1 SRD Pulse Generators

SRDs are p-i-n diodes and are typically constructed on Si or GaAs substrates. Their DC behavior is similar to a standard pn junction, but their dynamic behavior is different and important to switching applications [79]. Under forward bias, an SRD is in a low impedance state and stores charge. Under reverse bias, the SRD

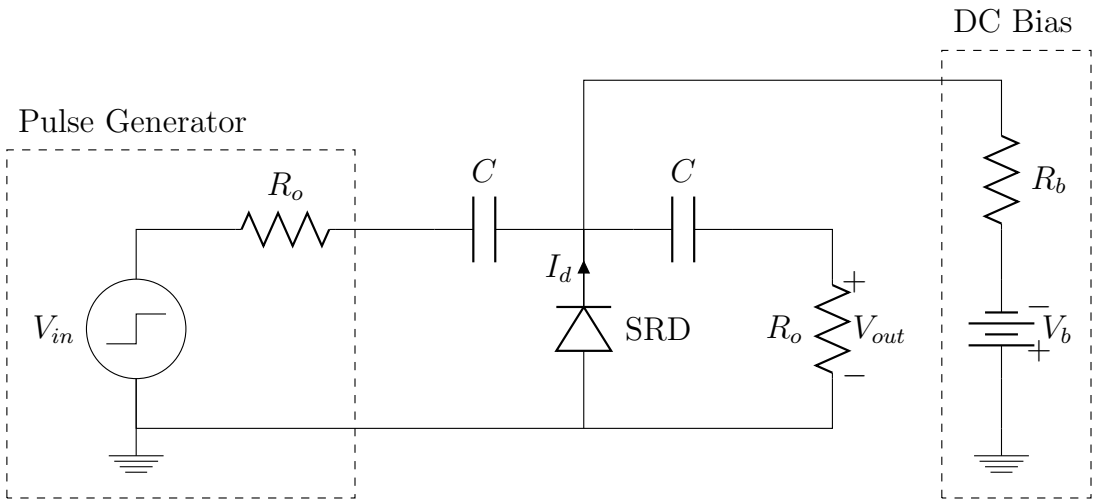

Figure 4.2: *SRD Pulse Sharpener.* An SRD circuit can be used to sharpen the edge of a voltage step, as illustrated in the waveforms of Figure 4.3.

discharges; once the diode is discharged, which occurs rapidly, it behaves as a high impedance. Due to its behavior under forward and reverse bias conditions, an SRD can be used to sharpen the edge of a voltage step. Consider the circuit in Figure 4.2. The DC bias induces a forward bias current through the SRD and charges the diode junction while the RF input is 0 V, as illustrated in the signal waveforms of Figure 4.3. The generator applies a voltage step with a finite rise time, which reverse biases the SRD. The current flow through the diode reverses polarity and continues to flow until the stored charge is depleted. During this period, the diode is in its low impedance state, and the output voltage is 0 V. Once the charge is depleted, the SRD quickly transitions to its high impedance state, and the diode current drops to zero. The transition time depends on the diode characteristics and defines the rise time of the voltage step at the output of the circuit, as seen in Figure 4.3. A single SRD circuit can sharpen the rise time of a voltage step from 10 ns to 300 ps [79]. Pairs of SRDs can be used to sharpen both the rising and falling edges of a square pulse.

SRDs can also be coupled with other discrete or distributed components

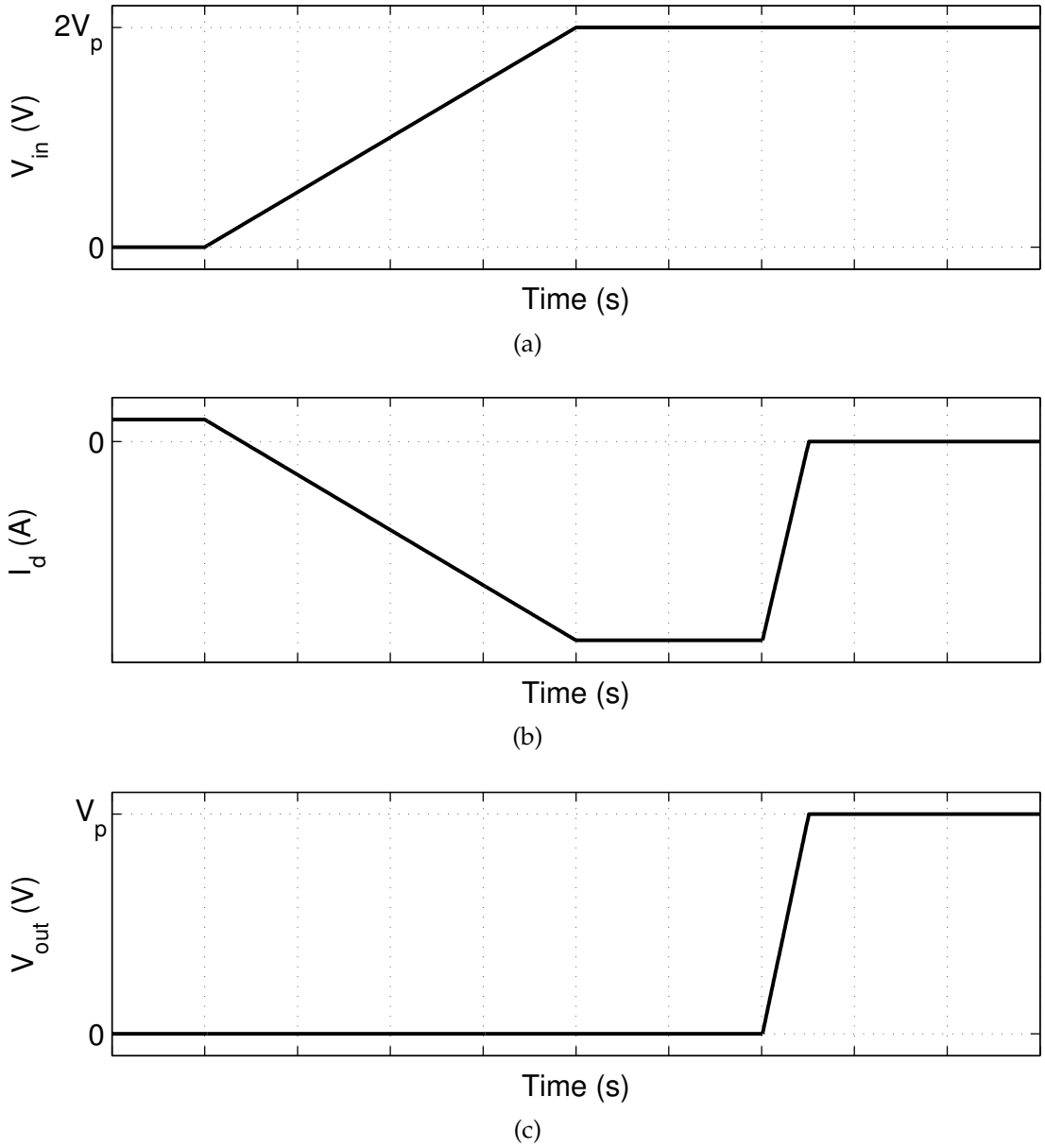

Figure 4.3: *SRD Pulse Sharpener Signals.* The SRD circuit of Figure 4.2 can be used to sharpen the edge of a voltage step, as illustrated in the waveforms.

to create pulse generators. SRD pulse generators have been used extensively in the literature. A tunable monocycle SRD pulse generator is presented in [80], and its circuit diagram is shown in Figure 4.4. The generator centers on a series SRD and a shunt, shorted transmission line. A square wave is applied to the input of the pulse generator, and the output of the SRD is a short voltage

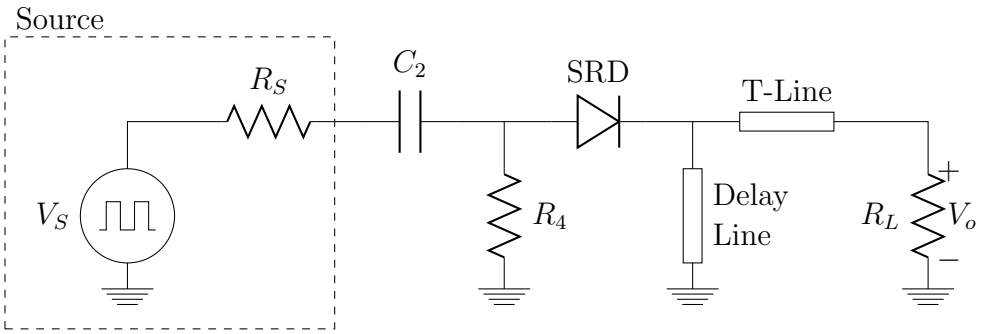

Figure 4.4: *SRD Pulse Generator.* The pulse generator of [80] centers on an SRD.

pulse with a Gaussian-like envelope. A direct voltage wave travels through the transmission line to the load. A second voltage wave travels along the delay line and is reflected by the short. The polarity of the wave is reversed, and the reflected wave reaches the load after some delay, which is established by the length of the stub. The superposition of the direct and reflected waves produces a Gaussian-like monocycle at the output of the pulse generator. The pulsewidth can be adjusted from 450 ps to 1170 ps with pulse amplitudes from 5.8 V to 9.8 V.

[81] presents a similar topology; however, the authors employed various digitally-controlled delay lines to allow both Gaussian-like and Gaussian-like monocycle pulse generation with adjustable pulsewidths. The resulting pulsewidths are comparable to [80] (300–1000 ps), but the peak operating voltages are lower, between 0.8 V and 1.6 V.

In [82], a pair of SRDs are used in a shunt topology to compress the edges of a sinusoidal input and generate a square output pulse with 720 ps rise and fall times, as shown in Figure 4.5. This is similar to the pulse sharpening circuit of Figure 4.2. The two coupled branches provide additional outputs derived from the square wave. In one branch, the square wave is differentiated to generate a 290 ps Gaussian-like pulse. In the other branch, the square wave is differentiated twice to produce a 590 ps Gaussian-like monocycle. The output voltage levels

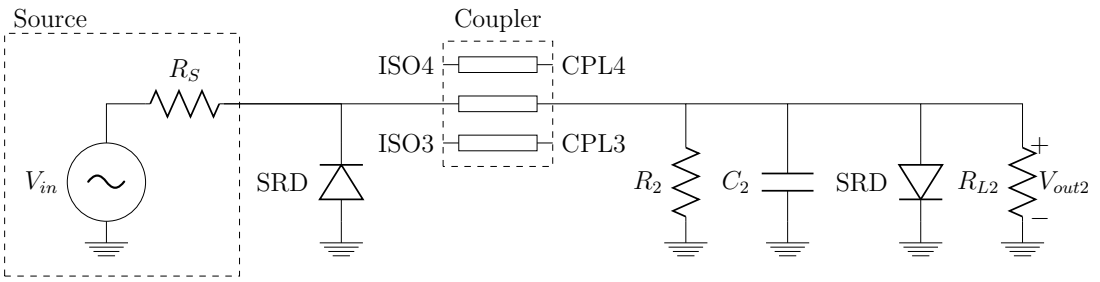

Figure 4.5: *SRD Pulse Generator.* The pulse generator of [82] centers on an SRD.

are less than 100 mV.

Many other examples of SRD pulse generators exist in the literature, which operate with a range of pulsewidths (~100 ps to ~2 ns), Gaussian-like or Gaussian-like monocycle pulse shapes, and various peak voltages from 100 mV to 10 V. The versatility of SRD circuits comes at a price. SRDs exploit two diode characteristics that typically result in high noise levels: large input drive levels and the quick transient current under reverse bias conditions [83]. Large input drive levels, associated with large peak output voltages (3–10 V), are used to charge the intrinsic region of the diode under forward bias, and the current levels can exceed the shot current relation, resulting in excess current noise and degrading the phase noise of the pulse generator [83]. During the transition to the high impedance state, the carriers stored in the intrinsic region are discharged. The carriers interact with the semiconductor lattice, resulting in statistical variation in the discharge time which is observed as added phase noise [83]. These characteristics are intrinsic to the operation of the SRDs.

As noted, SRDs are normally fabricated on microwave substrates. However, they are not available in most standard MMIC processes, so most SRD pulse generators, including those mentioned in this section, are hybrid circuits.

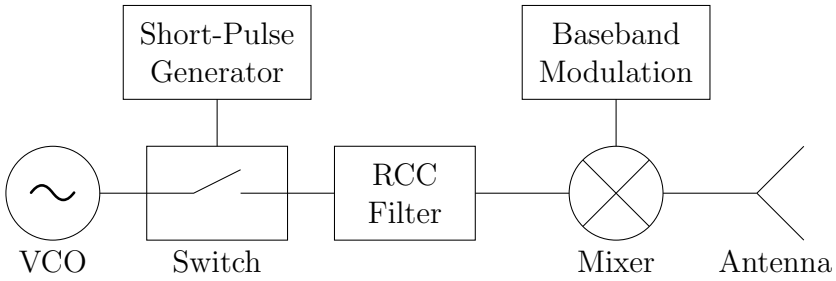

Figure 4.6: *Passive Pulse-Shaping Circuit.* [84] presents a passive pulse-shaping circuit.

4.2.2 Passive Pulse Generators and Pulse-Shaping Circuits

Passive components such as switches, transmission lines, filters, and antennas can be used to generate or shape a short pulse.

Switch-Based Pulse Generators

[84] presents a short-pulse generator design in which the carrier is gated using a switch, as illustrated in Figure 4.6. The root-raised cosine filter provides spectral filtering so the output conforms to the FCC's UWB spectral mask. In this design, an upconversion stage is not required, and the mixer is employed to apply pulse tagging. [85] employs a similar architecture but uses a second gating stage to further reduce the transmitted pulsewidth.

Switch-based short-pulse gating circuits have challenging requirements and are somewhat limited in operation:

- The switch must have subnanosecond rise and fall times as well as subnanosecond on and off times to generate a subnanosecond pulse.
- A short-pulse generator is required to generate the baseband switch control signal.

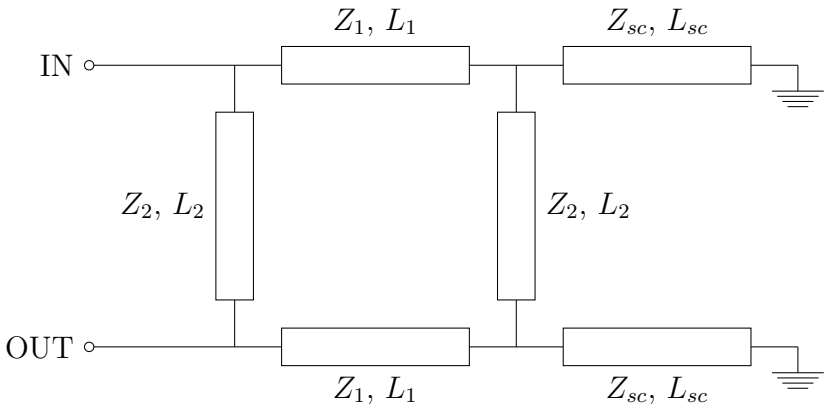

Figure 4.7: *Passive Pulse-Shaping Circuit.* [86] presents a passive pulse-shaping circuit.

- Fast switches generally have limited isolation, and several switching stages may be required to achieve sufficient transmitter on-off isolation.
- The pulse shape is often limited to a rectangular pulse.

Despite these limitations, switch-based circuits can be useful in UWB pulse generation.

Transmission Line Pulse Generators

[86] describes a passive pulse-shaping circuit in which the pulse is generated at baseband. As illustrated in Figure 4.7, the design is based on a hybrid structure in which the two through ports are terminated in shorted stubs. A voltage step is applied at the input port, and the reflections from the stubs add in the time domain, resulting in a subnanosecond Gaussian-like monocycle.

Pulse-Shaping Filters

Pulse-shaping filters are used extensively in communications applications to provide additional spectral filtering to meet the FCC's UWB spectral mask, as in [84]. [87]–[91] include examples of pulse-shaping filters and will be discussed in

the next section. The radar in this work operates outside the FCC's UWB band, and spectral filtering is not a primary concern.

Pulse-Shaping Antennas

UWB antennas can also be exploited to shape the transmitted UWB pulse. Antennas provide spectral filtering and can behave as temporal differentiators [92], as will be discussed in Chapter 7. The differentiation resulting from the antenna system must be considered in the pulse selection and design of the receiver, especially if the period of the carrier is comparable to the pulsewidth of the envelope. [93] and [94] are both examples where the time differentiation property was used to establish the desired transmitted pulse spectrum.

Pulse shaping via the antenna system's transfer function is primarily utilized for impulse radars and radars whose pulsewidth is comparable to the period of the carrier. The desired pulse envelope for this work is wide enough to allow a few cycles of the carrier frequency to be transmitted. As will be discussed in Chapter 7, this means the time differentiation property of the antenna system will not significantly impact the pulse envelope of the radar signal. As a result, the antenna system in this work is not designed to provide significant time-domain pulse shaping of the radar signal.

4.2.3 Digital Pulse Generators

A variety of digital pulse generator topologies exist in the literature. Similar to the hybrid-based pulse generator that was presented, some digital pulse generators employ time delays to generate short pulses. In [87], a 100 MHz square wave is split between two paths, as shown in Figure 4.8. One path inverts the signal and introduces a voltage variable delay through a varactor diode. The two paths are applied to the input of a NAND gate, resulting in a narrow pulse

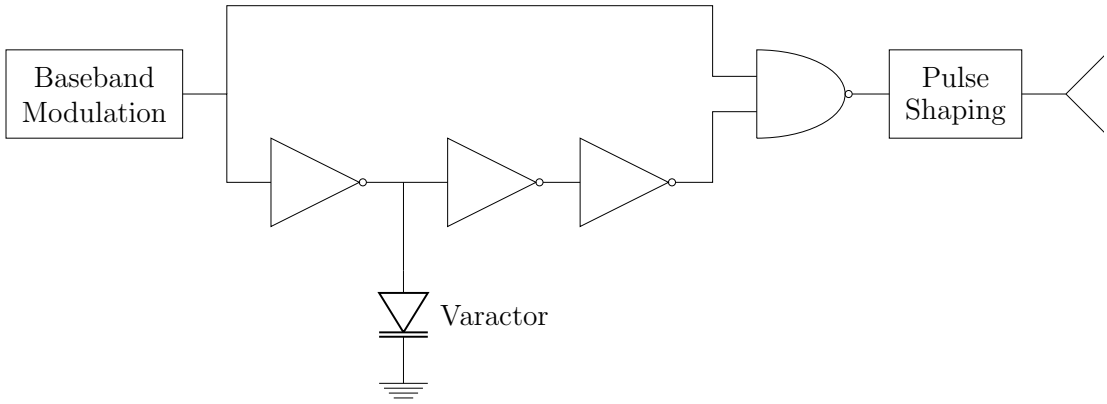

Figure 4.8: *Digital Pulse Generator.* [87] presents a digital pulse generator.

whose pulsewidth is defined by the time delay. A high pass filter integrates the pulse, and the final pulsewidth is on the order of 300 ps. [88], [89], and [90] use similar topologies, resulting in ~100 ps to ~300 ps Gaussian-like monocycles, ~300 ps 2nd-order Gaussian-like pulses, and 340 ps Gaussian-like monocycles, respectively. The peak output voltage for digital pulse generators is limited by the supply rail. For example, the peak voltage is less than 0.5 V in [88].

In [91], the LO provides the input signal for a digital pulse generator, as seen in the block diagram in Figure 4.9a. The pulse generator, detailed in Figure 4.9b, is composed of a set of digital frequency dividers and AND gates. Each frequency divider reduces the signal frequency by half, and the number of dividers sets the PRF of the pulse generator. The AND gates reduce the duty cycle from 50% to $(100/2^n)$%, where n is the number of AND gates, as illustrated by the waveforms of Figure 4.10; any number of stages can be selected. The duty cycle can be increased for a given PRF by removing some of the AND gate stages. The envelope is shaped using a Gaussian filter and mixed with the carrier; the final pulsewidth is 1 ns and the PRF is 125 MHz. Since the pulse envelope is derived from the carrier, the circuit ensures synchronization between the carrier and envelope. Synchronization between the two is not required for a homodyne

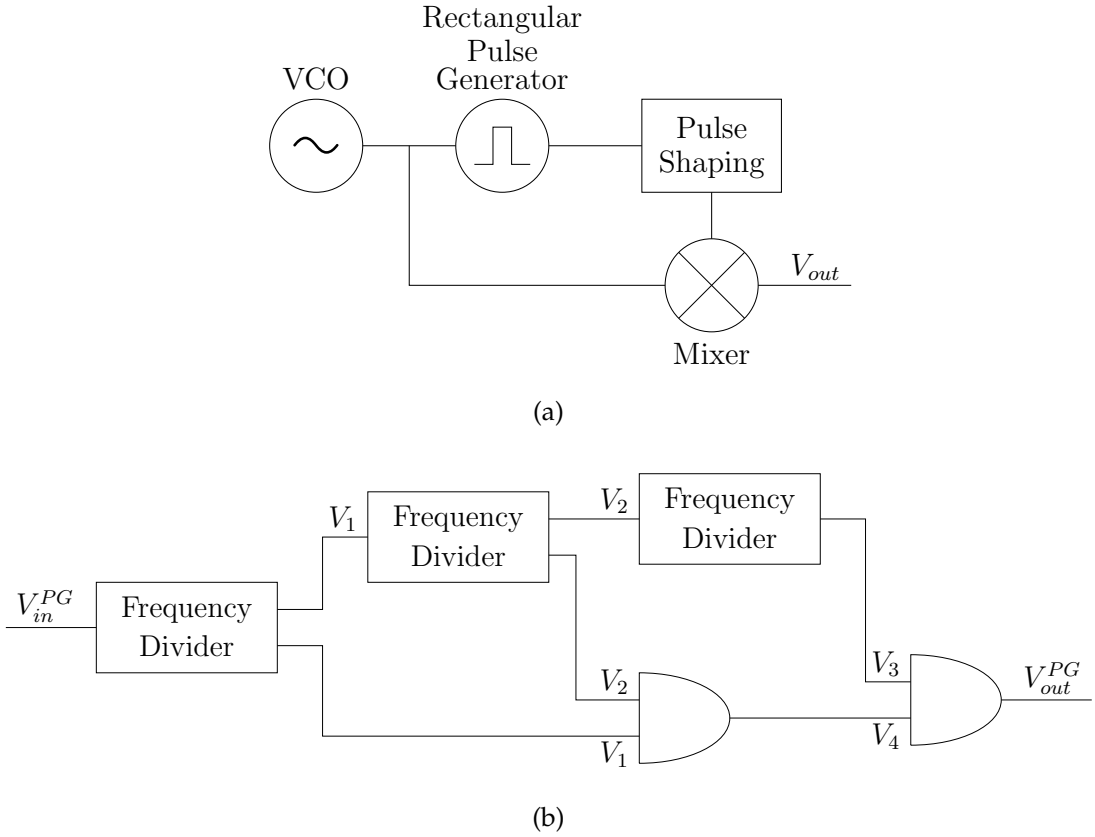

Figure 4.9: *Digital Pulse Generator.* [91] presents a digital pulse generator. The block diagram is illustrated in (a) and the pulse generator architecture is illustrated in (b).

pulse Doppler radar but can improve the performance by limiting the phase noise and increasing the coherent processing interval. Similar techniques will be discussed in Chapter 9 as possible improvements to the radar described in this thesis.

Many of the pulse generators in the section were designed for operation in the 3.1–10.6 GHz UWB band and focus on meeting the FCC's spectral mask. As a result, some of the designs are more akin to impulse radars ([87]–[90]) and would not be suitable generators for a pulse Doppler radar design. However, the basic digital pulse forming techniques described in these works typically result in rectangular or triangular pulses and can be used for pulse Doppler radar if

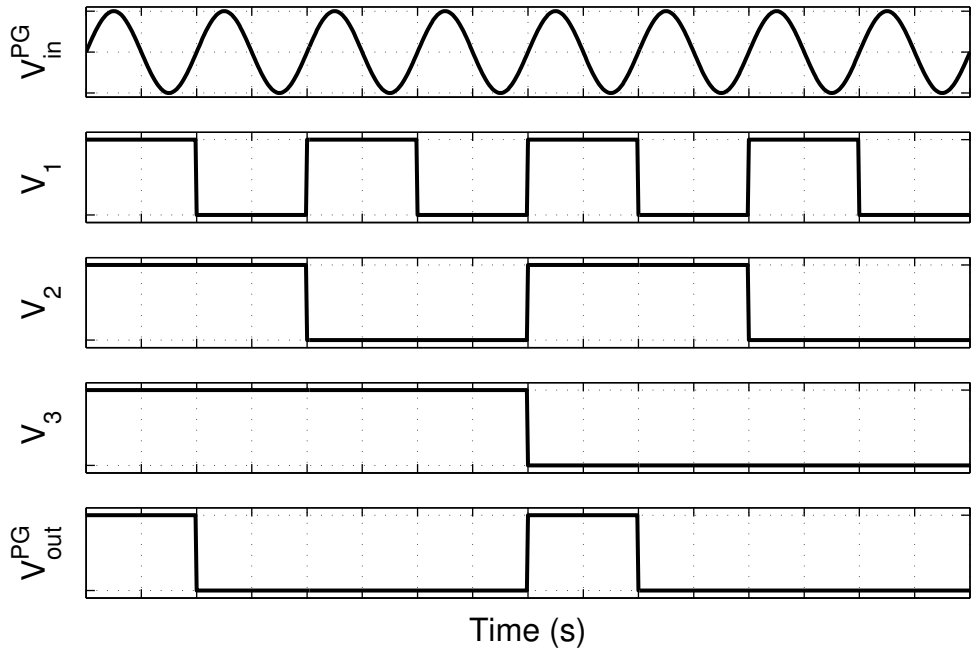

Figure 4.10: *Digital Pulse Generator.* [91] presents a digital pulse generator. The waveforms, which correspond to the circuit diagram in Figure 4.9b, are plotted.

the pulse-shaping filters are not included.

4.2.4 Transistor-Based Pulse Generators

A variety of digital pulse generators exist in the literature. One example, which is illustrated in Figure 4.11, employs a CMOS triangular pulse generator and ring oscillator which are triggered from the same source [95]. The output is a train of 200 mV, 1.1-4.5 ns, Gaussian-like pulses. Like the design in [91], this design ensures synchronicity between the envelope and carrier and presents a means to reduce the phase noise of the transmitted signal for future radar iterations.

In [96] a triangular pulse generator and a mixer were designed in a BiCMOS process. The mixer not only upconverts the triangular pulse train, but also shapes the pulse so the final pulse envelope is ~1 ns wide and Gaussian-like. The design is well suited for an integrated circuit (IC) design but not for a COTS design. As

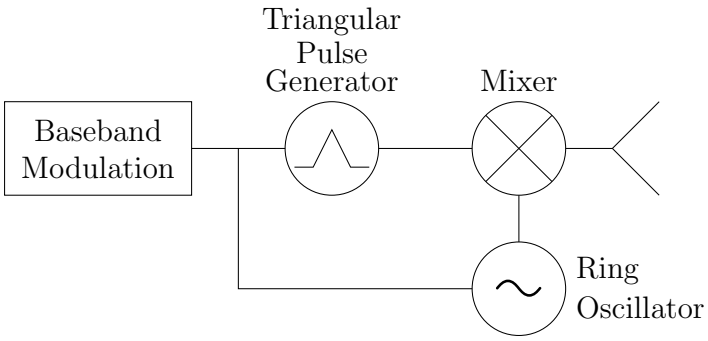

Figure 4.11: *Digital Pulse Generator.* [95] presents a digital pulse generator.

such, it would be appropriate to consider for future iterations of the radar design to provide additional spectral shaping but is not appropriate for the initial radar prototype.

[97] uses a pHEMT distributed amplifier to shape and approximately synthesize a 4 GHz carrier with a Gaussian-like envelope. While the output of the design resembles an upconverted pulse train, the circuit does not utilize an LO. As a result, it can not be used in a pulse Doppler radar design.

4.2.5 Nonlinear Transmission Lines

The model of an NLTL is similar to a standard distributed transmission line model except either the inductors or capacitors are nonlinear [98], as shown in Figure 4.12. In practice, the implementation in Figure 4.12b is selected, as nonlinear capacitors are more readily available in standard processes than nonlinear inductors. Nonlinear capacitors can be implemented using varactor or Schottky diodes [98], [99]. Discrete NLTLs are implemented using discrete inductors and varactors [100], [83], and distributed NLTLs are implemented by periodically loading a microstrip [101] or coplanar waveguide (CPW) [99], [102] transmission line with diodes. NLTLs accept a periodic input signal and compress it into a series of rectified pulses. In addition to standard NLTL circuits

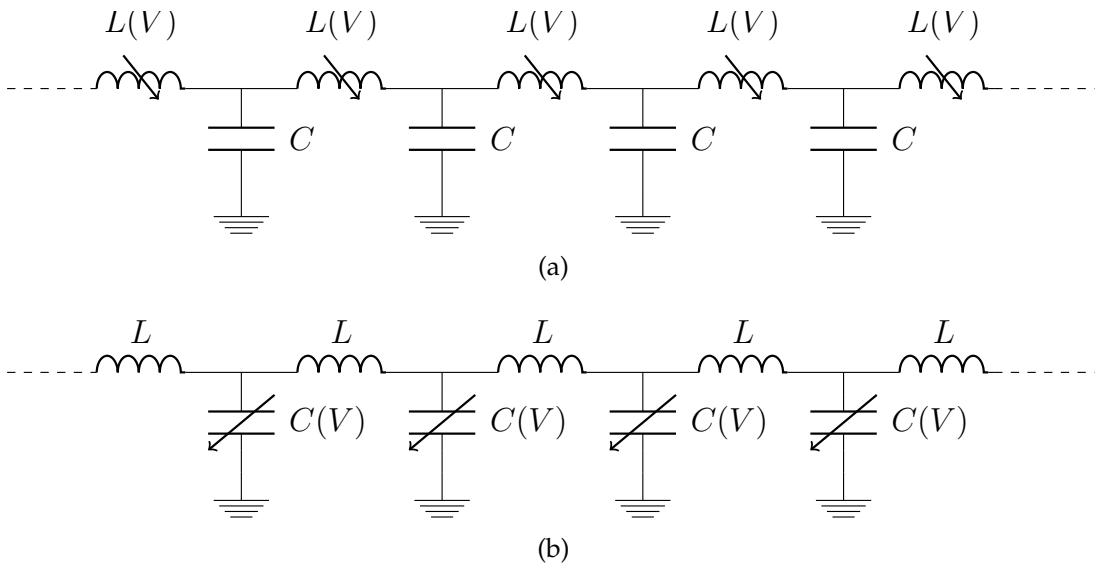

Figure 4.12: *NLTL Model.* An NLTL model is similar to a distributed transmission line model, except either the inductors or capacitors are nonlinear. An NLTL can compress a periodic input signal to generate a series of baseband pulses.

which require an RF source at the input, free-running [103] and injection-locked [104] NLTL oscillators have also been demonstrated. The mechanics of NLTLs will be discussed in detail in Section 4.3.

Under forward-bias conditions, the phase noise of a varactor diode is dominated by shot noise [83]. The noise mechanisms are less established for a varactor under reverse bias conditions, and the phase noise of a discrete NLTL was explored in [83]. [83] found that the additive phase noise of the NLTL under study was near the noise floor of the measurement system. The phase noise was, however, impacted by the bias circuitry; optimizing the bias circuitry provides a means to minimize the phase noise of an NLTL, which is advantageous for coherent radar design.

4.2.6 UWB Pulse Generator Trade-Offs

The characteristics of the various pulse generators presented in the previous sections are summarized in Tables 4.1 and 4.2. As noted previously, a variety of criteria contribute to the pulse generator selection.

As discussed in Section 4.1.1, a Gaussian pulse envelope is desired for this work. SRD and NLTL circuits can generate a Gaussian-like pulse envelope directly. The output of the other pulse generators can be shaped using filters or other components (e.g. a mixer) to create the desired Gaussian pulse shape.

As discussed in Section 4.1.2, the pulse generator should produce a baseband pulse train which can be applied to the output of the LO via a mixing or switching

Table 4.1: UWB Pulse Generator and Pulse-Shaping Circuits

CIRCUIT TYPE	PHASE NOISE	COMPATIBLE WITH MMICS?	COMPATIBLE WITH HYBRID DESIGN?
SRD Pulse Generators	High	No	Yes
Passive Pulse Generators: Switch-Based	Limited by control signal stability	Yes	Yes
Passive Pulse Generators: T-Line Designs	Low	Yes, but component size can be restrictive.	Yes
Passive Pulse-Shaping Circuits: Filter-Based	Low	Yes, but component size can be restrictive.	Yes
Digital Pulse Generators	Design dependant	Yes	Yes, but challenging if devices must be matched.
Transistor-Based Pulse Generators	Design dependant	Yes	Yes, but challenging if devices must be matched.
NLTLs	Low	Yes	Yes

process. With the exception of the design in [97], any of the pulse generation techniques presented in the references can be adapted to this purpose. The pulse generator should also exhibit low phase noise. Most of the pulse generators can be designed for low phase noise, but SRD pulse generators will typically have poor phase noise performance compared to other technologies for the reasons highlighted in Section 4.2.1.

As noted in Section 4.1.3, it is desirable to select a pulse generator topology that is compatible with both hybrid and MMIC design. SRD pulse generators are compatible with hybrid design, but not with MMIC design. Transmission line based pulse generators work well in hybrid circuits but can be quite large in a MMIC design; real estate is expensive on a MMIC, so transmission line designs are not ideal. Like transmission line designs, filter-based pulse-shaping circuits work well in hybrid designs but can be quite large when designed on a MMIC. Digital and transistor-based pulse generators work well in MMIC designs but can be challenging to implement in a hybrid circuit. Both switch-based and NLTL pulse generators can be implemented as hybrid circuits and in MMIC technology, so both pulse generator topologies can be employed in the initial COTS prototype and future integrated radar designs. As noted previously, both technologies are compatible with a pulse Doppler radar architecture and can be designed with low phase noise. These characteristics, combined with the Gaussian-like pulse envelope of an NLTL pulse generator, make switch-based and NLTL-based pulse generators excellent technologies for the radar presented in this thesis. The NLTL-based pulse generator is presented in the following sections, and the switch-based designs are presented in Sections 5.1.2 and 5.1.3.

Table 4.2: UWB Pulse Generator and Pulse-Shaping Circuits

CIRCUIT TYPE	INPUT WAVEFORMS AND/OR CONTROL SIGNALS	OUTPUT PULSE SHAPES	COMPATIBLE WITH PULSE DOPPLER RADAR?	REFERENCES
SRD Pulse Generators	Input: square or sinusoidal Control: DC bias for some	Gaussian-like, Gaussian-like monocycle	Yes	[79], [80], [81], [82]
Passive Pulse Generators: Switch-Based	Input: LO signal Control: short-pulse switch control signal	Rectangular	Yes	[84], [85]
Passive Pulse Generators: T-Line Designs	Input: step in [86] but rectangular also possible Control: none required	Gaussian monocycle in [86] but Gaussian-like or rectangular also possible.	Yes	[86]
Passive Pulse-Shaping Circuits: Filter-Based	Input: baseband or RF pulse train Control: none required	Spectral shaping is normally applied so the transmitted signal conforms with a spectral mask.	Yes	[84], [92], [87], [88], [89], [90], [91]
Digital Pulse Generators	Input: square or sinusoid Control: none required	Typically rectangular or triangular. The reference examples include extra pulse shaping.	Yes	[87], [88], [89], [90], [91]
Transistor-Based Pulse Generators	Input: baseband pulse train Control: none required	Triangular and Gaussian in references but others possible.	Yes, if an LO is employed (i.e. not [97]).	[95], [96], [97]
NLTLs Pulse Generators	Input: sinusoid Control: optional DC bias	Gaussian-like	Yes	[99], [100], [83], [101], [102]

4.3 Varactor-Diode PCC Design

The PCC in this work is based on a discrete NLTL with varactor diodes, as shown in Figure 4.13. The input to the PCC is a DC-offset 200 MHz sinusoid, which the circuit compresses to form a train of subnanosecond, positive baseband pulses with a PRF of 200 MHz. When the SMV1236 varactor diodes are forward biased, they conduct, providing a low impedance path to ground. Consequently, the output voltage is approximately 0 V when the input voltage is sufficiently negative to turn the diodes on. When the diodes are reverse biased, they behave as variable capacitors, and the PCC can be approximated as a finite NLTL, as in Figure 4.12b. Since the capacitance is nonlinear with voltage, the phase velocity of an infinite NLTL is also a function of voltage:

$$v_{ph}(V_R) = \frac{1}{\sqrt{LC(V_R)}} \tag{4.1}$$

where v_{ph} is the phase velocity, V_R is the reverse bias voltage across the varactor, and L and C are the reactances per unit length of line. For a finite, discrete approximation of an NLTL, the expression for phase velocity must be adapted, but it remains proportional to Eqn. (4.1):

$$v_{ph}(V_R) = \frac{f(\kappa)}{\sqrt{LC(V_R)}} \tag{4.2}$$

where $f(\kappa)$ is a function of the wave number and describes a weak dispersion relation [105]. The inductances of the PCC are constant, and the capacitance of the varactor diodes decreases with increasing reverse bias. Therefore, the phase velocity increases with increasing reverse bias, and if a sinusoid is applied at the input to the PCC, the positive half-cycle will be compressed to form a positive voltage pulse.

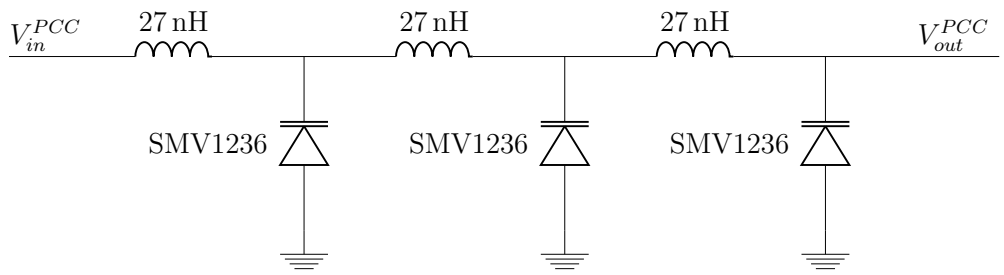

(a)

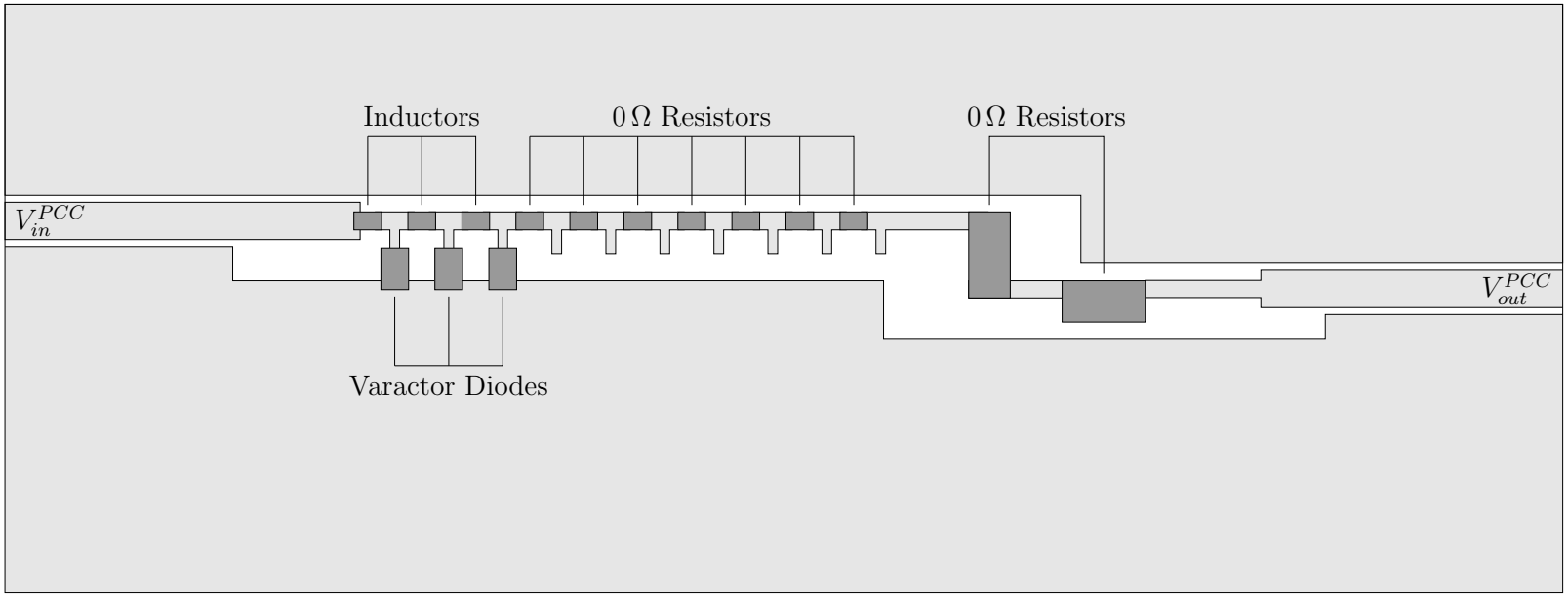

(b)

Figure 4.13: *PCC*. The PCC schematic is shown in (a), and the layout is shown in (b). The PCC is based on a discrete NLTL and converts a 200 MHz sinusoidal input into a 200 MHz PRF, subnanosecond pulse train. The number of *LC* stages can be adjusted from 1–10. The varactor diodes are manufactured by Skyworks.

4.3.1 Pulse Shape

Theoretically, if the dispersion of an NLTL perfectly balances the nonlinearity of the line, a solitary wave will form [98]. Assuming that the output of the PCC is similar to that of an NLTL, it can be approximated by the soliton solution of the form:

$$V_{out}^{PCC}(t) \simeq \sum_{n=1}^{\infty} V_{out,p}^{PCC} \text{sech}^2\left(\frac{1.763(t - nT_{PCC})}{\tau_V}\right) \tag{4.3}$$

where $V_{out,p}^{PCC}$ is the peak output voltage, n is an integer, T_{PCC} is the period of the input sinusoid, and τ_V is the FWHM pulsewidth of the voltage pulse, following from the single pulse expressions in [98] and [99]. A Gaussian-like pulse envelope is used for many UWB applications and is desired for this work. The Taylor expansions, up to the third term, for a Gaussian and the sech^2 function in Eqn. (4.3) are:

$$\text{sech}^2(bt) \simeq 1 - b^2t^2 + \frac{2b^4}{3}t^4 \tag{4.4}$$

$$\exp(-b^2t^2) \simeq 1 - b^2t^2 + \frac{b^4}{2}t^4 \tag{4.5}$$

The first two terms of the expansions are identical, and the third terms match to within a multiplicative constant. The similarity between the two functions is shown graphically in Figure 4.16a and compared with the simulated and measured output of the PCC. The output of the PCC can be further approximated as:

$$V_{out}^{PCC}(t) \simeq \sum_{n=1}^{\infty} V_{out,p}^{PCC} \exp\left(-a\left(\frac{t - nT_{PCC}}{\tau_V}\right)^2\right) \tag{4.6}$$

where a is a constant. For a Gaussian pulse, $a = 4\ln(2) \simeq 2.773$. Based on Eqns. (4.3)–(4.6), a = 3.103, which is within 15% of the theoretical Gaussian coefficient.

The preceding expressions use the FWHM pulsewidth of the voltage pulse. The FWHM pulsewidth of the power pulse is of interest for this work, and Eqn.

(4.6) can be rewritten as follows:

$$V_{out}^{PCC}(t) \simeq \sum_{n=1}^{\infty} V_{out,p}^{PCC} \exp\left(-\frac{a}{2}\left(\frac{t - nT_{PCC}}{\tau}\right)^2\right) \tag{4.7}$$

where τ is the FWHM pulsewidth of the power pulse.

Since the time-domain output of the PCC is Gaussian-like, the frequency-domain output will also be Gaussian-like. The time-bandwidth product for a Gaussian pulse is:

$$\tau\beta_{3dB} = \frac{4}{\pi} \ln\left(\frac{1}{\sqrt{0.5}}\right) \simeq 0.44 \tag{4.8}$$

where β_{3dB} is the bandwidth of the pulse [106]. This relationship is important to the design of the receiver's matched filter (see Chapter 6).

4.3.2 PCC Design

The SMV1236 hyper-abrupt varactor diode was selected for this work. As implied by its hyper-abrupt categorization [107], it provides a wide range of capacitances (3.5–25 pF at 1 MHz). In addition, it allows for voltages up to 15 V across the diode. Standing waves along an NLTL-like circuit can result in high node voltages; therefore, it is important to ensure the diode break-down voltage is not exceeded at any point in the circuit [83]. Simulations verify that the PCC in this work can operate under sinusoidal excitation with amplitudes up to 6 V peak without exceeding the reverse break-down voltage.

NLTL designs can employ constant or tapered inductance values [99]; in this work, the inductances are equal. The inductance was selected to provide a 50 Ω input impedance for a mid-range reverse bias level ($V_R = 2$ V) by approximating the input impedance as:

$$Z_{in}(V_R) \simeq \sqrt{\frac{L}{C(V_R)}} \tag{4.9}$$

The input and output impedances, and thus matches, will change as the input voltage changes. The worst case mismatch occurs when the diodes are forward

biased and the input impedance is a short circuit.

The PCC will have a corner frequency of [99]:

$$f_l(V_R) \simeq \frac{1}{\pi\sqrt{LC(V_R)}} \tag{4.10}$$

The corner frequency is a result of the periodic structure of the PCC, and is referred to as the Bragg frequency in NLTL literature [99]. For an impulse compression NLTL, the corner frequency should lie just beyond the desired harmonic content of the output signal [99]. The $V_R = 2\,\text{V}$ corner frequency for the PCC is 600 MHz. An input frequency of 200 MHz was selected, so the first two harmonics are within the frequency range of the PCC. If a lower frequency is selected, the period of the input sinusoid is wider, and the output pulse will also be wider. If a higher frequency is selected, the 2$^{\text{nd}}$ and 3$^{\text{rd}}$ harmonics undergo more attenuation, which counteracts the compressive effect of the PCC; if the harmonics are attenuated too much, the output pulse would resemble a rectified sinusoid rather than a Gaussian-like pulse.

The PCC was modeled in Agilent's Advanced Design System (ADS) using time-domain simulations. The varactor and inductor SPICE models, shown in Figure 4.14, were provided by Skyworks and Coilcraft, respectively, and include parasitic effects. The PCC was simulated with 3–10 *LC* stages to match the physical PCC board design. The PCC was laid out on an FR4 substrate and accommodates up to 10 *LC* stages, as illustrated in Figure 4.13b. The layout also includes space for an optional matching network or a SOIC-8 packaged component.

4.4 Varactor-Diode PCC Characterization

For the PCC characterization, a 200 MHz signal is applied to the input, and the output voltage is measured with an HP54752A 50 GHz, equivalent-time

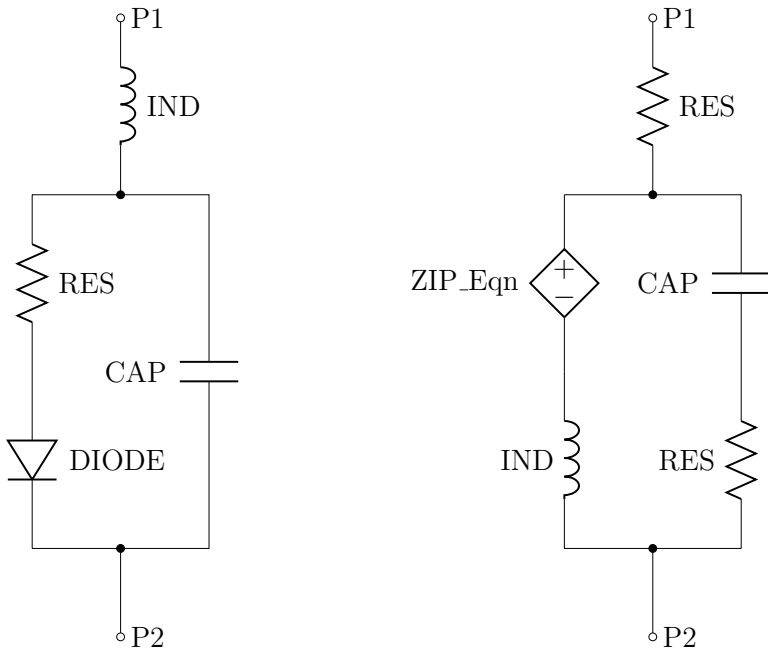

Figure 4.14: *Varactor and Inductor Models.* The varactor (a) and inductor (b) models were provided by Skyworks and Coilcraft, respectively.

oscilloscope and a spectrum analyzer over a range of input RF power levels and DC biases provided through an external bias-T. The PCC length is adjusted from 3-9 *LC* sections. The design of the PCC allows the flexibility to select a peak RF input voltage from approximately 2–4 V and a DC bias from 500–1000 mV.

The number of stages impacts both the peak output voltage and the pulsewidth. As the number of stages increases, the output pulses undergo additional attenuation and the pulsewidth broadens. The results are summarized in Table 4.3.

The input RF and DC voltage levels impact the peak output voltage and the pulsewidth, as summarized in Tables 4.4 and 4.5. In general, as the RF and/or DC voltage increases, the peak output voltage increases and the pulsewidth decreases. The input signal also impacts the output pulse shape. As the DC

Table 4.3: PCC *LC* Sections

LC Sections	τ (ns)	$V_{out,p}^{PCC}$ (V)
3	720	4.4
5	1050	3.8
7	1030	3.6
9	1330	2.1

Table 4.4: PCC Pulsewidth

	τ (ps)		
$V_{DC,in}^{PCC}$ (mV)	$V_{RF,in}^{PCC} = 2.0\,\text{V}$	$V_{RF,in}^{PCC} = 2.5\,\text{V}$	$V_{RF,in}^{PCC} = 3.0\,\text{V}$
500	940	850	760
600	925	830	755
700	935	815	720
800	960	810	695
900	1000	805	680
1000	1065	825	675

Table 4.5: PCC Peak Voltage

	$V_{out,p}^{PCC}$ (V)		
$V_{DC,in}^{PCC}$ (mV)	$V_{RF,in}^{PCC} = 2.0\,\text{V}$	$V_{RF,in}^{PCC} = 2.5\,\text{V}$	$V_{RF,in}^{PCC} = 3.0\,\text{V}$
500	2.4	2.8	2.9
600	2.5	3.0	3.3
700	2.6	3.1	3.6
800	2.6	3.2	3.8
900	2.7	3.3	4.0
1000	2.7	3.4	4.1

voltage is increased, the output pulse deviates from a Gaussian-like envelope, as shown in Figure 4.15.

The main observations from the PCC characterization are:

- The output pulsewidth decreases and the peak output voltage increases as the DC bias increases (see Tables 4.4 and 4.5).

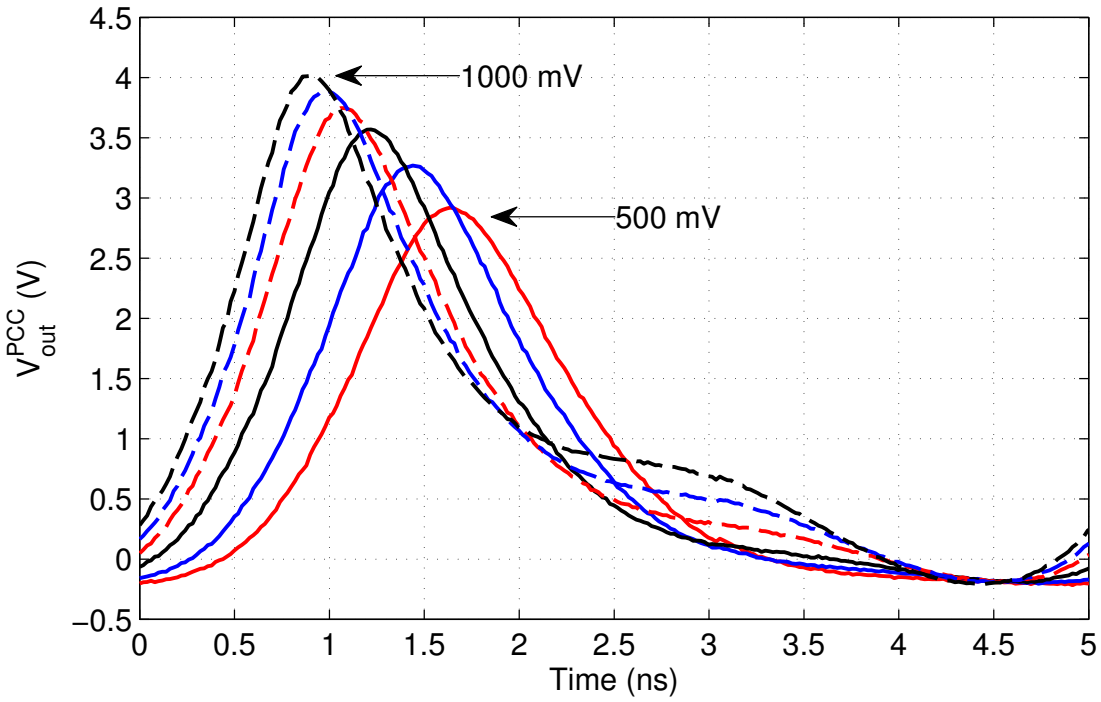

Figure 4.15: *PCC DC Bias.* As the DC bias applied at the input of the PCC increases, the pulse envelope at the output begins to distort. The measured data corresponds to $V_{RF,in}^{PCC} = 3\,V_p$ and $V_{DC,in}^{PCC} = 500 : 100 : 1000\,mV$.

- The DC bias impacts the shape of the pulse envelope (see Figure 4.15).
- The PCC generates harmonics of the input tone (see Figure 4.16b).

4.4.1 PCC Operation for UWB Radar

A 3-section PCC with a 200 MHz, 3 V_p RF, 700 mV DC input signal was selected for this work. The output is plotted in the time and frequency domains in Figure 4.16. The measured data was taken using an HP54752A oscilloscope and a spectrum analyzer. The simulated results were established through time-domain simulations in ADS. The theoretical $sech^2$ and Gaussian time-domain outputs

are based on the following expressions:

$$V_{out}^{PCC}(t) = \sum_{n=1}^{\infty} V_{out,p}^{PCC} \text{sech}^2\left(\frac{1.212(t - nT_{PCC})}{\tau}\right) \quad (4.11)$$

$$V_{out}^{PCC}(t) = \sum_{n=1}^{\infty} V_{out,p}^{PCC} \exp\left(-2\ln(2)\left(\frac{t - nT_{PCC}}{\tau}\right)^2\right) \quad (4.12)$$

where $V_{out,p}^{PCC}$ and τ are measured values. The theoretical Gaussian frequency-domain output is based on the following expression:

$$P_{out}^{PCC}(f) = P_{out,p}^{PCC} \exp\left(-4\ln(2)\left(\frac{f}{\beta_{3dB}}\right)^2\right) \quad (4.13)$$

where $P_{out,p}^{PCC}$ is extrapolated from the measured spectrum and $\beta_{3dB} = 0.44/\tau$ is based on the measured value of τ.

The desired transmitted PRF is 20 MHz, and the PRF at the output of the PCC is 200 MHz. The remaining transmitter components down-sample the PRF, as discussed in Chapter 5.

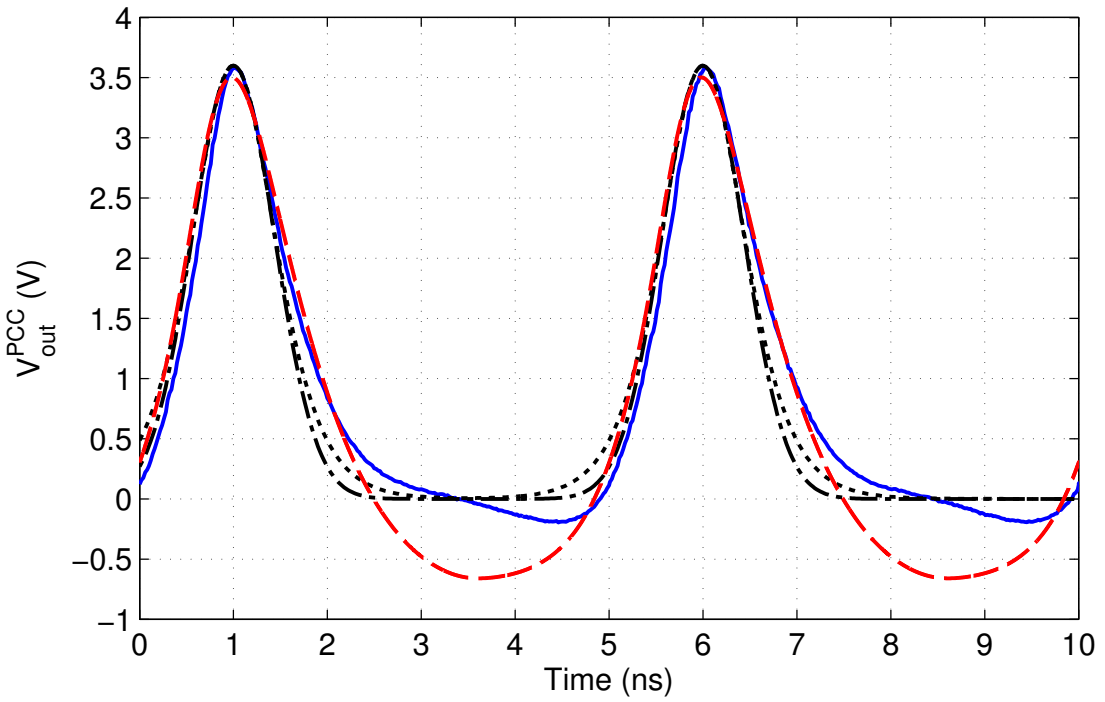

(a)

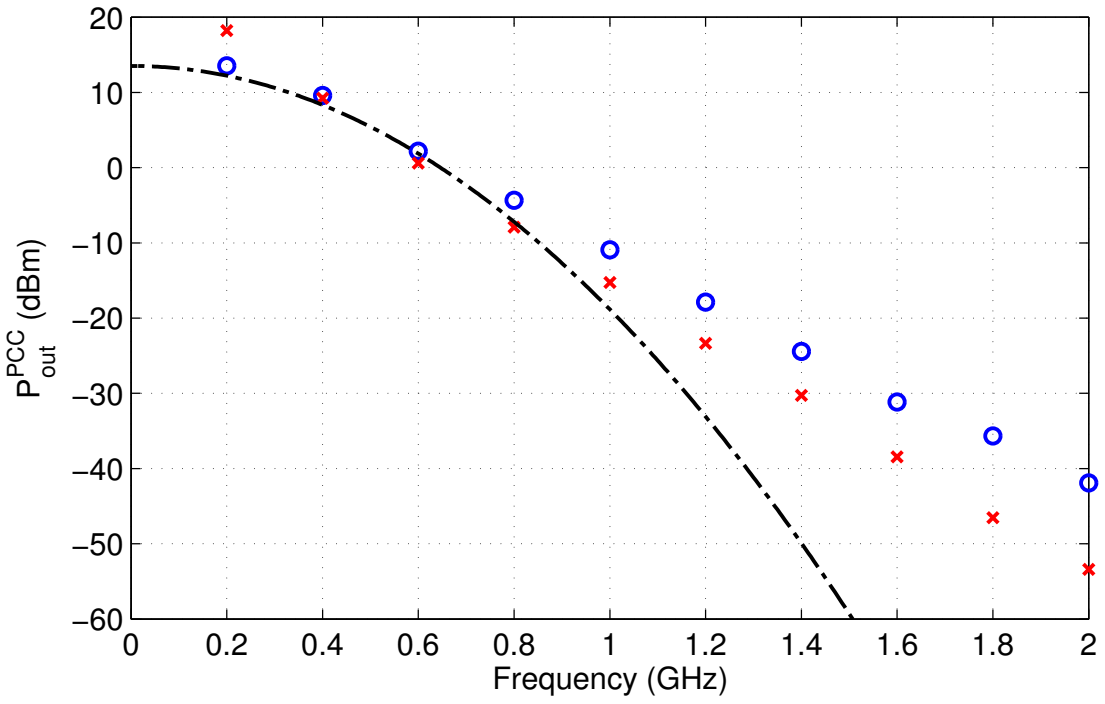

(b)

Figure 4.16: *PCC Output for UWB Radar.* The PCC's input signal for the remainder of this thesis is a 20 dBm, 200 MHz sinusoidal input with a 700 mV DC offset. The measured output is shown in solid blue (circle data markers), the simulated output is shown in dashed red (x data markers), the sech^2 theoretical output is shown in dotted black, and the Gaussian theoretical output is shown in dash-dotted black.

Chapter 5

UWB Transmitter

The transmitter block diagram was presented in Chapter 3, and is repeated in Figure 5.1 for convenience. The PCC was discussed in Chapter 4, and this chapter details the transmitter design and operation.

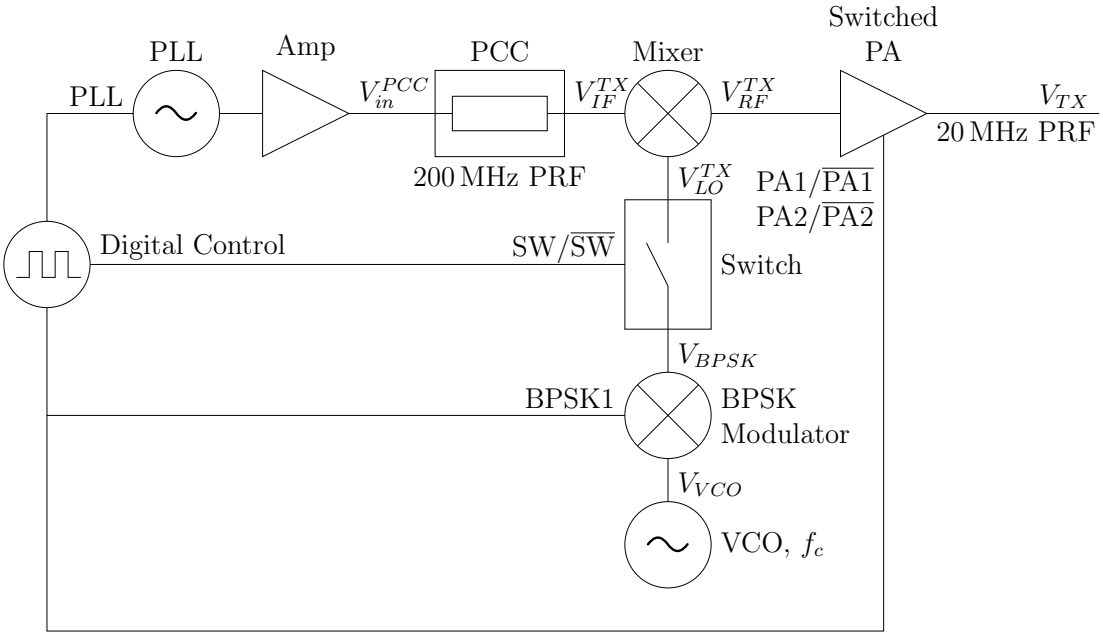

Figure 5.1: *Transmitter Block Diagram.*

5.1 UWB Transmitter Components

The primary functions of the transmitter are to:

- generate a baseband pulse train with subnanosecond FWHM pulsewidths;
- reduce the PRF of the baseband pulse train from 200 MHz to 20 MHz for transmission;
- modulate the baseband pulse train with a 2.5 GHz carrier;
- apply a pseudo-random BPSK tag to each transmitted pulse;
- amplify the upconverted pulse train to meet the minimum peak power specification of $P^{TX}_{on,min} = 0.6\,\mathrm{W}$;
- provide sufficient off-state isolation to meet the maximum peak off-state requirement of $P^{TX}_{off,max} = 12\,\mu\mathrm{W}$.

The desired transmitter functionality presents a set of challenges that center on the narrow transmitted pulsewidth and the wide transmission bandwidth:

- As discussed in Chapter 4, the output bandwidth of the PCC is $\beta_{10dB} = 1\,\mathrm{GHz}$, so the upconverter and switched PA must cover the 2–3 GHz band with uniform gain and group delay.
- The switch and switched PA must operate at 20 MHz with a duty cycle no greater than 10% in order to effectively reduce the PRF and achieve the desired transmitter on-off isolation.
- The switching components must have sub-nanosecond on, off, rise, and fall times to avoid distorting the pulse envelope.
- The FPGA must be able to produce 20 MHz, 10% duty cycle control signals for the switch and switched PA.

- The BPSK modulator must operate at a rate of 20 MHz to match the transmitted PRF.

The transmitter design and hardware challenges are addressed in detail in the following sections.

5.1.1 PCC and Driver Circuitry

As discussed in Section 4.4.1, a 200 MHz, 3 V RF signal with a 700 mV DC bias was selected as the input for the PCC in this work. The FPGA, PLL, and amplification stages in the block diagram generate the required signal and are shown in more detail in Figure 5.2. The two gain blocks provide linear amplification up to the desired $3\,V_p$ (19.6 dBm) output. The amplifiers also provide better than 40 dB reverse isolation from DC to 2 GHz, so the input is well isolated from the fundamental and harmonics generated by the PCC. The output of the PCC driver circuitry is:

$$V_{in}^{PCC}(t) = V_{RF,in}^{PCC}\cos(2\pi f_{in}^{PCC}t) + V_{DC,in}^{PCC} \tag{5.1}$$

where $V_{RF,in}^{PCC} = 3\,V$, $f_{in}^{PCC} = 200\,MHz$, and $V_{DC,in}^{PCC} = 700\,mV$. The sinusoid is compressed by the PCC, as discussed in Chapter 4. The output of the PCC is given by Eqn. (4.7) and rewritten here for convenience:

$$V_{out}^{PCC}(t) \simeq \sum_{n=1}^{\infty} V_{out,p}^{PCC}\exp\left(-2\ln(2)\left(\frac{t-nT_{PCC}}{\tau}\right)^2\right) \tag{5.2}$$

where $V_{out,p}^{PCC} = 3.6\,V$, $T_{PCC} = 5\,ns$, and $\tau = 730\,ns$. There is a small attenuator at the PCC output, so the input to the upconverter is:

$$V_{IF}^{TX}(t) \simeq \sum_{n=1}^{\infty} V_{IF,p}^{TX}\exp\left(-2\ln(2)\left(\frac{t-nT_{PCC}}{\tau}\right)^2\right) \tag{5.3}$$

where $V_{IF,p}^{TX} = 1.4\,V$.

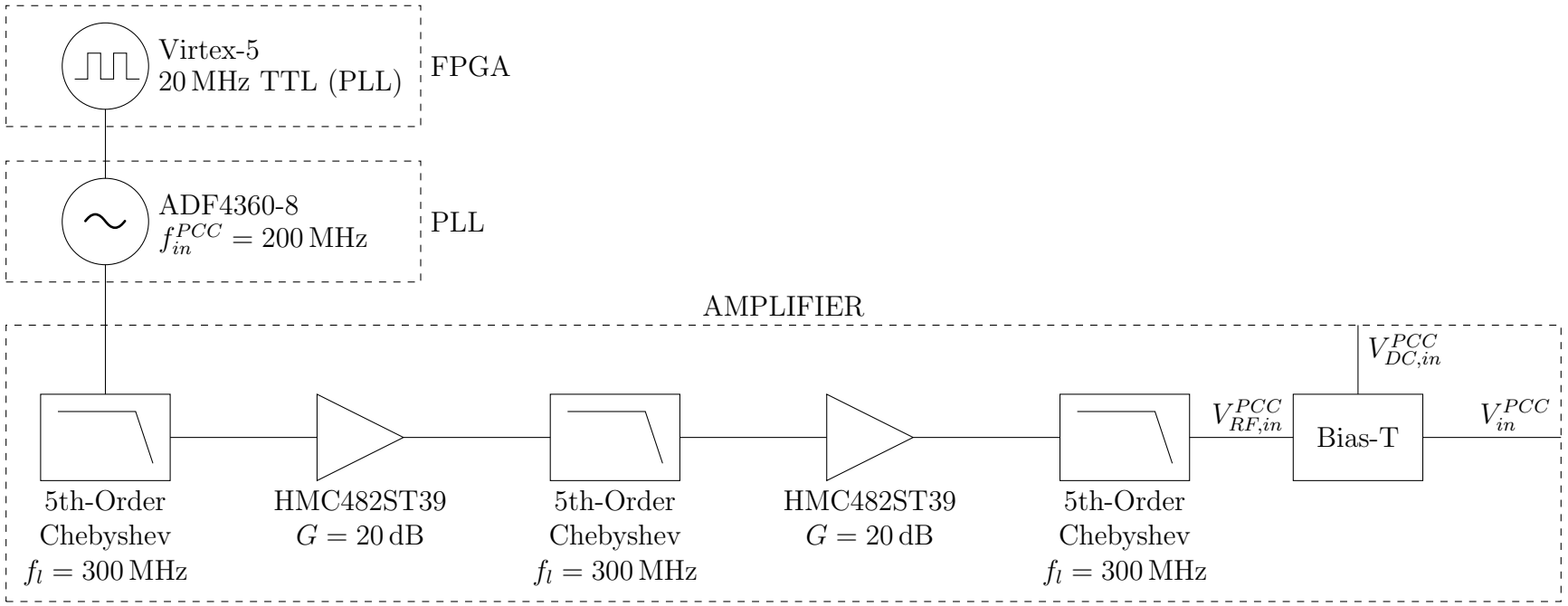

Figure 5.2: *PCC Driver Circuitry.* The PCC driver circuitry provides a 200 MHz, 3 V_p sinusoidal signal with a 700 mV DC offset for the input of the PCC. The FPGA is manufactured by Xilinx, the PLL is manufactured by Analog Devices, and the amplifiers are manufactured by Hittite.

5.1.2 VCO and Modulation

The LO signal for both the transmitter and receiver is provided by a 2.5 GHz VCO, as shown in Figure 5.3. The output of the VCO is filtered and power divided between two paths: the transmitter VCO path and the receiver VCO path. A resistive power divider was selected to provide a compact, broadband solution, but it provides only 6 dB of isolation. The transmitter and receiver VCO paths must be isolated from one another. The outputs of each (V_{VCO} and V_{LO}^{RX}) are pure sinusoidal tones; however, the output of the transmitter VCO path will be phase modulated by the BPSK modulator and amplitude modulated by the switch, as illustrated in the transmitter block diagram. If the phase code leaks back through the transmitter VCO path and into the receiver VCO path, the received signal will be correlated with the BPSK code before it is sampled by the post processor. As a result, target detectability would be compromised, and it would not be possible to distinguish between in- and out-of-range targets. The switch amplitude modulates the transmitter's VCO signal at a rate of $f_s = 20$ MHz. The output spectrum of the switch will be rich in harmonics spaced at 20 MHz, as will be discussed later in this section; if the additional frequency components leak into the receiver VCO path, the received signal will be distorted upon downconversion. The circulator and filters provide additional isolation to bolster the isolation of the power divider.

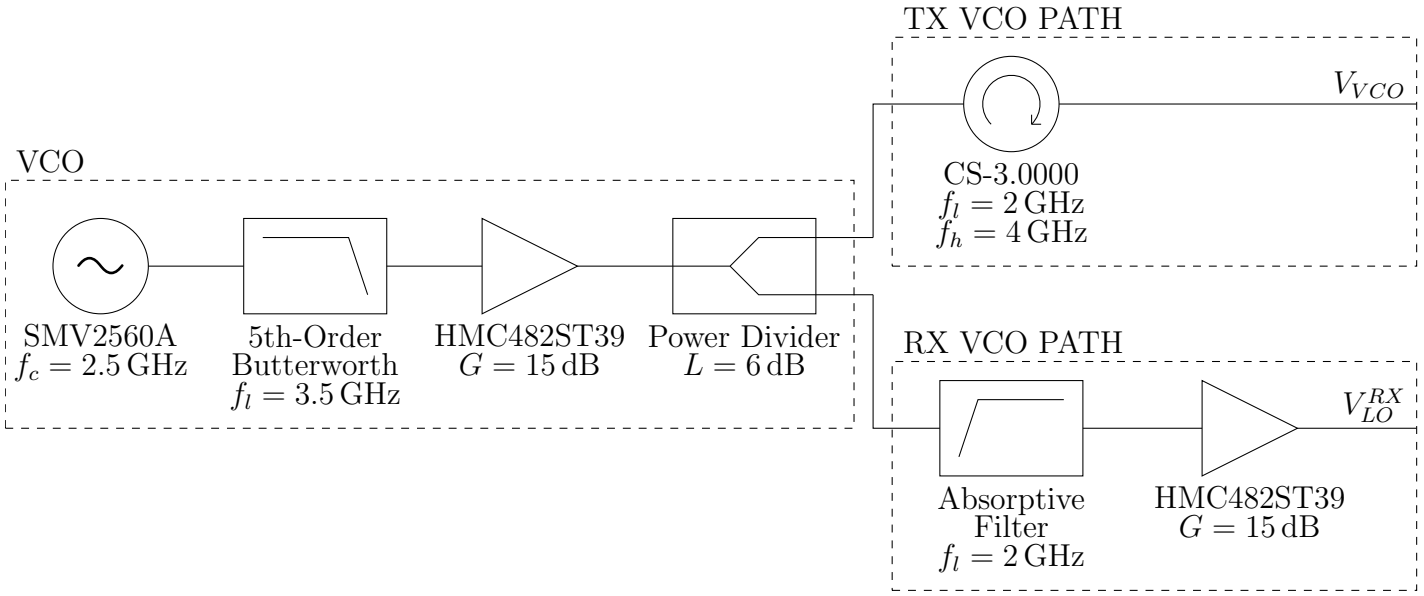

Figure 5.3: *VCO Circuitry.* The VCO signal is divided to provide a coherent LO for the transmitter and receiver. The VCO is manufactured by Z Communications, the amplifiers are manufactured by Hittite, and the circulator is manufactured by Meca Electronics. The absorptive filter is a high-pass filter adaptation of the low-pass filter design presented in [108], [109]

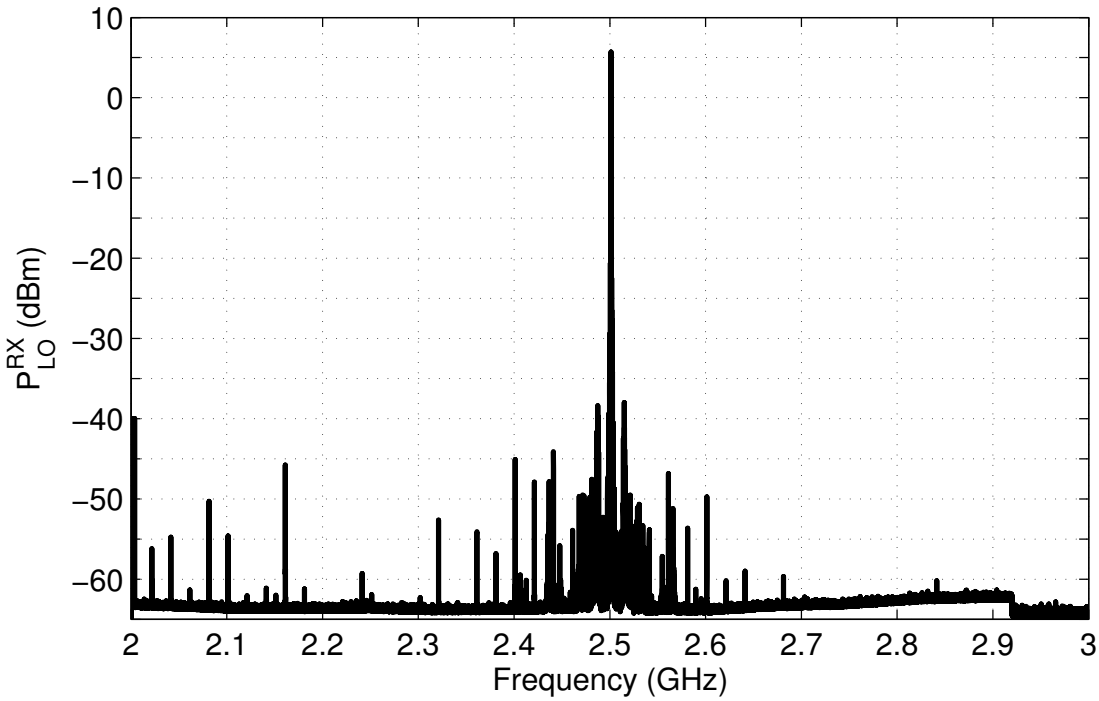

Figure 5.4: *RX VCO Path Output.* The spectral output of the receiver VCO path indicates that the isolation between the transmitter and receiver VCO paths is sufficient. The resolution bandwidth for this measurement was 10 kHz.

The output spectrum of the receiver VCO path, $P_{LO}^{RX}(f)$, was measured to verify that it resembles a pure 2.5 GHz tone. As shown in Figure 5.4, the largest measured spectral component at the output of the receiver VCO path is -44 dBc relative to the fundamental tone, so the output can be reasonably expressed as a pure sinusoid:

$$V_{LO}^{RX}(t) = V_{LO,p}^{RX} \cos(2\pi f_c t) \tag{5.4}$$

where $V_{LO,p}^{RX} = 0.6\,\text{V}$ and $f_c = 2.5\,\text{GHz}$. As noted, the output of the transmitter VCO path is phase and amplitude modulated. The modulation hardware is discussed in the following sections.

BPSK Modulator

BPSK pulse tagging was chosen to allow in- and out-of-range target discrimination. The pulse tags are applied to the output of the transmitter VCO path (V_{VCO}), as shown in Figure 5.5. As indicated in the figure, the FPGA generates the control signal for the BPSK modulator. The signal is a pseudo-random bi-phase code generated using a maximum-length 28-bit LFSR. The output of the LFSR changes on the rising edge of the FPGA's 20 MHz clock, so each transmitted pulse is uniquely coded. As noted in Sections 3.4 and 3.5, a copy of the phase code is generated by the FPGA, sampled by the post processor, and correlated with the sampled output of the receiver ($V_{in}^{pp'}$) to achieve in- and out-of-range target discrimination.

The output of the BPSK modulator is amplified to the mixer's LO drive level and filtered. The output of the BPSK modulator is:

$$V_{BPSK}(t) = V_p^{BPSK} \cos(2\pi f_c t) V_{pc}(t) \tag{5.5}$$

$$V_{pc}(t) = \sum_{m=1}^{\infty} V_m^{pc} \text{rect}\left(f_s t - \frac{m}{2f_s}\right) \tag{5.6}$$

where $V_p^{BPSK} = 0.95$ V, m is an integer, and $V_m^{pc} = \pm 1$, based on the pseudo-random phase code. The frequency-domain output of the BPSK modulator is plotted in Figure 5.6; the frequency spreading is typical of a pseudo-random phase code.

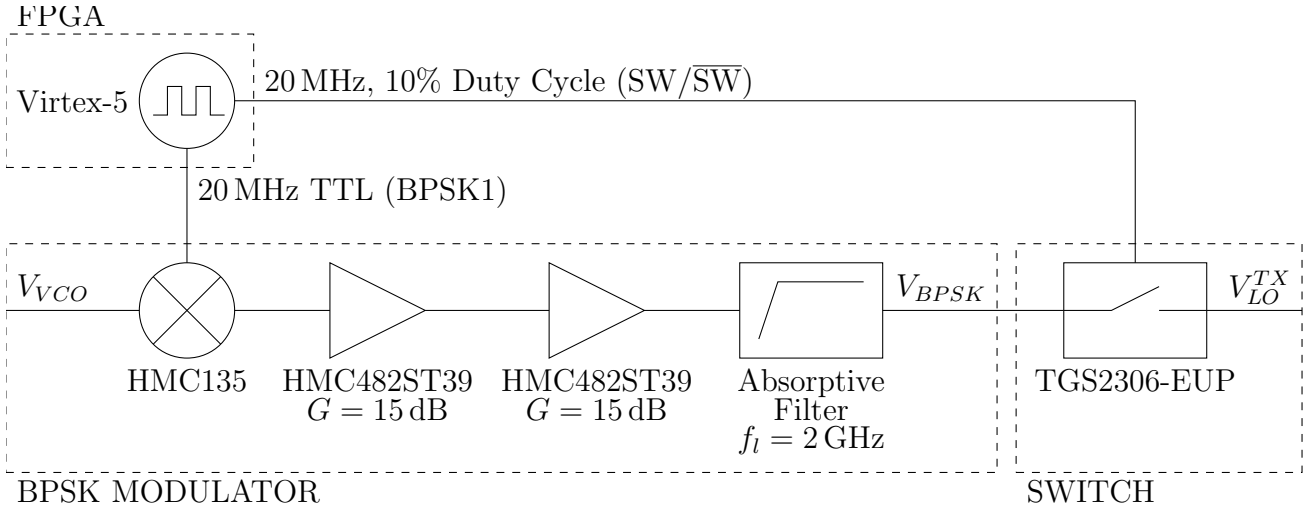

Figure 5.5: *BPSK Modulator Circuitry.* The BPSK modulator phase-modulates the VCO signal. The FPGA is manufactured by Xilinx, the BPSK modulator and amplifiers are manufactured by Hittite, and the switch is manufactured by Triquint.

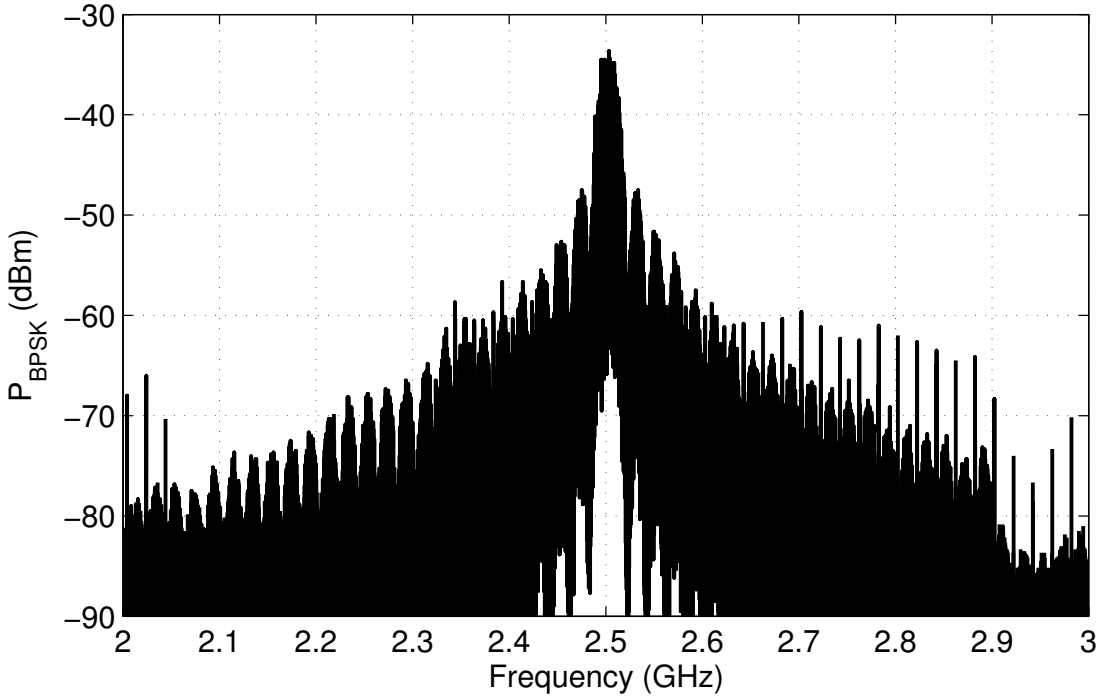

Figure 5.6: *BPSK Modulator Output.* The spectral spreading around the 2.5 GHz carrier is typical of a pseudo-random phase code. The resolution bandwidth for the measurement was 10 kHz.

Switch

The switch follows the BPSK modulator components, as shown in Figure 5.5. The switch is used to reduce the PRF of the transmitter from 200 MHz at the output of the PCC to 20 MHz at the output of the transmitter. The FPGA generates the control signals for the switch, as discussed in Section 3.4. The time- and frequency-domain outputs of the switch are plotted in Figure 5.7. The time-domain output can be written as follows:

$$V_{LO}^{TX}(t) = \frac{V_{BPSK}(t)}{V_p^{BPSK}} \begin{cases} V_{LO,on}^{TX} & \frac{\ell}{f_s} < t < \frac{\tau/T+\ell}{f_s} \\ V_{LO,off}^{TX} & \frac{\tau/T+\ell}{f_s} < t < \frac{\ell+1}{f_s} \end{cases} \tag{5.7}$$

where $V_{LO,on}^{TX} = 0.65\,\text{V}$ is the peak voltage at the output of the switch in its on-state, $V_{LO,off}^{TX} = 0.1\,\text{V}$ is the peak voltage at the output of the switch in its off-state, and ℓ is an integer. $V_{LO,on}^{TX}$ is sufficient to turn the upconverter on, and $V_{LO,off}^{TX}$ is below

the LO threshold of the upconverter. As a result, the upconverter is switched on and off according to $V_{LO}^{TX}(t)$. The output of the PCC provides the IF input to the upconverter (see Figure 5.1), so the switch also down-samples the PCC's pulse train from a PRF of 200 MHz to 20 MHz.

The Triquint switch has subnanosecond rise and fall times and can generate nearly ideal, 5 ns windows. The fast rise and fall times minimize the amplitude modulation of the LO signal and, thus, the distortion of the PCC's pulse envelope.

5.1.3 Upconverter and Switched PA

The upconverter upconverts the output of the PCC, phase codes the output pulses, and reduces the PRF from 200 MHz to 20 MHz. The output of the PCC has significant spectral components from 200–1000 MHz (see Figure 4.16b), so a mixer was selected that is well matched over the entire IF frequency range. This is important because any reflections from the mixer will distort the pulse envelope at the output of the PCC. The conversion loss of the mixer is flat (8 ± 2 dB) over the entire 2-3 GHz RF frequency band.

The peak output voltage of the PCC is $V_{out,p}^{PCC} = 3.6\,\text{V}$ (see Figure 4.16a). The mixer must be capable of handling the peak IF voltage without distorting the pulse envelope, so the upconverter should have a 1 dB compression (P1dB) point greater than 21 dBm. After an extensive search, the Hittite mixer was the best choice for a broadband, high P1dB mixer, but its 17 dBm compression point is too low for the existing PCC. To compensate, an attenuator was placed at the output of the PCC to reduce the leakage voltage at the IF input of the mixer to $V_{IF,p}^{TX} = 1.4\,\text{V}$, as noted in Section 5.1.1. The reduced voltage prevents the mixer from compressing, and thus distorting, the pulse envelope.

The output of the upconverter is plotted in Figure 5.8 and can be written as

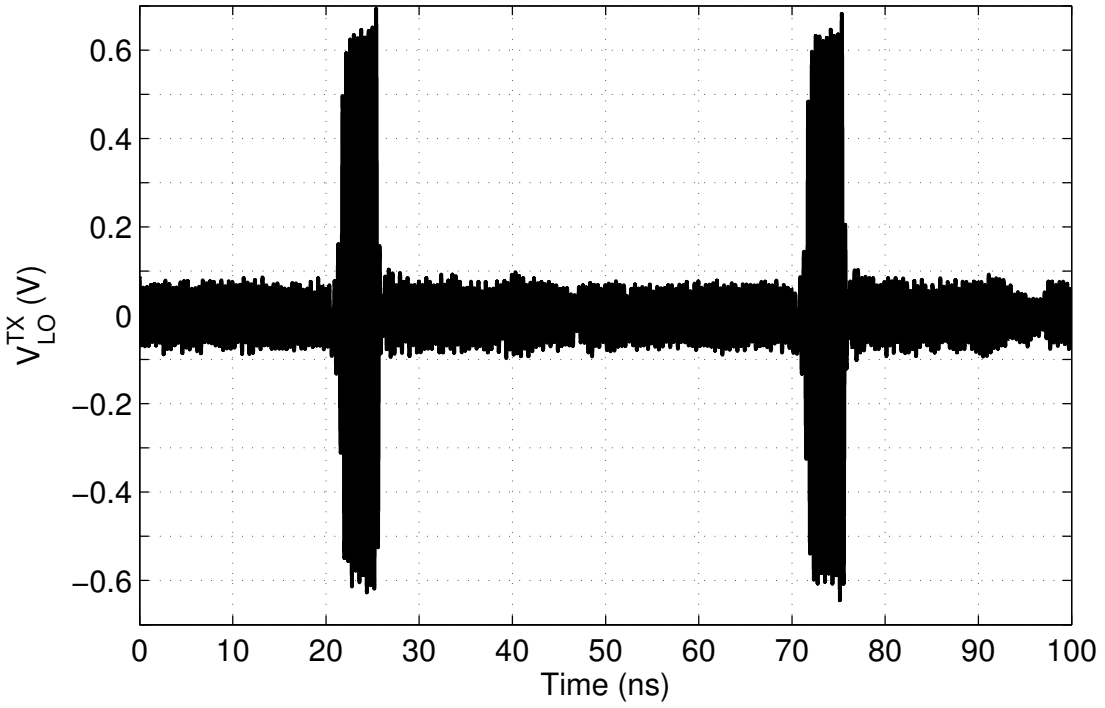

(a)

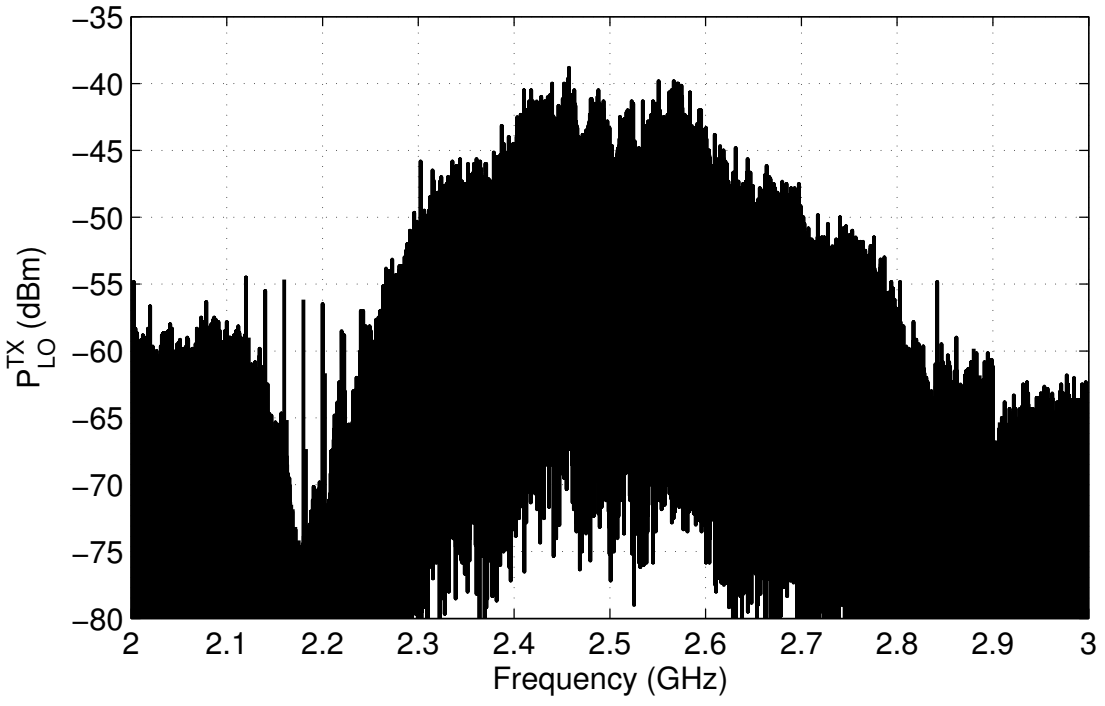

(b)

Figure 5.7: *Switch Output.* The switch is used to turn the mixer on at a rate of 20 MHz with a duty cycle of 10%. The time-domain signal (a) was measured with a Tektronix TDS7404B 4 GHz, 20 GS/s real-time oscilloscope. The resolution bandwidth for the frequency-domain measurement (b) is 10 kHz.

follows:

$$V_{RF}^{TX}(t) = V_{RF,p}^{TX}(t)\frac{V_{IF}^{TX}(t)}{V_{IF,p}^{TX}}\frac{V_{BPSK}(t)}{V_{p}^{BPSK}} \tag{5.8}$$

$$V_{RF,p}^{TX}(t) = \begin{cases} V_{RF,on}^{TX} & \frac{\ell}{f_s} < t < \frac{\tau/T+\ell}{f_s} \\ V_{RF,off}^{TX} & \frac{\tau/T+\ell}{f_s} < t < \frac{\ell+1}{f_s} \end{cases} \tag{5.9}$$

where $V_{RF,on}^{TX} = 0.9\,\text{V}$ is the peak voltage at the output of the upconverter in its on-state and $V_{RF,off}^{TX} = 0.2\,\text{V}$ is the peak voltage at the output of the upconverter in its off-state.

The on-off isolation of the waveform is $20\log(V_{RF,on}^{TX}/V_{RF,off}^{TX}) = 13\,\text{dB}$, and the peak output power is $P_{RF}^{TX} = 16\,\text{mW}$. As such, the switched PA, which is detailed in Figure 5.9, must amplify the signal and increase the on-off isolation of the waveform to meet the desired system specifications outlined in Chapter 3. The PA provides adequate gain with ±1.5 dB gain flatness over the 2–3 GHz bandwidth of the pulse train. The PA's P1dB point is 30 dBm, so it operates as a linear amplifier for the transmitter design. This is important for two reasons. First, if the PA saturates, then the transmitter on-off isolation will be degraded due to clipping. Second, PA saturation will distort and broaden the pulse envelope. Dispersion can also distort the pulse envelope. For the Ciao device, the PA group delay variation is limited to ±300 ps from 2–3 GHz, so the PA does not distort the pulse envelope through dispersion.

The switches shown in Figure 5.9 improve the on-off isolation of the waveform. The switches provide an additional 41 dB of isolation, resulting in a final transmitter on-off isolation of $I_{on/off}^{TX} = 54\,\text{dB}$. The output of the transmitter is:

$$V_{TX}(t) = V_{p}^{TX}(t)\frac{V_{IF}^{TX}(t)}{V_{IF,p}^{TX}}\frac{V_{BPSK}(t)}{V_{p}^{BPSK}} \tag{5.10}$$

$$V_{p}^{TX}(t) = \begin{cases} V_{on}^{TX} & \frac{\ell}{f_s} < t < \frac{\tau/T+\ell}{f_s} \\ V_{off}^{TX} & \frac{\tau/T+\ell}{f_s} < t < \frac{\ell+1}{f_s} \end{cases} \tag{5.11}$$

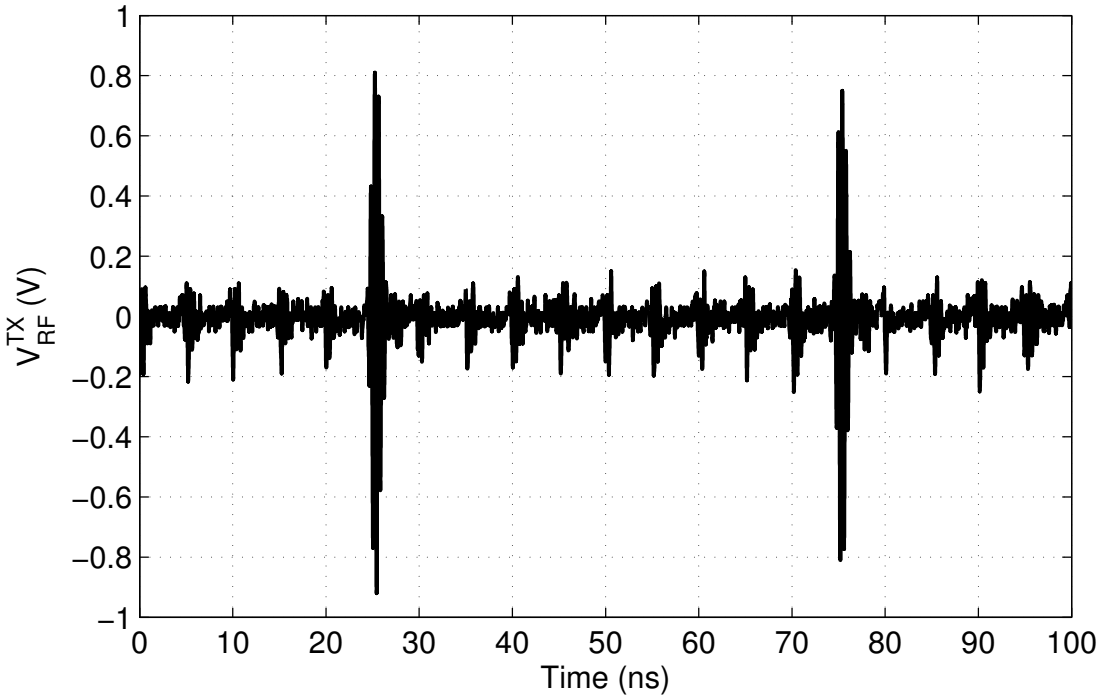

(a)

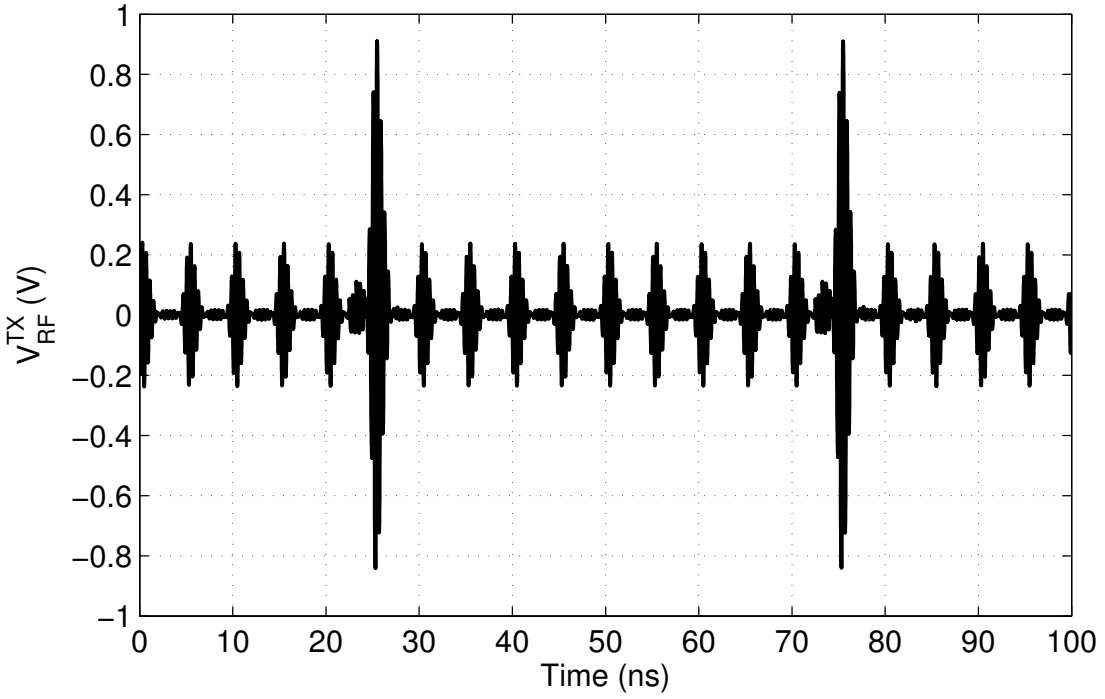

(b)

Figure 5.8: *Upconverter Output.* The output of the upconverter is a series of phase coded pulses with a PRF of 20 MHz. (a) The signal was measured with a Tektronix DPO72004B 20 GHz, 50 GS/s real-time oscilloscope. (b) The signal was simulated using the ADS model described in Section 5.2.

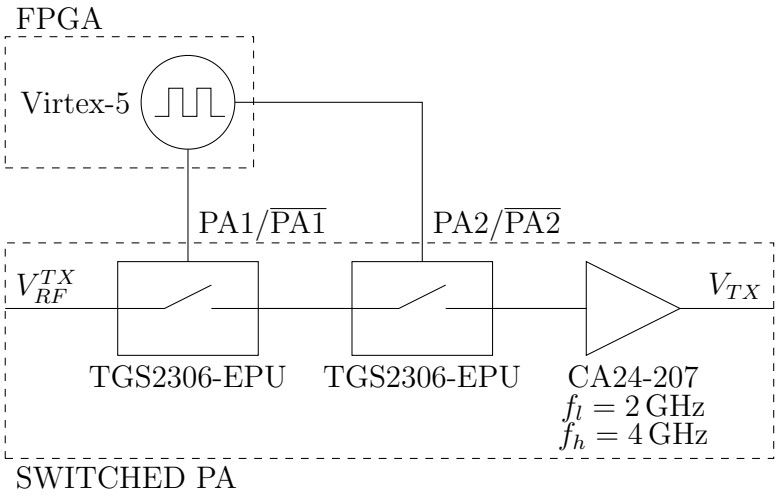

Figure 5.9: *Switched PA Circuitry.* The switched PA amplifies the output of the upconverter and increases the TX on-off isolation. The FPGA is manufactured by Xilinx, the switches are manufactured by Triquint, and the amplifier is manufactured by Ciao Wireless.

where $V_{on}^{TX} = 7.7\,\text{V}$ is the peak voltage at the output of the transmitter in its on-state and $V_{off}^{TX} = 15\,\text{mV}$ is the peak voltage at the output of the transmitter in its off-state. The time- and frequency-domain outputs of the transmitter are plotted in Figures 5.10 and 5.11 and will be discussed in Section 5.3.

5.2 Transmitter Simulation Model

The transmitter was modeled in Agilent's ADS. Since the transmitted pulsewidth is on the order of the period of the carrier frequency, it is possible to perform all system-level simulations using only the RF capabilities of the software. In other words, a true system-level simulator, such as Agilent's Ptolemy, is not required.

The transmitter simulation is performed in the time-domain with a discrete step size; it includes pseudo-random noise from DC to 4 GHz. The FPGA, VCO, amplifiers, switches, attenuators, bi-phase modulator, and upconverter are modeled as behavioral components, which include gain, noise figure, and

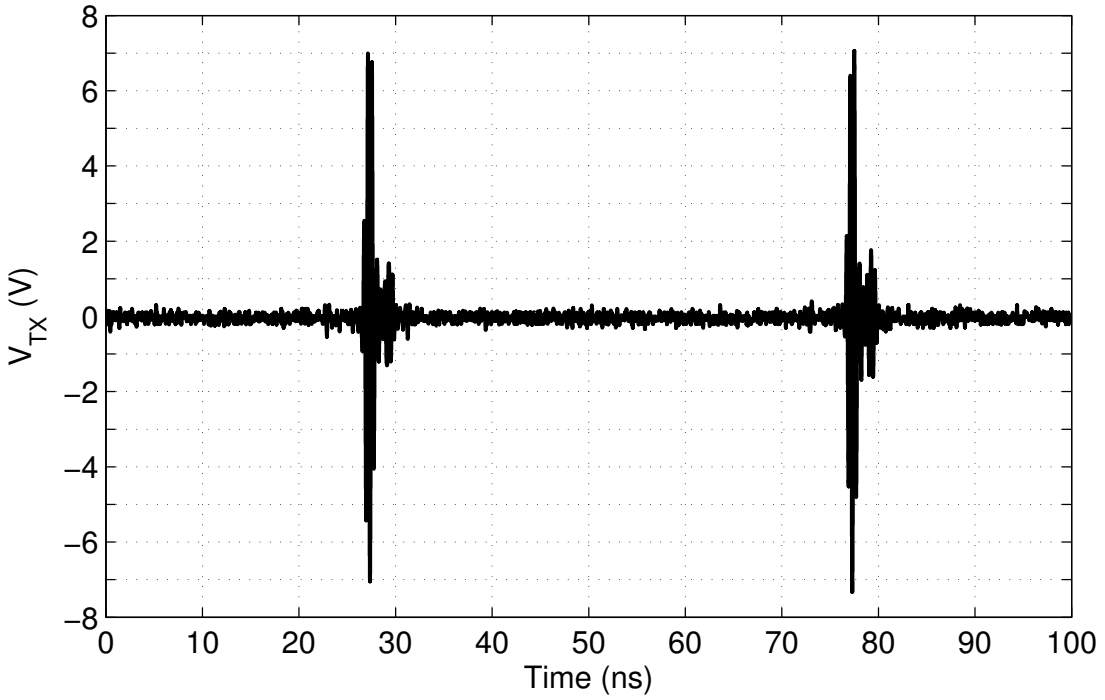

(a)

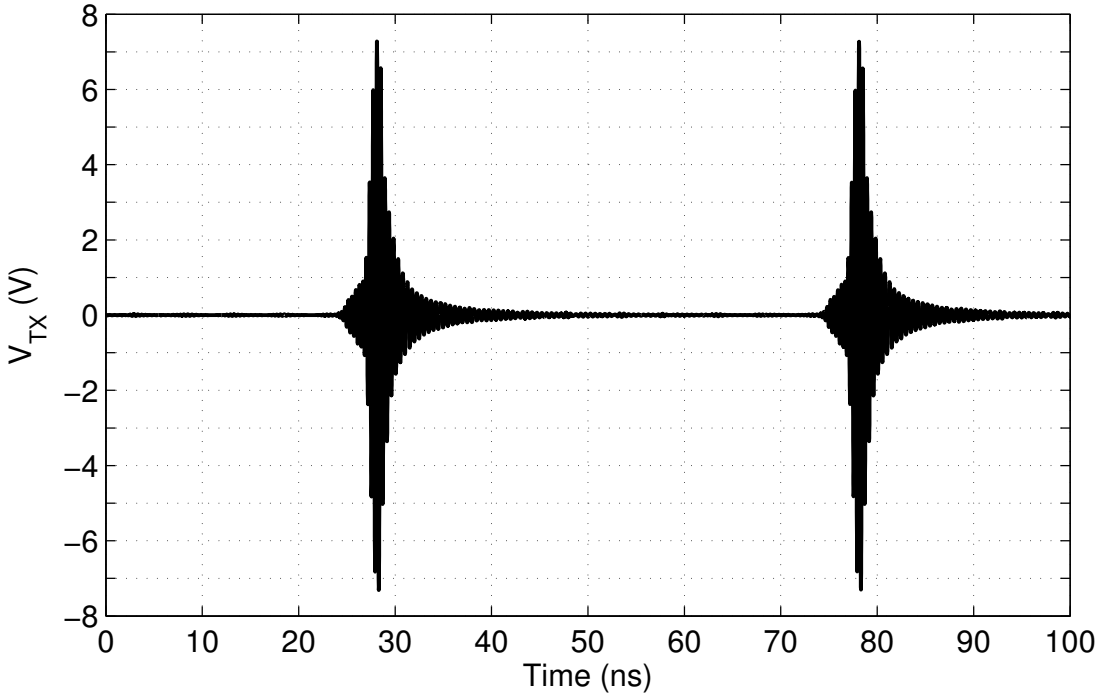

(b)

Figure 5.10: *Time Domain Transmitter Output.* The output of the transmitter is a series of phase coded pulses with a PRF of 20 MHz and a carrier frequency of 2.5 GHz. (a) The signal was measured with a Tektronix TDS7404B 4 GHz, 20 GS/s real-time oscilloscope. (b) The signal was simulated using the ADS model described in Section 5.2.

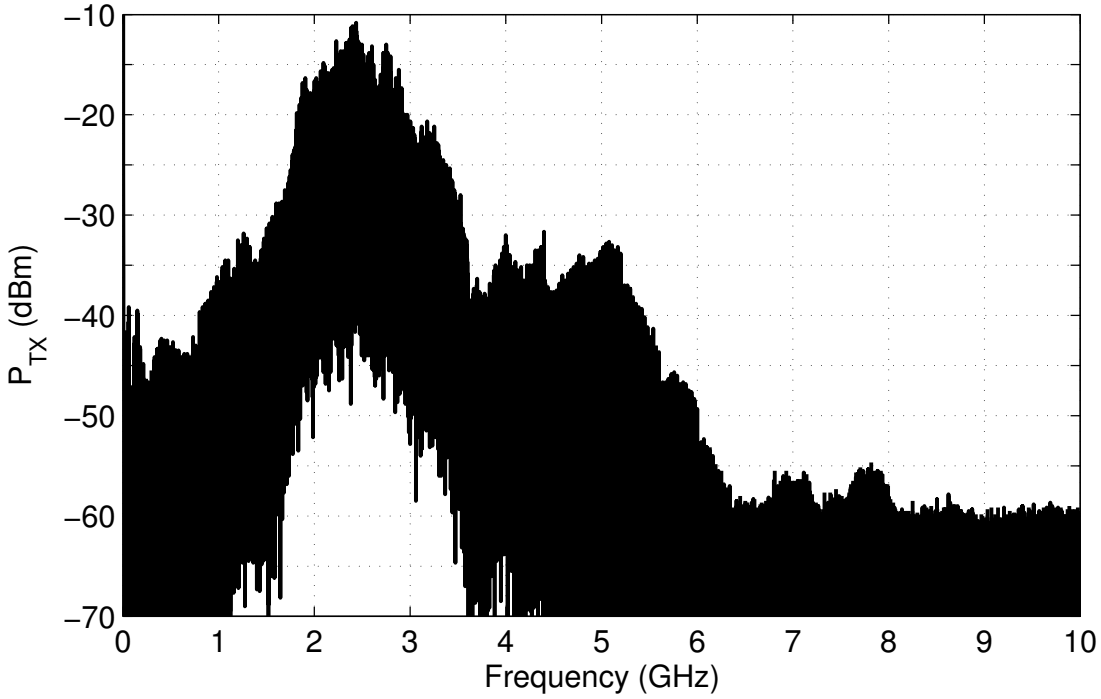

(a)

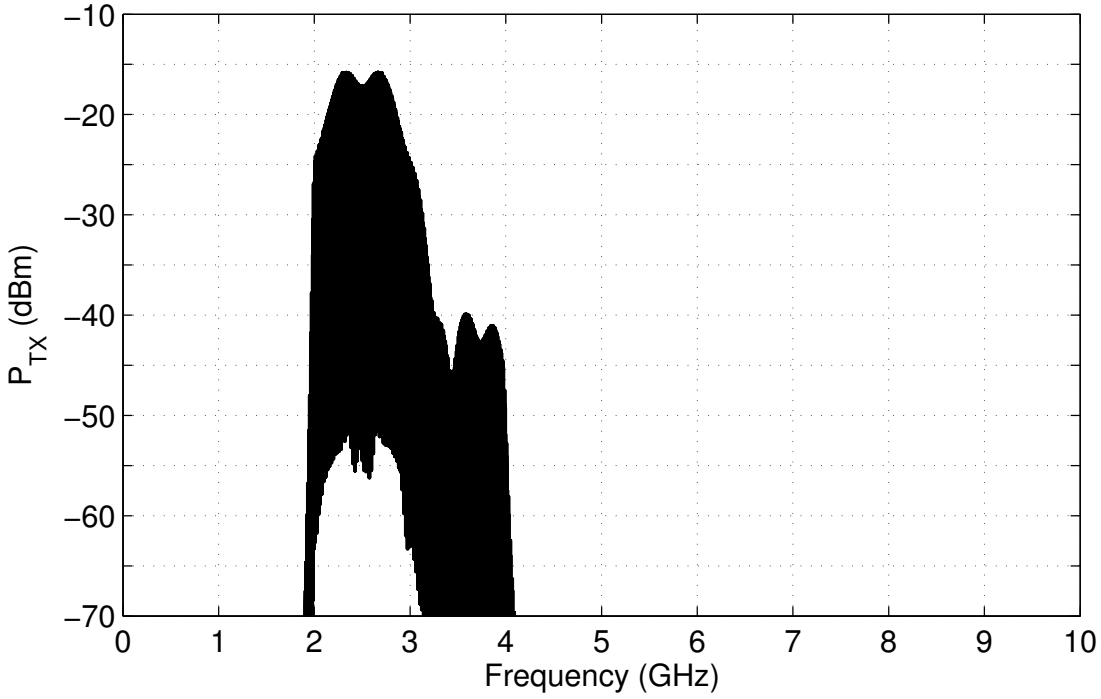

(b)

Figure 5.11: *Frequency Domain Transmitter Output.* The output spectrum of the transmitter is centered at 2.5 GHz with 20 MHz spectral spacing and additional spectral spreading due to the BPSK phase code. (a) The signal was measured with 1 MHz frequency resolution. (b) The signal was simulated using the ADS model described in Section 5.2.

compression points, as appropriate. The PCC and filters are modeled using circuit elements corresponding to their actual hardware implementations; the PCC model is discussed in Chapter 4.

5.3 Transmitter Performance

The output of the short-pulse transmitter is a train of 730 ps pulses that occupy the 2–3 GHz band. The 20 MHz PRF facilitates unambiguous range and Doppler detection, which minimizes the system complexity. The Gaussian-like pulse envelope, which is generated by the PCC, falls off smoothly in both the time and frequency domains, simplifying the receiver, channel model, and antenna system designs. Each pulse receives a pseudo-random phase shift of 0°/180° once per PRI.

The turn-off characteristics of the transmitted signal limit the minimum detectable range of the radar. The theoretical and measured turn-off times for various levels of transmitter on-off isolation are listed in Table 5.1; the theoretical turn-off times are based on the theoretical transmitted pulse envelope in Eqn. (4.12). As anticipated, the measured turn-off times are longer than the theoretical turn-off times. As can be seen, the measured turn-off time is not a linear function of the transmitter on-off isolation; it changes as the pulse decays. It can be roughly broken into three turn-off rates based on the transmitter on-off isolation. It is $R_{to}^{TX} = 10.0\,\text{dB/ns}$ for $0\,\text{dB} \leq I_{on/off}^{TX} \leq 30\,\text{dB}$; it is $R_{to}^{TX} = 2.9\,\text{dB/ns}$ for $30\,\text{dB} < I_{on/off}^{TX} \leq 45\,\text{dB}$; and it is $R_{to}^{TX} = 0.7\,\text{dB/ns}$ for $45\,\text{dB} < I_{on/off}^{TX} \leq 55\,\text{dB}$. The minimum ranges are also listed in the table and were calculated using Eqn. (3.16). The minimum range of the radar will depend on the TX-RX isolation, which will be discussed in Section 8.7.

The frequency-domain performance of the transmitter is also important. The

Table 5.1: Turn-Off Characteristics of Transmitter

$I^{TX}_{on/off}$ (dB)	Theoretical t^{TX}_{to} (ns)	Measured t^{TX}_{to} (ns)	Measured R_{min}
30	1.2	3.0	R_{lk} + 1.2 m
35	1.3	4.2	R_{lk} + 1.4 m
40	1.3	5.4	R_{lk} + 1.6 m
45	1.4	8.2	R_{lk} + 2.0 m
50	1.5	14.3	R_{lk} + 2.9 m
55	1.6	22.6	R_{lk} + 4.1 m

spectral output of the PCC exhibits strong spectral components spaced at 200 MHz with a Gaussian-like envelope, as seen in Figure 4.16. Upon upconversion, the spectral content is shifted to a double-sideband spectrum centered at f_c = 2.5 GHz. Since the LO is amplitude modulated with a 20 MHz switching rate, each spectral component is transformed to a discrete sinc function with 20 MHz spacing between the spectral components. Finally, the spectrum is further spread about each spectral component due to the pseudo-random phase code.

The 10-dB bandwidth of the transmitter signal is approximately 1 GHz. The effective bandwidth, which is calculated from the theoretical pulse envelope, is 1.6 GHz. Referring to Eqn. (**??**), this corresponds to a range accuracy of ±0.15 m, assuming a minimum detectable SNR of -13.5 dB. This is well within the range accuracy specification for this work.

The Doppler accuracy can be calculated using Eqn. (2.4). The effective time duration is approximately α = 1.9 ns, and the Doppler accuracy is 1.8 GHz. The Doppler accuracy isn't sufficient for this work, so integration will be employed to improve it.

Both simulation and measurement demonstrate the desired characteristics summarized in Chapter 3. The PRF, center frequency, envelope pulsewidth, and output power can be adjusted, within limits, as desired; if the PRF or envelope pulsewidth are adjusted, the PCC design must be reconsidered. It is also possible

to improve the transmitter on-off isolation by adding additional switches to the switched PA.

The transmitter demonstrates successful integration of UWB techniques with a traditional coherent, pulsed transmitter topology. The transmitted waveform facilitates unambiguous range and Doppler detection and allows for coherent processing by a UWB receiver. In addition, the waveform was designed to minimize the shortest detectable range, which is the primary goal of this thesis.

Chapter 6

UWB Receiver

The receiver block diagram for this thesis was presented in Chapter 3, and this chapter details the receiver design and operation.

6.1 UWB Receiver Components

The receiver block diagram is shown in Figure 3.3 and repeated in Figure 6.1 for convenience. The following components and their performance are discussed in the following sections:

- *Range Gate.* The range gate turns the receiver on and off to limit the observation time and set the observation range of the receiver. It provides $I_{RG} = 49$ dB on-off isolation.
- *RF LNA.* The RF LNA is implemented as a pair of amplifiers, each of which operates with a 3.5 dB noise figure and 20 dB of gain, for a total gain of $G_{RF} = 40$ dB.
- *Downconverter and IF LNA.* The downconverter mixes the received RF signal to baseband, and the signal is amplified by the IF LNA. The conversion loss

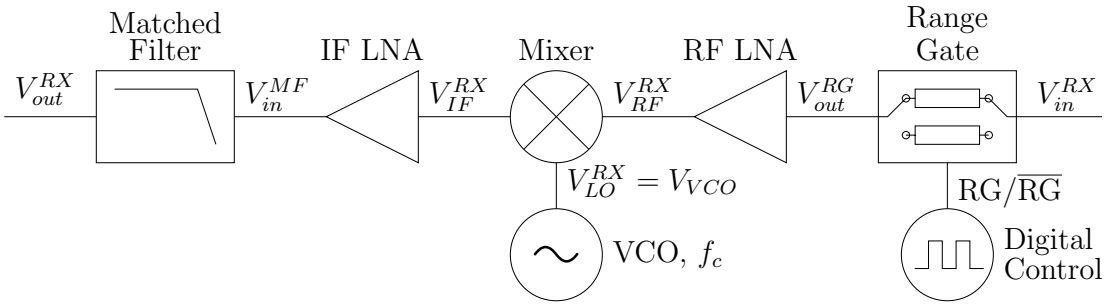

Figure 6.1: *Receiver Block Diagram.*

of the downconverter is $L_C = 8\,\text{dB}$, the gain of the IF LNA is $G_{IF} = 33\,\text{dB}$, and the noise figure of the IF LNA is 3 dB.

- *Matched Filter.* The matched filter has a Gaussian-like transfer function to match the Gaussian-like pulse envelope of the transmitted signal. The noise bandwidth of the filter is $\beta_N = 520\,\text{MHz}$.

6.1.1 Range Gate

The range gate is implemented as a set of switched attenuators controlled by the FPGA, as shown in Figure 6.2; a single pair of terminating resistors was used for the multi-drop control line, as recommended in [110]. As noted in Table 3.1, the control signals operate at 20 MHz with a 20% duty cycle, resulting in a 10 ns wide range gate. The observable range delay, t_R^{obs}, is equal to the time delay between the peak of the transmitted pulse and the center of the range gate; it corresponds to an observed range $R_{obs} = t_R^{obs} c_o/2$. In the setup for this thesis, t_R^{obs} can be adjusted in 25 ps steps.

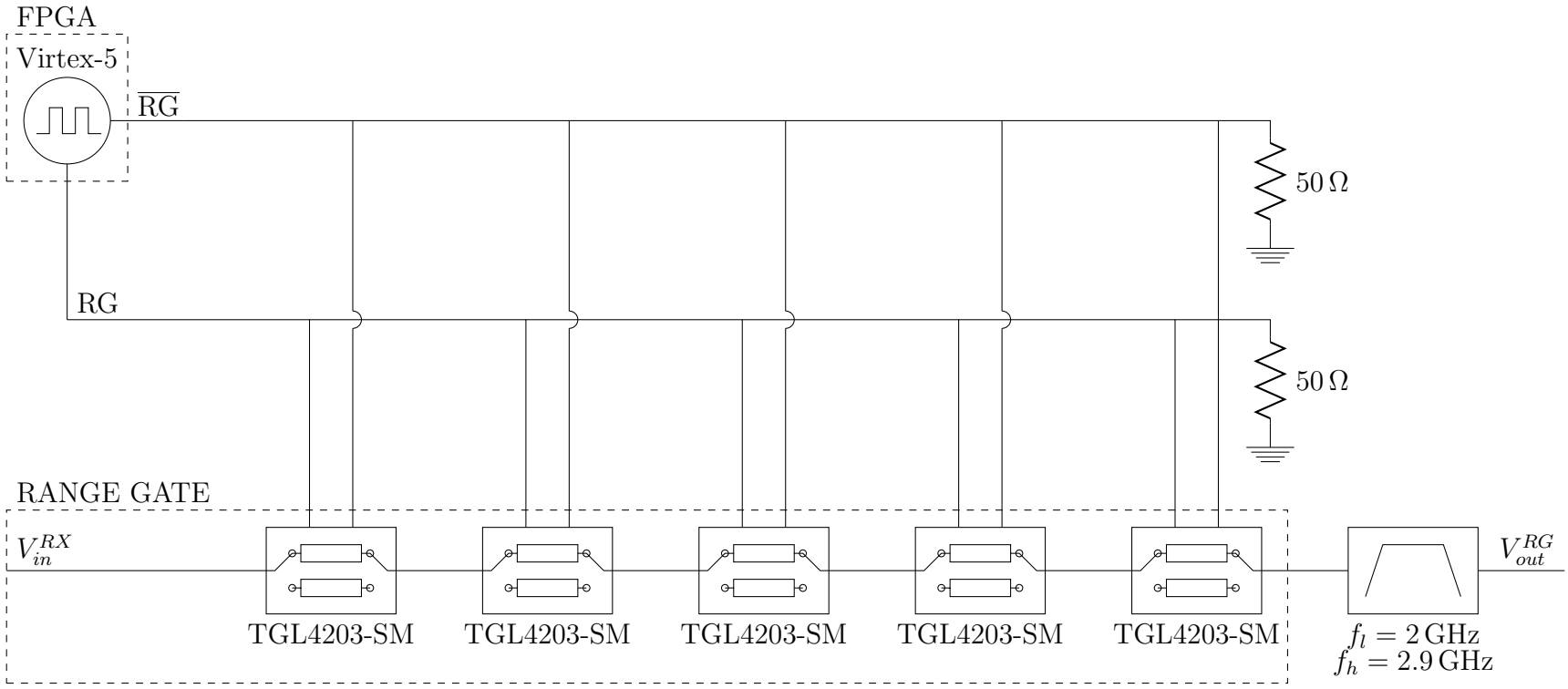

Figure 6.2: *Range Gate Circuitry.* The range gate provides 49 dB receiver on-off isolation with 6.5 dB static insertion loss. The FPGA is manufactured by Xilinx and the switched attenuators are manufactured by Triquint.

The range gate was measured statically in its on- and off-states. The input and output return loss are better than 9 dB in the on-state and better than 8 dB in the off-state, from 2–3 GHz. The on-state insertion loss is 6.5 ± 0.5 dB. The range gate provides 49 dB on-off isolation, $I^{RX}_{on/off}$, corresponding in a total off-state attenuation of 55.5 dB. The range gate was also measured dynamically; the control signals were pulsed at a rate of 20 MHz with a 20% duty cycle, as they will be under normal operating conditions. Under dynamic conditions, the insertion loss is about 3 dB worse than indicated by the static measurement.

The output of the range gate in its on-state is:

$$V^{RG}_{out}(t) = \frac{V^{TX}_{p}(t)}{L_{ch}L_{RG}} \frac{V^{TX}_{IF}(t)}{V^{TX}_{IF,p}} V_{pc}(t) \cos(2\pi(f_c \pm f_D)t) \tag{6.1}$$

where $V^{TX}_{p}(t)$, $V^{TX}_{IF}(t)$, and $V_{pc}(t)$ are defined in Eqns. (5.11), (5.3), and (5.6); L_{ch} is the channel loss; L_{RG} is the insertion loss of the range gate; and f_D is the Doppler shift imposed by the target. A positive Doppler shift corresponds to a closing target, and a negative Doppler shift corresponds to an opening target.

The output of the range gate in its off-state is:

$$V^{RG}_{out}(t) = \frac{V^{TX}_{p}(t)}{L_{ch}L_{RG}I_{RG}} \frac{V^{TX}_{IF}(t)}{V^{TX}_{IF,p}} V_{pc}(t) \cos(2\pi(f_c \pm f_D)t) \tag{6.2}$$

where $I_{RG} = 49$ dB is the range gate on-off isolation. The following equations assume the receiver is in its on state, unless stated otherwise.

6.1.2 RF LNA

The RF LNA consists of two cascaded Hittite HMC609LC4 amplifiers. Each amplifier provides 20 ± 1 dB gain with input and output return loss better than 10 dB. The noise figure of the amplifiers is 3.5 dB, limiting the noise figure of the receiver. The output of the RF LNA is:

$$V^{RX}_{RF}(t) = \frac{G_{RF}V^{TX}_{p}(t)}{L_{ch}L_{RG}} \frac{V^{TX}_{IF}(t)}{V^{TX}_{IF,p}} V_{pc}(t) \cos(2\pi(f_c \pm f_D)t) \tag{6.3}$$

where $G_{RF} = 40$ dB is the gain of the RF LNA.

6.1.3 Downconverter and IF LNA

A Hittite HMC135 mixer is employed as the downconverter in the receiver, as well as the upconverter in the transmitter. Since double-sideband upconversion was employed for transmission, a double-sideband downconverter was selected for the receiver. Often, an image-reject mixer would be chosen instead in order to allow closing- and opening-target discrimination; however, the upconversion step eliminates the ability to discriminate between the two, so a double-sideband downconverter was used instead. The output of the downconverter is a series of baseband pulses modulated by the Doppler frequency:

$$V_{RF}^{RX}(t) = \frac{G_{RF} V_p^{TX}(t)}{L_{ch} L_{RG} L_C} \frac{V_{IF}^{TX}(t)}{V_{IF,p}^{TX}} V_{pc}(t) \cos(2\pi f_D t) \tag{6.4}$$

where $L_C = 8$ dB is the conversion loss of the downconverter.

An Advanced Control Components W500F-10 amplifier was selected for the IF LNA. The amplifier provides 34 dB gain from 1-500 MHz with a 25 dBm P1dB point and a 3 dB noise figure. The output of the amplifier is:

$$V_{in}^{MF}(t) = \frac{G_{RF} G_{IF} V_p^{TX}(t)}{L_{ch} L_{RG} L_C} \frac{V_{IF}^{TX}(t)}{V_{IF,p}^{TX}} V_{pc}(t) \cos(2\pi f_D t) \tag{6.5}$$

where $G_{IF} = 33$ dB.

6.1.4 Matched Filter

Since the received pulse is Gaussian-like (Eqn. (6.5)), the corresponding matched filter should be Gaussian-like to minimize the matched filter loss [106]. A 7^{th} order, lumped, absorptive Gaussian-like LPF was designed based on [108] and [109]; the circuit diagram is shown in Figure 6.3a. The component values were

selected as follows:

$$R = Z_o \tag{6.6}$$

$$C = \frac{1}{2\pi f_l^{MF} Z_o \sqrt{n-1}} \tag{6.7}$$

$$L = Z_o^2 C \tag{6.8}$$

where f_l^{MF} is the corner frequency of the filter and n is the number of reactive elements. The measured response of the filter is plotted in Figure 6.3b; the theoretical Gaussian voltage transfer function is also plotted for comparison.

The matched filter defines the noise bandwidth of the receiver. The noise bandwidth, assuming a single-sideband downconversion is:

$$\beta_N = \frac{\int_0^\infty |H(f)|^2 df}{|H_{max}(f)|^2 df} \tag{6.9}$$

where β_N is the noise bandwidth, $H(f) = S_{21}$ is the transfer function of the filter, and $H_{max}(f)$ is the peak response of the filter [16]; since a double-sideband downconverter is used in this work, the noise bandwidth will be twice that of Eqn. (6.9). The measured noise bandwidth of the matched filter is 520 MHz, and the measured 3-dB bandwidth is 540 MHz. As expected [16], the two are similar.

The voltage transfer function of the filter can be approximated as:

$$H(f) = \exp\left(-2\ln(2)\left(\frac{f}{f_l^{MF}}\right)^2\right) \tag{6.10}$$

where $f_l^{MF} = 540$ MHz is the 3-dB bandwidth of the filter; this expression was plotted in Figure 6.3b for comparison with the measured filter response. The output of the matched filter is:

$$V_{out}^{RX}(t) = \frac{G_{RF}G_{IF}V_p^{TX}(t)}{L_{ch}L_{RG}L_C}\frac{V_{IF}^{TX}(t)}{V_{IF,p}^{TX}}V_{pc}(t)\cos(2\pi f_D t) \star h(t) \tag{6.11}$$

$$h(t) = f_l^{MF}\sqrt{\frac{\pi}{2\ln(2)}}\exp\left(\frac{-(\pi f_l^{MF})^2 t^2}{2\ln(2)}\right) \tag{6.12}$$

where $h(t)$ is the impulse response of the filter; it is the Fourier transform of $H(f)$.

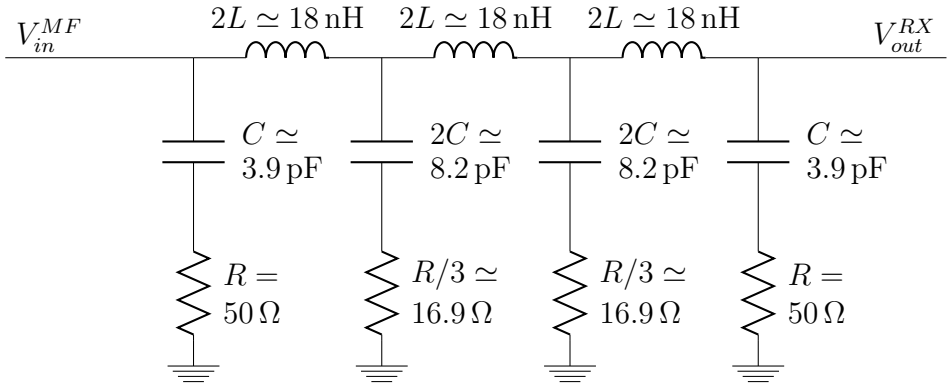

(a)

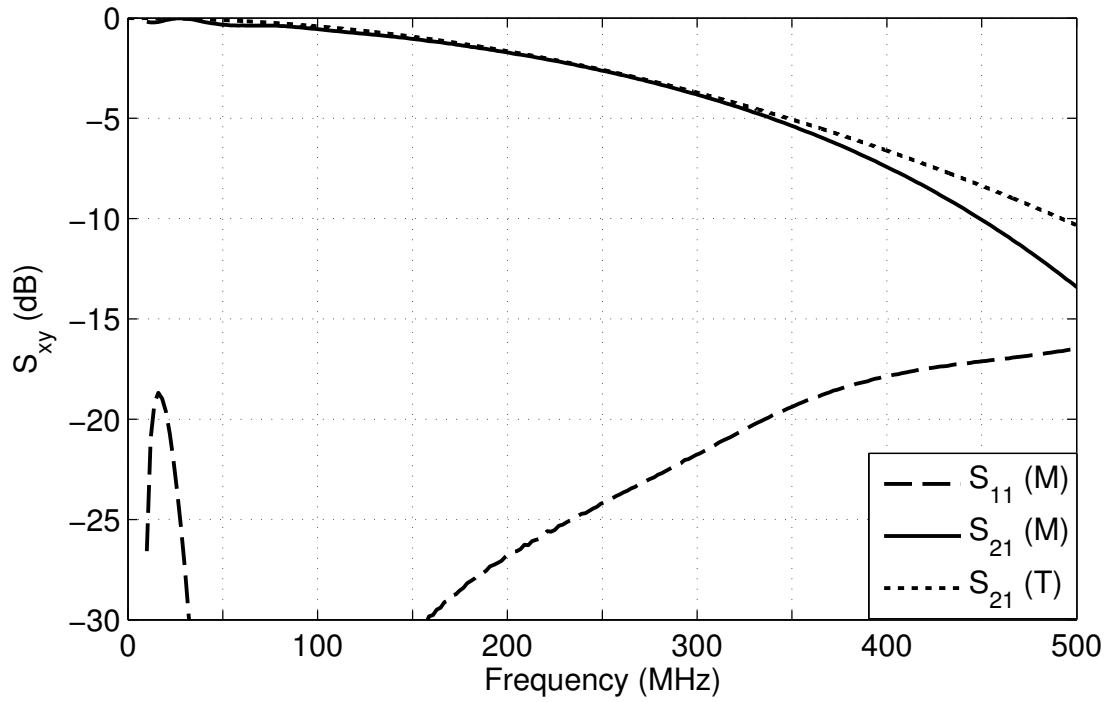

(b)

Figure 6.3: *Matched Filter.* The matched filter is an absorptive Gaussian-like LPF. The circuit diagram is shown in (a). The measured (M) S-parameters and the theoretical (T) voltage transfer function are plotted in (b). The theoretical response is based on Eqn. (6.10).

6.2 Receiver Simulation Model

Like the transmitter, the receiver was modeled in Agilent's ADS. The range gate, FPGA, amplifiers, and downconverter were modeled as behavioral components, which include gain, noise figure, and compression points, as appropriate. The matched filter was modeled using circuit elements corresponding to the actual hardware implementation. The time-domain simulation includes noise from DC to 4 GHz, which is especially important in the receiver portion of the radar model.

6.3 Receiver Performance

The receiver is turned on and off, as discussed in Section 6.1.1. The on- and off-state receiver gain is plotted in Figure 6.4. The on-state gain at the center of the band is $G_{RX} = 55$ dB, and peak on-state gain is $G_{RX} = 57$ dB. The 3 dB bandwidth is $\beta_{3dB}^{RX} \simeq 500$ MHz. The off-state gain at the center of the band is $G_{off}^{RX} = 3$ dB, and peak off-state gain is $G_{off}^{RX} = 5$ dB. The worst case receiver on-off isolation is $I_{on/off}^{RX} = 49$ dB from 2–3 GHz, a result of the 49 dB range gate on-off isolation. As noted in Section 6.1.1, the dynamic insertion loss of the range gate is about 3 dB worse than the static insertion loss. As such, it is anticipated that the receiver gain under pulsed operation will be at least 3 dB lower than shown in Figure 6.4. For the remainder of this thesis, a pulsed receiver gain of $G_{pulsed}^{RX} = 52$ dB will be assumed.

The P1dB point of the receiver is dependant on the compression point of each of the components in the receiver chain and can be calculated using the following:

$$P_{1dB}^{o} = \left(\frac{1}{G_2 G_3 ... G_N P_{1dB}^{1}} + ... + \frac{1}{G_{N-1} G_N P_{1dB}^{N-2}} + \frac{1}{G_N P_{1dB}^{N-1}} + \frac{1}{P_{1dB}^{N}} \right) \tag{6.13}$$

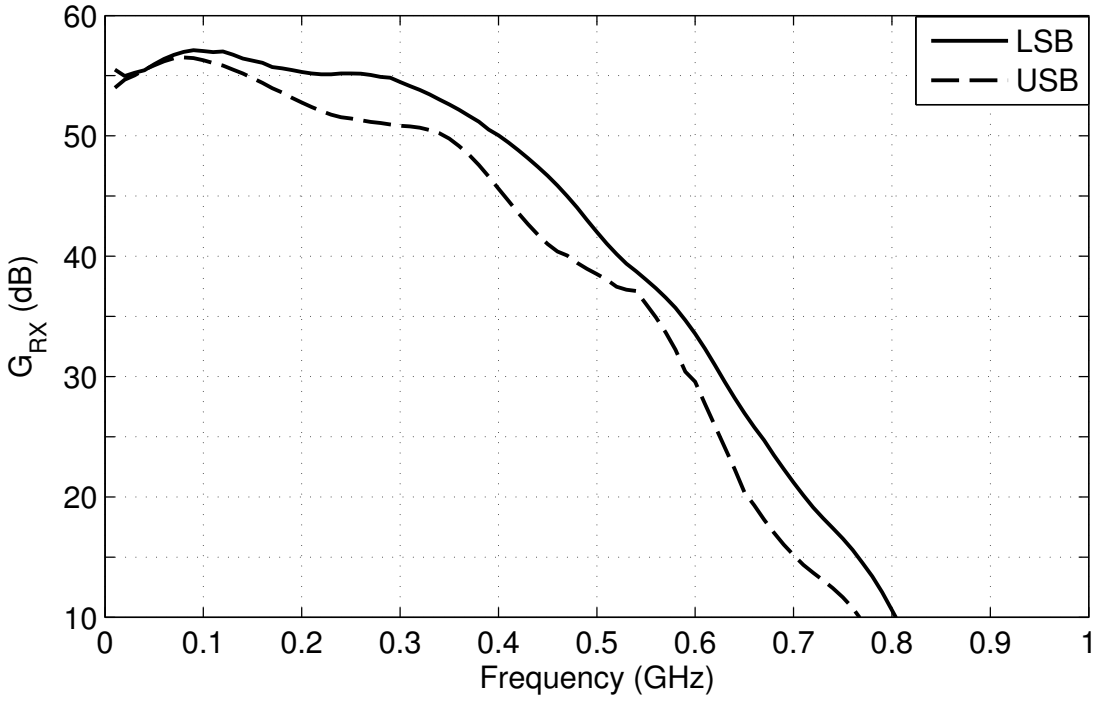

(a)

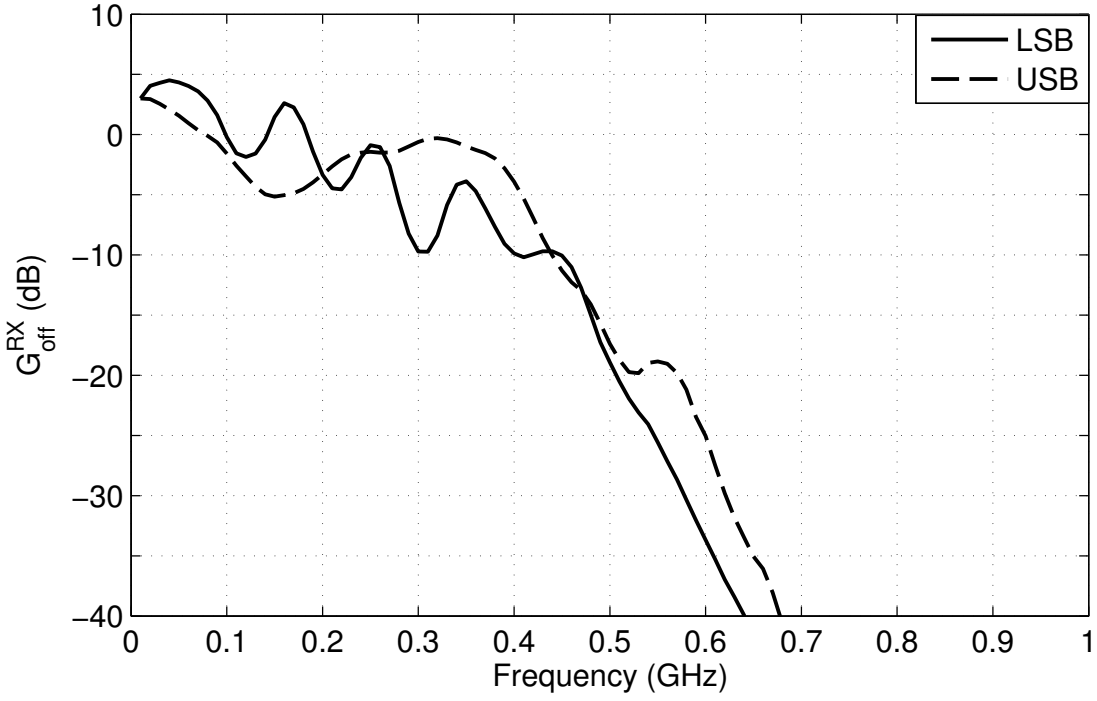

(b)

Figure 6.4: *Receiver Gain.* The receiver input frequency was swept from 1–4 GHz in 10 MHz steps. The output power of the receiver was measured, and the gain was calculated. The lower sideband corresponds to input frequencies from 1–2.5 GHz, and the upper sideband corresponds to input frequencies from 2.5–4 GHz. (a) is the receiver gain when the range gate is open, and (b) is the receiver gain when the range gate is closed.

where P^o_{1dB} is the P1dB point at the output of the cascade, G_n is the gain of the n$^{\text{th}}$ device, and P^n_{1dB} is the output P1dB point of the n$^{\text{th}}$ device [27].[1] Based on Eqn. (6.13), the anticipated output P1dB point of the receiver is 25 dBm at the center of the band. The measured output P1dB point is 24 dBm at the center of the band. The P1dB-based dynamic range of the receiver is DR = $P^o_{1dB}/(\text{SNR}^{out}_{1,min}P^{RX}_{out,N})$, where $P^o_{1dB} = 24$ dBm is the P1dB point of the receiver, $\text{SNR}^{out}_{1,min} = -13.5$ dB is the minimum detectable single-pulse SNR at the output of the receiver, and $P^{RX}_{out,N} = k_B T_o \beta_N G^{RX}_{pulsed} F^{RX}_{pulsed} = -20$ dBm is the noise power; the dynamic range is DR = 57.5 dB.

The noise figure of the receiver impacts the SNR at the output of the receiver, the sensitivity of the receiver, and the quantization noise of the post processor. The theoretical noise figure, from Eqn. (1.11), is $F_{RX} = 10$ dB, and the measured noise figure is $F_{RX} = 11.8$ dB. The noise figure was measured using a signal generator at the input of the receiver and a power meter at the output of the receiver. The output of the receiver was measured with the signal generator off; the output was $P^{RX}_{out} = P^{RX}_{out,N} = -17$ dBm. Next, the output was measured with the signal generator on, and the input power was adjusted so the measured output power was twice the noise power, or $P^{RX}_{out} = -14$ dBm; the input power for this measurement was $P^{RX}_{in} = -75.2$ dBm. In this case, the signal power at the output of the receiver is equal to the noise power at the output of the receiver: $P^{RX}_{out,S} = P^{RX}_{out,N}$. From Eqn. (1.9), the noise figure can be calculated as:

$$\begin{aligned} F_{RX} &= \frac{\text{SNR}^{in}_1}{\text{SNR}^{out}_1} \\ &= \frac{P^{RX}_{in} P^{RX}_{out,N}}{P_N P^{RX}_{out,S}} \\ &= \frac{P^{RX}_{in} P^{RX}_{out,N}}{k_B T_o \beta_N P^{RX}_{out,S}} \end{aligned} \tag{6.14}$$

[1] The equation in [27] is to determine the cascaded third-order intercept point, but is also valid for the P1dB point.

Since $P_{out,S}^{RX} = P_{out,N}^{RX}$ for this measurement, the expression can be simplified:

$$F_{RX} = \frac{P_{in}^{RX}}{k_B T_o \beta_N} \tag{6.15}$$

where $P_{in}^{RX} = -75.2\,\text{dBm}$ is the signal power at the input of the receiver and $\beta_N = 520\,\text{MHz}$ is the measured noise bandwidth of the matched filter; the result is the quoted noise figure: $F_{RX} = 11.8\,\text{dB}$. The noise figure was measured statically. Since the dynamic insertion loss of the range gate is about 3 dB worse than the static insertion loss, the dynamic noise figure will also be about 3 dB worse than the measured value. For the remainder of this thesis, a pulsed receiver noise figure of $F_{pulsed}^{RX} = 14.8\,\text{dB}$ will be used.

The receiver was designed as a complement to the pulsed transmitter. The range gate can be adjusted to accommodate ranges from 0.75–6.75 m; the set of ranges will be further limited by the interaction between the transmitter and receiver, as will be discussed in Chapter 8. If the PRF, center frequency, or envelope pulsewidth of the transmitted signal are adjusted, then the receiver design must be reevaluated. Specifically, the PRF impacts the range gate control signals, the center frequency impacts the required bandwidth of the various RF components, and the envelope pulsewidth impacts the matched filter design and possibly the range gate pulsewidth. It is possible to improve the receiver on-off isolation by increasing the on-off isolation of the range gate. It is also possible to improve the noise figure of the receiver by placing the range gate after the RF LNA, rather than before. The range gate was placed before the RF LNAs in this work to ensure the noise at the output of the receiver was sufficient to toggle the LSB of the digitizer when the full-scale voltage of the digitizer is $V_{fs} = 5\,\text{V}$, limiting the quantization noise (see Section 3.5 and the next section). If the gain of the receiver is increased, the range gate can be moved, as will be discussed in Section 9.2.3.

6.4 Receiver and Post Processor

In Section 3.5, it was noted that the gain and noise figure of the receiver should be designed so the noise power at the output of the receiver will toggle at least the LSB of the ADC. The noise power at the output of the receiver is:

$$P_{out,N}^{RX} = k_B T_o \beta_N F_{pulsed}^{RX} G_{pulsed}^{RX} \tag{6.16}$$

Based on the measured receiver behavior, $P_{out,N}^{RX} = -20\,\text{dBm}$. To compare this to the LSB of the ADC, the power must be converted to the rms voltage: $V_N^{out} = 22\,\text{mV}$. The maximum full-scale range of the ADC is $V_{fs} = 5\,\text{V}$, resulting in a LSB of $V_{fs}/2^b = 20\,\text{mV}$, so even for the maximum full-scale voltage, the noise power at the output of the receiver is sufficient to limit the quantization noise.

The P1dB point of the receiver is $P_{1dB}^o = 24\,\text{dBm}$, which corresponds to a peak voltage of 5 V. The maximum voltage range of the ADC is ±2.5 V, so the ADC limits the dynamic range of the radar. Assuming the maximum full-scale voltage range, the dynamic range is 6 dB lower than calculated for the receiver: DR = 51.5 dBm. For low-level signals, such as the minimum detectable signal with a -13.5 dB SNR, it is advantageous to reduce the full-scale voltage range to increase the resolution of the digitized signal. For some of the testing in this work, the dynamic range of the radar will be sacrificed for better digitization resolution; the full-scale voltage range of the ADC will be noted for all measurements.

Chapter 7

UWB Antenna System

Proper antenna design is vital to UWB radar operation because the dispersion of the transmit and receive antennas can distort the transmitted waveform. Antenna types, UWB antenna considerations, and the antenna system design for this thesis are presented in the following sections.

7.1 UWB Antenna Types

A variety of antenna elements can be used for UWB applications. Several typical antennas as listed in Table 7.1; they are categorized as 3-dimensional (3D) or 2-dimensional (2D) and directional or omni-directional. Frequency-independent and traveling-wave antennas, such as Vivaldi, tapered slot, horn, beverage, log-periodic, Yagi, and spiral antennas, provide fairly constant behavior over a wide range of frequencies; however, there are trade-offs. The final slot width of Vivaldi and slot antennas should be at least one-half of the free-space wavelength at the lowest frequency of operation [111], so they can be large. Horn antennas can also be bulky, which can be problematic for portable devices [112]. While it has been illustrated in the literature that it is possible to adapt a log-periodic

Table 7.1: Single-Element UWB Antennas (adapted from [112])

	Directional	**Omni-Directional**
2D	Vivaldi [111], [118], [119], [120] Tapered Slot [111], [120] Printed Folded Beverage [121] Log-Periodic [113], [122], [123] Printed Quasi-Yagi [114] Spiral [124] Broadband Patch [125], [126]	Planar Dipole [119], [120] Planar Monopole [118], [119], [120] [92] Folded Beverage [121] Slot [118], [120]
3D	TEM Horn [120] Ridge Horn [120] Reflector [120]	Loaded Cylindrical Dipole Biconical [127], [120] Discone [120] Roll [112], [92]

design to minimize the dispersion of the antenna for UWB applications [113], the phase center of standard log-periodic, Yagi, and spiral antennas shifts with frequency, which normally leads to pulse distortion (dispersion) [112]. Dipole, monopole, slot, and patch antennas are standing-wave, resonant structures. As such, broad-banding design techniques must be applied for UWB standing-wave antennas. Antenna arrays based on broadband elements can also be employed, as discussed in [114], [111], [115], [116], and [117].

The required directivity of the transmit and receive antennas depends on the application. This thesis presents a generic approach to UWB short-pulse Doppler radar, and the application is not defined. As such, a pair of moderately directive, planar antennas will be utilized; the antenna design will be presented in Section 7.3. First, it is helpful to consider some important UWB antenna characteristics and how they relate to standard, narrowband antenna design.

7.2 UWB Antenna System Considerations

The fidelity of a UWB antenna system, which consists of the transmit and receive antennas, is extremely important. The fidelity is a measure of the correlation between the transmitted and received waveforms; a high-fidelity antenna system will have little impact on the received pulse characteristics [128]. An antenna's fidelity is waveform dependant, so the antenna system design must account for the transmitter characteristics [129]. The first step to understanding the antenna system's fidelity is to consider each antenna's transfer function and impulse response.

7.2.1 Transfer Function and Impulse Response

The transfer function and impulse response of an antenna are derived, following [130], [131], and [132]. The derivation assumes transverse electro-magnetic (TEM) feeds, $Z_o = 50\,\Omega$ source and load impedances, antennas set up as shown in Figure 7.1, and far-field separation between the antennas.

The transmitted electric field is:

$$\mathbf{E}_{TX}(\mathbf{r}, f) = 2V_{TX}(f)\frac{Z_A^{TX}}{Z_A^{TX} + Z_o}\frac{e^{-\jmath\beta r}}{r}\mathbf{F}_{TX}(\hat{r}, f) \tag{7.1}$$

where $\mathbf{E}_{TX}(\mathbf{r}, f)$ is the transmitted electric field, $\mathbf{r}$ is the position vector, $V_{TX}(f)$ is the voltage at the input of the transmit antenna, Z_A^{TX} is the input impedance of the transmit antenna, $\beta = 2\pi f/c_o$, $r = |\mathbf{r}|$, and $\mathbf{F}_{TX}(\hat{r}, f)$ is the pattern factor. The factor of 2 is to approximate the Thevenin voltage source in Figure 7.1a; if the antenna is not well matched to the system impedance (i.e. $Z_A^{TX} \neq Z_o$), then Eqn. (7.1) and Figure 7.1a should be reconsidered.

The antenna pattern factor, $\mathbf{F}_{TX}(\hat{r}, f)$, can be related to the transmit antenna's

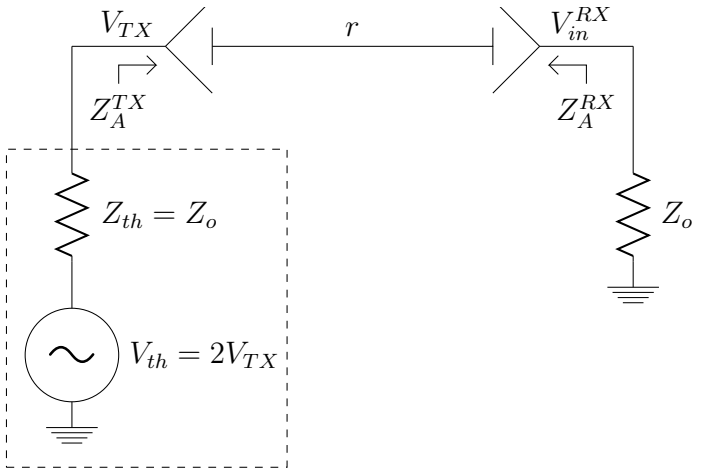

(a)

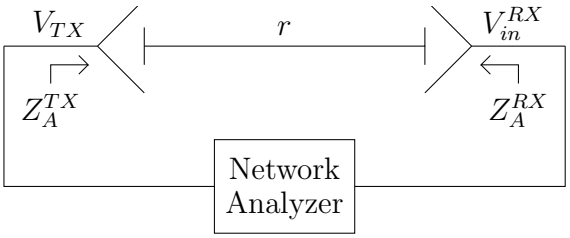

(b)

Figure 7.1: *Antenna System Setup.* Two identical antennas, spaced at a distance r, are employed to determine the transfer function and impulse response of the antenna.

vector effective length as follows:

$$\begin{aligned} \mathbf{F}_{TX}(\hat{r}, f) &= -\frac{\jmath f \mu_o}{Z_A^{TX}} \bar{\mathbf{r}} \cdot \mathbf{h}_{TX}(-\hat{r}, f) \\ &= -\frac{\jmath f \eta}{c_o Z_A^{TX}} \bar{\mathbf{r}} \cdot \mathbf{h}_{TX}(-\hat{r}, f) \qquad (7.2) \\ \bar{\mathbf{r}} &= \hat{x}\hat{x} + \hat{y}\hat{y} + \hat{z}\hat{z} - \hat{r}\hat{r} \qquad (7.3) \end{aligned}$$

where μ_o is the free space permeability, $\bar{\mathbf{r}}$ is the position dyadic defined in Eqn. (7.3), $\mathbf{h}_{TX}(-\hat{r}, f)$ is the vector effective length or transfer function of the transmit antenna, η is the impedance of free space, and $\hat{x}$, $\hat{y}$, $\hat{z}$ are the unit position vectors. For simplicity, assume a polarization vector $\hat{P}$ such that $\hat{P} \cdot \hat{r} = 0$ (TEM plane wave). Assuming polarization $\hat{P}$, the expressions for the electric field, pattern

factor, and vector effective length can be simplified as follows:

$$E_{TX}^{P}(r,f) = \mathbf{E}_{TX}(\mathbf{r},f)\cdot\hat{P} \tag{7.4}$$

$$F_{TX}^{P}(f) = \mathbf{F}_{TX}(\hat{r},f)\cdot\hat{P} \tag{7.5}$$

$$h_{TX}^{P}(f) = \mathbf{h}_{TX}(-\hat{r},f)\cdot\hat{P} \tag{7.6}$$

The polarized form of Eqn. (7.1) is:

$$E_{TX}^{P}(r,f) = -\frac{\jmath f\eta}{c_o Z_A^{TX}} 2V_{TX}(f)\frac{Z_A^{TX}}{Z_A^{TX}+Z_o}\frac{e^{-\jmath\beta r}}{r}h_{TX}^{P}(f) \tag{7.7}$$

The effective length can be replaced by a normalized transfer function, defined as follows:

$$h_{TX}^{P,N}(f) = \frac{2\sqrt{Z_o\eta}}{Z_A^{TX}+Z_o}h_{TX}^{P}(f) \tag{7.8}$$

Using Eqn. (7.8), the transmitted electric field is:

$$\frac{E_{TX}^{P}(r,f)}{\sqrt{\eta}} = \frac{-\jmath f}{c_o\sqrt{Z_o}}\frac{e^{-\jmath\beta r}}{r}h_{TX}^{P,N}(f)V_{TX}(f) \tag{7.9}$$

The time-domain electric field can be determined by taking the Fourier transform of Eqn. (7.9). Two expressions are possible:

$$\frac{E_{TX}^{P}(r,t)}{\sqrt{\eta}} = \frac{1}{2\pi r c_o\sqrt{Z_o}}\frac{\partial h_{TX}^{P,N}(t)}{\partial t}\star V_{TX}(t)\star\delta\left(t-\frac{r}{c_o}\right) \tag{7.10}$$

$$\frac{E_{TX}^{P}(r,t)}{\sqrt{\eta}} = \frac{1}{2\pi r c_o\sqrt{Z_o}}h_{TX}^{P,N}(t)\star\frac{\partial V_{TX}(t)}{\partial t}\star\delta\left(t-\frac{r}{c_o}\right) \tag{7.11}$$

where $\star$ is the convolution operator, $\delta()$ is a delta function, and $h_{TX}^{P,N}(t)$ is the impulse response of the transmit antenna. Eqn. (7.11) will be assumed for the remainder of this work.

The received voltage, in the frequency domain, will be:

$$V_{in}^{RX}(f) = \frac{2Z_o}{Z_A^{RX}+Z_o}\mathbf{h}_{RX}(\hat{r},f)\cdot\mathbf{E}_{TX}(\mathbf{r},f) \tag{7.12}$$

where Z_A^{RX} is the input impedance of the receive antenna and $\mathbf{h}_{RX}(\hat{r},f)$ is the vector effective length or transfer function of the receive antenna. The expression

accounts for any antenna mismatch. Assuming polarization $\hat{P}$ and the following normalization:

$$h_{RX}^{P,N}(f) = \frac{2\sqrt{Z_o \eta}}{Z_A^{RX} + Z_o} h_{RX}^{P}(f) \tag{7.13}$$

the received voltage can be simplified:

$$\frac{V_{in}^{RX}(f)}{\sqrt{Z_o}} = h_{RX}^{P,N}(f) \frac{E_{TX}^{P}(r,f)}{\sqrt{\eta}} \tag{7.14}$$

$$\boxed{V_{in}^{RX}(f) = \frac{-\jmath f}{c_o} \frac{e^{-\jmath\beta r}}{r} h_{TX}^{P,N}(f) h_{RX}^{P,N}(f) V_{TX}(f)} \tag{7.15}$$

The equivalent time-domain expression is:

$$\boxed{V_{in}^{RX}(t) = \frac{1}{2\pi r c_o} h_{TX}^{P,N}(t) \star h_{RX}^{P,N}(t) \star \frac{\partial V_{TX}(t)}{\partial t} \star \delta\left(t - \frac{r}{c_o}\right)} \tag{7.16}$$

where $h_{RX}^{P,N}(t)$ is the impulse response of the receive antenna.

Once $h_{RX}^{P,N}(t)$ and $h_{TX}^{P,N}(t)$ have been established, the time-domain output of the antenna system, $V_{in}^{RX}(t)$, can be determined in terms of the output of the transmitter, $V_{TX}(t)$. It is also possible to determine $V_{in}^{RX}(t)$ by taking the inverse Fourier transform of $V_{in}^{RX}(f)$.

To determine $h_{TX}^{P,N}(t)$ or $h_{TX}^{P,N}(f)$, consider the setup in Figure 7.1b, and assume the antennas are identical and that their patterns mirror one another. In this case, $h_{TX}^{P,N}(f) = h_{RX}^{P,N}(f)$. Making this substitution and solving Eqn. (7.15) for $h_{TX}^{P,N}(f)$ results in:

$$h_{TX}^{P,N}(f) = \sqrt{\frac{r c_o}{\jmath f} e^{\jmath\beta r} \frac{V_{in}^{RX}(f)}{V_{TX}(f)}} \tag{7.17}$$

Eqn. (7.17) can be related to S-parameters as follows:

$$\boxed{h_{TX}^{P,N}(f) = \sqrt{\frac{r c_o}{\jmath f} \exp\left(\frac{\jmath 2\pi f r}{c_o}\right) S_{21}(r,f)}} \tag{7.18}$$

The impulse response can be determined from the inverse Fourier transform of the transfer function:

$$\boxed{h_{TX}^{P,N}(t) = \mathscr{I}\left\{h_{TX}^{P,N}(f)\right\}} \tag{7.19}$$

When calculating the transfer function using Eqn. (7.18), it is important to unwrap the phase and account for the square root in order to achieve a physical phase response [130]. The transfer function or impulse response can be used in conjunction with simulation software to examine the effects of the antenna system.

Measuring the Transfer Function/Impulse Response

The transfer function or impulse response of an antenna can be measured in the frequency domain or the time domain; however, it is typically simpler to perform the measurement in the frequency domain. The measurement setup in Figure 7.1b can be used. Two identical antennas should be used and must be separated by a distance r such that the antennas lie within one another's far field. The required separation can be determined from the highest expected transmitted frequency. The standard narrowband far-field definition is $r \geq 2D^2/\lambda$, where D is the largest antenna dimension and λ is the transmitted, free-space wavelength [133]. This is not necessarily valid for short time pulses. It has been proposed that the far field can be defined as $r \gtrsim D^2/(c_o\tau)$ [132]. For this work, both definitions provide similar results. If the antennas are located in one another's far field, the calculated transfer function and impulse response will scale with range. The measured frequency range should extend well beyond the expected spectrum of the transmitted signal to ensure valid calculation of the impulse response.

Practical Transfer Function Definition

The transfer function and impulse response of Eqns. (7.18) and (7.19) are related to the vector effective length of the antenna, so they are not unitless but rather in terms of distance. While the expressions are useful for examining the behavior of the antenna system, a unitless transfer function is simpler to use in an RF

simulator, such as Agilent's ADS. An alternate form of the transfer function can be derived from a signal flow diagram describing a pair of identical antennas [134]:

$$H_{TX}^{P}(f) = \sqrt{4\pi r \exp\left(\frac{\jmath 2\pi f r}{c_o}\right) S_{21}(r,f)} \tag{7.20}$$

where $S_{21}(r,f)$ is the measured S-parameter sweep at a given distance. To derive the transfer function, consider the cascade of one- and two-port devices in Figure 7.2a that represents the antenna measurement setup in Figure 7.1b. In this case the transmitter is port one and the load is port two of the network analyzer. The corresponding signal flow diagram is shown in Figure 7.2b. The nodes and branches are as follows:

- The nodes are labeled with the appropriate voltage waves, corresponding to Figure 7.2a.
- Γ_{TX} is the reflection coefficient looking into the output of the transmitter.
- $\Gamma_{A,1}^{TX}$ and $\Gamma_{A,1}^{RX}$ are the reflection coefficients looking into the transmit and receive antennas.
- Γ_L is the reflection coefficient looking into the load.
- Γ_{FS}^{TX} and Γ_{FS}^{RX} are the reflection coefficients looking into the antennas from free-space and can be considered equal to zero.
- $H_{TX}^{P}(f)$ and $H_{RX}^{P}(f)$ are the transfer functions for the transmit and receive antennas, which are considered reciprocal (for transmission only).
- $\exp(-\jmath\beta r)/(4\pi r)$ is the free space Green's function.

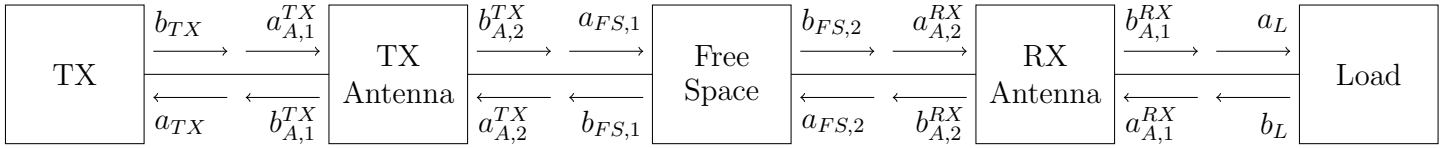

(a)

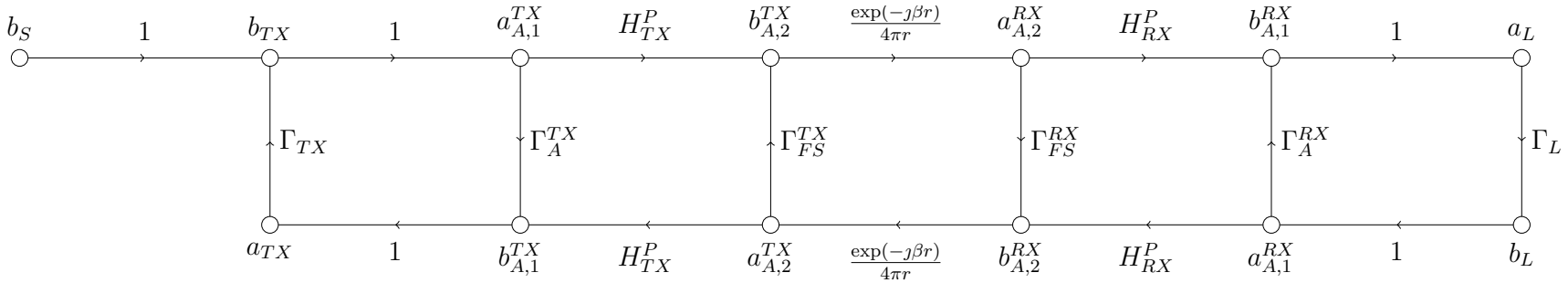

(b)

Figure 7.2: *Practical Transfer Function.* The antenna measurement setup of Figure 7.1b can be represented as a cascade of one- and two-port devices as illustrated in (a). The equivalent signal flow diagram is illustrated in (b).

Assuming everything is well matched, we can write an approximate expression for a_L in terms of b_{TX}:

$$a_L \simeq H_{TX}^P(f) H_{RX}^P(f) \frac{e^{-\jmath\beta r}}{4\pi r} b_{TX} \tag{7.21}$$

Since the antennas are assumed to be identical, the expression can be simplified and solved for the transfer function of the antennas as follows:

$$\begin{aligned} H_{TX}^P(f) &\simeq \sqrt{4\pi r \exp\left(\frac{\jmath 2\pi f r}{c_o}\right) \frac{a_L}{b_{TX}}} \\ &\simeq \sqrt{4\pi r \exp\left(\frac{\jmath 2\pi f r}{c_o}\right) S_{21}(r,f)} \end{aligned} \tag{7.22}$$

which is the desired transfer function. If needed, reflections can be accounted for to achieve a more accurate result [135]; additionally, the location of the antenna's phase center can be determined to more accurately establish the separation between the antennas [130], [136].

7.2.2 Temporal Differentiation of V_{TX}

As seen in Eqn. (7.16), one result of transmission through the antenna system is that the transmitted voltage, V_{TX}, is differentiated. For short pulses, the time derivative can significantly impact the pulse envelope. Consider the single-pulse output of the transmitter under study:

$$V_{TX}(t) = V_p^{TX} \exp\left(-2\ln(2)\left(\frac{t}{\tau}\right)^2\right) \cos(2\pi f_c t) \tag{7.23}$$

The time derivative of V_{TX} is:

$$\begin{aligned} \frac{\partial V_{TX}(t)}{\partial t} &= -2\ln(2) V_p^{TX} \frac{2t}{\tau^2} \exp\left(-2\ln(2)\left(\frac{t}{\tau}\right)^2\right) \cos(2\pi f_c t) \\ &\quad \ldots - 2\pi V_p^{TX} f_c \exp\left(-2\ln(2)\left(\frac{t}{\tau}\right)^2\right) \sin(2\pi f_c t) \end{aligned} \tag{7.24}$$

The first term introduces a 180° phase shift at the peak of the envelope. The second term is proportional to $V_{TX}(t)$, but the carrier is shifted by 90°. The two

terms are plotted separately in Figure 7.3a, and the full normalized expression is plotted in Figure 7.3b. The undifferentiated waveform is also plotted in Figure 7.3b. As can be seen, the second term dominates the final expression, and the time derivative has little impact on the pulse envelope, for the transmitted waveform in this thesis. If a narrower pulse is used, or if the radar is an impulse radar, the time derivative will have a more significant effect on the pulse envelope, and the temporal differentiation must be considered in the overall radar design. For this work, temporal differentiation will be neglected in analysis and simulation to simplify the system model and equations.

7.2.3 Compensation Techniques

A variety of techniques have been explored to provide a dispersionless antenna system without relying on extremely wideband antennas. For example, [137] employs optical waveform generation in the transmitter, so the phase response of the transmitter is opposite that of the antenna system. The received pulse has a flat phase response and is not affected by the dispersion of a non-ideal antenna system. [138] uses photonic phase filters in the receiver front-end to compensate for dispersion due to the antenna system. [139] considers a pair of antennas, each with a half-derivative transfer function; to achieve this, the corresponding antenna must transmit and receive cylindrical waves efficiently. The resulting antenna system should, ideally, transmit and receive a UWB signal without distorting it. Another option is to use different types of antennas for transmission and reception so their dispersive behavior cancels [140]. The analysis leading to Eqn. (7.16) assumes TEM antennas; if a different type of antenna were utilized, the waveform would be of a different form at the input of the receiver.

The compensation techniques overviewed above can be useful for UWB antenna system design. However, for this thesis, a low dispersion antenna was

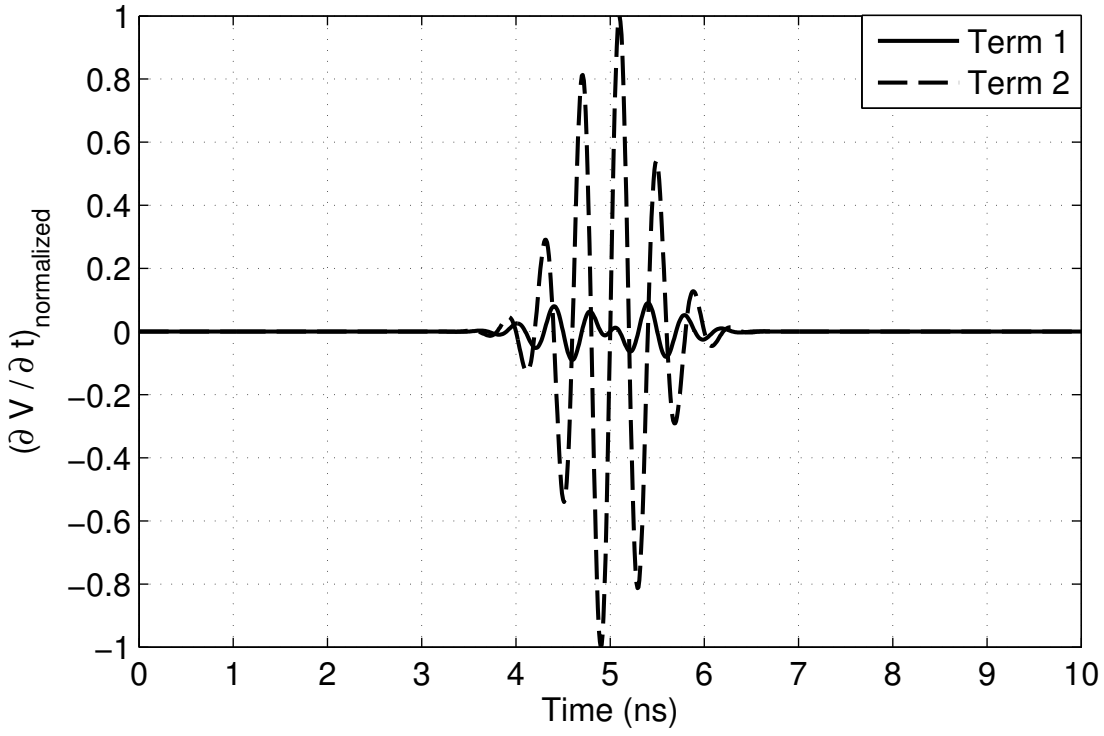

(a)

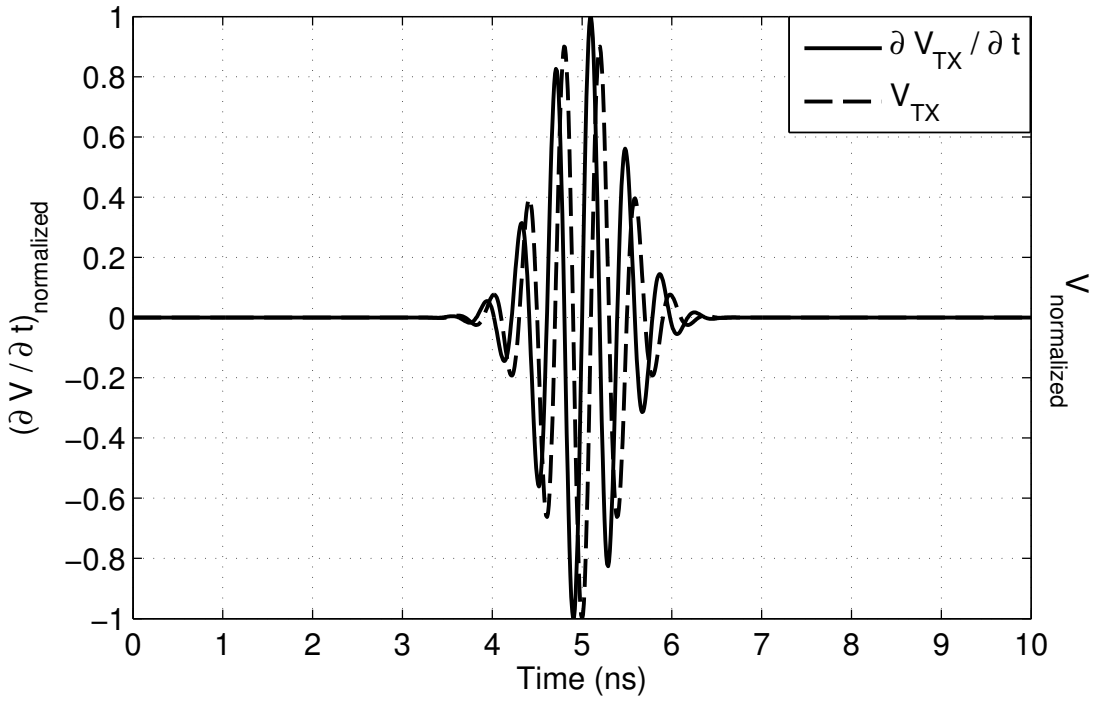

(b)

Figure 7.3: *Temporal Differentiation of Transmitted Waveform.* The two terms of Eqn. (7.24) are normalized and plotted separately in (a). The full, normalized expression and the undifferentiated, normalized expression are plotted in (b).

Table 7.2: Antenna Design

Parameter	Value
h	0.79 mm
W_m	1.5 mm
W	150 mm
L	152.3 mm
L_c	38.75 mm
R_a	75 mm
R_b	73.5 mm
R_c	37.5 mm
R_d	36.75 mm
R_e	120 mm

designed, which does not necessitate dispersion compensation techniques.

7.3 UWB Antenna System

A pair of microstrip-fed, elliptically-tapered, antipodal slot antennas were designed for the UWB radar described in this thesis. The antennas are detailed in the following sections.

7.3.1 Antenna Design

An elliptically-tapered, antipodal slot antenna was designed, following [141] and [111], to operate from 2–3 GHz, as shown in Figure 7.4. A tapered slot antenna was selected for its directivity and near-constant phase center; since a pair of transmit and receive antennas will be employed, directivity can intrinsically improve the TX-RX isolation of the antenna system. An elliptical taper was selected as a compromise between E-plane and H-plane beamwidth [111]. An antipodal architecture with a microstrip feed was selected to allow simple integration with the transmitter and receiver. The design parameters for the antenna are summarized in Table 7.2.

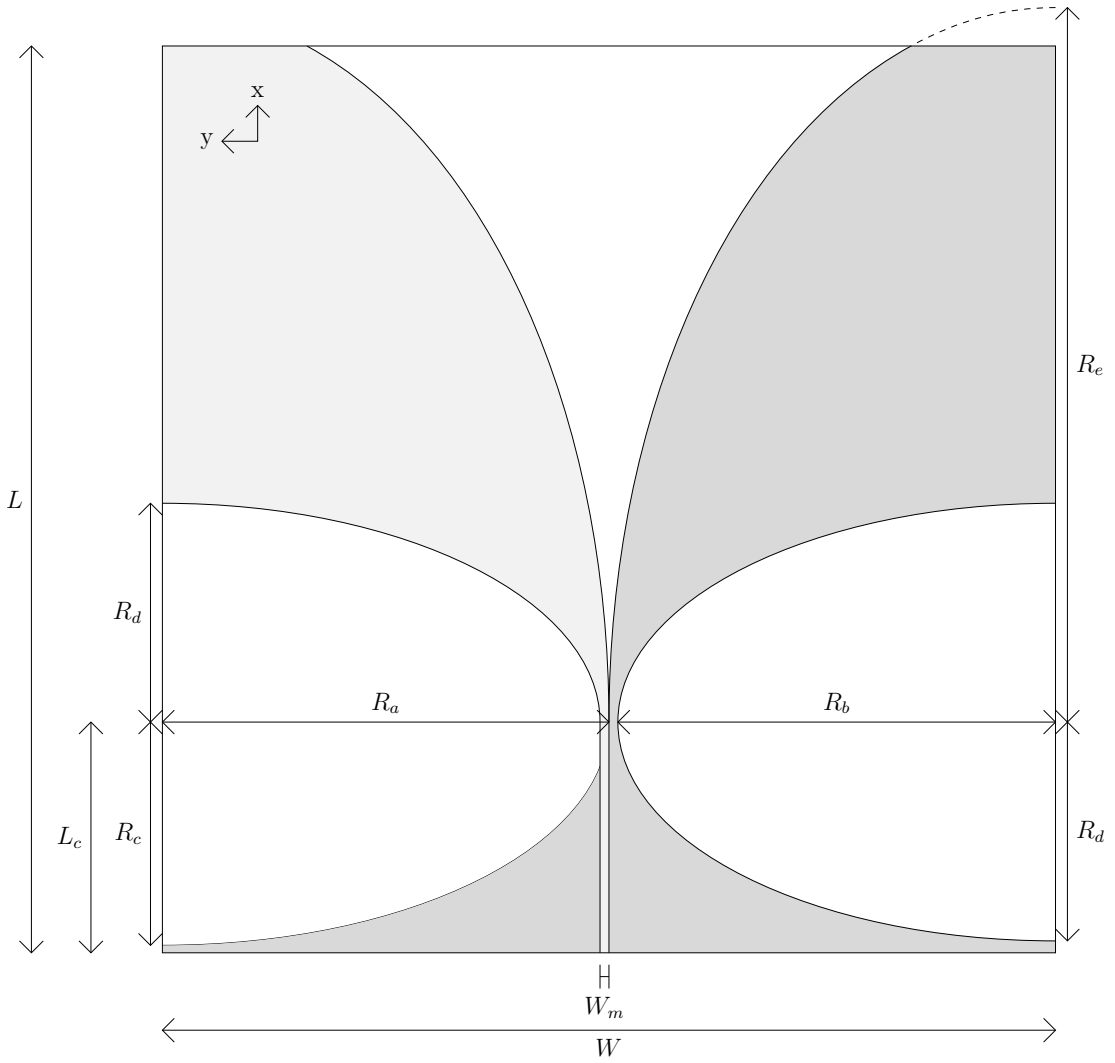

Figure 7.4: *Elliptically-Tapered Antipodal Slot Antenna.* The antenna system for this thesis is comprised of a pair of identical tapered slot antennas. The two gray sections indicate metallization on opposite sides of a two-layer FR4 substrate of thickness h. The dimensions used for this thesis are summarized in Table 7.2.

The antenna was designed on a 0.79 mm FR4 substrate. Ansoft's high frequency structure simulator (HFSS), which is a finite element method (FEM) simulator, was used for the antenna design. The simulations show that the substrate thickness has a slight impact on the E- and H-plane beamwidths and a more significant impact on the angle at which the peak gain occurs. Since the antenna elements are on different layers, the thickness of the substrate creates a

small angle between the antenna layers. The height can be adjusted to steer the main lobe. A height of 0.79 mm, along with an FR4 substrate, was selected to align the peak gain at $\phi = 0°$ and $\theta = 90°$, as illustrated in the simulated and measured pattern data of Figure 7.5. The dielectric constant of the substrate also has a small impact on the E- and H-plane beamwidths as well as the angle at which the pattern peak occurs. $\epsilon_r = 10$ (Rogers 6010) and $\epsilon_r = 4.4$ (FR4) were considered. Based on the results, FR4 was selected as an inexpensive solution.

The final width of the taper opening should be at least one-half the free-space wavelength at the lowest frequency [111]. In this case, it should be at least $\lambda/2 = 75$ mm, and it is, as indicated in Table 7.2. Increasing the length-to-width ratio, L/W, of the antenna increases the directivity of the antenna [111] and extends the bandwidth of the antenna by reducing the lower corner frequency. However, it was also discovered through simulation that the return loss of the antenna is degraded as L/W is increased. For this work, $L/W \simeq 1$ was selected as a compromise between return loss, beamwidth, and bandwidth. The length of the feedline, L_c, was selected to ensure a microstrip-like feed, while minimizing the overall length of the antenna.

The two tapered arms are defined by two ellipses. The smaller ellipse is defined by radii R_b and R_d, and its upper right (or left) quadrant indicates where the metallization should begin, as can be seen in Figure 7.4. The larger ellipse is defined by radii R_a and R_e, and its upper right (or left) quadrant indicates where the metallization should end. The ground plane is also defined by a pair of ellipses. The right side of the ground plane is defined by an ellipse with radii R_b and R_d, and the left side is defined by an ellipse with radii R_a and R_c. Radii $R_a = W/2$ and $R_b = W/2 - W_m$ are set by the width of the antenna and microstrip feedline. Radii R_d and R_e were selected to achieve a simulated return loss of 10 dB or better from 2–6 GHz; the simulated and measured return are plotted in

Figure 7.8a. Radius R_c was selected so $R_c = R_d R_a / R_b$.

7.3.2 Measured Antenna Pattern

The antenna pattern was measured using a standard gain horn (Sunol Sciences DRH-118) with a CW sinusoidal excitation. The copole phi- and theta-cuts at 2 and 3 GHz are plotted in Figure 7.5, where the coordinate system is defined in Figure 7.4. The boresight gain is $G_A = 5$ dB at 2 GHz and is $G_A = 7$ dB at 3 GHz. The front-to-back ratio is 15 dB at 2 GHz and 12 dB at 3 GHz. The E-plane beamwidth is 56° at 2 GHz and 36° at 3 GHz; the H-plane beamwidth is 132° at 2 GHz and 80° at 3 GHz.

The antenna polarization was examined at angles of 45° and 135°. The patterns are plotted in Figure 7.6 and indicate the antenna is predominately linearly polarized. This assertion was verified with crosspole measurements; the crosspole ratio was about 25 dB at 2 GHz and 35 dB at 3 GHz. As expected, there is some variation between the 45°- and 135°-slant patterns; this occurs because the two antenna arms are on different metal layers, leading to an electric field vector that is somewhat offset from the x-y plane.

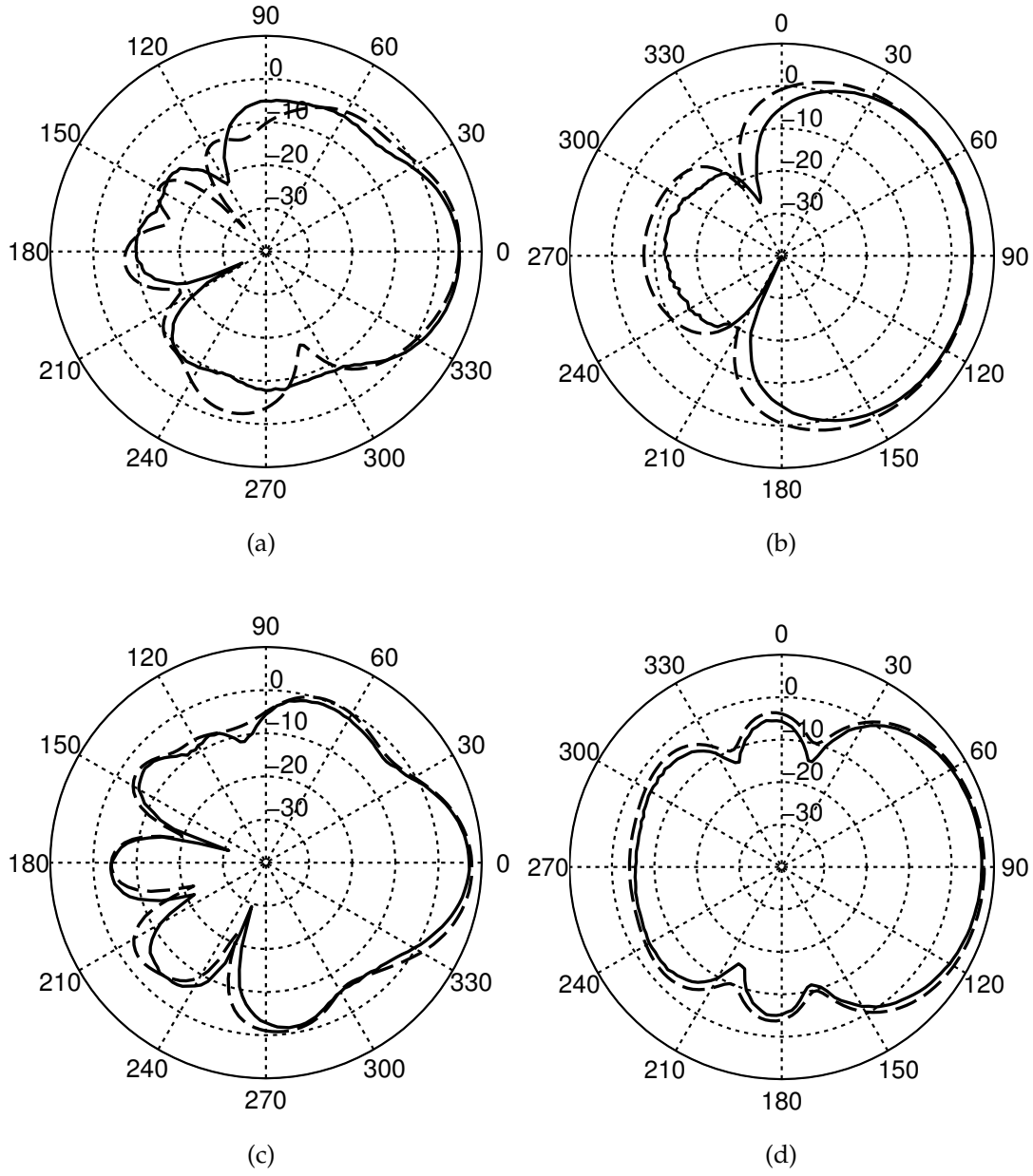

Figure 7.5: *Copole Antenna Patterns.* The measured and simulated copole antenna patterns are plotted in solid and dashed line, respectively. (a) is the 2 GHz E-plane pattern; (b) is the 2 GHz H-plane pattern; (c) is the 3 GHz E-plane pattern; and (d) is the 3 GHz H-plane pattern.

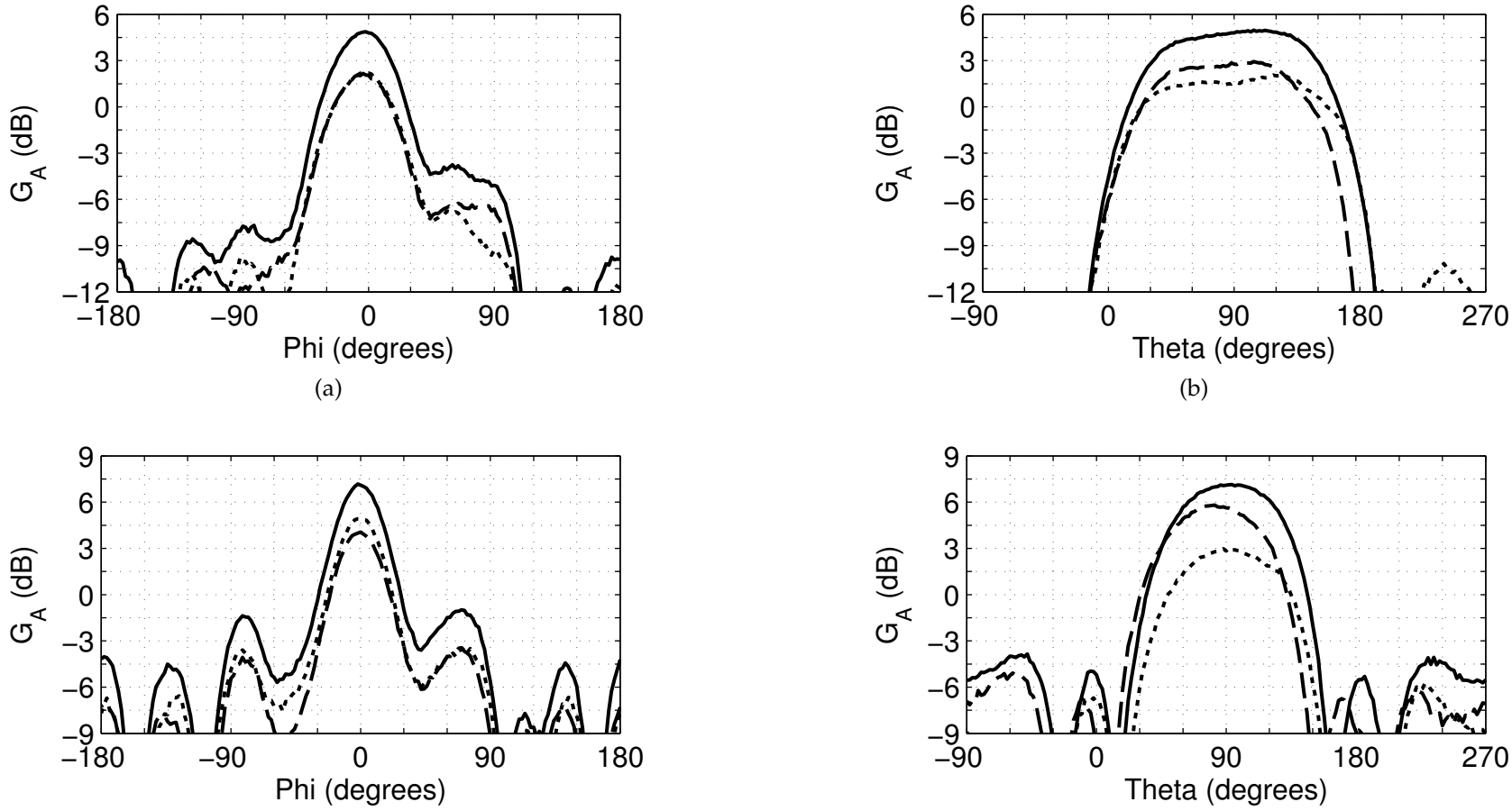

Figure 7.6: *45° Antenna Patterns.* The measured and simulated copole antenna patterns are plotted in solid lines and the 45°-slant and 135°-slant patterns are plotted in dashed and dotted lines, respectively. (a) is the 2 GHz E-plane pattern; (b) is the 2 GHz H-plane pattern; (c) is the 3 GHz E-plane pattern; and (d) is the 3 GHz H-plane pattern.

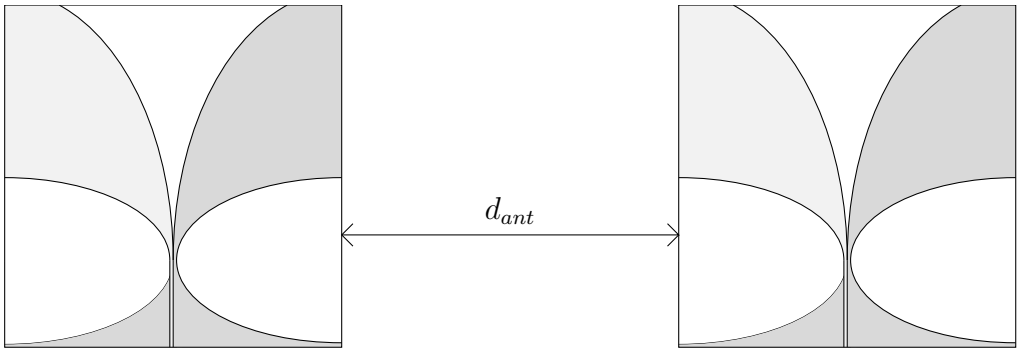

Figure 7.7: *Antenna Coupling Measurement Setup.* A pair of elliptically-tapered slot antennas were measured side-by-side in an anechoic chamber with a separation distance d_{ant}.

7.3.3 Measured Antenna System Isolation

The coupling between a pair of elliptically-tapered slot antennas was measured by placing two antennas side-by-side in an anechoic chamber, as shown in Figure 7.7. The distance between the antennas was varied from $d_{ant} = 0.15\,\text{m}$ to $d_{ant} = 2.0\,\text{m}$. Consistent with the radar parameters described in this thesis, the coupling between the antennas is characterized as the TX-RX isolation of the antenna system, and the isolation for various antenna separations is noted in Table 7.3; the apparent leakage ranges and range delays are also listed in the table. As discussed in Sections 3.7.2 and 3.7.3, the minimum theoretical TX-RX isolation is 84 dB. The measured TX-RX isolation for the pair of elliptically-tapered slot antennas falls short of this requirement. The TX-RX isolation can be improved by redesigning the antennas or by adding a physical structure to reduce the coupling between the antennas (e.g. antenna mounting structure or absorber). Alternatively, the maximum rejectable SNR, $\text{SNR}_{1,max}^{out,rej}$; the minimum detectable SNR, $\text{SNR}_{1,min}^{out}$; and the minimum range, R_{min}, specifications can be adjusted. The trade-offs between these specifications and the minimum TX-RX isolation will be discussed in more detail in Chapter 8.

Table 7.3: TX-RX Isolation of Antenna System

d_{ant} (m)	Apparent Leakage Range Delay (m)	Leakage Time Delay (ns)	TX-RX Isolation (dB)
0.15	0.075	0.5	35.6
0.3	0.15	1.0	38.4
0.45	0.225	1.5	41.6
1.0	0.5	3.3	46.2
1.45	0.725	4.8	49.4
2.0	1.0	6.7	54.1

7.3.4 Measured Transfer Function

The boresight transfer function was measured using two elliptically-tapered slot antennas. The antennas were aligned to face one another at boresight with a far-field separation distance. The antennas were connected to two ports of a network analyzer, as shown in Figure 7.1b, and the frequency was stepped from 0–9 GHz using a step time large enough to allow the signal to propagate through the antenna system. The network analyzer was calibrated up to the antenna ports using an Agilent electronic calibration unit. The transfer function was calculated using Eqn. (7.22) and is plotted in Figure 7.8a. The simulated and measured reflection coefficients are also plotted in the figure.

The transfer function establishes the approximate behavior of each antenna, where the antenna is represented as a two-port component. Based on the transfer function measurement, the boresight gain varies from 5–7 dB from 2–3 GHz, which matches the behavior observed from the pattern measurements. The antenna gain is flat, and the antenna is well matched over the band of interest, which suggests the group delay of the antenna should be consistent over the frequency band. The measured group delay[1] verifies this assertion; it only varies by ±500 ps from 2–3 GHz, as shown in Figure 7.8b. This is comparable to the

[1] The group delay is calculated as $-\Delta\phi/\Delta\omega$ using the default parameters in ADS, where ϕ is the phase of the transfer function and ω is the angular frequency.

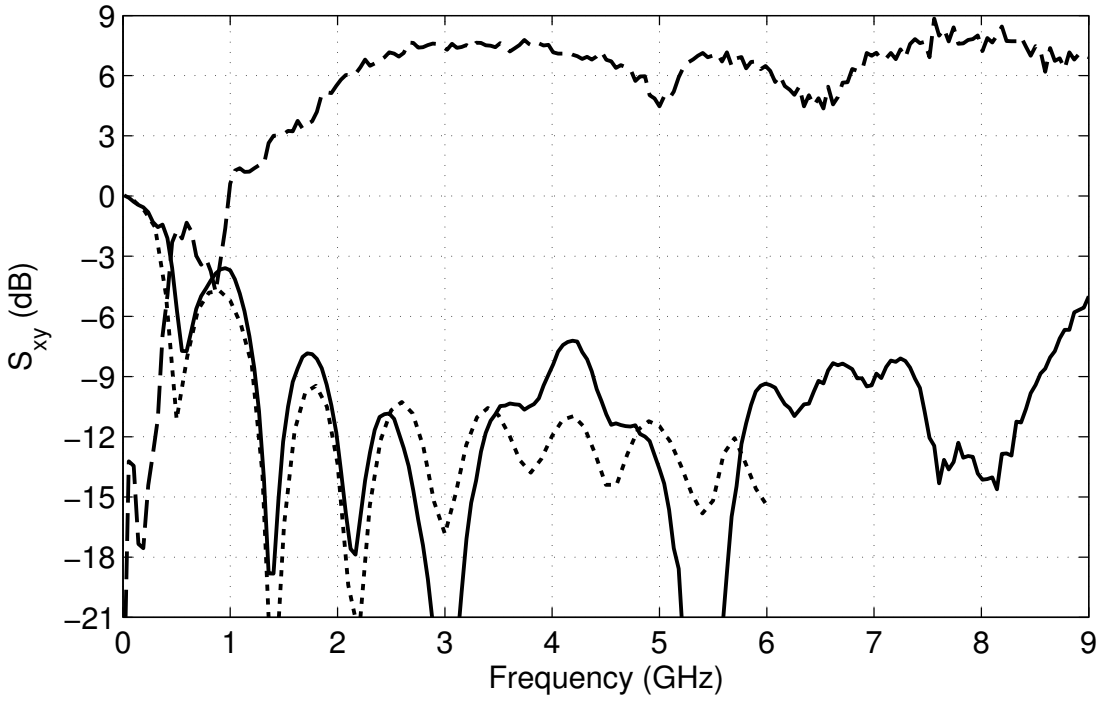

(a)

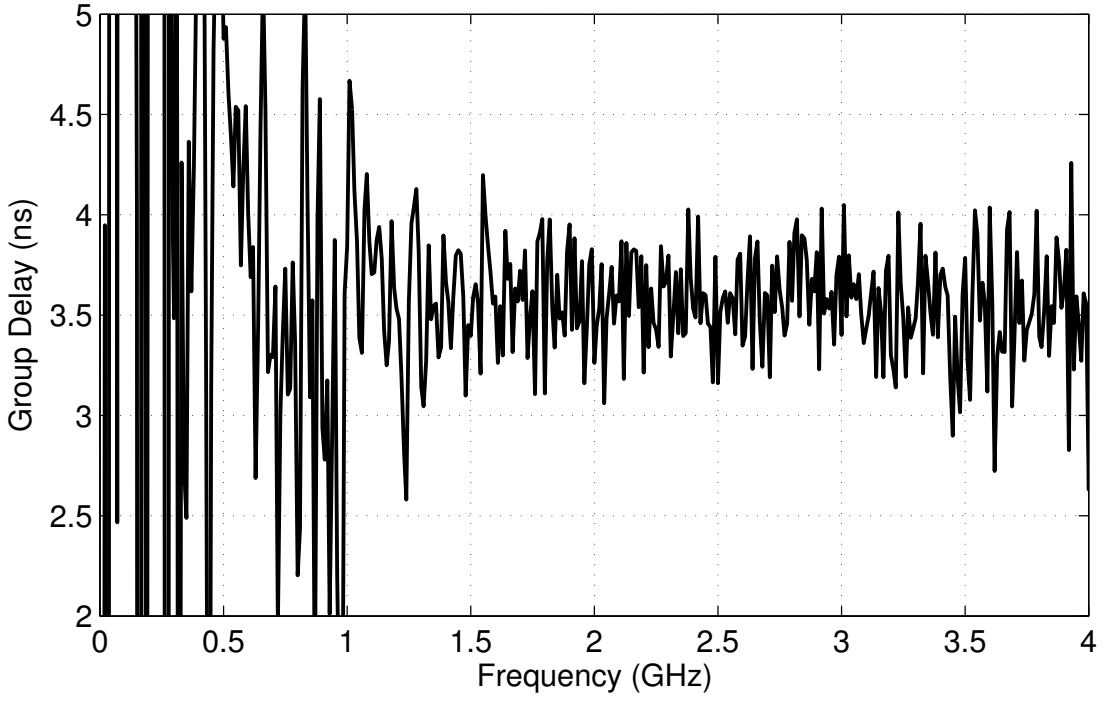

(b)

Figure 7.8: *Transfer Function and Return Loss.* The transfer function of the elliptically-tapered slot antenna was calculated from measured data and plotted with a dashed line in (a). The measured and simulated reflection coefficients are plotted in (a) in solid and dotted lines, respectively. The group delay, calculated from the transfer function, is plotted in (b).

group delay of other UWB antennas [112], [142], [143].

7.3.5 Measured Time-Domain Behavior

The time-domain behavior of the antenna system was measured using the transmitter and an oscilloscope. Two elliptically-tapered antennas were aligned to face one another at boresight, as shown in Figure 7.1a. The signal source was the transmitter, and the load was an oscilloscope. The transmitted and received waveforms are plotted in Figure 7.9. Based on the measured transfer function, the pulse envelope should undergo minimal distortion through the antenna system. As can be seen from the measured response, this is the case.

The distortion can be analyzed quantitatively using signal fidelity or by correlating the transmitted and received signals. The correlation coefficient is 0.93 for the measured transmitted and received signals in Figure 7.9, so the agreement between the waveshapes is excellent. The correlation coefficient was calculated using Pearson's linear correlation coefficient:

$$r = \frac{\sum_{i=1}^{N} \left(V_{TX,i} - \overline{V_{TX}}\right)\left(V_{in,i}^{RX} - \overline{V_{in}^{RX}}\right)}{(N-1)\sigma_{TX}\sigma_{TX}} \tag{7.25}$$

where r is the correlation coefficient, N is the number of time samples, V_{TX} and V_{in}^{RX} are the time vectors, $\overline{V_{TX}}$ and $\overline{V_{in}^{RX}}$ are the mean values of the vectors, and σ_{TX} and σ_{RX} are the covariance values of the vectors.

7.3.6 Improvements to Antenna System

A variety of techniques have been employed in the literature to improve upon the simple tapered slot antenna presented in this work. In [144], additional shaping was applied to the arms of a Vivaldi antenna to improve the bandwidth and provide additional control over the beamwidth. In [145], the authors added

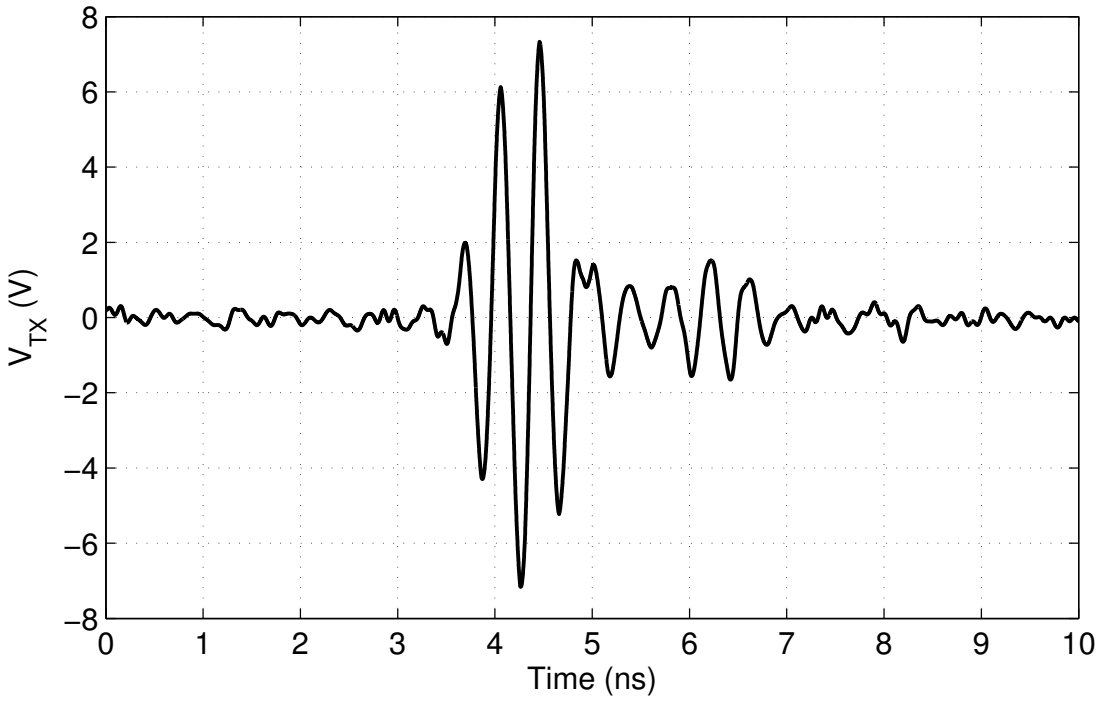

(a)

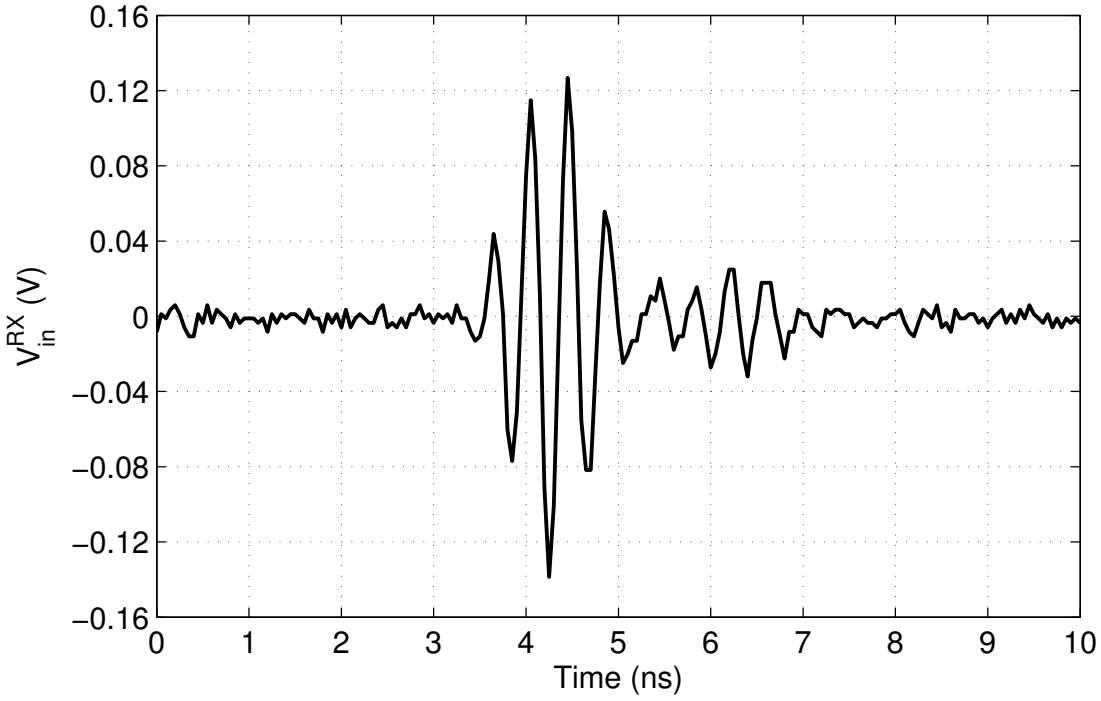

(b)

Figure 7.9: *Time-Domain Antenna System Behavior.* The transmitted and received time-domain waveforms are plotted in (a) and (b), respectively.

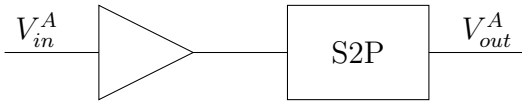

Figure 7.10: *Antenna Model.* The antenna can be modeled in a time-domain ADS simulation using a behavioral gain block and a passivated S-parameter block.

corrugations to the flat edges of the antenna arms to improve the bandwidth and front-to-back ratio of a standard Vivaldi antenna. [146] added diffractive gratings to a tapered slot antenna to improve the directivity of the antenna. In [147], a resistive coating was applied to a tapered slot antenna to improve the front-to-back ratio; resistive coatings are common in UWB antenna design [148]. [149] and [150] use crossed Vivaldi pairs for dual polarization. These techniques, as well as other antenna designs, should be considered based on the requirements for a specific UWB pulse Doppler radar application.

7.3.7 Antennas in System Model

The antenna system can be represented in the ADS channel model using a time differentiator and a pair of S-parameter blocks. The S-parameters are as follows: S_{11} and S_{22} are equal to the measured reflection coefficient of the antenna and S_{21} and S_{12} are equal to the measured transfer function. As discussed in Section 7.2.2, the time differentiator can be neglected for the radar system in this work. Since the system simulations are performed in the time domain, rather than the frequency domain, the S-parameter blocks should be passivated for use in the system model. A standard gain block can be placed before the S-parameter block to account for the antenna gain, as shown in Figure 7.10. The antenna model can be used for open-loop radar simulations.

Chapter 8

Closed-Loop UWB Radar Testing

The full UWB radar is presented in this chapter, including details of the physical setup and closed-loop radar testing results. The closed-loop channel model, which simulates the propagation channel, is repeated in Figure 8.1 for convenience.

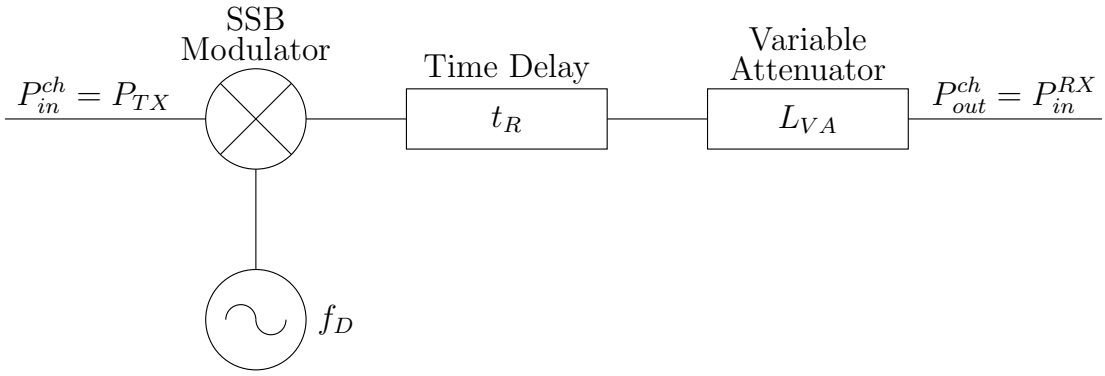

Figure 8.1: *Closed-Loop Channel Model.*

8.1 Closed-Loop Channel Model

The initial radar characterization was performed using closed-loop radar testing, as described in Section 3.6. Closed-loop testing provides a simple technique to analyze the basic radar operation without the added effects associated with a wireless link.

8.1.1 Components

The physical implementation of the closed-loop channel model is illustrated in Figure 8.2. The SSB modulator is implemented using a Polyphase Microwave QD2040B quadrature modulator. The simulated Doppler shift is generated using a pair of synchronized Hewlett Packard (HP) 3314A function generators. The I/Q outputs of the function generators can be adjusted from 0.001 Hz to 19.99 MHz. A 50 kHz Doppler shift was selected for this work to easily discriminate between the target return and the leakage signal, whose energy is centered at DC. The results of this chapter can easily be extended to lower Doppler shifts; however, it will be more difficult to differentiate between signal and leakage for low SNRs, making it more challenging to fully characterize the radar. The I/Q signals are amplified using a pair of National Semiconductor LMH6552 differential amplifiers and applied to the IF ports of the SSB modulator. The input of the SSB modulator is protected by a 20 dB attenuator. The modulator itself introduces an additional 24 dB of loss, resulting in a minimum closed-loop channel loss of 44 dB.

The time delay is implemented using coaxial cable and is used to simulate the round-trip propagation delay between the radar and the simulated target. The cable length can be adjusted to simulate various target ranges. The attenuation is implemented using a pair of 10 dB and 100 dB manually variable attenuators,

which can be adjusted from 0–110 dB in 1 dB steps. The attenuators simulate range losses, as well as any additional propagation losses. Including the SSB modulator loss, the closed-loop channel loss can be adjusted from 44–154 dB.

The coaxial cable introduces an additional loss of about 0.4 dB. The insertion loss of the attenuators varies with frequency and attenuation state; the average insertion loss for each attenuator is 0.4 dB. The additional losses will be accounted for when calculating the measured channel losses and theoretical SNRs in this thesis.

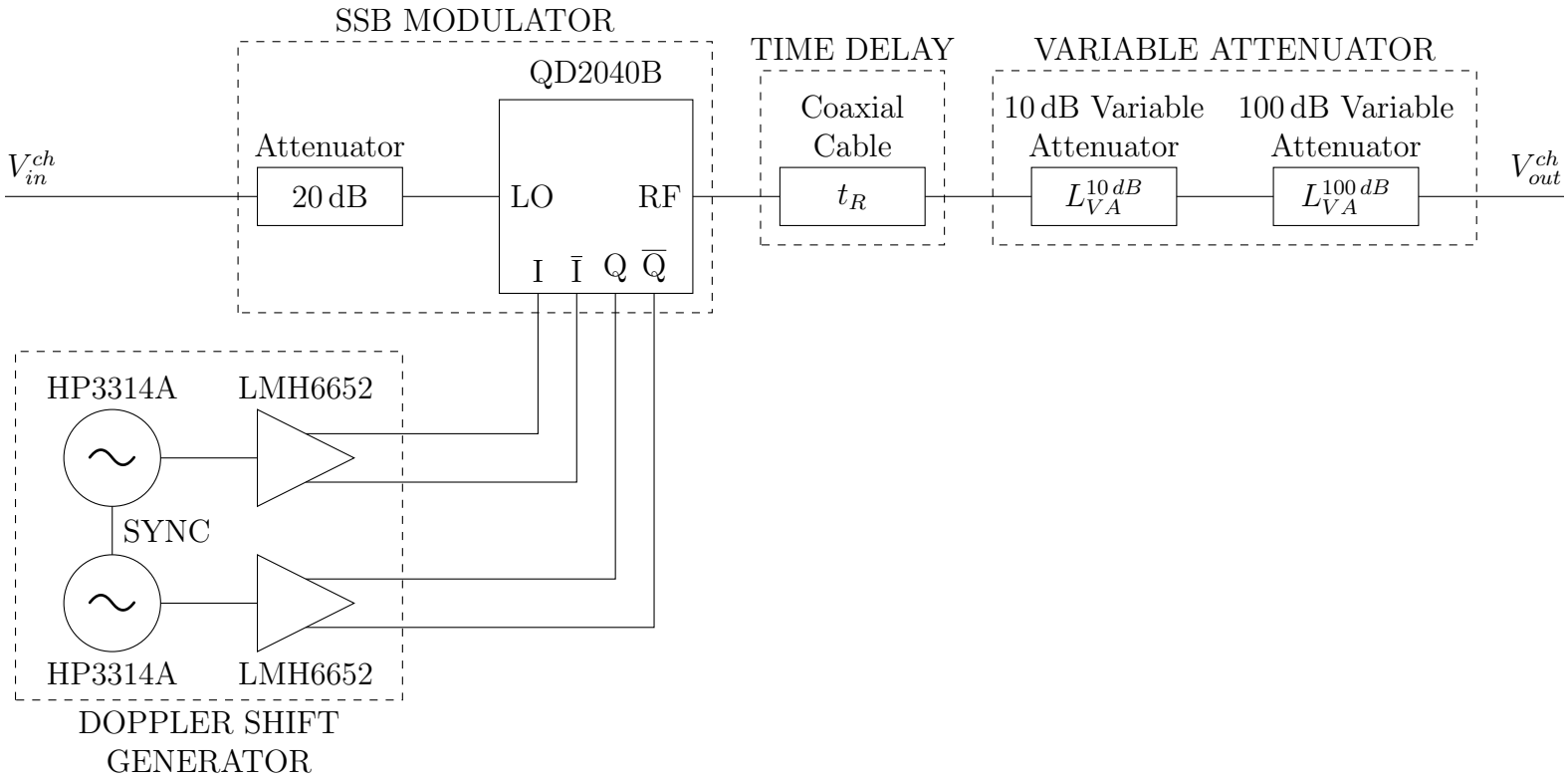

Figure 8.2: *Physical Closed-Loop Channel Model.* The full closed-loop channel model is shown. The SSB modulator is manufactured by Polyphase Microwave, the differential amplifiers are manufactured by National Semiconductor, and the function generators are manufactured by Hewlett Packard.

8.1.2 Channel Losses

The radar range equation was presented in Eqn. (1.3) and is repeated here for convenience:

$$P_{in}^{RX} = \frac{P_{TX} G_{A,TX} G_{A,RX} \lambda^2 \sigma}{(4\pi)^3 R^4 L_A^{ch} L_A^{sys}} \tag{8.1}$$

Based on the equation, the total channel loss is:

$$\begin{aligned} L_{ch} &= -10\log\left(\frac{G_{A,TX} G_{A,RX} \lambda^2}{4\pi}\right) + 20\log(4\pi R^2) + 10\log(L_A^{ch}) \\ &\quad \ldots - 10\log(\sigma)[\text{dB}] \end{aligned} \tag{8.2}$$

assuming the system losses are $L_A^{sys} = 0\,\text{dB}$. The first term is fixed for any given radar. Assuming $G_{A,TX} = G_{A,RX} = 0\,\text{dB}$ for the closed-loop channel model, the first term is equal to:

$$-10\log\left(\frac{G_{A,TX} G_{A,RX} \lambda^2}{4\pi}\right) = -10\log\left(\frac{c_o^2}{4\pi f_c^2}\right) = 29.4\,\text{dB} \tag{8.3}$$

The second term describes the range losses. The range losses at various ranges relevant to this work are summarized in Table 8.1.

The third term accounts for any additional channel losses resulting from propagation effects, and the fourth term accounts for the RCS of the target. Both terms depend on the application and environment. This thesis does not assume a specific application or environment, so these terms are difficult to predict. To illustrate the impact of the target shape, we consider a spherical target and a metallic plate. For simplicity, we assume the target is in the far field of the radar, and vice versa. Using the narrowband definition of the far-field, the maximum target dimension, D_{max}, for the radar described in this thesis is:

$$D_{max} = \sqrt{\frac{R\lambda}{2}} = \sqrt{\frac{R}{16.7}} \tag{8.4}$$

The maximum target dimension for various ranges is also listed in Table 8.1.

Table 8.1: Channel Losses: Spherical Target with Radius $D_{max}/2$

Range (m)	Range Losses (dB)	D_{max} (m)	Scattering Region	σ_{max} (m^2)	RCS Losses (dBsm)
3	41.1	0.42	Optical	~ 0.14	8.5
4	46.1	0.49	Optical	~ 0.19	7.3
5	49.9	0.55	Optical	~ 0.24	6.3
6	53.1	0.60	Optical	~ 0.28	5.5
7	55.8	0.65	Optical	~ 0.33	4.8

First, consider a spherical target of radius $D_{max}/2$. As discussed in Section 1.2.3, the target behavior can be divided into the Rayleigh, optics, and resonance scattering regions based on the circumference of the target. The scattering region, approximate RCS, and RCS losses for a spherical target of radius $D_{max}/2$ at various ranges are also summarized in Table 8.1. As seen in the table, the maximum size spherical target behaves as an optical reflector, and the RCS is on the order of 0.1 m. If the spherical target is smaller, the RCS will decrease and the RCS losses will increase, resulting in greater channel loss.

Now consider a square, metallic plate oriented in the plane transverse to the radar signal's propagation vector. In this case, the reflection from the target is specular and the RCS can be approximated as $\sigma = 4\pi A^2/\lambda^2$, where A is the area of the plate [151]. The RCS and RCS losses for the metal plate are summarized in Table 8.2, assuming the width and height of the plate are equal to D_{max}. The specular reflection from the metallic plate is quite directional and reduces quickly as the angle of incidence changes [151]. As a result, the peak RCS for a metallic plate is quite large compared to a spherical target. For the conditions in the table, the RCS is greater than 1 m^2, resulting in negative RCS losses.

Based on the RCS calculations for a spherical target and a metallic plate, it is easy to see that without a specific target in mind, the impact of the target on the overall channel losses is difficult to predict. It is also difficult to predict any

Table 8.2: Channel Losses: Metallic Plate Target with Width and Height of D_{max}

Range (m)	D_{max} (m)	σ_{max} (m^2)	RCS Losses (dBsm)
3	0.42	28.2	-14.5
4	0.49	50.1	-17.0
5	0.55	78.2	-18.9
6	0.60	112.6	-20.5
7	0.65	153.3	-21.9

additional losses without specifying an application or environment. As such, the radar characterization in this thesis will assume total channel loss values and will not specify how the loss is distributed among the various loss mechanisms. The total channel loss for the closed-loop radar model in this thesis is:

$$L_{ch} = 20\,\text{dB} + L_{SSB} + L_{cable} + L_{VA}^{10dB} + L_{VA}^{100dB}[\text{dB}] \tag{8.5}$$

where $L_{SSB} = 24\,\text{dB}$ is the loss of the SSB modulator, L_{cable} is the loss of the cable used to simulate the time delay, L_{VA}^{10dB} is the attenuation of the 10 dB variable attenuator, and L_{VA}^{100dB} is the attenuation of the 100 dB variable attenuator; the remaining 20 dB of channel loss is due to the 20 dB attenuator included at the input of the SSB modulator.

8.2 UWB Radar Setup Considerations

As discussed in Chapter 3, the full UWB radar consists of a transmitter (see Chapters 4 and 5), receiver (see Chapter 6), antenna system (see Chapter 7), digital control circuit (see Section 3.4), post processor (see Section 3.5), and channel (see Section 3.6). Integrating the subsystems requires additional characterization and is addressed in the following sections.

8.2.1 Timing

Relative time delays play an important role in the UWB radar design in this work. First, the time delay between the peak of the transmitted pulse and the middle of the range gate must be set to select a specific observable target range, as illustrated in Figure 8.3. The time delay corresponding to observable range R_{obs} is $t_R^{obs} = 2R_{obs}/c_o$; the delay must be characterized for each desired observable range. The time-delay characterization can be performed using closed-loop testing. Referring to Figure 8.1, the time delay of the channel model is set to match the desired observable range, so $t_R = t_R^{obs}$. Next, the time delay of the range gate control signals, RG and $\overline{\text{RG}}$, is adjusted so the peak of the received signal corresponds to the center of the range gate, as shown in the figure.

It is also important to characterize the time delay between the digitizer's external clock and the output of the receiver. The digitizer samples the output of the receiver at each rising edge of the sample clock, so the time delay must be adjusted to ensure the sample point coincides with the peak of the received signal. Like the time delay for the range gate control signals, the time delay for the sample clock must be characterized for each desired observable range. Since the transmitted pulse has a subnanosecond pulsewidth, it is critical to align the sample point accurately; if the pulse is not sampled at its maximum amplitude, the measured SNR will be degraded due to sampling losses [16]. The sampling loss can be as high as 2–3 dB for high probability of detection (0.9–0.95) when a single sample per PRI is taken [152]. This work assumes a single sample per PRI and a probability of detection of 0.99, so the sampling loss can be significant. Sampling loss contributes to the overall system losses and can be accounted for in the radar range equation as discussed in Section 1.2.

The transition point of the BPSK phase code is also important in both the transmitter and the post processor. Consider the transmitter block diagram

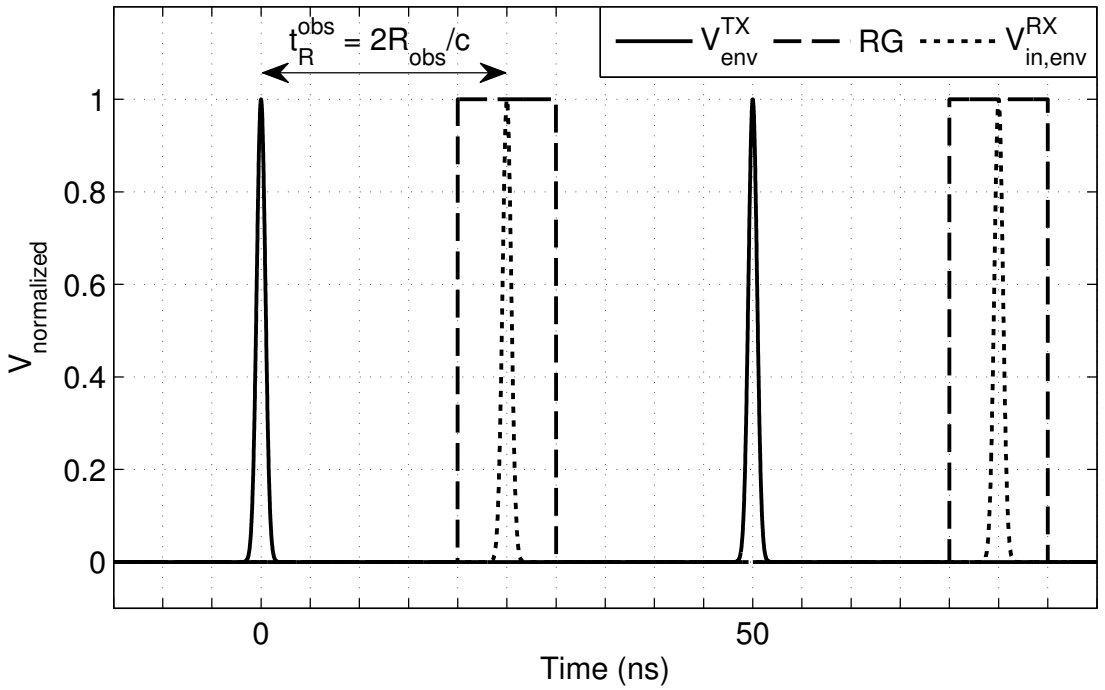

Figure 8.3: *Range Gate Timing.* The relative time delay between the peak of the transmitted pulse envelope, V_{env}^{TX} in the figure, and the center of the range gate, is set by the control signals RG and $\overline{\text{RG}}$ and determines the observable target range. The peak of the received signal, $V_{in,env}^{RX}$ in the figure, should align with the middle of the range gate.

in Figure 3.2. The phase code is applied to the carrier signal using the BPSK modulator and controls the polarity of the pulse envelope. The phase code must transition during the off-time of the transmitted pulse to ensure the phase code is consistent throughout each transmitted pulse. The BPSK signal is sampled by the post processor; the signal is sampled once per PRI and must not be sampled at the transition point.

8.2.2 Leakage Signals

As discussed in Section 3.7, the desired minimum detectable SNR is -13.5 dBm, which corresponds to a received power of $P_{in}^{RX} = -86$ dBm. For this case, the channel loss is $L_{max}^{ch} = 113$ dB, so the received signal is over eleven orders of

magnitude smaller than the transmitted signal. As a result, small leakage signals can have a significant impact on radar performance and must be minimized. Leakage signals arise from a variety of sources:

- *Radiative and Direct Leakage Paths.* Radiative leakage paths refer to paths between transmitter components that radiate low-level signals and receiver components that receive those signals. Most microwave components radiate unintentionally and at a low level; however, radiative leakage paths are a concern due to the large disparity between the transmitted and received signal power levels. Direct leakage paths result from wired connections between the transmitter and receiver. For example, the transmitter and receiver in this work share a VCO, so a direct leakage path exists through the VCO. The transmitter and receiver are also directly linked through the FPGA and the DC supplies. It is difficult to separate radiative and direct leakage paths, and the two will be lumped under the term "radiative leakage paths" for the remainder of this thesis.

- *Channel Model Feed-Through Leakage Path.* Figure 8.1 illustrates a closed-loop channel model, which uses a SSB modulator to simulate the Doppler shift. Mixers have finite port-to-port isolations; for the SSB modulator in this work, the LO to RF isolation is about 35–40 dB. As a result, the output of the modulator will have frequency components at $f_c + f_D$ (or $f_c - f_D$) and f_c. Only the Doppler-shifted component is desired, so the component at f_c is a leakage signal. The leakage path through the SSB modulator exists for any test setup in which the Doppler shift is simulated using a mixer, such as the open-loop channel model in Figure 3.6. While it does not exist for a radar system under real operating conditions, it should be quantified.

- *Antenna System Leakage Path.* As discussed in Sections 3.7.2 and 7.3.3, a finite isolation exists between the transmitter and receiver due to coupling between the transmit and receive antennas. This leakage path depends on the antenna system design and tends to be the largest of the three leakage paths noted here. The antenna system leakage path will limit the minimum range of the radar and will be discussed in more detail in Section 8.7.

- *Clutter and Multipath.* Strictly speaking, clutter and multipath are not leakage signals. However, clutter and multipath can mask target returns or contribute to false alarms, and the effects must be mitigated. The pulsed nature of the receiver helps mitigate these effects as it attenuates any received clutter or multipath signals when the receiver is off, which is $[100(T - \tau_{RG})/T]\%$ of the time.

In order to separate the various leakage effects, three types of leakage signals are considered in this work: phase-coded, unmodulated, and Doppler-modulated leakage signals. Phase-coded leakage signals are modulated with the BPSK phase code, while unmodulated leakage signals are not. Doppler-modulated leakage signals are modulated with both the BPSK phase code and a Doppler shift.

Radiative leakage signals are typically unmodulated or phase-coded. For the radar in this work, unmodulated radiative leakage signals can originate from transmitter components prior to the BPSK modulator, such as the LO (see Figure 3.2). Phase-coded leakage paths can originate from the BPSK modulator, switch, mixer, or switched PA. The FPGA's BPSK output could also serve as an origin for a radiative phase-coded leakage path; however, it operates at 20 MHz, which is very low frequency compared to the 2.5 GHz carrier. For an electrically small component, the radiation efficiency is typically lower at 20 MHz than 2.5 GHz; as such, the focus of this work is to minimize radiative leakage from the transmitter

components at the LO frequency.

The 2.5 GHz radiative leakage paths terminate in the receiver's RF front end; referring to Figure 3.3, the leakage signal could be received by the range gate, the RF LNA, or the mixer. Both the phase-coded and unmodulated radiative leakage signals are downconverted to DC and sampled by the post processor. As discussed in Section 3.5, the DC component is subtracted from the sampled signal. This step is primarily performed to remove any DC offset resulting from the ADC; however, it also reduces the unmodulated 2.5 GHz leakage signal. The phase-coded leakage signal is minimally affected by this step as its mean is approximately 0 V. Next, the sampled signal is correlated with the BPSK phase-code. The phase-coded leakage signal will correlate well with the BPSK signal, and the calculated PSD will include a DC frequency component whose power corresponds to the radiative leakage power. The unmodulated leakage signal will not correlate well with the BPSK signal, so any remaining unmodulated leakage power will be distributed throughout the calculated PSD, resulting in a noise-like spectrum. As such, low-level unmodulated leakage signals are difficult to detect and of minimal concern. However, if the leakage signal power is high enough, the noise floor of the PSD will be higher than the theoretical noise floor, leading to reduced radar sensitivity.

Channel model feed-through leakage is phase-code modulated. Like radiative phase-coded leakage signals, it can be detected by examining the calculated PSD, as it will contribute to the DC component of the spectrum.

Antenna system leakage is phase-coded and can be Doppler-modulated. If the leakage is only phase-coded, it will contribute to the DC component of the calculated PSD. If it is also Doppler-modulated, which can occur if the radar system is airborne, it will be visible in the PSD as a spectral component offset from DC. The power level of the spectral component will match the signal power

of the leakage signal and will depend on the TX-RX isolation of antenna system.

Like antenna system leakage, clutter and multipath are phase-coded and can be Doppler-modulated. If it is only phase-coded, the clutter or multipath signal corresponds to a stationary target; if it is Doppler-modulated, it corresponds to a moving target. Clutter and multipath are difficult to predict, whereas the other leakage mechanisms can generally be characterized through closed- or open-loop testing, as will be discussed in Section 8.3.

The radar in this work assumes a moving target, and any stationary targets are ignored. As a result, phased-coded leakage can be ignored, since it will look like a stationary target ($f_D = 0\,\text{Hz}$). However, it can limit the sensitivity of the radar for low Doppler frequencies, as will be illustrated in Section 8.3. Doppler-modulated leakage signals are more problematic than phase-coded leakage signals since they contribute leakage signal power at frequencies that could correspond to moving targets. Since Doppler-modulated leakage signals can arise from antenna system leakage paths, we assume the antenna system leakage signal is Doppler-modulated for closed-loop testing. This assumption allows the simulated antenna system leakage to be separated from the other leakage sources. As a result, it simplifies the time-domain SNR response measurement and the determination of the minimum range and minimum TX-RX isolation of the radar.

Mitigating Leakage Signals

The radar components were arranged to maximize the distance between the transmitter and receiver components, given a set test-bench area, in order to minimize the radiative coupling between the components. Every component in the radar system that operates in the S-band is packaged in a metal box or a commercial package, as illustrated in Figure 8.4. The metal boxes provide

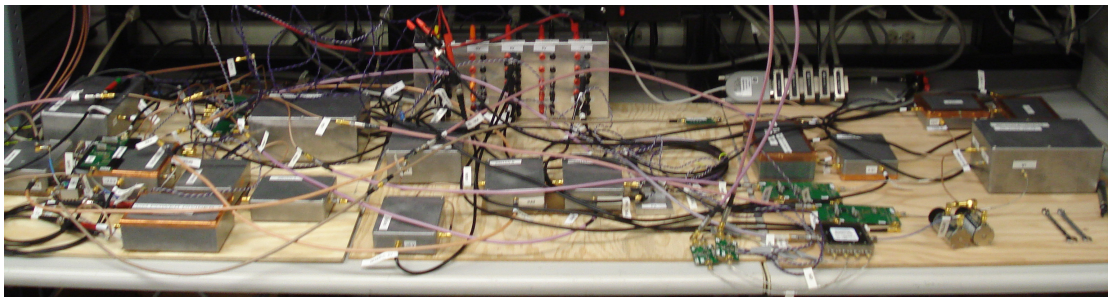

Figure 8.4: *Closed-Loop Radar System Test Bench.* The closed-loop radar test bench is illustrated. Each of the components that operates in the S-band is enclosed in a metal box.

shielding for the components within, but the box seams and connectors are also potential sources of radiative leakage. The box seams are sealed with copper tape, as needed, to reduce the radiative leakage paths. Each box includes SMA feed-through connectors for both the RF and DC ports to reduce the radiative leakage due to the connectors; emissions from connector assemblies have been studied in the electromagnetic interference (EMI) and electromagnetic compatibility (EMC) literature [153]. Some of the boxes are large enough to act as resonant cavities at S-band, so absorber was included in the boxes to reduce the Q-factor and eliminate the possibility of undesired oscillations.

8.3 Radiative and Channel Model Feed-Through Leakage

Two measurements were performed to determine the impact of radiative and channel model feed-through leakage. First, the transmitter's output and the receiver's input were terminated in 50 Ω, and the radar was powered on. With this test setup, the radiative leakage signals are isolated, and the calculated PSD is a measure of system noise and radiative leakage. The calculated PSD is

plotted in Figure 8.5; the PSDs were calculated using one million samples and seven hundred thirty samples. As can be calculated from the PSDs, the radiative leakage power is approximately -28.7 dBm.

The radiative phase-coded leakage power can limit the sensitivity of the radar, depending on the number of integrated samples. For one million samples, the leakage power is concentrated around DC, and the frequency resolution is fine enough that the leakage signal will not severely limit the sensitivity of the radar, as seen in Figure 8.5a. However, the number of pulses that can be integrated is limited for moving targets, as discussed in Section 3.6.1. Assuming a single-channel receiver with a static sampler, seven hundred thirty samples is a worst-case example of the number of samples that can be integrated for the transmitted waveform in this work. As can be seen from Figure 8.5b, the leakage energy is spread over a wider range of frequencies than for the one million samples case since the frequency resolution is lower for fewer samples. As a result, the leakage signal effectively raises the noise floor and can reduce the sensitivity of the radar for lower Doppler shifts; the impact is more significant for lower Doppler shifts.

The second type of leakage measurements were taken with the closed-loop channel model in place. The time delay of the channel model was set to model a target at the desired observable range, so $R = R_{obs}$. The simulated Doppler shift was set to 50 kHz, and the channel attenuation was adjusted from $L_{ch} = 70$ dB to $L_{ch} = 110$ dB in 5 dB steps. The full-scale voltage of the digitizer, V_{fs}, was set based on the maximum anticipated voltage for each attenuation state, and the values for the measurements in this thesis are listed in Table 8.3; the measured channel attenuation is also listed. Three digitized data sets were recorded at each attenuation step, and the results were processed using one million samples. As discussed, the combination of the radiative leakage signal and the channel

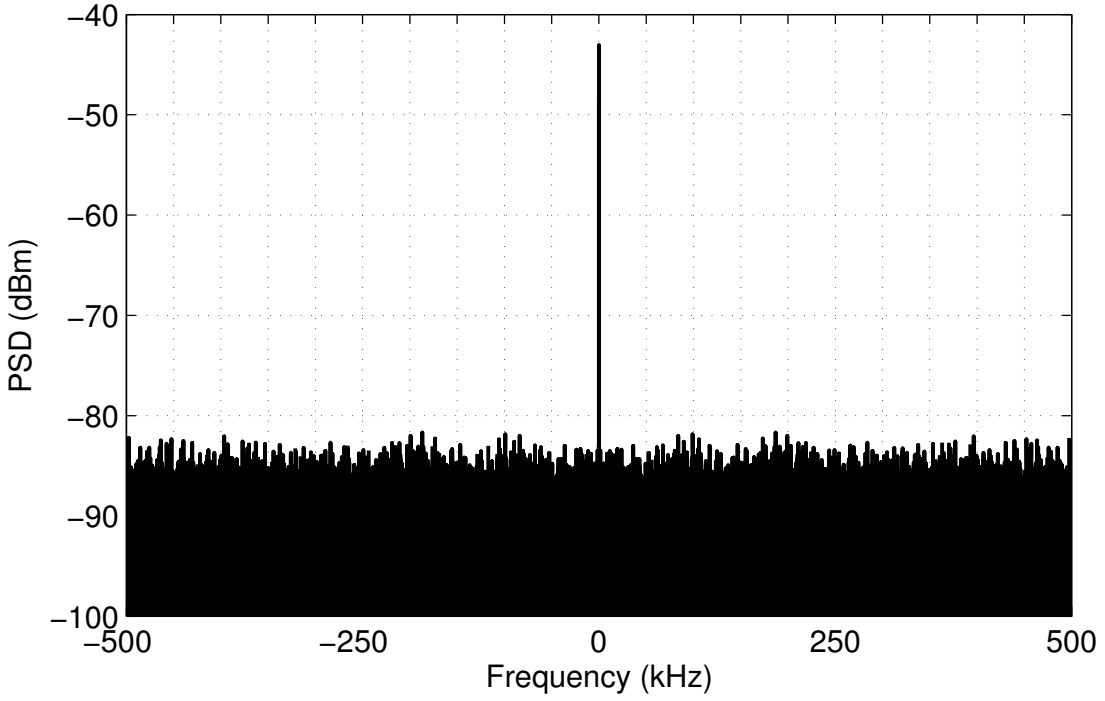

(a)

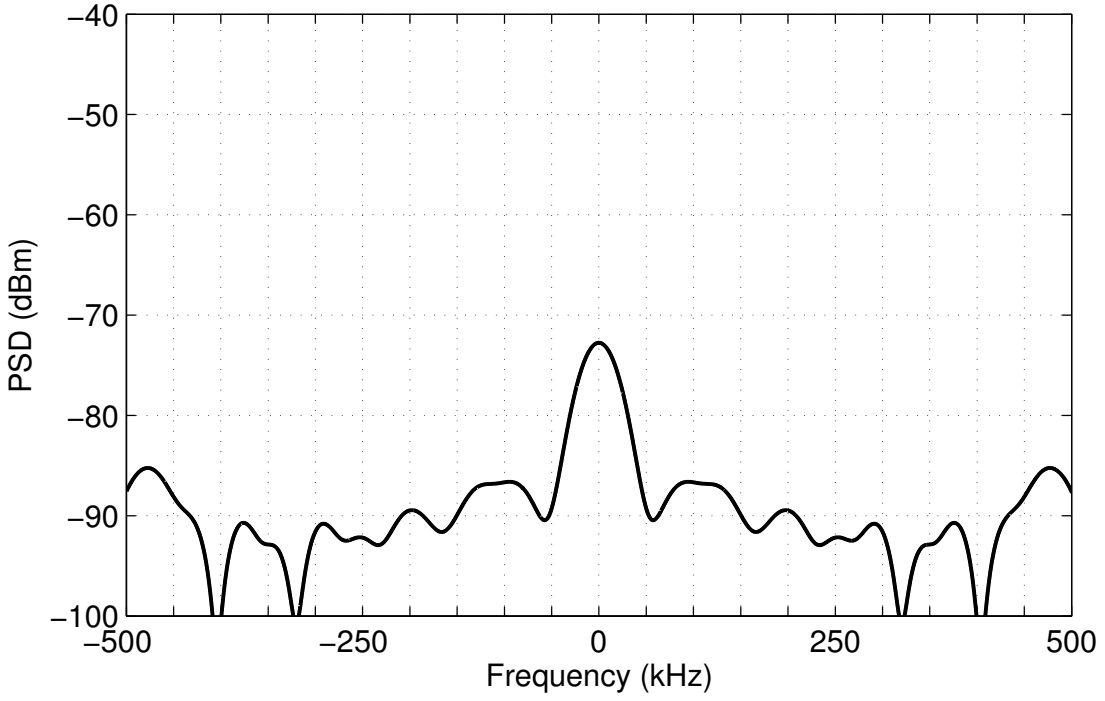

(b)

Figure 8.5: *Radiative Leakage.* The radiative leakage was measured by terminating the transmitter's output and the receiver's input in 50 Ω and sampling the output of the receiver. The PSD is calculated using one million samples (a) and seven hundred thirty samples (b). The digitizer's full-scale voltage range was set to 1 V.

Table 8.3: Channel Attenuation and Full-Scale Voltage of Digitizer

Nominal L_{ch} (dB)	Measured L_{ch} (dB)	V_{fs} (V)
70	70.0	5
75	75.1	5
80	80.0	2
85	84.9	2
90	89.8	1
95	94.7	1
100	99.6	0.5
105	104.9	0.5
110	109.8	0.5

Table 8.4: Radiative and Channel-Model Feed-Through Leakage Measurements

Nominal L_{ch} (dB)	Total Leakage Power (dBm)
70	-18.8
75	-19.7
80	-17.3
85	-19.4
90	-16.5
95	-20.3
100	-18.4
105	-18.4
110	-19.8

model feed-through leakage signal can be observed as the DC component of the calculated PSD. The total measured leakage power is the average of the leakage power calculated from the three data sets for each attenuation state and is tabulated in Table 8.4.

The total leakage power is roughly constant for the various channel attenuations; the average leakage power is -19.0 dBm and varies by ±2.5 dB. This suggests radiative leakage dominates over channel-model feed-through leakage. If the reverse were true, the total leakage power would decrease linearly with increasing channel attenuation. It is interesting to note the total leakage power is about 10 dB higher than for the radiative leakage only measurement. This

suggests that connecting the closed-loop channel model to the output and input of the transmitter and receiver creates additional coupling paths and increases the radiative leakage strength.

8.4 Single-Pulse SNRs and Radar Losses

As discussed in Section 3.7.1, part of the radar characterization is determining the single-pulse SNR for several channel attenuation states. The single-pulse SNR is the SNR at the output of the receiver and corresponds to the SNR that would be calculated by the post processor if a single pulse was employed. The single-pulse SNR can be related directly to the characteristics of the transmitter, channel, and receiver, making it simpler to back out radar characteristics like radar losses.

For this measurement, the time delay of the channel model was set to model a target at the desired observable range, so $R = R_{obs}$. The simulated Doppler shift was set to 50 kHz, and the channel attenuation was adjusted from $L_{ch} = 70$ dB to $L_{ch} = 110$ dB in 5 dB steps. Three digitized data sets were recorded at each attenuation step, and the results were processed using one million samples. The three calculated SNRs were averaged for each attenuation state. The theoretical and measured single-pulse SNRs for each attenuation state are tabulated in Table 8.5. The theoretical single-pulse SNR is calculated using the following expression:

$$\mathrm{SNR}_1^{out} = P_{TX} - L_{ch} - P_N - F_{pulsed}^{RX}[\mathrm{dB}] \tag{8.6}$$

where L_{ch} is the measured channel loss, $P_N = -87$ dBm is the noise power at the input of the receiver, and $F_{pulsed}^{RX} = 14.8$ dB is the noise figure of the receiver. The rms transmitted power is approximately:

$$P_{TX} = 10\log\left(\frac{(V_{on}^{TX})^2}{2Z_o}\frac{1}{1\,\mathrm{mW}}\right)[\mathrm{dBm}] \tag{8.7}$$

Table 8.5: Theoretical and Measured Single-Pulse SNRs (N = 1E6)

Nominal L_{ch} (dB)	Theoretical SNR_1^{out} (dB)	Measured SNR_1^{pp}(dB)	SNR_{error} (dB)
70	29.9	13.4	16.5
75	24.8	12.2	12.6
80	18.9	8.9	10.0
85	15.0	5.6	9.4
90	10.1	-0.2	10.3
95	5.2	-3.2	8.4
100	0.3	-8.9	9.2
105	-5.0	-13.1	8.1
110	-9.9	-18.6	8.7

The measured single-pulse SNR is calculated as discussed in Section 3.5:

$$\text{SNR}_1^{pp} = 10\log\left(\frac{P_S^{pp}}{P_N^{pp}}\right)[\text{dB}] \tag{8.8}$$

where P_S^{pp} and P_N^{pp} are the signal power and noise power calculated from the measured PSD. There is a significant discrepancy, up to 17 dB, between the theoretical and measured SNRs. To determine the sources of the error, the signal and noise powers are discussed separately in the following sections.

8.4.1 Signal Power

The theoretical and measured signal powers are summarized in Table 8.6. The theoretical value is calculated as:

$$P_{out,S}^{RX} = P_{TX} - L_{ch} + G_{pulsed}^{RX}[\text{dBm}] \tag{8.9}$$

where $P_{out,S}^{RX}$ is the signal power at the output of the receiver and $G_{pulsed}^{RX} = 52$ dB is the gain of the receiver. As discussed in Section 3.5, the measured signal power is calculated as follows:

$$P_S^{pp} = \int_{-f_{sig}-\beta_{int}/2}^{-f_{sig}+\beta_{int}/2} P_{pp}(f)df + \int_{f_{sig}-\beta_{int}/2}^{f_{sig}+\beta_{int}/2} P_{pp}(f)df \tag{8.10}$$

Table 8.6: Theoretical and Measured Signal Power (N = 1E6)

Nominal L_{ch} (dB)	Theoretical $P_{out,S}^{RX}$ (dBm)	Measured P_S^{pp} (dBm)	Signal Power Error (dB)
70	9.7	6.8	2.9
75	4.6	1.5	3.1
80	-0.3	-3.6	3.3
85	-5.2	-9.0	3.8
90	-10.1	-13.9	3.8
95	-15.0	-19.4	4.4
100	-19.9	-24.0	4.1
105	-25.2	-29.8	4.6
110	-30.1	-34.2	4.1

where $P_{pp}(f)$ is the PSD calculated from the measured data set, f_{sig} is the signal frequency, and β_{int} is the integration bandwidth.

As seen in the table, the measured signal power is on average 3.8 dB lower than the theoretical signal power. The measured signal power does, however, decrease linearly with increasing channel attenuation; the signal power error, which is the difference between the theoretical and measured signal power, only varies from its mean value of 3.8 dB by ±0.9 dB.

The signal power error indicates that there are radar loss mechanisms, such as sampling loss, that have not been accounted for in the theoretical signal power calculation. As discussed in Section 8.2.1, sampling losses result when the pulsed signal is not sampled at its maximum amplitude.

The impact of sampling loss can be estimated using the test setup in Figure 8.6 along with the single-pulse SNR measurements. The oscilloscope in the test setup is triggered by the FPGA and set to infinite persistence to determine the peak voltage at the output of the receiver. The peak voltage is listed in Table 8.7 for various attenuation states; only attenuation states that result in a positive SNR were considered. The peak sampled voltage, taken from the measured data sets, and the approximate sampling loss for each case are also recorded in the

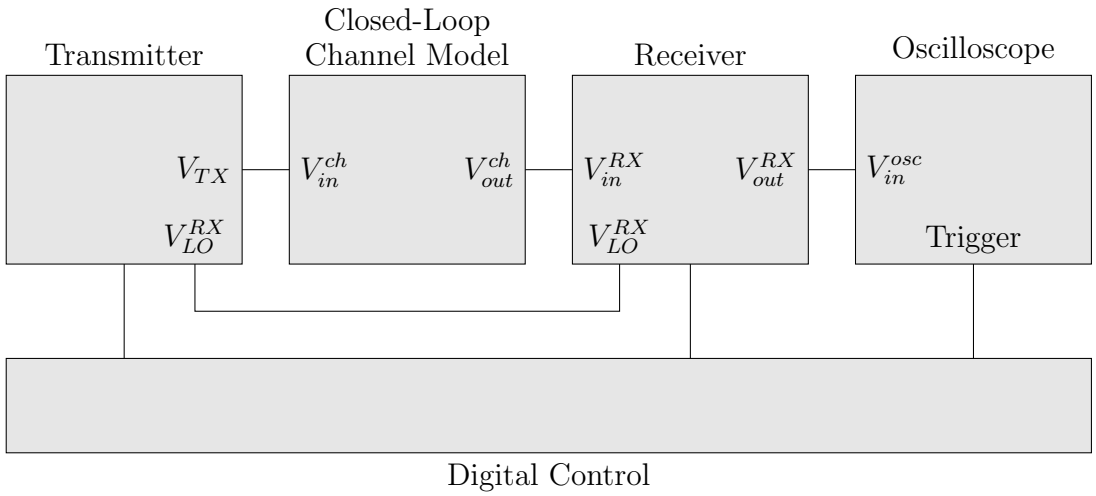

Figure 8.6: *Radar Loss Test Setup.* The test setup, along with the standard closed-loop radar test setup, is used to determine the radar losses due to sampling loss.

table. The average measured sampling loss is 1.6 dB. As discussed in Section 8.2.1, the sampling loss can be as high as 2–3 dB for the radar described in this work, so the measured loss is on par with the expected sampling loss.

Additional radar loss mechanisms in the closed-loop radar test setup include interconnection loss (e.g. power loss in coaxial connections), nonmatched filter loss, straddling loss, and other signal processing losses [16]. Based on the sampling loss measurements, the additional loss mechanisms can contribute 1–3 dB to the total radar loss. It is anticipated that the radar loss will degrade the minimum detectable single-pulse SNR of the radar from its expected value of -13.6 dB by 3–4 dB.

Table 8.7: Sampling Loss

Nominal L_{ch} (dB)	Oscilloscope: $V_{out,p}^{RX}$ (V)	Post Processor: P_p^{pp} (V)	Sampling Loss (dB)
70	1.1	0.86	2.1
75	0.70	0.60	1.3
80	0.45	0.38	1.5

8.4.2 Noise Power

The theoretical and measured noise powers are summarized in Table 8.8. The theoretical noise power is calculated as:

$$P_{out,N}^{RX} = P_N + G_{pulsed}^{RX} + F_{pulsed}^{RX}[\text{dBm}] \tag{8.11}$$

where $P_{out,N}^{RX}$ is the noise power at the output of the receiver. As discussed in Section 3.5, the measured noise power can be calculated as:

$$P_N^{pp} = \int_{-f_s/2}^{f_s/2} P_{pp}(f)df - P_S^{pp} \tag{8.12}$$

where f_s is the sample rate of the digitizer and P_S^{pp} is defined in Eqn. (8.10).

The noise power should be constant for all channel attenuation states; however, as seen in the table, the calculated noise power varies significantly with attenuation. The calculated noise power is much higher than expected for low attenuation states and approaches an average value of -16.0 dBm when the channel attenuation is at least 95 dB.

First, consider the low channel attenuation states ($L_{ch} \leq 90$ dB). As seen from Eqn. (8.12), the calculated noise power is the total power minus the calculated signal power. As a result, any distortion or leakage will contribute to the average noise power even though, strictly speaking, distortion is not noise. Typically, the distortion terms are subtracted from total noise power when computing the SNR; if they are not, the SNR will be somewhat degraded and is more accurately referred to as the signal-to-noise-and-distortion ratio (SINAD) [65]. Technically,

Table 8.8: Theoretical and Measured Noise Power (N = 1E6)

Nominal L_{ch} (dB)	Theoretical $P_{out,N}^{RX}$ (dBm)	Measured P_N^{pp} (dBm)	Noise Power Error (dB)
70	-20.2	-6.5	13.7
75	-20.2	-10.4	9.8
80	-20.2	-12.5	7.7
85	-20.2	-14.6	5.6
90	-20.2	-13.8	6.4
95	-20.2	-16.2	4.0
100	-20.2	-15.1	5.1
105	-20.2	-16.7	3.5
110	-20.2	-15.6	4.6

the measured "SNR" in this work is SINAD, but is referred to as SNR throughout the thesis.

The calculated PSD for $L_{ch} = 70$ dB is plotted in Figure 8.7a. The signal frequency is 50 kHz, and strong distortion components are visible at the odd harmonics of the signal. The distortion components and leakage raise the average noise power from the theoretical -20.2 dBm to -6.5 dBm when $L_{ch} = 70$ dB.

For comparison, the PSD for $L_{ch} = 90$ dB is plotted in Figure 8.7b. The third-harmonic distortion components are evident in the spectrum, but the higher-order distortion components are near the noise floor of the spectrum. As a result, the theoretical and calculated noise powers agree more closely than for lower channel attenuation states (see Table 8.8).

Now consider the high channel attenuation states ($L_{ch} \geq 95$ dB). The PSD for $L_{ch} = 95$ dB is plotted in Figure 8.8. The third-harmonic distortion power is approximately -40 dBc relative to the fundamental signal power and has little impact on the calculated noise power. The DC leakage contribution, however, is considerable. Referring to Table 8.4, the average leakage power is -19.0 dBm and is comparable to the theoretical noise power of -20.2 dBm; as such, when distortion does not play a significant role, the average noise power will be

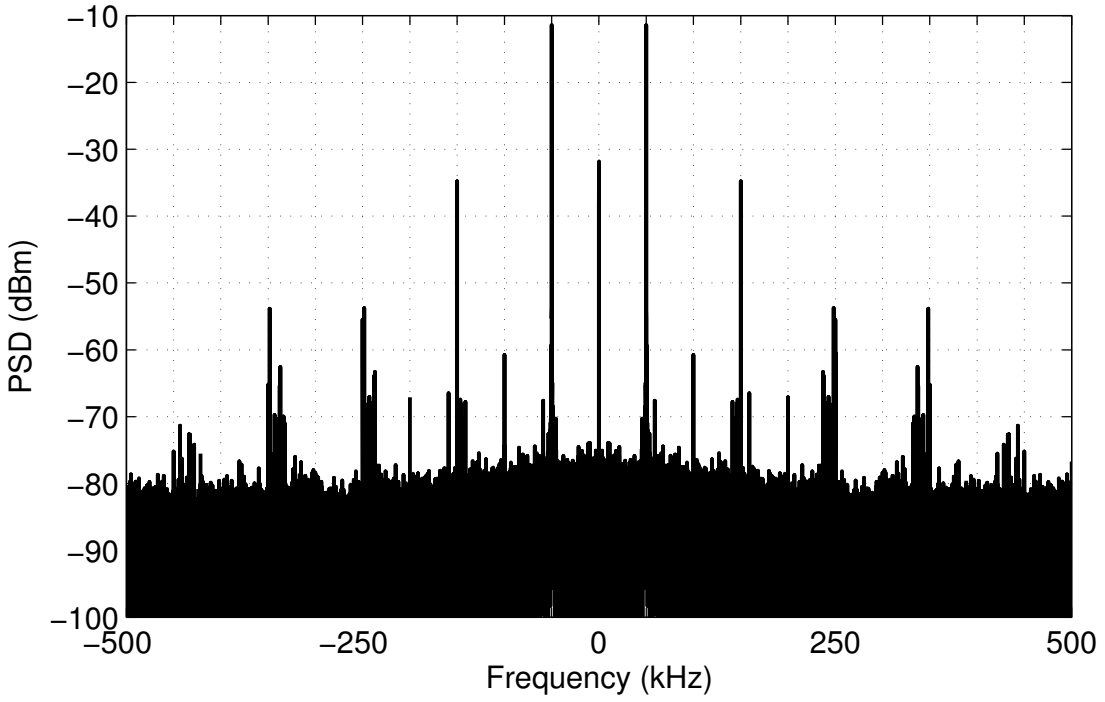

(a)

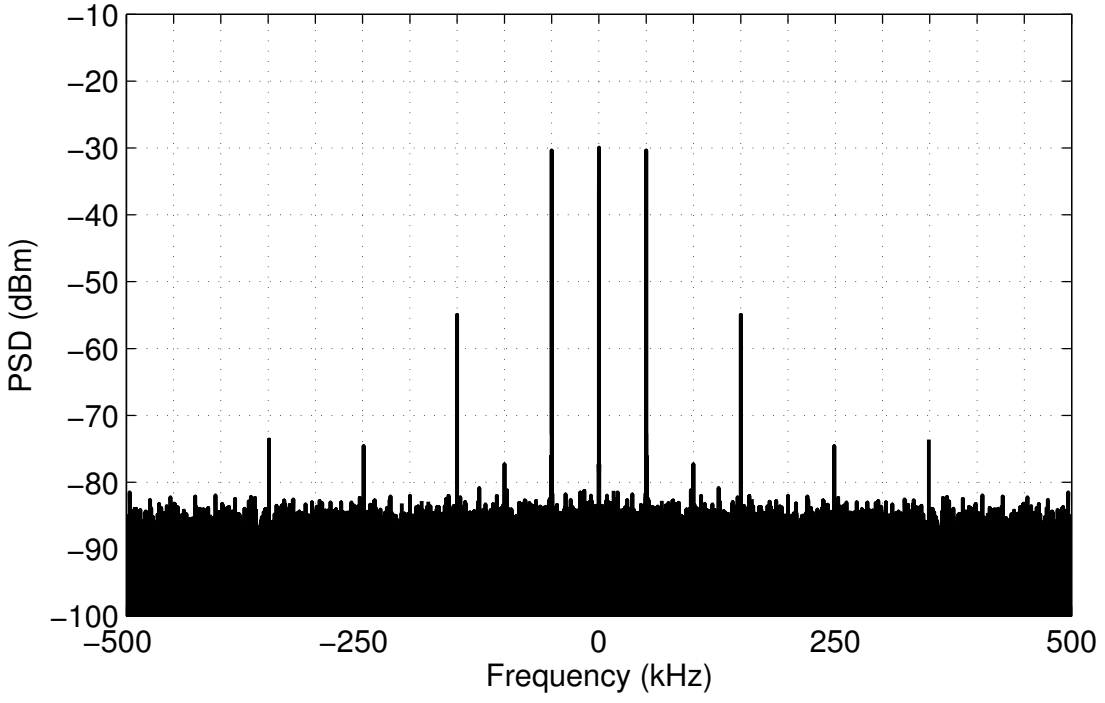

(b)

Figure 8.7: *PSDs for* L_{ch} = 70 dB *and* L_{ch} = 90 dB. The PSDs were calculated using one million samples. The L_{ch} = 70 dB PSD is plotted in (a), and distortion is evident at the odd harmonics of the signal frequency, f_{sig} = 50 kHz. The L_{ch} = 90 dB PSD is plotted in (b), and distortion is evident at the third harmonic of the signal frequency, f_{sig} = 50 kHz.

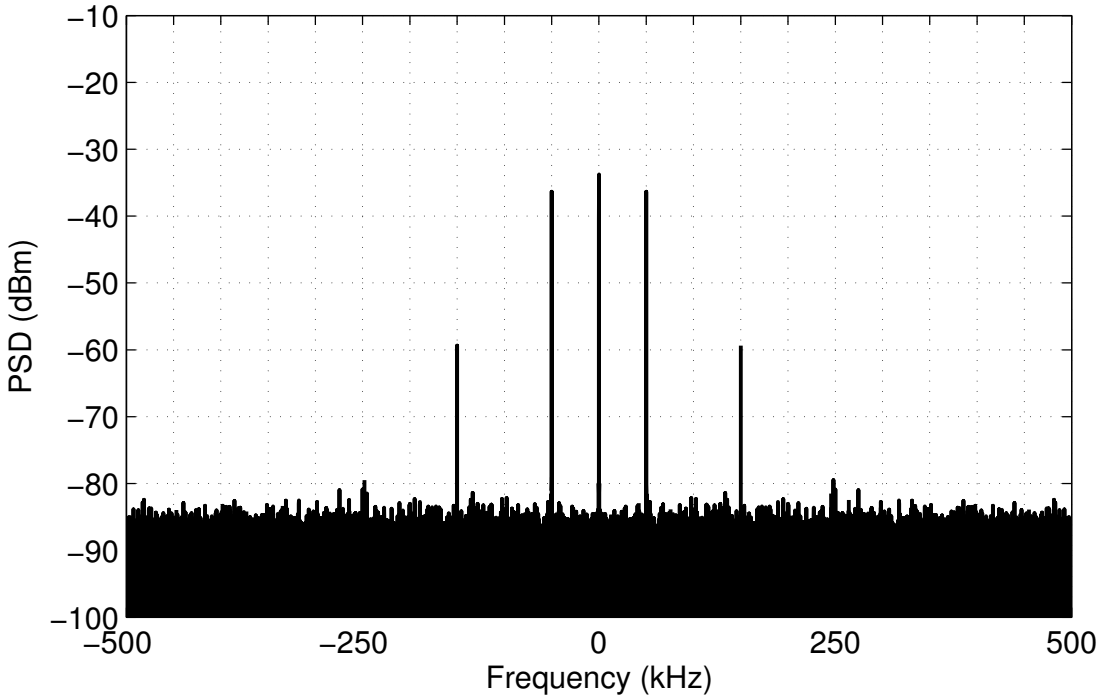

Figure 8.8: *PSD for* L_{ch} = 95 dB. The PSD was calculated using one million samples. Distortion does not contribute significantly to the noise power, but the DC leakage term does.

increased to about -16 dBm due to the leakage signal. For low SNRs, the SINAD and SNR metrics are comparable.

Distortion and leakage both increase the calculated noise power, degrade the calculated single-pulse SNR, and reduce the sensitivity of the radar. Depending on the application, the distortion and/or leakage signals can be subtracted from the spectrum to maintain the radar's sensitivity. However, for this work, distortion and leakage will be included in the noise power calculations and will degrade the minimum detectable SNR of the radar by 3–4 dB. Combined with the 3–4 dB degradation due to radar losses, the new theoretical minimum detectable single-pulse SNR is about -5 dB, which corresponds to a maximum channel attenuation of 105 dB.

8.5 Coherent Processing Interval

The CPI defines the period of time over which the radar signal is coherent. It is limited by the stability of the various signal sources, including the FPGA, PLL, and VCO. The CPI is experimentally determined by processing several sampled data sets using various numbers of samples. The processed SNR is calculated as:

$$\mathrm{SNR}_{pr} = \frac{P_{pp}(-f_{sig}) + P_{pp}(f_{sig})}{\frac{1}{N_{total} - 2}\left\{\sum_{f=-f_s/2}^{f_s/2} P_{pp}(f) - \left[P_{pp}(-f_{sig}) + P_{pp}(f_{sig})\right]\right\}} \tag{8.13}$$

where N_{total} is the total number of samples, including zero padding. In other words, it is assumed that the signal occupies a single frequency bin in both the positive and negative portions of the spectrum, and the remaining power is noise. The resulting SNR values can be used to determine the CPI.

The SNR was calculated for each data set using N = 1E3, 1E4, 1E5, and 1E6 samples. Zero padding was employed so that the total number of data points was the same for each calculation:

$$N_{total} = N_{zp} + N \tag{8.14}$$

where N_{total} is the total number of data points, N_{zp} is the number of zero-padded data points, and N is the number of samples. While the frequency resolution is inversely proportional to the number of samples, the number of frequency bins is proportional to the total number of data points. By maintaining a constant number of data points, one can consistently select the desired 50 kHz frequency bin, regardless of the number of samples, and thus resolution.

The SNR processing gain is calculated as:

$$G_{int}(N) = \frac{\mathrm{SNR}_{pr}(N)}{\mathrm{SNR}_{pr}(N = 1)} \tag{8.15}$$

The average SNR processing gains are based on the average SNR processing gain of three data sets and are listed in Table 8.9; the SNR gains are normalized

Table 8.9: Processing SNR Gain

Samples	Integration Time (ms)	Average Processing Gain (dB)	Processing Gain Variation (dB)
1E3	0.05	30	—
1E4	0.5	40.3	±0.5dB
1E5	5	50.3	±0.6dB
1E6	50	56.7	±5.8dB

to $G_{int}(N = 1E3) = 30$ dB. The processing gain variation indicates how much the individual SNR processing gains vary about the average value. For a coherent signal, the processing gain should go as $10\log(N)$, and the expected average gains are $G_{int} = 30$, 40, 50, and 60 dB for N = 1E3, 1E4, 1E5, and 1E6, respectively. The actual processing gains align well with the theoretical gains for N = 1E3, 1E4, and 1E5; in addition, the processing gain only varies by ±0.6 dB about the average value. However, the processing gain does not increase by 10 dB between N = 1E5 and N = 1E6; rather, it increases by 6.4 dB and varies significantly about the average gain. This is consistent with noncoherent integration, for which the integration gain is typically between $10\log(\sqrt{N})$ and $10\log(N)$. The variation in the processing gain for N = 1E6 is significant because of the probabilistic nature of the noise and the somewhat probabilistic nature of the signal, which is no longer fully coherent.

Based on the measured data, the CPI is about 5 ms. This is less than the integration time for one million samples (50 ms), which has been employed in the thesis thus far; therefore, the SNRs calculated with one million samples include some noncoherent integration. This is the trade-off for achieving the desired -50 dB SNR floor discussed in Section 3.7.1.

While the CPI is too short to allow coherent integration of one million pulses, it is more than sufficient for an integration time of 36.5 μs (N = 730), which is the actual integration time considered in this work. In fact, the CPI is about 100

times longer than is required, which is desirable. The 5 ms CPI was calculated from closed-loop measurements. In practice, a wireless link and a physical target will reduce the CPI. For example, as a physical target moves through the range bin, it is sampled at different points along its envelope; in other words, the synchronicity between the sample clock and the received pulse envelope is degraded due to the motion of the target [72]. As such, it is critical that the ideal CPI is longer than needed.

8.6 Sensitivity and Minimum Detectable SNR

In the previous sections, the measured data sets have been processed using up to one million samples. While a large number of samples can be used to accurately characterize the radar system, only a relatively small number of pulses will be integrated in practice. The maximum number of samples is limited by the transmitted pulsewidth and the maximum target velocity, as in Eqn. (3.12):

$$N \leq \frac{c_o \tau}{2vT} \tag{8.16}$$

For this work, seven hundred thirty pulses are integrated as a worst-case example.

The measured single-pulse SNR (Eqn. (8.8)), signal power (Eqn. (8.10)), and noise power (Eqn. (8.12)) were each calculated for 70 dB $\leq L_{ch} \leq$ 110 dB using N = 730 pulses for comparison to the SNRs calculated using N = 1E6 pulses. The results for N = 730 and N = 1E6 are tabulated in Table 8.10.

As seen in the table, the single-pulse SNRs for N = 730 do not decrease linearly with the channel attenuation. Similar behavior is observed when N = 1E6 pulses were employed. As discussed in Section 8.4, both the signal and noise power calculations contribute to the differences between the theoretical and measured SNRs.

Table 8.10: Measured Single-Pulse SNRs, Signal Power, and Noise Power

L_{ch} (dB)	SNR_1^{pp}(dB)		P_S^{pp} (dBm)		P_N^{pp} (dBm)	
	$N = 730$	$N =$ 1E6	$N = 730$	$N =$ 1E6	$N = 730$	$N =$ 1E6
70	17.3	13.4	6.8	6.8	-10.4	-6.5
75	15.7	12.2	1.6	1.5	-14.1	-10.4
80	13.6	8.9	-3.1	-3.6	-16.7	-12.5
85	9.1	5.6	-8.8	-9.0	-17.9	-14.6
90	6.0	-0.2	-11.8	-13.9	-17.8	-13.8
95	2.1	-3.2	-16.5	-19.4	-18.6	-16.2
100	2.1	-8.9	-16.4	-24.0	-18.4	-15.1
105	-1.8	-13.1	-20.6	-29.8	-18.8	-16.7
110	-0.2	-18.6	-18.7	-34.2	-18.5	-15.6

The signal power for $N = 730$ is within 0.5 dB of the signal power for $N =$ 1E6 when $L_{ch} \leq 85$ dB; as such, the analysis of Section 8.4.1 applies. However, the difference between the calculated signal powers is significant for $L_{ch} > 85$ dB. To understand why, consider the integration bandwidth for a 30 dB Hamming main-lobe, which was presented in Section 3.5:

$$\beta_{int} = \frac{3.6 f_s}{N} \tag{8.17}$$

For $f_s = 20$ MHz and $N = 730$, the integration bandwidth is $\beta_{int} = 98.6$ kHz. The measured PSDs for $L_{ch} = 70$, 90, and 105 dB are plotted in Figures 8.9 and 8.10; the simulated radar results are also plotted and will be discussed in the next section. To calculate the signal power, the PSD is integrated from approximately -100 kHz to 100 kHz (see Eqn. (8.10)). For $L_{ch} = 70$ dB, the signal power is high enough to mask the DC leakage signal, so the signal power matches the higher frequency resolution case ($N =$ 1E6). For $L_{ch} = 90$ dB, the DC leakage signal is visible in the spectrum and contributes to the overestimation of the signal power. For the $L_{ch} = 105$ dB case, the DC leakage signal dominates the signal spectrum, and the signal power is significantly overestimated.

Referring to the table, the noise power calculated with $N = 730$ is 3–4 dB

lower than the noise power calculated with N = 1E6. The integration bandwidth β_{int} = 98.6 kHz also explains the 3 dB reduction in noise power when the number of samples is reduced from N = 1E6 to N = 730. As discussed in Section 8.4, the DC leakage signal contributes 3 dB to the noise power when N = 1E6; for N = 730, the DC leakage signal contributes to the signal power rather than the noise power, so the noise power is closer to the theoretical -20.2 dBm. To conclude, the frequency resolution is lower when fewer samples are used; as a result, the DC leakage power present in the radar system has a more detrimental impact on the single-pulse SNR calculation than if a larger number of samples is used.

While the single-pulse SNR is helpful when considering the transmitter and receiver characteristics, the processed, or integrated, SNR is needed to determine the sensitivity of the radar. As discussed in Section 3.7.1, the probability of detection, probability of false alarm, and the processed SNR are interrelated, so the processed SNR was calculated with N = 730 using Eqn. (8.13). The signal power is the numerator of the equation:

$$P_S^{pr} = P_{pp}(-f_{sig}) + P_{pp}(f_{sig}) \tag{8.18}$$

The noise power is the denominator of the equation:

$$P_N^{pr} = \frac{1}{N_{total} - 2} \left\{ \sum_{f=-f_s/2}^{f_s/2} P_{pp}(f) - \left[P_{pp}(-f_{sig}) + P_{pp}(f_{sig}) \right] \right\} \tag{8.19}$$

The processed SNRs, signal powers, and noise powers are summarized in Table 8.11. As seen in table, the processed SNRs do not decrease linearly with the channel attenuation. However, the signal power does, so the nonlinearity in the processed SNRs is primarily due to the average noise power. Distortion and leakage raise the total noise power and, thus, the average noise power. As seen in Eqn. (8.19), the processed SNR employs the average noise power, which is

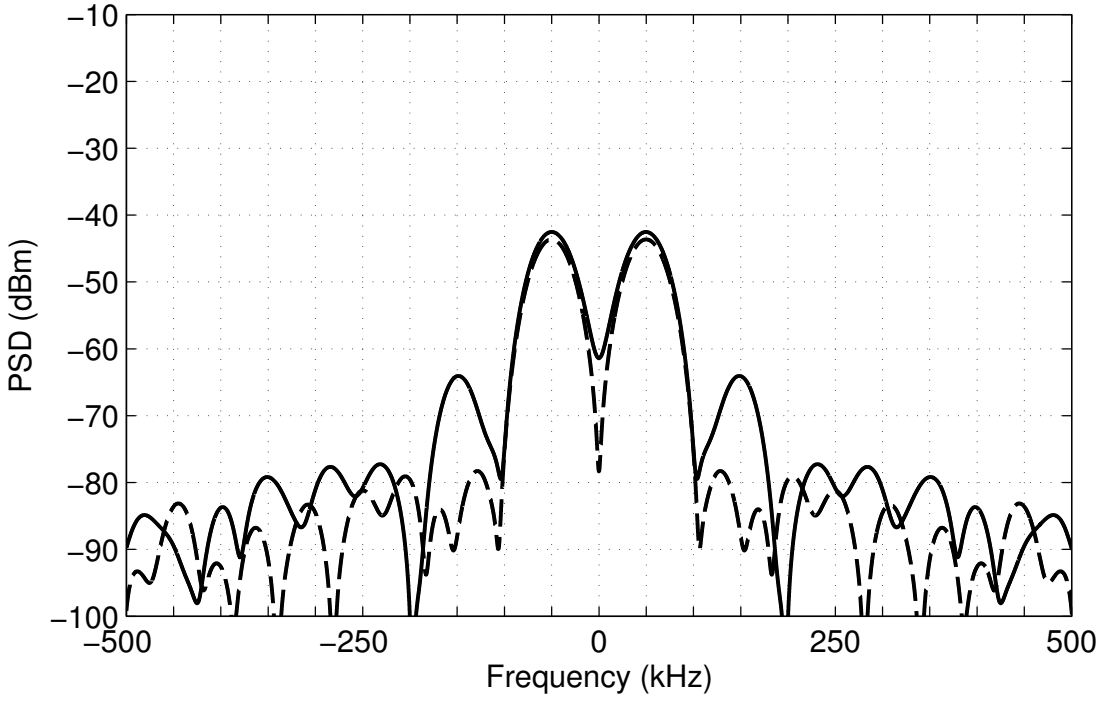

(a)

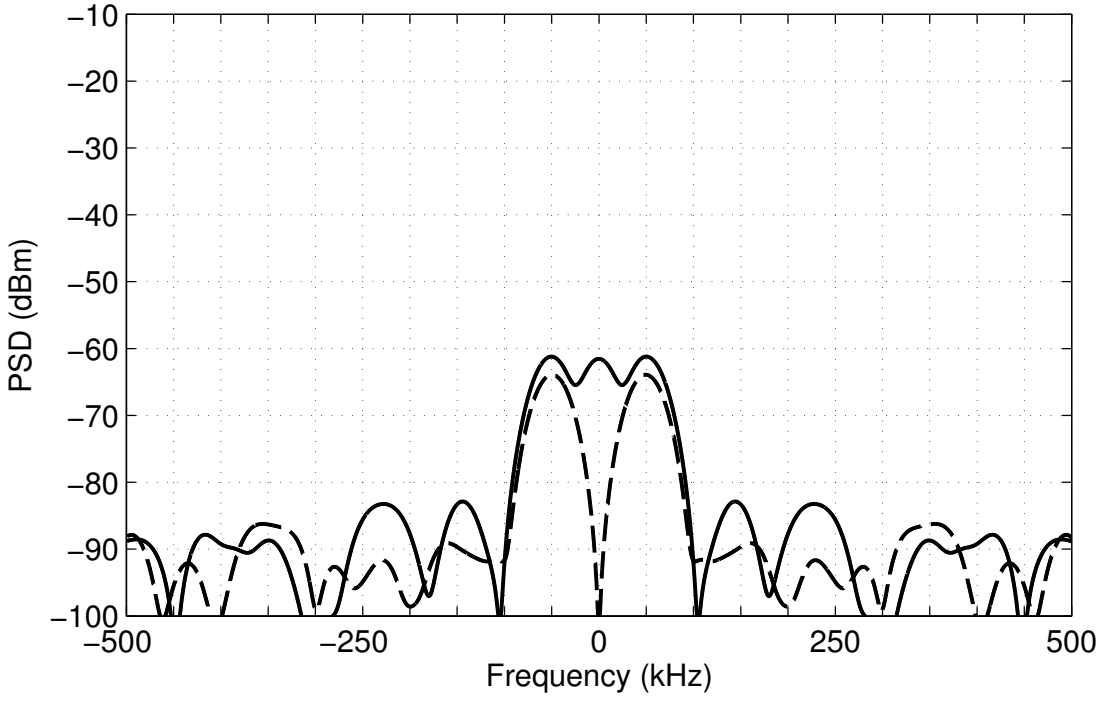

(b)

Figure 8.9: *Measured and Simulated PSDs for* $L_{ch} = 70\,\text{dB}$ *and* $L_{ch} = 90\,\text{dB}$. The measured and simulated PSDs were calculated using $N = 730$ samples and $N_{total} = 2^{20}$ total data points. The $L_{ch} = 70\,\text{dB}$ PSD is plotted in (a), and the $L_{ch} = 90\,\text{dB}$ PSD is plotted in (b). The measured PSDs are plotted in solid lines, and the simulated PSDs are plotted in dashed lines.

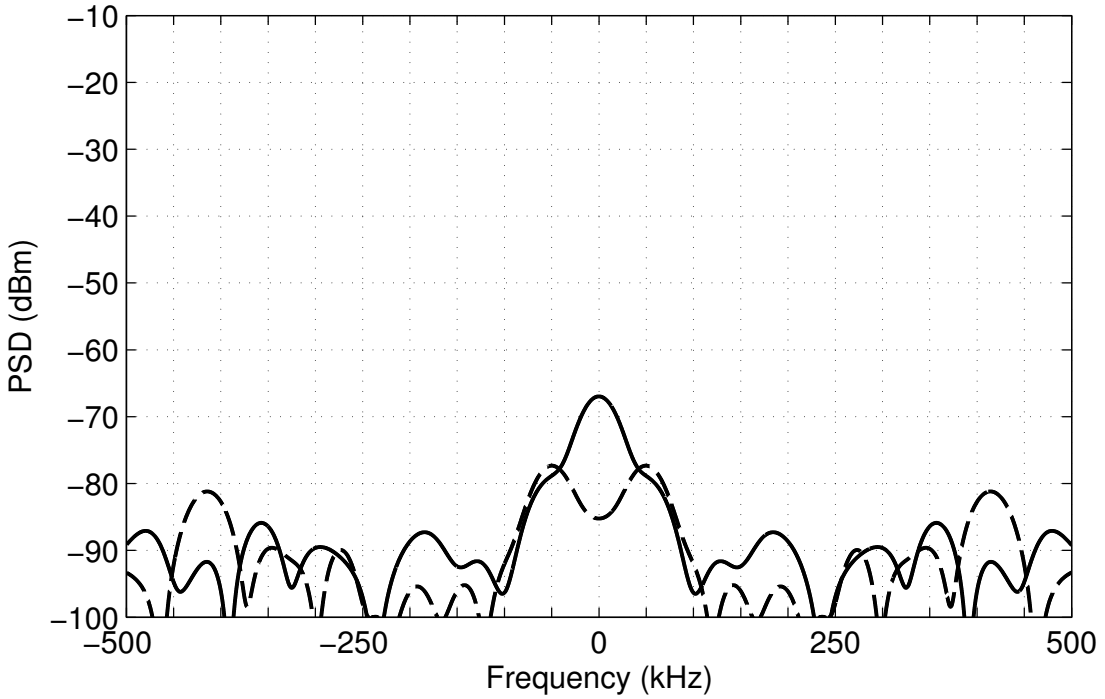

Figure 8.10: *Measured and Simulated PSDs for* L_{ch} = 105 dB. The measured and simulated PSDs were calculated using $N = 730$ samples and $N_{total} = 2^{20}$ total data points. The measured PSD is plotted in solid lines, and the simulated PSD is plotted in dashed lines. L_{ch} = 105 dB is the maximum channel attenuation to achieve a processed SNR near SNR_{pr} = 15 dB.

Table 8.11: Processed SNRs, Signal Power, and Noise Power ($N = 730$)

L_{ch} (dB)	SNR_{pr} (dB)	P_S^{pr} (dBm)	P_N^{pr} (dBm)
70	27.2	-39.5	-66.6
75	27.1	-44.6	-71.6
80	26.7	-54.1	-75.7
85	26.8	-58.2	-80.9
90	25.2	-64.7	-83.2
95	22.5	-69.0	-86.6
100	18.7	-75.8	-87.2
105	13.7	-78.8	-89.4
110	7.8	-89.3	-88.4

overestimated for low channel attenuation states; as a result, the processed SNR is underestimated for $L_{ch} \leq 90$ dB.

The minimum detectable processed SNR for this thesis is 15 dB to achieve a probability of detection of 0.99 and a probability of false alarm of 1E-7. As noted in Section 8.4, this corresponds to a theoretical minimum detectable single-pulse SNR of -5 dB and a maximum channel attenuation of 105 dB when radar losses are considered. Referring to Table 8.11, these assertions are approximately correct; the processed SNR is $\text{SNR}_{pr} = 15\,\text{dB}$ somewhere in the range $100\,\text{dB} \leq L_{ch} \leq 105\,\text{dB}$. Referring to Table 8.5, this corresponds to a theoretical single-pulse SNR in the range $-5.0\,\text{dB} \leq \text{SNR}_1^{out} \leq 0.3\,\text{dB}$ and a measured single-pulse SNR in the range $-13.1\,\text{dB} \leq \text{SNR}_{pr} \leq -8.9\,\text{dB}$. As discussed in Section 3.7.1, the anticipated measured minimum detectable single-pulse SNR is -13.6 dB, so the sensitivity of the radar is as anticipated, once radar losses and leakage are accounted for.

8.6.1 Radar Simulation Model

The full radar system was simulated in Agilent's ADS. The simulation is performed in the time-domain with a discrete step size; it includes pseudo-random noise from DC to 4 GHz. The transmitter and receiver are modeled as discussed in Sections 5.2 and 6.2; the components used in the transmitter, receiver, closed-loop channel, and post processor models can be summarized as follows:

(1) Transmitter Model:

- The FPGA, VCO, amplifiers, switches, attenuators, bi-phase modulator, and upconverter are modeled as behavioral components, which include gain, noise figure, and compression points, as appropriate.
- The PCC and filters are modeled using circuit elements corresponding to their actual hardware implementations.

(2) Receiver Model:

- The range gate, FPGA, amplifiers, and downconverter were modeled as behavior components.
- The matched filter was modeled using circuit elements corresponding to the actual hardware implementation.

(3) Closed-Loop Channel Model:

- The attenuation and time delay are modeled using behavioral models.
- The SSB modulator is modeled as a voltage multiplier.

(4) Post Processor Model:

- The digitizer is modeled using a behavioral sample-and-hold circuit and a quantizer.

Two changes were made to the basic radar simulation model to account for radar losses. First, a 7 dB attenuator was added to the receiver to simulate the signal losses. Second, a noise multiplier was added to the transient setup. The 7 dB attenuator, as well as the various other attenuators in the setup, does not include a noise figure parameter, so it attenuates both signal and noise. The noise multiplier accounts for this nonphysical behavior.

The simulated PSDs were calculated using $N = 730$, and plotted for $L_{ch} = 70$, 90, and 105 dB in Figures 8.9a, 8.9b, and 8.10, respectively. As seen in the figures, the noise floors and the 50 kHz signal levels of the simulated and measured PSDs are comparable. One significant difference between simulation and measurement occurs near DC. While the simulation model accounts for channel model feed-through leakage, it does not account for radiative leakage, which dominates for the radar in this thesis. As a result, the simulated PSDs are idealized.

The distortion terms are also somewhat underestimated in the simulation for low channel attenuations. Consider the $L_{ch} = 70$ dB PSD. The third-order

distortion term is evident at ±150 kHz in the measured data, but not in the simulated data. The simulation model accounts for compressive and intermodulation effects in the radar system, but underestimates them for high SNRs.

Despite the underestimated leakage and distortion terms, there is excellent agreement between the measured and simulated data. It is extremely helpful to have an accurate simulation model, especially when considering changes to the radar architecture. For example, miniaturization is one future goal for this work; as new components are designed, they can be added to the simulation model before being fabricated to ascertain the impact of the new circuit design on the overall radar performance. As discussed in Section 7.3.7, an open-loop channel model can be simulated by including the transmit and receive antenna models. In addition, the radar model can be further developed to more accurately include leakage and distortion effects.

8.7 Minimum Detectable Range and Minimum TX-RX Isolation

As discussed in Section 3.7.2, the time-domain SNR response is used to characterize the minimum detectable range of the radar under test. A fixed observable range, corresponding to t_R^{obs}, was selected for the time-domain SNR response measurements. The channel time delay was varied from $t_R = t_R^{obs}$ to $t_R = t_R^{obs} + T$ in 2 ns steps. By varying the channel time delay, the received waveform is sampled throughout the PRI, the received pulse envelope can be reconstructed, similar to how a sampling oscilloscope works. Based on the measurement, it is possible to approximate the turn-off rate of the waveform, accounting for the transient effects of the transmitter and receiver components. Based on this information, the turn-off time and minimum TX-RX isolation can be specified, and the minimum

range can be determined using Eqn. (3.17):

$$R_{min} = c_o \left(\frac{t_{lk}}{2} + \frac{t_{to}}{2} + \frac{\tau_{RG}}{4} \right) \tag{8.20}$$

Figures 8.11 and 8.12 illustrate the time-domain SNR response measurement. The sample point remains fixed at the center of the range gate (t_R^{obs}). Figure 8.11a shows the case where $t_R = t_R^{obs}$; in this instance, the post processor samples the received signal at its peak voltage. Figure 8.11b shows the case where $t_R = t_R^{obs} + 2\,\text{ns}$; in this case, the post processor samples the signal along the leading edge of the pulse. Figure 8.12a shows the case where $t_R = t_R^{obs} + 26\,\text{ns}$; in this case, the post processor samples the signal during the "off" time of the pulse. Figure 8.12b shows the case where $t_R = t_R^{obs} + 48\,\text{ns}$; in this case, the post processor samples the signal along the trailing edge of the pulse. The data points can be plotted in the time domain, and the resulting waveform is the processed received pulse envelope sampled at a rate of 500 MHz.

To illustrate that the radar system time-domain SNR response characteristics are fairly linear, the time-domain SNR response was measured in three channel attenuation states: $L_{ch} = 70\,\text{dB}$, 80 dB, and 90 dB. For this testing, the channel attenuation corresponds to TX-RX isolation, and the sampled signal is representative of a leakage signal through, for example, the antenna system. The full-scale voltage of the digitizer was adjusted to match the anticipated received signal level for each attenuation state, as in Table 8.3.

A 50 kHz Doppler shift is applied to the signal; as discussed in Section 8.2.2, the leakage signal through the antenna system may or may not be Doppler modulated. For testing purposes, it is beneficial to employ a simulated Doppler shift to isolate the time-domain SNR characteristics of the radar waveform from the radiative and channel-model feed-through leakage signals, which are observed at DC.

Three sampled data sets were taken for each attenuation state and channel

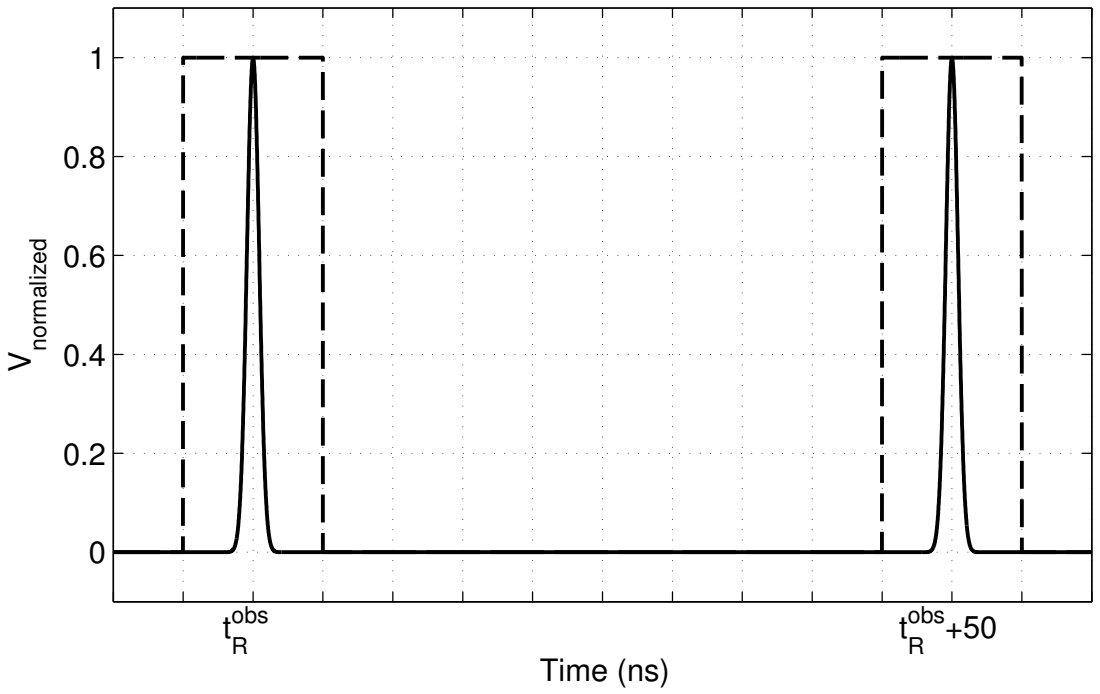

(a)

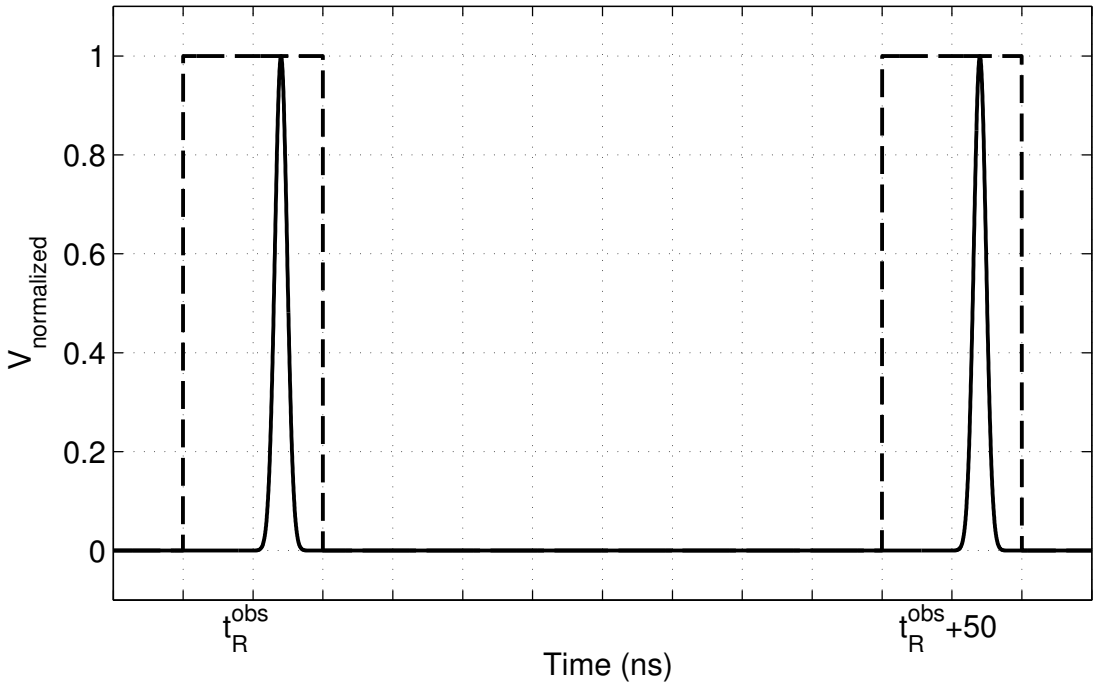

(b)

Figure 8.11: *Time-Domain SNR Response Measurements.* A set of time-domain SNR response measurements was taken by adjusting the range delay of the channel from $t_R = t_R^{obs}$ to $t_R = t_R^{obs} + T$ in 2 ns steps. Two of the data points are illustrated, as follows: (a) $t_R = t_R^{obs}$ and (b) $t_R = t_R^{obs} + 2$ ns. The range gate control signal, RG, is plotted as a dashed black line, and the theoretical received pulse envelope is plotted as a solid black line.

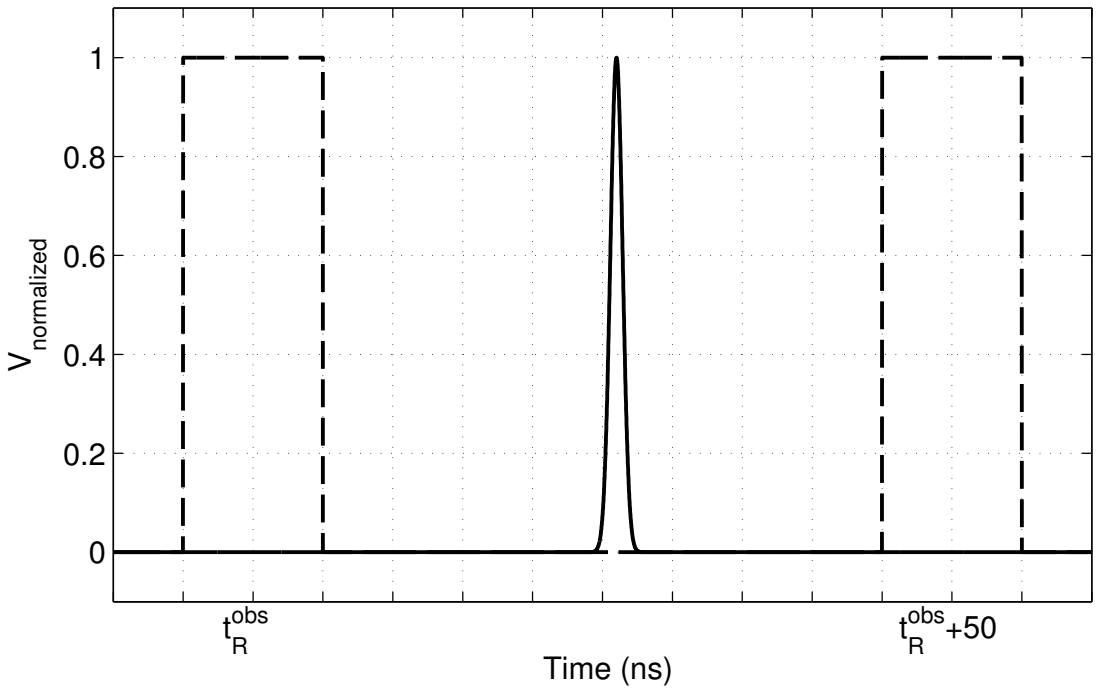

(a)

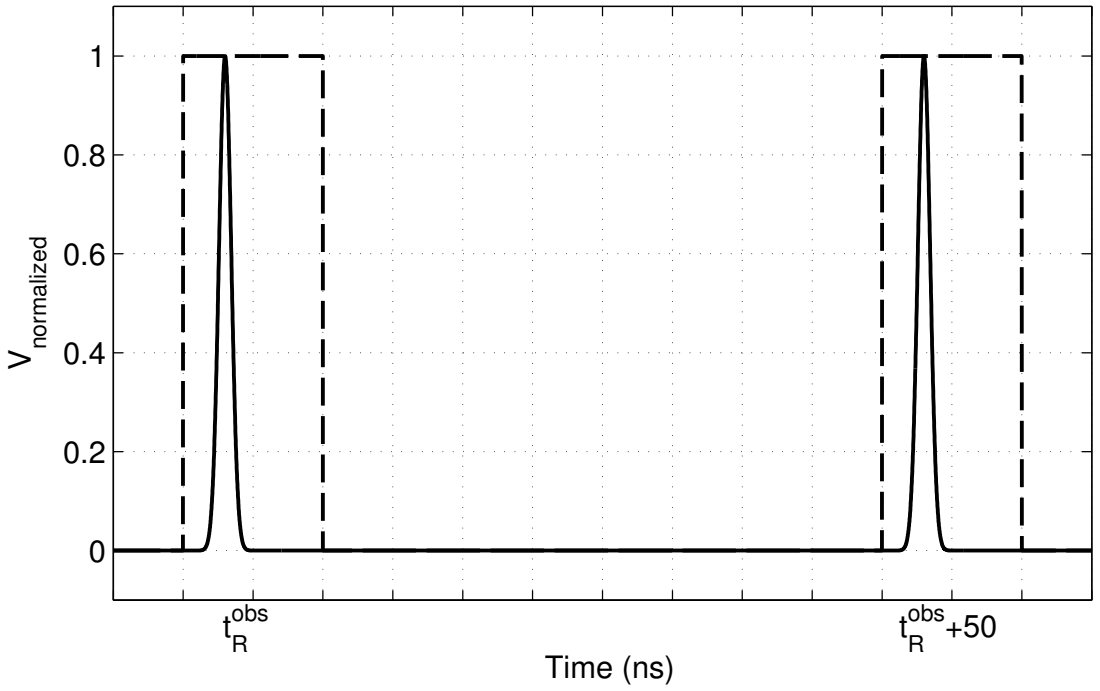

(b)

Figure 8.12: *Time-Domain SNR Response Measurements.* A set of time-domain SNR response measurements was taken by adjusting the range delay of the channel from $t_R = t_R^{obs}$ to $t_R = t_R^{obs} + T$ in 2 ns steps. Two of the data points are illustrated, as follows: (a) $t_R = t_R^{obs} + 26$ ns and (b) $t_R = t_R^{obs} + 48$ ns. The range gate control signal, RG, is plotted as a dashed black line, and the theoretical received pulse envelope is plotted as a solid black line.

time delay to ensure measurement repeatability. The single-pulse SNR was calculated for each data set using one million samples, and the three calculated SNRs were averaged for each attenuation state and channel time delay. One million samples corresponds to an SNR floor of -50 dB.

The received leakage signal for each attenuation state was reconstructed and plotted in Figures 8.13 and 8.14; the markers indicate the measured data points. The theoretical received pulse envelope is also plotted for comparison. The transmitted voltage envelope was converted to a received SNR envelope using the following expression:

$$\begin{aligned} \mathrm{SNR}_1^{out}(t) &= 10\log\left(\frac{(V_{env}^{TX}(t))^2}{2Z_o}\frac{1}{1\,\mathrm{mW}}\right) - L_{ch} - P_N - F_{pulsed}^{RX} \\ &\quad \ldots - \mathrm{SNR}_{error}[\mathrm{dB}] \end{aligned} \tag{8.21}$$

$$V_{env}^{TX}(t) = V_p^{TX}\exp\left(-2\ln(2)\left(\frac{t-t_{lk}}{\tau}\right)^2\right) \tag{8.22}$$

where $V_p^{TX} = 7.7\mathrm{V}$ is the measured peak transmitted voltage, t_{lk} is the time delay between the transmitted and leakage signals, $\tau = 730\,\mathrm{ns}$ is the transmitted pulsewidth, $Z_o = 50\,\Omega$, $P_N = -87\,\mathrm{dBm}$, $F_{pulsed}^{RX} = 14.8\,\mathrm{dB}$, and SNR_{error} is a correction factor between the theoretical and measured SNR (see Table 8.5).

As noted in Section 3.7, the theoretical maximum rejectable single-pulse SNR is $\mathrm{SNR}_{1,max}^{out,rej} = -30\,\mathrm{dB}$. As discussed in Sections 8.4 and 8.6, there is about a 10 dB difference between the theoretical and measured single-pulse SNRs due to radar losses and leakage. As a result, the measured minimum detectable SNR is -5 dB, rather than the theoretical -13.6 dB as put forth in the original specification. Despite the reduction in sensitivity, the measured maximum rejectable single-pulse SNR will be maintained as -30 dB; the result is a wider margin between detectable and rejectable SNRs.

The minimum TX-RX isolation when the transmitter is off and receiver is on is determined from the time-domain SNR response measurements. As seen in

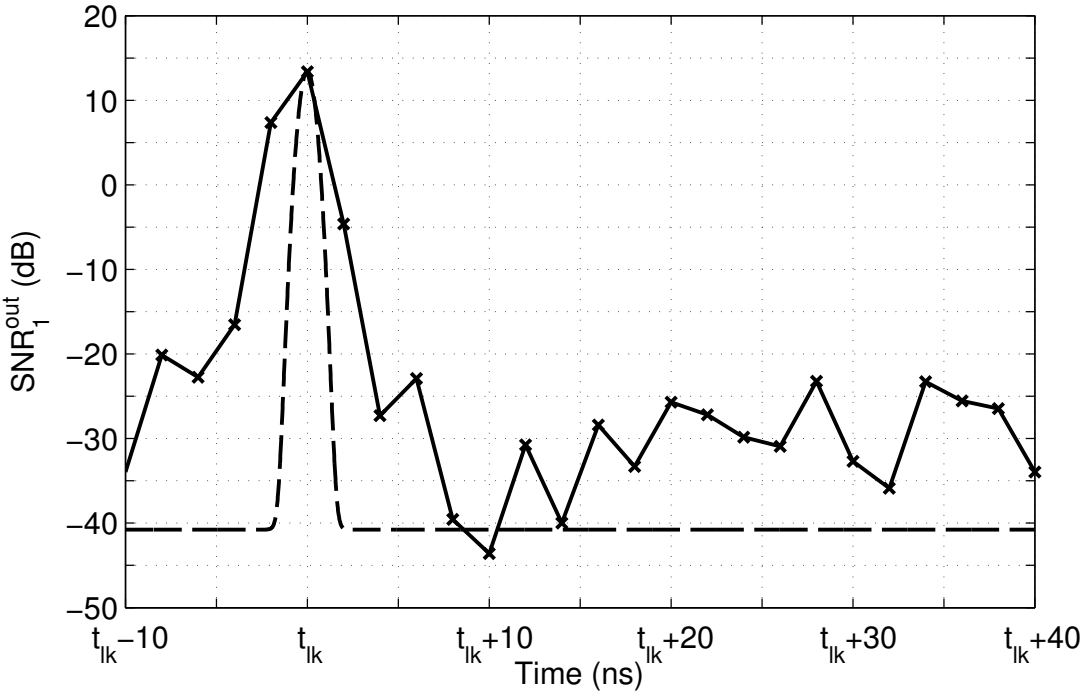

(a)

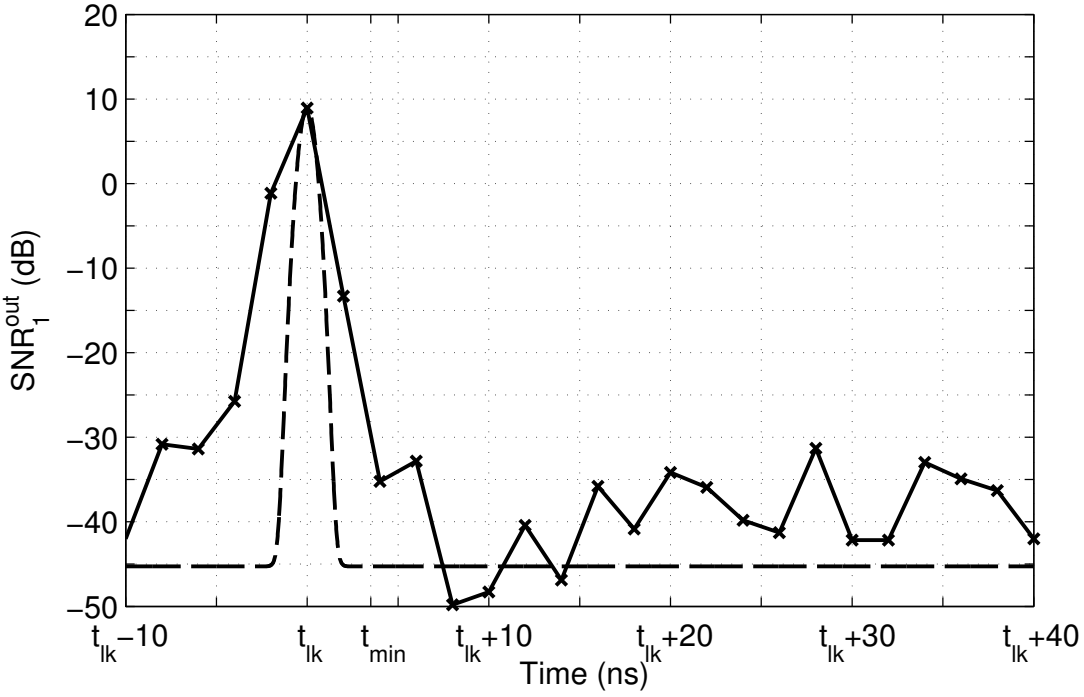

(b)

Figure 8.13: *Time-Domain SNR Response.* The time-domain SNR results are plotted for (a) $I_{TX/RX} = 70$ dB and (b) $I_{TX/RX} = 80$ dB TX-RX isolations. The measured results are plotted with solid lines, and the data markers indicate the measured data points. The theoretical received SNR envelope is plotted in dashed lines for comparison; the waveform was calculated using Eqn. (8.21).

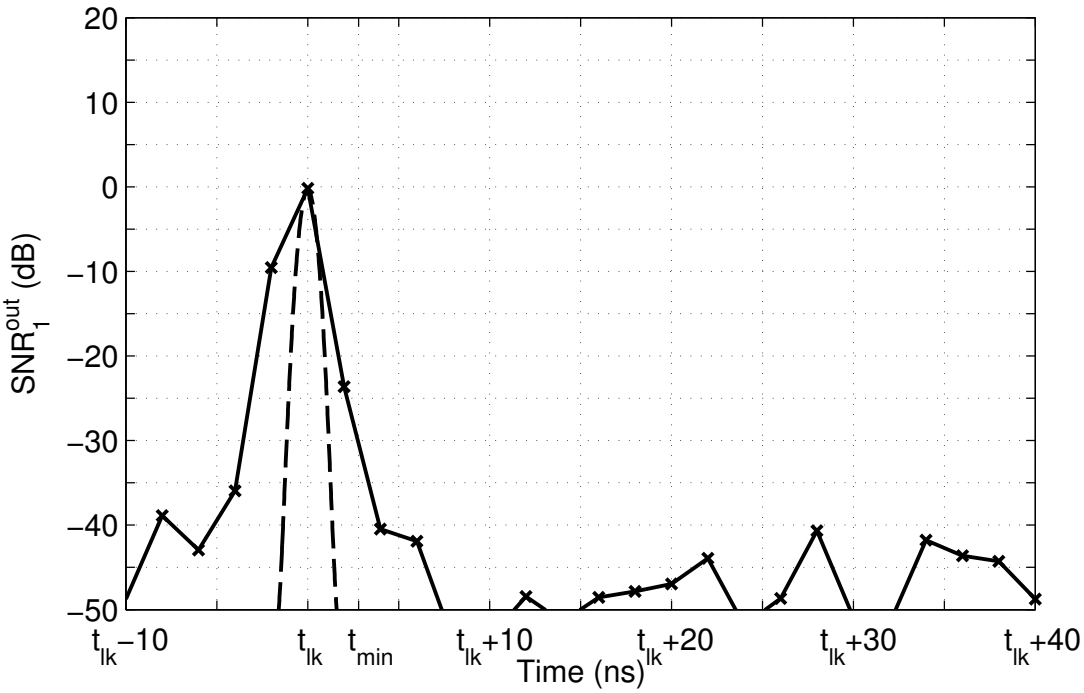

Figure 8.14: *Time-Domain SNR Response.* The time-domain SNR results are plotted for $I_{TX/RX} = 90$ dB TX-RX isolation. The measured results are plotted with solid lines, and the data markers indicate the measured data points. The theoretical received SNR envelope is plotted in dashed lines for comparison; the waveform was calculated using Eqn. (8.21).

Figure 8.13a, the off-state single-pulse SNR does not reach $\text{SNR}_{1,max}^{out,rej} = -30$ dB; based on this observation, $I_{TX/RX} = 70$ dB is not sufficient to prevent false alarms due to a leakage signal from the transmit to receive antenna. Figure 8.13b illustrates the case where $I_{TX/RX} = 80$ dB. For this case, the radar signal reduces from its peak to a single-pulse SNR of -30 dB in approximately 3.5 ns with a turn-off rate of 11.1 dB/ns. The $I_{TX/RX} = 90$ dB case is illustrated in Figure 8.14; the turn-off time and rate are 2.8 ns and 10.7 dB/ns, respectively. When $I_{TX/RX} = 80$ dB, the on-off isolation of the measured signal is 40 dB; when it is $I_{TX/RX} = 90$ dB, the on-off isolation is 30 dB. Referring to Table 5.1, the turn-off times of the transmitter with $I_{on/off}^{TX} = 40$ dB and $I_{on/off}^{TX} = 30$ dB are $t_{to}^{TX} = 5.4$ ns and $t_{to}^{TX} = 3.0$ ns, respectively. The radar and transmitter turn-off times are

Table 8.12: Single-Pulse SNR with Range Gate Closed ($N = 730$)

Nominal L_{ch} (dB)	Theoretical SNR_1^{out} (dB)	Measured SNR_1^{pp} (dB)
70	-19.1	-31.2
80	-29.1	-39.7
90	-38.9	-50.1

comparable. The radar turn-off times could be measured more accurately with better time resolution. Based on the time-domain SNR response measurements, the minimum TX-RX isolation is about 80 dB, and the minimum range of the radar is approximately $R_{min} = 1.3\,\text{m} + R_{lk}$.

As discussed in Section 3.7.3, this is only half the story; the case when the transmitter is on and the receiver is off must also be considered. To experimentally determine the minimum TX-RX isolation for this case, the digitizer was set to sample the signal at t_R, the target range; however, the observable range delay, t_R^{obs}, was delayed so that $t_R^{obs} = t_R + 7.5\,\text{ns}$. As a result, the digitizer samples the received signal at its peak while the receiver is in its off state. The theoretical and measured single-pulse SNRs are listed in Table 8.12. The theoretical SNRs are calculated as:

$$\text{SNR}_1^{out} = P_{TX} - L_{ch} - I_{RG} - P_N - F_{pulsed}^{RX}[\text{dB}] \tag{8.23}$$

where P_{TX} is given in Eqn. (8.7) and $I_{RG} = 49\,\text{dB}$ is the measured range gate isolation. The measured SNRs are calculated using Eqn. (8.8).

As discussed in Section 8.4, the measured SNRs are about 10–15 dB lower than the theoretical values. As a result, the measurement indicates a minimum TX-RX isolation of 70 dB will suffice, whereas a theoretical TX-RX isolation of 81 dB is required. As discussed in Section 3.7.3, the greater of the two minimum TX-RX isolation values must be selected. As such, the minimum TX-RX isolation for this work is $I_{min}^{TX/RX} = 80\,\text{dB}$.

8.8 Range Ambiguity Resolution

Pseudo-random BPSK pulse tagging is employed in this thesis to reject out-of-range targets. The out-of-range rejection is accomplished by correlating the sampled, received signal with the sampled BPSK phase code. If the target is in range, the two will correlate well; assuming the SNR is sufficient, the signal will be observable in the PSD, as illustrated in the PSD plots presented thus far in this thesis. If the target is out-of-range, the received signal and BPSK phase code will be poorly correlated, and the PSD will be noise-like. The PSD for an out-of-range target with $L_{ch} = 70$ dB is calculated with one million samples and plotted in Figure 8.15b; the PSD for an in-range target with $L_{ch} = 70$ dB is also calculated with one million samples and plotted in Figure 8.15a for comparison. As seen in the figure, the 50 kHz signal power is clearly evident for the in-range target but is barely visible above the noise floor for the out-of-range target. In addition, the noise floor for the out-of-range target is about 20 dB higher than for the in-range target.

The in-range target is at range $R = R_{obs}$, and the out-of-range ambiguities occur at ranges $R = R_{obs} + nc_oT/2$, where n is an integer. The SNRs for an in-range target and its first five range ambiguities are calculated using seven hundred thirty pulses, in keeping with the anticipated integration time. The channel attenuation is varied from 70 dB $\leq L_{ch} \leq$ 100 dB in 10 dB steps, and the single-pulse SNR for the in-range target and the average single-pulse SNR for the out-of range targets are recorded in Table 8.13. The out-of-range ambiguity rejection ratio, which is the ratio of the in-range SNR to the average out-of-range SNR, is also tabulated.

As discussed in Section 3.7.4, the out-of-range ambiguity rejection ratio is

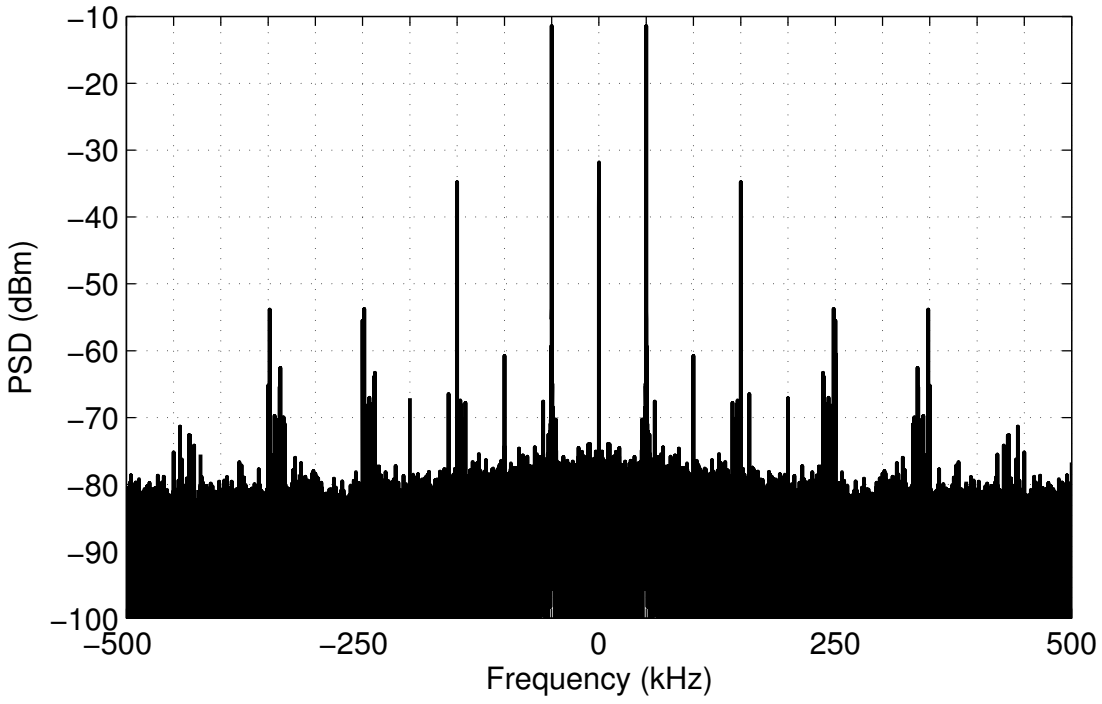

(a)

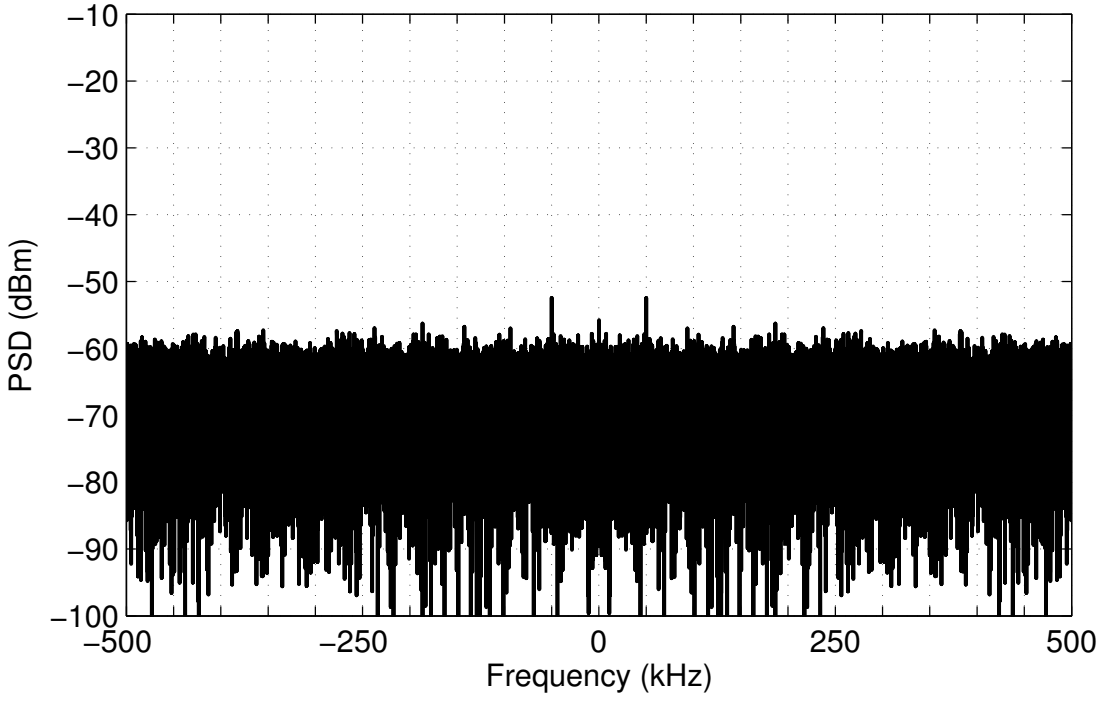

(b)

Figure 8.15: *PSD for In- and Out-of-Range Targets with* $L_{ch} = 70$ dB. The PSDs were calculated using one million samples. The in-range case is plotted in (a), and the out-of-range case is plotted in (b).

Table 8.13: Out-of-Range Ambiguity Rejection Ratio ($N = 730$)

Nominal L_{ch} (dB)	In-Range SNR_1^{pp}(dB)	Average Out-of-Range SNR_1^{pp}(dB)	Out-of-Range Ambiguity Rejection Ratio (dB)
70	16.9	-23.1	40.0
80	13.9	-20.9	34.8
90	6.7	-18.4	25.1
100	2.2	-18.3	20.5

limited by the SNR floor, which can be calculated using Eqn. (3.5):

$$\text{SNR}_{1,min}^{floor} \simeq \frac{P_{sig}}{P_N} = \frac{2\beta_{int}}{f_s - 2\beta_{int}} \tag{8.24}$$

For $N = 730$, the SNR floor is $\text{SNR}_{1,min}^{floor} \simeq -20\,\text{dB}$. As seen from the table, the average out-of-range SNRs are approximately equal to the noise floor, and the out-of-range ambiguity rejection ratio is limited by the SNR noise floor. The maximum value for $N = 730$ is 40.0 dB and decreases as the in-range SNR decreases.

8.9 Summary

A variety of topics and measurements were discussed in this chapter and can be summarized as follows:

- In order to integrate the radar subsystems, various system parameters must be characterized, including several time delays.
- Leakage paths arise from a variety of sources. Radiative leakage paths contribute about -19 dBm to the total spectral power at DC, effectively raising the noise floor from -20 dBm to -16 dBm.
- The DC leakage signal impacts the SNR calculation and degrades the sensitivity of the radar.

- The total radar losses are 3–4 dB; 1–3 dB of the loss is attributed to sampling loss.
- The CPI is about 5 ms, which far exceeds the desired integration time of 36.5 μs.
- The theoretical minimum detectable SNR is about 0 dB. This corresponds to a maximum channel attenuation of 100 dB.
- An accurate radar model was developed in Agilent's ADS. It will help facilitate future radar testing and radar development.
- The minimum TX-RX isolation of the radar is 80 dB.
- The minimum range of the radar is $R_{min} = 1.3\,\text{m} + R_{lk}$, where R_{lk} is approximately equal to half the separation between the transmit and receive antennas.
- BPSK pulse tagging was successfully employed to reject out-of-range targets.

Chapter 9

Future Work

This thesis has presented a COTS-based short-pulse Doppler radar. It employs UWB design principles to generate a subnanosecond pulse envelope which allows target detection at a minimum range of $R_{min} = 1.3\,\text{m} + R_{lk}$. Assuming a 36.5 µs integration time, a minimum detectable single-pulse SNR of $\text{SNR}_{1,min}^{out} = 0\,\text{dB}$ was demonstrated through closed-loop radar testing. The next steps, which are discussed in the following sections, are to:

- perform open-loop radar testing;
- consider improvements to the current radar architecture;
- consider how to progress for various application-specific requirements;
- consider improvements to the radar test setups;
- begin integrating the RF circuitry using IC technologies.

9.1 Open-Loop Radar Testing

Open-loop testing, which was discussed in Section 3.6, retains the simplicity of a simulated radar target that was achieved through closed-loop testing; however,

it adds a wireless link, creating a more realistic test environment. At the same time, nonidealities can be limited or simulated as desired by performing the radar testing in an anechoic chamber or a controlled laboratory environment. Two open-loop channel models were employed for proof-of-concept testing.

9.1.1 Open-Loop Test Setup 1

The first open-loop test setup employs a direct wireless link, as indicated in Figure 9.1. The antennas are separated by a distance r such that they are in one another's far field. The Doppler shift is simulated using a SSB modulator and a Doppler shift generator, and additional channel loss can be simulated using a variable attenuator. Like the closed-loop channel model, the SSB modulator, Doppler shift generator, and variable attenuator are implemented using a Polyphase Microwave QD2040B quadrature modulator, a pair of synchronized HP 3314A function generators, and a pair of 10 dB and 100 dB manually variable attenuators, as shown in Figure 9.1b. The elliptically-tapered slot antenna design described in Chapter 7 is used for both the transmit and receive antennas.

Channel Losses

Much of the channel loss discussion of Section 8.1.2 also applies to open-loop testing. However, the range equation for the open-loop test setup is different than the standard range equation (see Eqn. (1.3)) because the target is simulated using a direct wireless link. The radar range equation for this open-loop setup is:

$$P_{in}^{RX} = \frac{P_{TX} G_{A,TX} G_{A,RX} \lambda^2}{(4\pi)^2 r^2 L_{SSB} L_{VA}^{10dB} L_{VA}^{100dB} L_{cable} L_A^{ch}} \tag{9.1}$$

where $G_{A,TX} \simeq 6\,\text{dB}$ and $G_{A,RX} \simeq 6\,\text{dB}$ are the transmit and receive antenna gains, L_{VA}^{10dB} is the attenuation of the 10 dB variable attenuator, L_{VA}^{100dB} is the attenuation of the 100 dB variable attenuator, L_{cable} is the loss of the interconnecting cables

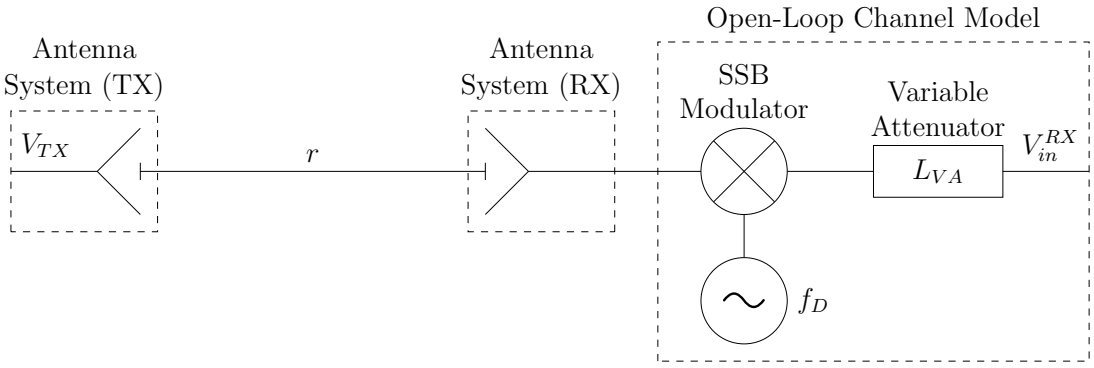

(a)

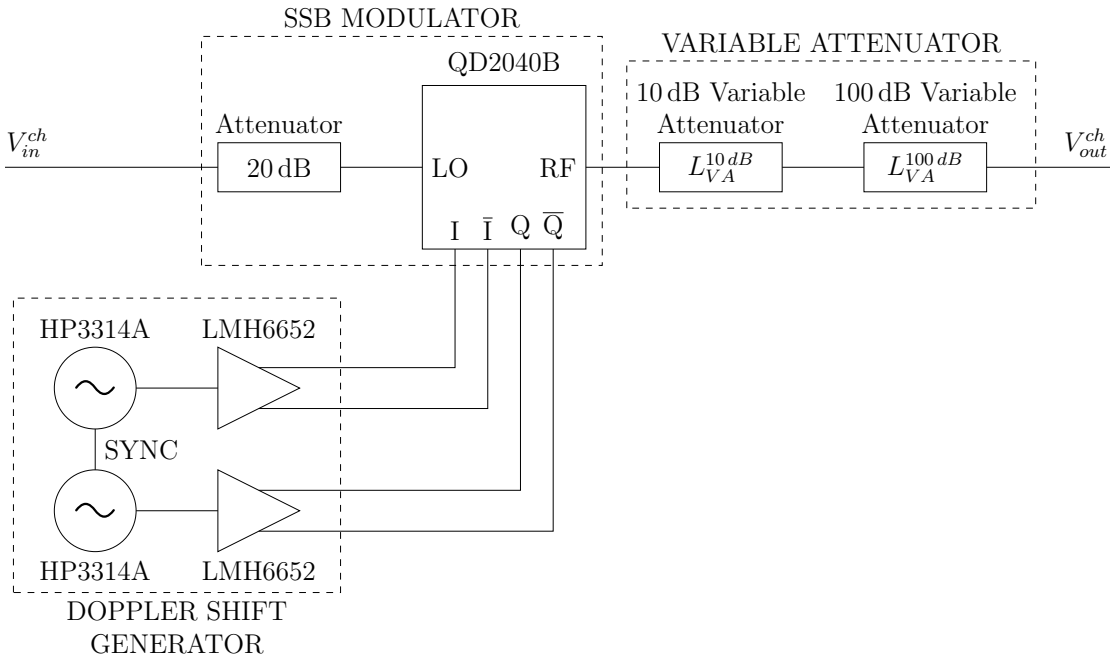

(b)

Figure 9.1: *Open-Loop Test Setup 1.* The open-loop test setup in (a) is used to characterize the radar system. It employs a direct wireless link between the transmitter and receiver. The open-loop channel model is comprised of a SSB modulator, a Doppler shift generator, and a variable attenuator. The open-loop channel model is shown in more detail in (b).

and L_A^{ch} is the additional channel loss due to propagation effects. The open-loop testing is performed in an anechoic chamber, and we assume $L_A^{ch} \simeq 1$. The total channel loss for the open-loop channel model is:

$$L_{ch} = -10\log\left(\frac{G_{A,TX}G_{A,RX}\lambda^2}{(4\pi)^2 r^2}\right) + L_{SSB} + L_{VA}^{10dB} + L_{VA}^{100dB} + L_{cable}[\text{dB}] \qquad (9.2)$$

A range of $r = 2\,\text{m}$ was considered for this experiment; for this range, the first term is equal to 34.5 dB. The loss introduced by the SSB modulator depends on the input power level and thus, the range r; it is $L_{SSB} \simeq 27\,\text{dB}$ for $r = 2\,\text{m}$. The cable loss for this setup is 6.8 dB.

Single-Pulse SNRs and Radar Losses

The single-pulse SNR was calculated for the following test conditions:

(1) The antenna separation is 2.0 m. The SSB modulator is not included in the open-loop channel model, so $f_D = 0\,\text{Hz}$. The variable attenuator introduces $L_{VA} = 35\,\text{dB}$ loss, resulting in a total measured channel loss of $L_{ch} = 77.1\,\text{dB}$.

(2) The antenna separation is 2.0 m. A $f_D = 50\,\text{kHz}$ Doppler shift is employed, and the variable attenuator introduces $L_{VA} = 0\,\text{dB}$ loss, resulting in a total channel loss of $L_{ch} = 69.1\,\text{dB}$.

The theoretical SNR, signal power, and noise power are calculated as follows:

$$\text{SNR}_1^{out} = P_{TX} - L_{ch} - P_N - F_{pulsed}^{RX}[\text{dB}] \qquad (9.3)$$

$$P_{out,S}^{RX} = P_{TX} - L_{ch} + G_{pulsed}^{RX}[\text{dBm}] \qquad (9.4)$$

$$P_{out,N}^{RX} = P_N + G_{pulsed}^{RX} + F_{pulsed}^{RX}[\text{dBm}] \qquad (9.5)$$

where $P_{TX} = 27.7\,\text{dBm}$ is the rms transmitted power, $L_{ch} = 68.3\,\text{dB}$ is the channel loss, $P_N = -87\,\text{dBm}$ is the noise power, $F_{pulsed}^{RX} = 14.8\,\text{dB}$ is the noise figure of

Table 9.1: Theoretical and Measured Results for Open-Loop Test Setup 1

Parameter	$f_D = 0$ Hz	$f_D = 50$ kHz	Theory/Measurement
L_{ch}	77.1 dB	69.1 dB	Measurement
SNR_1^{out}	22.8 dB	30.8 dB	Theory
SNR_1^{pp}	16.9 dB	0.7 dB	Measurement
$P_{out,S}^{RX}$	2.6 dBm	10.6 dBm	Theory
P_S^{pp}	1.0 dBm	6.2 dBm	Measurement
$P_{out,N}^{RX}$	-20.2 dBm	-20.2 dBm	Theory
P_N^{pp}	-15.9 dBm	5.4 dBm	Measurement

the receiver, and $G_{pulsed}^{RX} = 52$ dB is the gain of the receiver. The theoretical SNR, signal power, and noise power are recorded in Table 9.1 for both test conditions.

A data set was taken for each of the test conditions. The results were processed using one million samples, and the SNR, signal power, and noise power were calculated using the following equations:

$$\text{SNR}_1^{pp} = 10\log\left(\frac{P_S^{pp}}{P_N^{pp}}\right)[\text{dB}] \tag{9.6}$$

$$P_S^{pp} = \int_{-f_{sig}-\beta_{int}/2}^{-f_{sig}+\beta_{int}/2} P_{pp}(f)df + \int_{f_{sig}-\beta_{int}/2}^{f_{sig}+\beta_{int}/2} P_{pp}(f)df \tag{9.7}$$

$$P_N^{pp} = \int_{-f_s/2}^{f_s/2} P_{pp}(f)df - P_S^{pp} \tag{9.8}$$

where f_{sig} is the signal frequency, β_{int} is the integration bandwidth, $P_{pp}(f)$ is the measured spectrum, and $f_s = 20$ MHz is the sample rate. The measured values are listed in the table.

For the $f_D = 0$ Hz case, there is a 6 dB difference between the theoretical and measured SNRs. 1.6 dB of the difference can be attributed to the difference in the theoretical and measured signal power levels, which results from radar losses; 1.6 dB of loss is on the order of the 4–5 dB of radar losses noted in Chapter 8. The remaining 4 dB is due to the difference between the measured and theoretical

noise power. In Chapter 8, the measured noise power was also around -16 dBm, which aligns well with the result here.

For the $f_D = 50\,\text{Hz}$, the SNR error is much higher: 30.1 dB. The difference between the measured and theoretical signal power is only 4.4 dB, which is within the range of anticipated radar losses. Most of the error results from the measured noise power; there is a 25.6 dB error in the noise power measurement. As discussed in Section 8.4.2 and illustrated in Figure 9.2, the distortion terms contribute significantly to the measured noise power. The measurement should be repeated with more channel attenuation to establish a more reasonable estimate of the radar behavior. Unfortunately, the PA failed prior to completing the open-loop tests; as a result, the data provided here is only preliminary and more testing should be performed. However, the results thus far are promising and are comparable to the results of closed-loop testing.

9.1.2 Open-Loop Test Setup 2

An open-loop channel model was described in Section 3.6, and the block diagram is repeated in Figure 9.3a for convenience. The output of the transmitter is radiated by the transmit antenna, and the electric field is incident on the channel model antenna. The received signal is Doppler-modulated, attenuated, and re-radiated by the channel model antenna. The Doppler-modulated electric field is incident on the receive antenna, and processed by the receiver and post processor. The utility of this open-loop channel model is limited by the port-to-port isolation of the circulator. The 2–4 GHz circulator discussed in this work provides 20 dB isolation. The SSB modulator attenuates the signal by $L_{SSB} = 27\,\text{dB}$; as a result, the unmodulated radiated leakage signal is higher power than the Doppler-modulated radiated signal. This issue could be mitigated, without replacing any hardware, by adding a piece of coaxial cable between the variable attenuator

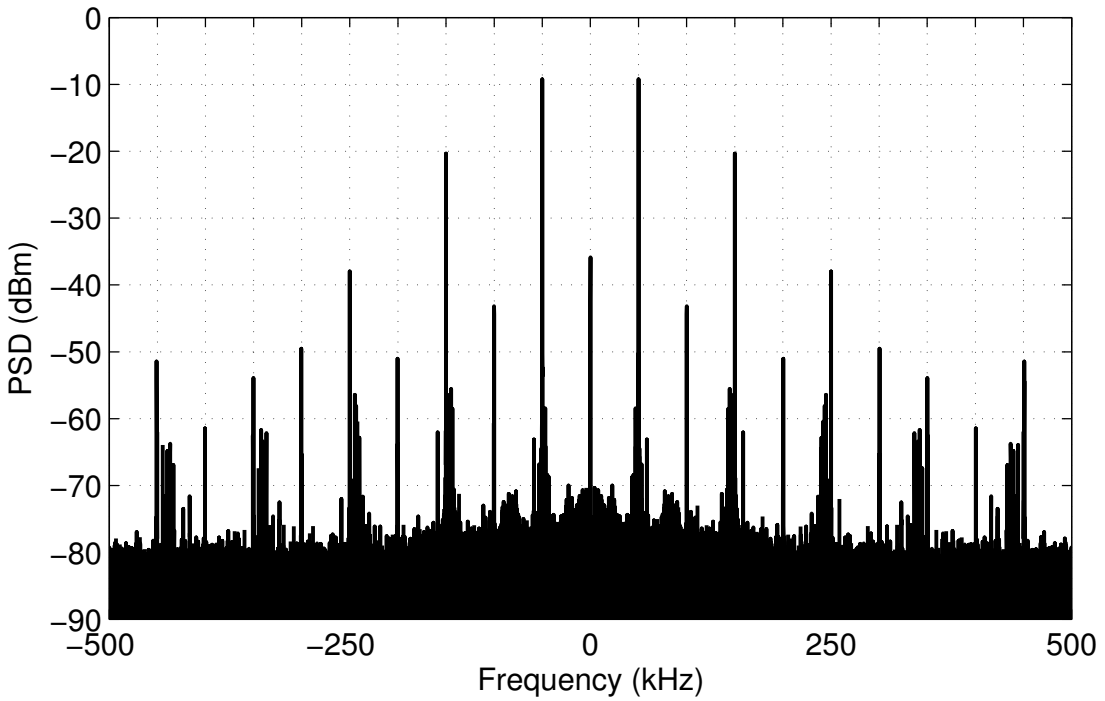

Figure 9.2: *PSD for Open-Loop Test Setup 1,* L_{ch} = 77.1 dB, f_D = 50 kHz. The PSD was calculated using one million samples. Distortion contributes a significant amount of power to the noise power.

and the circulator to produce a short time delay. If the time delay is longer than the transmitted pulsewidth, the undesired leakage signal and the desired Doppler-modulated signal are separated in time. However, this technique does not eliminate or reduce the amplitude of the leakage signal.

A different open-loop channel model architecture, shown in Figure 9.3b, was selected to minimize the impact of the leakage signal. This architecture employs two antennas. In this case, the amplitude of the leakage signal is limited by the coupling between the pair of antennas. For this work, a pair of elliptically-tapered slot antennas were selected (see Chapter 7). The antennas are linearly polarized and are oriented such that they are orthogonal to one another, as noted in the figure; they are separated by 0.5 m. The transmit and receive antennas are placed in the line-of-sight of the channel model antennas; they are oriented to match the

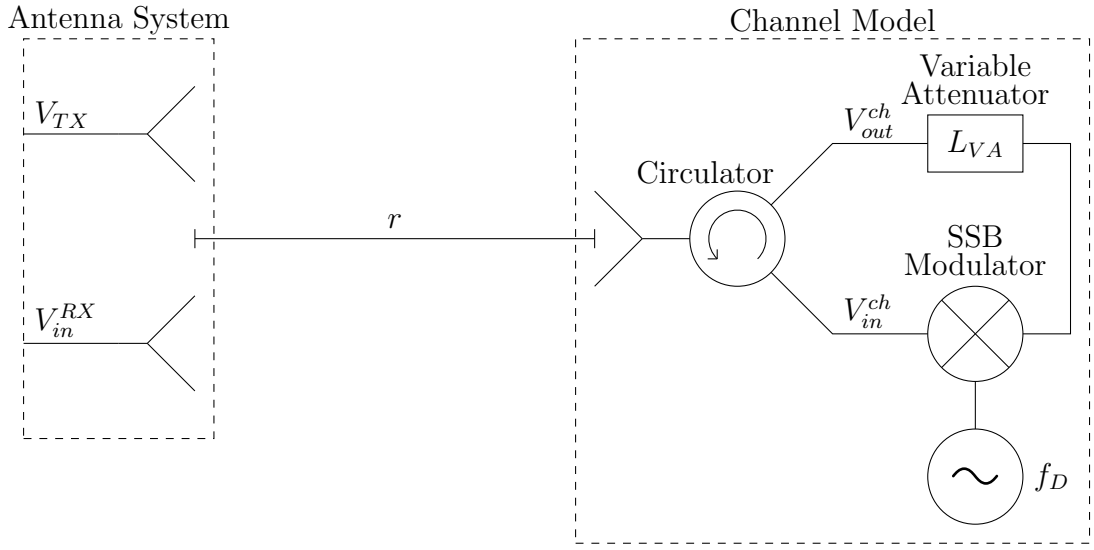

(a)

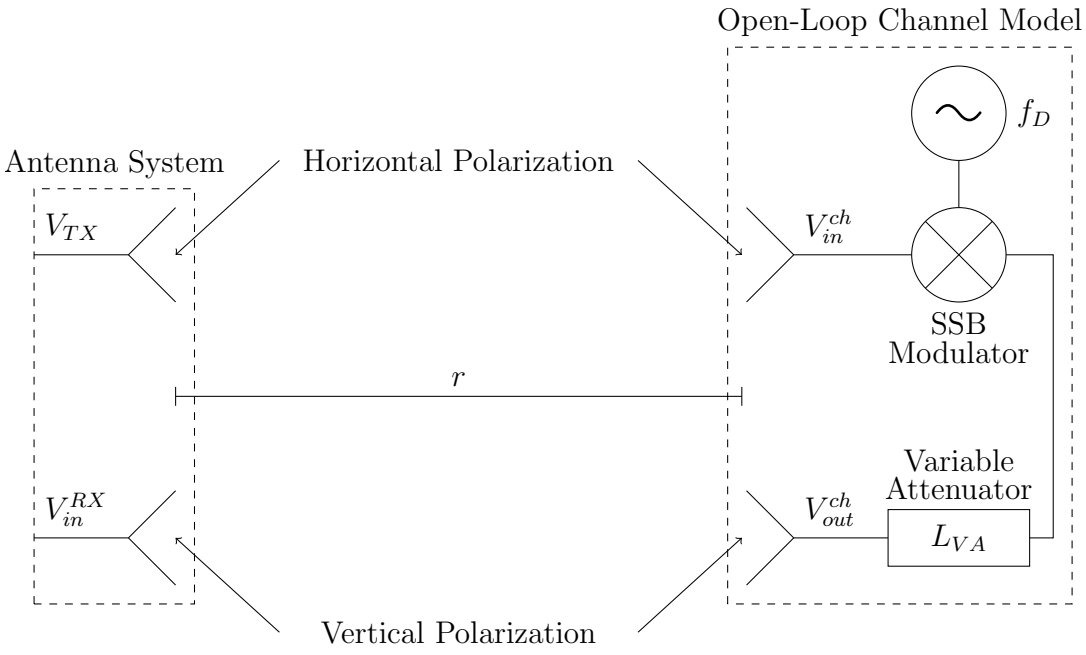

(b)

Figure 9.3: *Open-Loop Test Setup 2.* (a) and (b) illustrate two different open-loop channel models. Both models include a SSB modulator, a Doppler shift generator, and a variable attenuator; these components are detailed in Figure 9.1b. The open-loop channel model in (a) employs a single antenna and a circulator, and the model in (b) employs a pair of antennas. The setup in (b) is employed in this thesis.

polarization of the corresponding channel model antennas and are also separated by 0.5 m. The measured isolation between the channel model antennas is 50 dB at 2.5 GHz. Absorber was used to increase the TX-RX isolation between the transmit and receive antennas, so $I_{TX/RX} = 65$ dB. This is less than the minimum TX-RX isolation of $I_{min}^{TX/RX} = 80$ dB specified in Chapter 8 and can reduce the sensitivity of the radar by up to 15 dB.

The antenna system is separated from the channel model antennas by a distance r such that the antennas are in one another's far field. As before, the Doppler shift is simulated using a SSB modulator and a Doppler shift generator, and additional channel loss can be simulated using a variable attenuator. The open-loop channel model components are implemented as shown in Figure 9.1b.

Channel Losses

As noted in Section 9.1.1, the range equation for the open-loop test setup is different than the standard range equation (see Eqn. (1.3)) because the target is simulated using a wireless link. The radar range equation for this open-loop setup is:

$$P_{in}^{RX} = \frac{P_{TX} G_{A,TX} G_{A,Ch}^2 G_{A,RX} \lambda^4}{(4\pi)^4 r^4 L_{SSB} L_{VA}^{10dB} L_{VA}^{100dB} L_A^{ch}} \tag{9.9}$$

where $G_{A,Ch} \simeq 6$ dB is the gain of each channel model antenna. As before, we assume $L_A^{ch} \simeq 1$ since the measurement is performed in an anechoic chamber. The total channel loss for the open-loop channel model is:

$$L_{ch} = -10 \log \left(\frac{G_{A,TX} G_{A,Ch}^2 G_{A,RX} \lambda^4}{(4\pi)^4 r^4} \right) + L_{SSB} + L_{VA}^{10dB} + L_{VA}^{100dB} [\text{dB}] \tag{9.10}$$

A range of $r = 2$ m was considered for this experiment; for this range, the first term is equal to 69 dB. As in the previous measurement setup, the loss of the SSB modulator is $L_{SSB} \simeq 27$ dB for $r = 2$ m. The cable loss is 4.2 dB.

Single-Pulse SNRs and Radar Losses

The single-pulse SNR was calculated for the following test conditions:

- The antenna separation is 2 m. The SSB modulator is not included in the open-loop channel model, so $f_D = 0$ Hz. The variable attenuator introduces $L_{VA} = 0$ dB loss, resulting in a total measured channel loss of $L_{ch} = 74.0$ dB.

The theoretical SNR, signal power, and noise power are calculated using Eqns. (9.3) – (9.5), and the measured SNR, signal power, and noise power are calculated using Eqns. (9.6) – (9.8). The results are recorded in Table 9.2.

The SNR error for this measurement is 12.1 dB. The difference between the theoretical and measured signal power is 7.6 dB. This amount of radar loss is greater than the 4–5 dB anticipated from closed-loop testing and open-loop test setup 1; this experiment should be repeated to isolate the source of the increased loss. The difference between the theoretical and measured noise power is 4.6 dB and is on par with the result using open-loop test setup 1. As noted above, the PA failed before the open-loop testing was completed. As a result, there is not any measured data using this test setup and a Doppler shift. Additional tests should be performed with various channel attenuations, both with and without Doppler modulation.

9.1.3 Future Open-Loop Testing

Once the PA is replaced, additional open-loop testing can be performed; the closed-loop characterization performed in Chapter 8 can be repeated using an open-loop channel model to determine the radar losses, the impact of finite TX-RX isolation, the minimum detectable range, and other radar characteristics. A substantial improvement to the open-loop channel model would be to replace the SSB modulator with a device that introduces less loss. As discussed in Chapter

Table 9.2: Theoretical and Measured Results for Open-Loop Test Setup 2

Parameter	$f_D = 0$ Hz	Theory/Measurement
L_{ch}	74.0 dB	Measurment
SNR_1^{out}	25.9 dB	Theory
SNR_1^{pp}	13.8 dB	Measurment
$P_{out,S}^{RX}$	5.7 dBm	Theory
P_S^{pp}	-1.9 dBm	Measurment
$P_{out,N}^{RX}$	-20.2 dBm	Theory
P_N^{pp}	-15.6 dBm	Measurment

8, the channel loss should be limited to 100–105 dB based on the sensitivity of the radar. For test setup 2, the minimum channel loss is 101.6 dB, if Doppler modulation is employed. The loss of the modulator (27 dB) severely limits the dynamic range of the open-loop channel model; for test setup 2, it may be too large to reliably detect the target return. As such, it is critical that the loss introduced by the modulator is reduced. If a lower loss SSB modulator with the required bandwidth is not available, a broadband amplifier could be added to the open-loop channel model instead.

The open-loop channel model provides significant testing flexibility. For example, stationary clutter or multipath can be simulated by strategically placing reflectors around the chamber. Moving clutter or multipath can be simulated by building multiple open-loop channel models and placing them as desired around the chamber. Various test setups should be considered to take full advantage of the utility of open-loop testing.

9.2 Potential System Improvements

This thesis successfully demonstrated a short-pulse Doppler radar for short-range target detection; however, it is possible to improve the CPI and LO isolation, increase the efficiency and reduce the DC power consumption, and improve the sensitivity of the radar by implementing a few changes to the existing radar system.

9.2.1 Coherent Processing Interval and LO Isolation

In the current radar design, the transmitter and receiver share a common LO. While this architecture ensures coherent radar operation, it introduces a challenge: the transmitter and receiver VCO paths are linked and must be isolated from one another, as discussed in Section 5.1.2. It is possible to limit interaction between the transmitter and receiver's LO signals by using two separate signal sources, thereby completely separating the RF components of the transmitter and receiver. To maintain coherent radar operation, the two LOs must be phase coherent, which can be achieved by employing two PLLs that are triggered by the digital control circuitry, as illustrated in Figure 9.4. This architecture eliminates any direct hardware connections between the transmitter and receiver.

There is an added benefit of replacing the VCO with two PLLs: the carrier signals and pulse envelope are all triggered by the digital control circuitry and, thus, phase coherent. As discussed in Section 4.2.3, and illustrated in this work, it is not necessary for the envelope and carrier to be synchronized for a homodyne, pulse Doppler radar; however, if they are synchronized, the phase noise is potentially lower, leading to a longer CPI.

The hardware demonstrated in this thesis could be modified using a variety

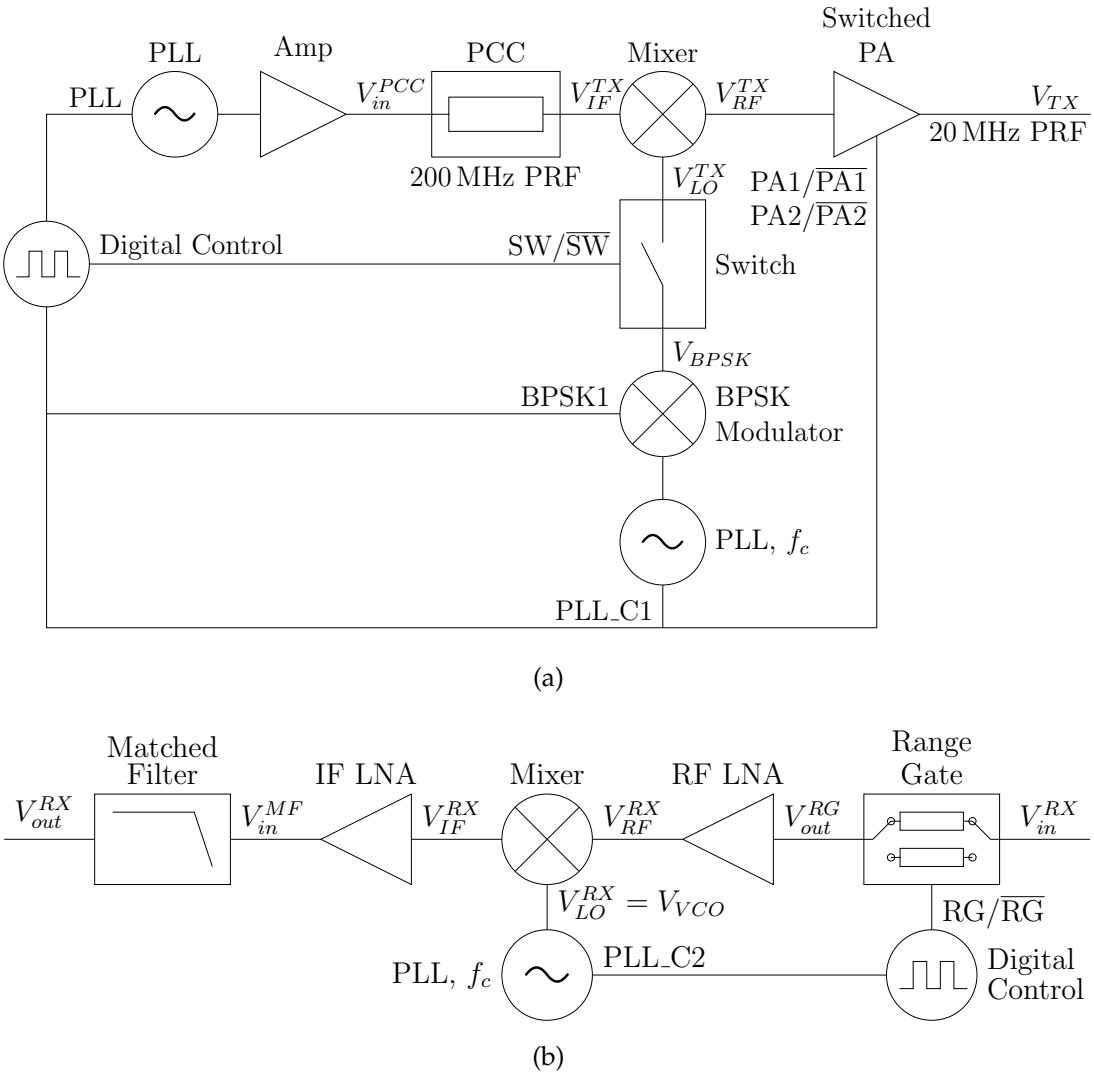

Figure 9.4: *Updated Transmitter and Receiver Block Diagram.* In this work, the transmitter and receiver share a VCO. The LO isolation and CPI can be improved if the VCO is replaced by two synchronized PLLs: (a) one which serves as the transmitter's LO and (b) one which serves as the receiver's LO. There is no direct connection between the transmitter and receiver's LOs in this architecture.

of commercially available PLLs, such as the Analog Devices AD4360-0 PLL.

9.2.2 Efficiency and DC Power Consumption

The short-pulse Doppler radar in this work lends itself to an efficient design with low DC power consumption for three reasons:

(1) The transmitted PRF was selected for both unambiguous range and Doppler detection. As a result, a single PRF can be employed, and the transmitter circuitry can be simpler and more efficient than a transmitter that operates with multiple PRFs. The receiver and post processor designs are also simpler when a single PRF is employed, so both subsystems can be designed for efficiency and low DC power consumption.

(2) The transmitter is designed for short-range target detection ($R \leq 7$ m), so the transmitted power level can be quite low compared to longer range pulse Doppler radars. Lowering the transmitted power requirement reduces the RF gain requirement, thereby reducing the DC power consumption.

(3) The effective bandwidth of the transmitter is $\beta_{eff} = 1.6$ GHz due to the subnanosecond transmitted pulsewidth selected for short-range target detection. As seen in Eqn. (**??**), the achievable range accuracy improves when either the bandwidth or signal power is increased. Since the radar signal is UWB, the signal power can be lower than for a standard, narrowband pulse Doppler radar.

The prototype radar was not optimized for efficiency or DC power consumption, and both can be improved. For example, as discussed in Section 5.1.3, a small attenuator was placed at the output of the PCC to prevent the mixer from operating under compression. The attenuator, and the resulting inefficiency, can

be removed if the PCC is redesigned to operate at a lower output RF power level that is within the linear operating region of the mixer. Alternatively, the mixer can be redesigned with a higher compression point; however, as discussed in Section 5.1.3, this is challenging due to the other mixer specifications.

To design a low-power NLTL-based PCC, a varactor diode must be selected that exhibits a large capacitance ratio over a narrow reverse bias range. For example, the varactor used in this work has a capacitance ratio of $C(V_R = 1\,\text{V})/C(V_R = 6\,\text{V}) = 3$, where C is capacitance and V_R is the reverse bias voltage.[1] If a varactor with a lower reverse bias voltage range but a similar capacitance ratio is selected, the input and output voltage levels could be reduced while maintaining the desired pulsewidth. While a few discrete varactor diodes with lower reverse bias ranges exist, it is likely that an integrated approach will be required. Changing the varactor impacts other properties of the PCC, including the characteristic impedance and the corner frequency, both of which are critical to the operation of the PCC. As such, careful consideration must be given to an updated NLTL-based PCC design.

9.2.3 Sensitivity

As discussed in Chapter 8, the sensitivity of the radar is degraded by any radar losses and leakage signals. As shown in Table 8.4, the radiative leakage power for the radar system is about -19 dBm. This is on the order of the total noise power; since the leakage power contributes to the noise calculation, it degrades the sensitivity of the radar. The leakage power could be reduced by rearranging the transmitter and receiver components, sealing the seams of all of the metal boxes, or adding absorptive material between the components. Since the theoretical noise power and the measured leakage power are comparable in the current

[1] Measured at 1 MHz

setup, the noise floor is increased by about 3 dB due to the leakage signal; if the leakage power is reduced, the sensitivity of the radar could potentially be improved by 3 dB.

The noise power at the output of the receiver also limits the sensitivity of the radar. In the current setup, the noise figure of the receiver is $F_{RX} = 14.8$ dB; the insertion loss of the range gate is $L_{RG} = 9.5$ dB. Since it is the first component in the receiver chain, it limits the minimum achievable noise figure of the receiver. The range gate could be placed at the output of the RF LNA or between the two RF LNA stages instead; the new noise figure would be approximately 4–5 dB, resulting in up to 10 dB improvement in sensitivity. If the range gate is moved, the receiver gain should be increased to ensure the noise power at the output of the receiver is sufficient to toggle at least the LSB of the ADC when the full-scale voltage is $V_{fs} = 5$ V, as discussed in Sections 3.5 and 6.4.

9.3 Application-Specific System Improvements

The radar prototype in this work was designed for a generic short-range application. Various receiver, post processor, and antenna system parameters can be adjusted to optimize the radar performance for a specific application; alternate architectures can also be employed.

9.3.1 Advanced Receiver and Post Processor Architectures

The integration time for the radar in this work is 36.5 µs ($N = 730$). While this worst-case integration time is sufficient to meet the goals for the prototype

radar, it may not be sufficient for some applications. For example, the frequency resolution is limited to $f_s/N = 27.4\,\text{kHz}$. If the exact target velocity is of interest, the number of samples should be increased. Increasing the number of samples also improves the sensitivity of the radar. As such, it is worthwhile to consider techniques to improve the integration time of the radar.

The first, and simplest, option is to integrate more samples. This option is viable, depending on the application.

If the overall integration time cannot be increased, it is possible to instead increase the transmitted pulsewidth. As discussed in Section 2.3, one goal of this work was to minimize the shortest detectable range by employing a subnanosecond transmitted pulsewidth. Time-domain SNR response testing indicates that the minimum detectable range is $R_{min} = 1.3\,\text{m} + R_{lk}$, were R_{lk} depends on the antenna system design. Depending on the application, a longer minimum range may be acceptable; if such is the case, the transmitted pulsewidth and, thus, the integration time (see Eqn. (3.12)) can be increased.

A third option is to increase the sample rate of the post processor. In the current system, the digitizer only samples the received signal once per PRI, so the sample rate could be increased to collect multiple signal samples for each received pulse. For this technique to be effective, the sample rate must be high enough to sample the pulse multiple times during the 730 ps pulsewidth of the signal, so the sample rate should be $f_s \geq 1/\tau = 1.4\,\text{GHz}$. An ADC that is capable of sampling at this rate is currently state-of-the-art and likely to be prohibitively expensive. As such, increasing the sample rate is not a cost-effective option at this time. Alternatively, it is possible to effectively increase the sample rate without increasing the ADC requirements by channelizing the post processor as in the architecture shown in Figure 9.5a [154]. The received radar signal is power divided to form multiple channels. Each channel is delayed in the time domain

by a different amount before being digitized by an ADC; the result is multiple samples of a single pulse, as illustrated in Figure 9.5b. The relative time delay, Δt in the figure, defines the new, effective sample rate: $f_{eff}^{S} = 1/\Delta t$. The number of channels should be limited so the total sample time is $C\Delta t \leq \tau$, where C is the number of channels; this limit is set to minimize the number of noise-only samples. This technique increases the complexity of the post processor.

A fourth option is to employ multiple receiver channels that are set to sample the received signal at slightly different ranges, as illustrated in Figure 9.6. In this architecture, multiple range bins are employed. For example, channel one could sample the signal at R_{obs}, channel two could sample the signal at $R_{obs} - c_o\tau$, and channel three could sample the signal at $R_{obs} - 2c_o\tau$. As the moving target approaches the radar, it would be visible at range one, then range two, then range three; the radar would effectively track the target's progress, allowing a longer integration time. This technique increases the amount of receiver hardware that is required and increases the complexity of the post processor.

A final option is to employ range tracking techniques to adjust the sample point of the post processor so that it tracks the peak of the received signal. As illustrated in Figure 9.7, a feedback loop is required to adjust the sample point based on the sampled output of the ADC. As discussed in [72], this technique can be quite useful in extending the integration time of a UWB signal; however, it can complicate clutter rejection. In addition, this technique adds a layer of complexity to the post processor design (and potentially the receiver design) as it requires the implementation of a tracking algorithm.

9.3.2 Antenna System

The antenna system in this thesis is a generic two antenna design to demonstrate the radar capabilities. The transmit and receive antennas can be redesigned

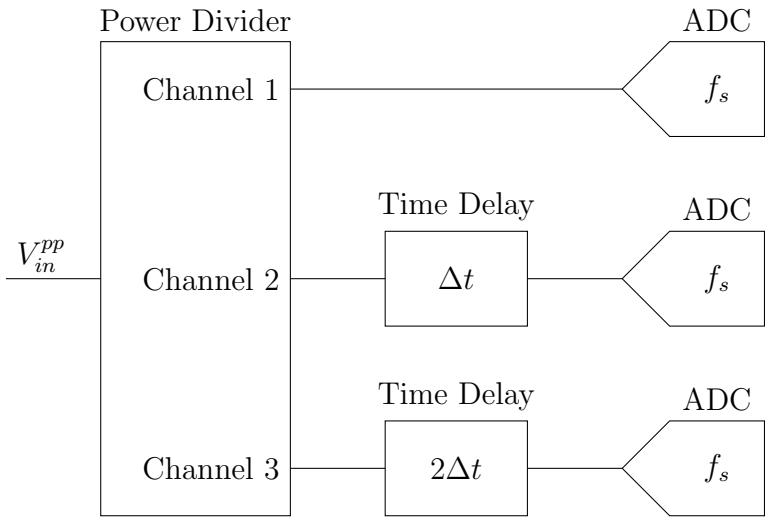

(a)

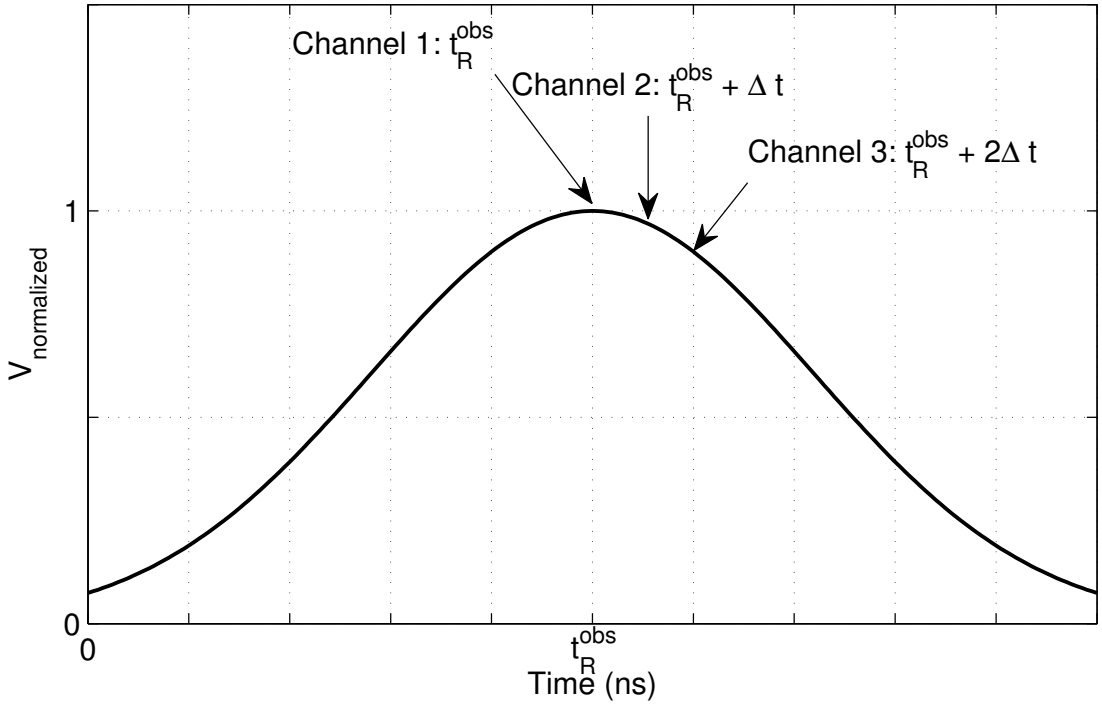

(b)

Figure 9.5: *Channelized Post-Processor Design.* (a) The sample rate of the radar can be effectively increased by channelizing the post processor in the time domain (Adapted from [154]). (b) The new sample points are illustrated in the normalized, received waveform.

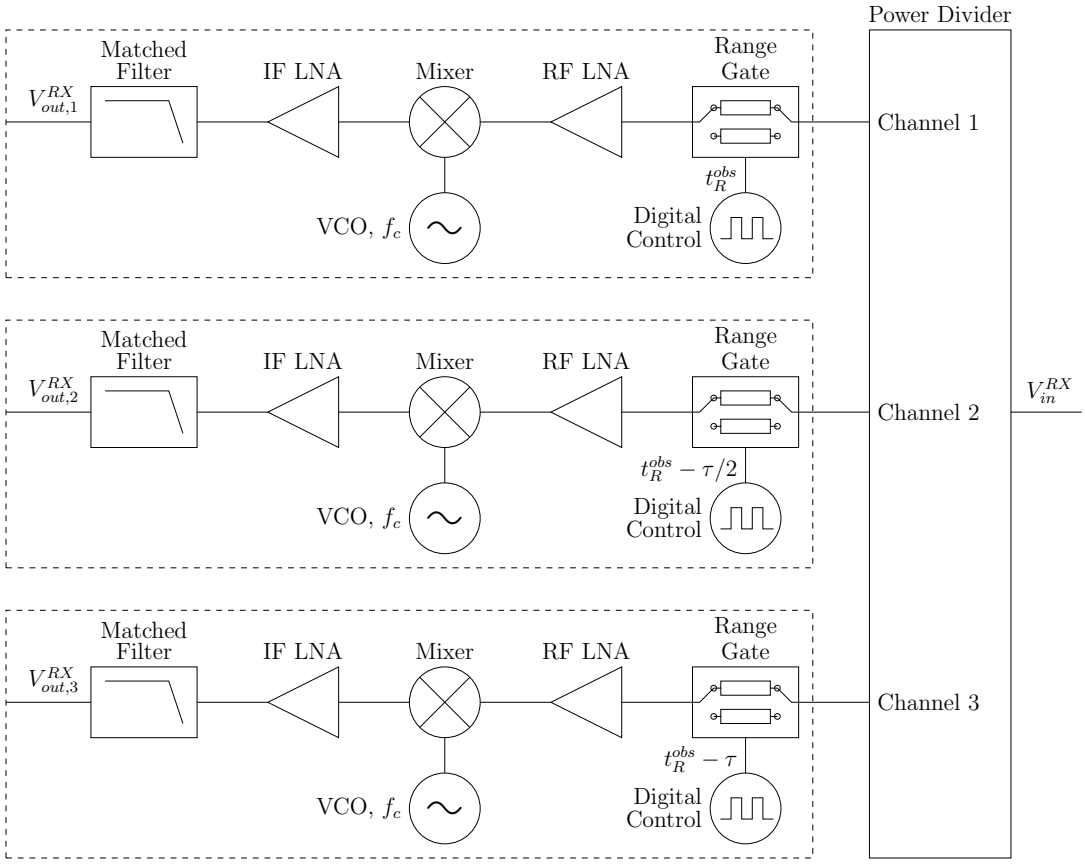

Figure 9.6: *Channelized Receiver Design.* Multiple receiver channels can be employed to allow additional range bins and a longer integration time.

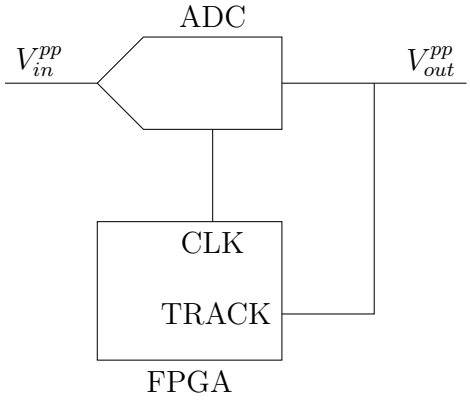

Figure 9.7: *Range-Tracking Post Processor.* The integration time of the radar can be increased by implementing a feedback loop that dynamically adjusts the sample point to track the peak of the sampled signal as the target range changes.

given a specific application. In addition, the mechanical supports for the antenna system can be built to enclose the transmitter and receiver, once the radar components have been integrated.

9.4 Radar Testing

The closed- and open-loop channel models in this thesis were designed to perform basic radar characterization. For future radar development, it could be helpful to expand the capabilities of the testing setups. Potential improvements to the open-loop channel model were discussed in Section 9.1.3.

The closed-loop testing capabilities could be expanded to include the impact of TX-RX isolation and multipath. The current closed-loop channel model facilitates a variety of measurements, including radar sensitivity and TX-RX isolation characterization; however, it only has a single channel and can only characterize one parameter at a time. If additional channels are added, as shown in Figure 9.8, radar sensitivity measurements could be performed while accounting for nonidealities such as finite TX-RX isolation or multipath. The attenuation, time delay, and Doppler shift of each channel could be adjusted as desired, and the nonidealities could be accounted for in a controlled, predictable manner.

After the radar is well characterized, it is desirable to observe how it operates in the field. A realistic moving target can be selected based on the desired application.

9.5 RF Circuit Integration

The prototype radar in this work is quite large; as shown in Figure 8.4, it occupies a full test bench. An important next step is to miniaturize the radar components;

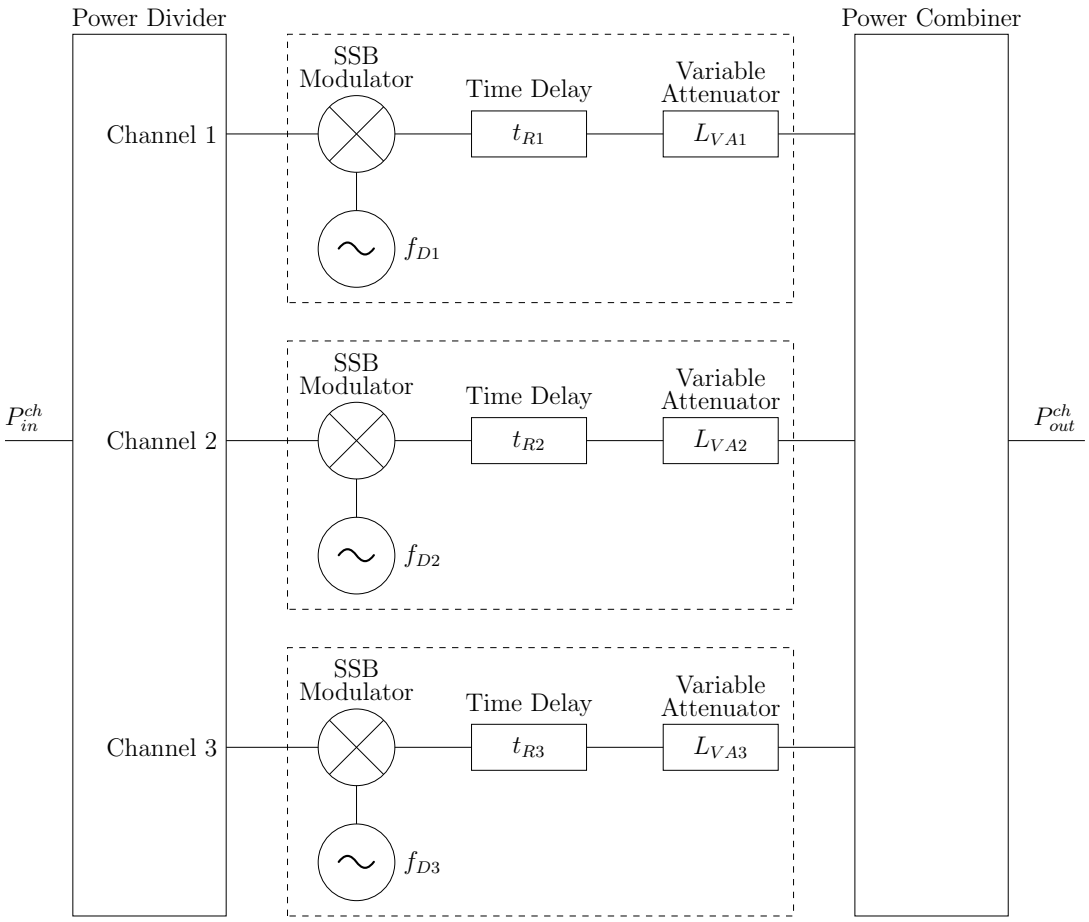

Figure 9.8: *Closed-Loop Channel Model with Multiple Channels.* The closed-loop channel model can include multiple channels to simulate, in a bench-top measurement, the impact of TX-RX isolation or multipath. Each channel can include a unique channel attenuation, time delay, and Doppler shift.

this can be achieved by redesigning each component as a MMIC. The challenges and potential paths forward for the various components are presented in the following sections.

9.5.1 Short-Pulse UWB Circuits

The PCC, switches, switched PA, and range gate impact the transmitted pulsewidth and the on time of the receiver. As a result, they must be capable of high switch rates; these designs are critical to the operation of the UWB pulse Doppler radar.

Pulse Compression Circuit

The PCC in this work operates with a PRF of 200 MHz and produces 730 ps FWHM Gaussian-like basedband pulses. The integrated pulse generator should operate with a comparable output. As discussed in Section 9.2.2, one potential improvement to the PCC design is to limit the output voltage to complement the compression point of the upconverter. As such, it will be advantageous to consider the PCC and upconverter designs simultaneously.

Numerous examples of integrated NLTL-based pulse generators exist in the literature. However, most of these examples operate with higher PRFs and narrower pulsewidths than are desired for this work [101], [155], [156]. As discussed in Section 4.3, the phase velocity, characteristic impedance, and cutoff frequency of the NLTL-based PCC all depend on the nonlinear capacitance of the diode. The capacitance range must be wide enough to compress the input sinusoid, and it must be large enough to limit the cutoff frequency of the circuit to about 200 MHz. In addition, the combination of the inductance and capacitance of the line should result in a reasonable range of characteristic impedances centered around 50 Ω.

An integrated PCC was designed in Triquint's TQPED pseudomorphic high electron mobility transistor (pHEMT) process. At the time, varactor diodes were not available in the process, so diode-connected pHEMTs were used instead; the diode-connected pHEMTs behaved as weak varactor diodes under reverse bias. Several pHEMTs were connected in parallel to increase the nonlinear capacitance, and discrete inductors were employed; an *LC* section of an NLTL-based PCC is illustrated in Figure 9.9a. A photograph of the die is shown in Figure 9.9b. The total chip area is 25 mm^2, and three different designs were placed on the chip. The lowest possible input frequency was limited to 1.1 GHz due to the total capacitance of the parallel diode-connected pHEMTs; for lower frequencies, the

output is rectified but not compressed. While the PCCs worked as designed, they can not be used for the radar in this work due to their 1.1 GHz PRF. It will be important to design a nonlinear capacitance, using transistors or diodes, that is large enough to allow low frequency operation.

The new integrated PCC does not have to be discrete; the discrete inductors can be replaced with microstrip or CPW transmission lines at the designer's discretion. In addition, an NLTL-based oscillator topology, as in [103], [104], can be considered; if an oscillator is designed, it must be phase-locked to the digital control signal to ensure coherence between the pulse envelope and the post processor's sample clock.

Switches

A switch must be designed to gate the LO signal in the transmitter, as shown in Figure 3.2. The on, off, rise, and fall times must all be subnanosecond to gate the pulse at a rate of 20 MHz with no more than 10% duty cycle. The isolation must be sufficient to ensure the LO signal power is below the LO threshold of the mixer when the transmitter is supposed to be off. In the current architecture, the switch must pass a 2.5 GHz signal and may be narrowband. If the switch is designed to cover the full 2–3 GHz bandwidth of the radar, it may be adapted for use in the range gate design.

A switch may be designed using diodes or transistors; examples of switch architectures and helpful design considerations are covered in [157]. The Triquint switch in this work is a transistor-based design on a GaAs substrate. A variety of fast, UWB CMOS switches have been demonstrated in the literature [158], [159]. Several UWB switches have been designed for the 24 GHz automotive UWB band, such as the SiGe design in [160]; while the switches were designed for a different frequency band, the topologies could be adapted to work at S-band.

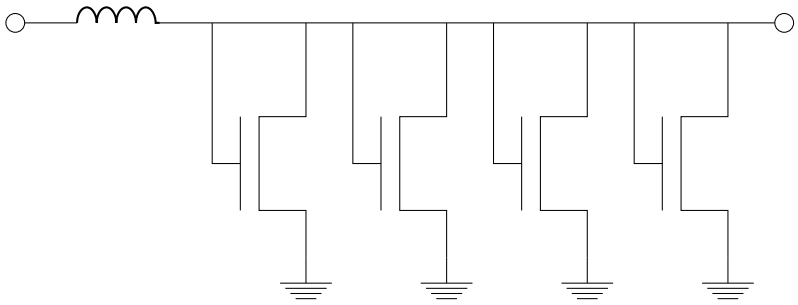

(a)

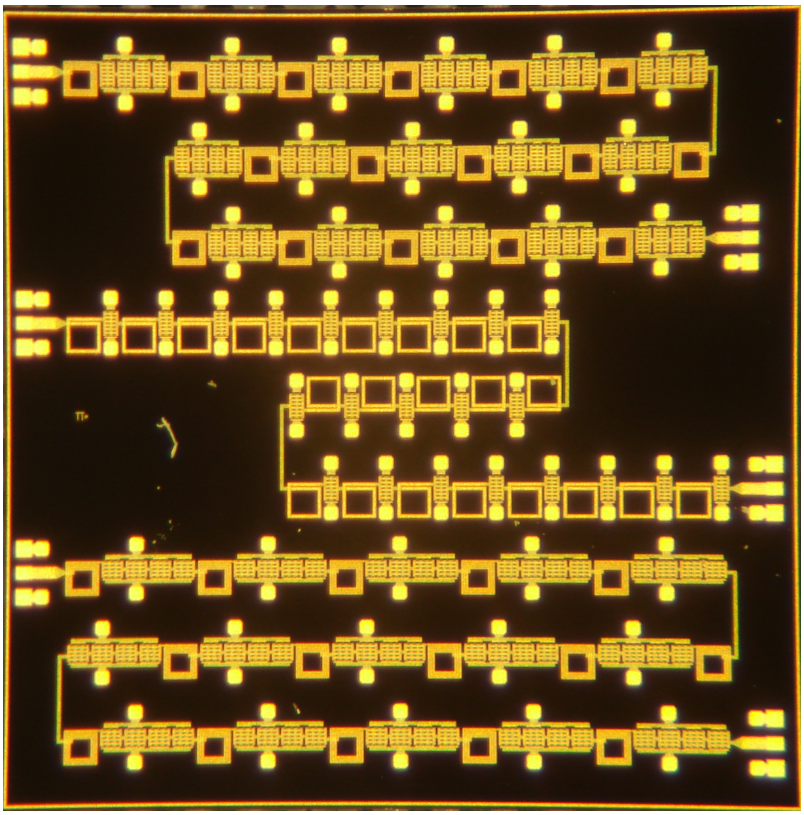

(b)

Figure 9.9: *Integrated NLTL-Based PCC.* An integrated NLTL-based PCC was designed in Triquint's TQPED process. (a) An *LC* section is illustrated in (a), and the photographed die is shown in (b). The die size is 5 mm by 5 mm; three PCCs are included on the die.

Switched PA

The switched PA in this thesis is a 2–3 GHz class-A amplifier, which is implemented as a PA followed by a pair of switches. The gain of the current PA is 22 ± 1.5 dB, and the PA provides 41 dB of transmitter on-off isolation. The MMIC PA should at least meet, if not exceed, the gain and on-off isolation specifications and operate linearly from 2–3 GHz when the amplifier is on. However, rather than switching the output of the PA on and off as needed, the PA itself should be switched.

First, it is important to consider how a wideband PA is designed. A variety of techniques have been put forth in the literature, including balanced amplifiers, resistive feed-back amplifiers, and distributed amplifiers [25], [161]. [162] presents a 0.01–2.4 GHz, 5 W PA with 8 ± 0.5 dB gain on SiC that employs resistive feedback. [163] describes a 0.03–2.5 GHz, 2 W amplifier with 21 ± 1 dB gain designed in GaAs using an architecture referred to as a high-voltage, high-impedance FET (HIFET) configuration, in which the transistors are stacked drain to source. [164] demonstrates a distributed amplifier designed on GaAs that operates from 1–20 GHz with 12 ± 1 dB gain; the saturated output power is 10 dBm. Whatever topology is selected it is vital that the amplifier does not distort the transmitted pulse envelope.

Next, consider how the PA can be switched. In a common-source topology, the drain voltage can be modulated to turn the amplifier on and off at a rate of 20 MHz with a 10% duty cycle; as a result, the drain modulation removes the need for the switches at the output of the PA. The bias network design for the PA can be challenging when high frequency drain modulation is employed. Traditionally a shunt capacitor bank is used to isolate the DC power supply from the incident RF signal. The 20 MHz control signal would have to drive the large capacitance, limiting the rise and fall times of the signal. As discussed in [165],

the capacitor bank can be removed and the bias circuitry redesigned to ensure the PA can switch at the desired rate.

Range Gate

The range gate in this work is implemented as a switched attenuator that operates from 2–3 GHz with 49 dB on-off isolation; it switches at a rate of 20 MHz with a duty cycle of 20%. The MMIC range gate should meet these minimum specifications; if possible, a lower duty cycle is desirable. A variety of topologies can be employed to design a switched attenuator, as discussed in [166]. The high-speed switching techniques discussed in [157] can be used to meet the switching speed requirements.

It is possible to implement the range gate using a single-pole, double-throw (SPDT) switch or by switching the power supplies on the amplifiers in the receiver. Switching all of the power supplies in the receiver is more complicated than using a switch or switched attenuator and is probably not the best option.

9.5.2 UWB Circuits

Several of the radar components, such as the LNAs, mixers, and filters, warrant extra attention as they must cover the 2–3 GHz bandwidth of the radar; however, they do not have the same stringent timing constraints as the components in the previous sections.

LNAs

The RF LNA in this work consists of two stages that operate from 2–3 GHz with 20 ± 1 dB gain and a noise figure of 3.5 dB. The IF LNA operates from 1–500 MHz with 34 dB gain and a noise figure of 3 dB. The integrated replacements should

meet these minimum requirements; as discussed in Section 9.2.3, the gain can be increased to improve the sensitivity of the radar.

As with the PA, a variety of techniques can be used to design wideband LNAs. [167] presents a 3.1–10.6 GHz CMOS distributed amplifier with 16 dB gain and a 3.2–6.0 dB noise figure. [168] presents a dual-gate transistor amplifier with resistive feedback designed in GaN; it operates from 0.3–3 GHz with 17.7 dB gain and a 1.2–2 dB noise figure. [169] illustrates a 3–10 GHz resistive-feedback SiGe amplifier with 20 dB gain and a 3.1–4.5 dB noise figure. [170] demonstrates a complimentary CMOS amplifier with 20 dB gain and a 2.4–3.4 dB noise figure from 2–10 GHz.

[171] presents a GaAs amplifier; it is not optimized as an LNA. However, it introduces a negative group delay circuit that equalizes the total group delay of the amplifier, resulting in flat group delay from 3.1-10.6 GHz. This technique can be applied to other UWB circuits as well.

Upconverter and Downconverter

The upconverter and downconverter in this work operate with a 0–1 GHz IF bandwidth and a 2–3 GHz RF and LO bandwidth. The P1dB point of the mixers is 17 dBm. These bandwidth specifications should be maintained for the upconverter; the IF bandwidth of the downconverter can be reduced to 500 MHz if needed. As discussed in Section 9.2.2, the PCC and upconverter should be designed simultaneously to determine the P1dB specification. The P1dB point of the downconverter can be reduced, but will impact the final dynamic range of the receiver. As such, the desired dynamic range of the receiver must be considered when specifying the P1dB point of the downconverter.

A variety of integrated UWB mixers have been illustrated in the literature. Gilbert-cell mixers [96], [172] –[175]; resistive-ring mixers [176], [177]; and

distributed mixers [178] have been successfully demonstrated. Any of these topologies can be explored. [176] presents a image reject mixer. As discussed in Section 6.1.3, an image reject mixer is not needed for this work. However, a quadrature demodulator, which is needed for an image reject mixer, can be useful for this radar system. If the quadrature outputs of the mixer are processed separately, additional processing gains can be achieved due to the vector nature of the signal [179].

Filters

Many UWB filters have been demonstrated in the literature. Many employ coupled transmission lines; a few examples are provided in [180] –[184]. Two 2–4 GHz coupled-line bandpass filters were designed on Rogers 4003 as part of this work, following [185]. The layouts are presented in Figure 9.10; a ground plane covers the back side of each board. As can be seen, the input and output feedlines are 50 Ω and are stepped to a higher impedance line. The high impedance line is capacitively coupled to a stepped-impedance resonator. The difference between the two designs is the discontinuity between the high- and low-impedance sections of the resonator.

The filters were simulated in Agilent's ADS, Agilent's Momentum, and Ansoft's HFSS and measured using a precision network analyzer (PNA). The resulting S-parameters for the design in Figure 9.10a are plotted in Figure 9.11; there is excellent agreement between simulation and measurement. The filter demonstrates a minimum of 10 dB match and $S_{21} = -0.6 \pm 0.4$ dB from 1.7–3.9 GHz. The simulated and measured group delays are plotted in Figure 9.12; the group delay only varies by ±100 ps over the 2.0–3.8 GHz band. The behavior of the filter in Figure 9.10b is comparable.

The filter performance could be improved further by focussing on the 2–

3 GHz bandwidth of the radar. If a coupled-line filter is used in the radar design, particularly in the receiver design, it should be well shielded. The design presented here is resonant in the 2–4 GHz range and can serve as a poor receiving antenna for leakage signals.

Circulators and Isolators

A circulator is employed in the current radar design, and circulators or isolators could be necessary in the integrated radar design. Wideband, active isolators [186] –[189] and circulators [190] have been demonstrated in the literature. The designs utilize transistors rather than ferrites and have been designed on various substrates, including SiGe [188] and GaAs [186], [189], [190]. An active circulator or isolator could prove useful in future iterations of the UWB radar design.

9.5.3 Narrowband Circuits

A variety of narrowband circuits are required for the radar design:

- *Phase-Locked Loops.* A 200 MHz PLL is required for the transmitter. A pair of 2.5 GHz PLLs are required to replace the VCO, as discussed in Section 9.2.1.
- *BPSK Modulator.* A 2.5 GHz BPSK modulator is required; it must switch at a rate of 20 MHz with a 10% duty cycle.
- *Digital Control.* A digital controller, like the FPGA, is required to generate the control signals listed in Table 3.1.
- *Voltage Regulators.* A variety of voltage regulators are required to produce the DC supply signals for the radar.

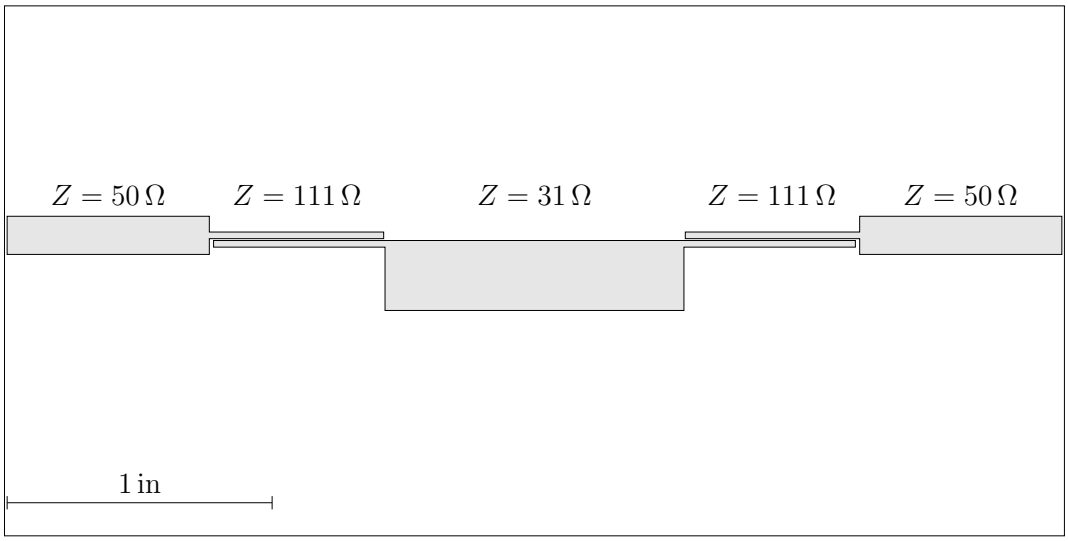

(a)

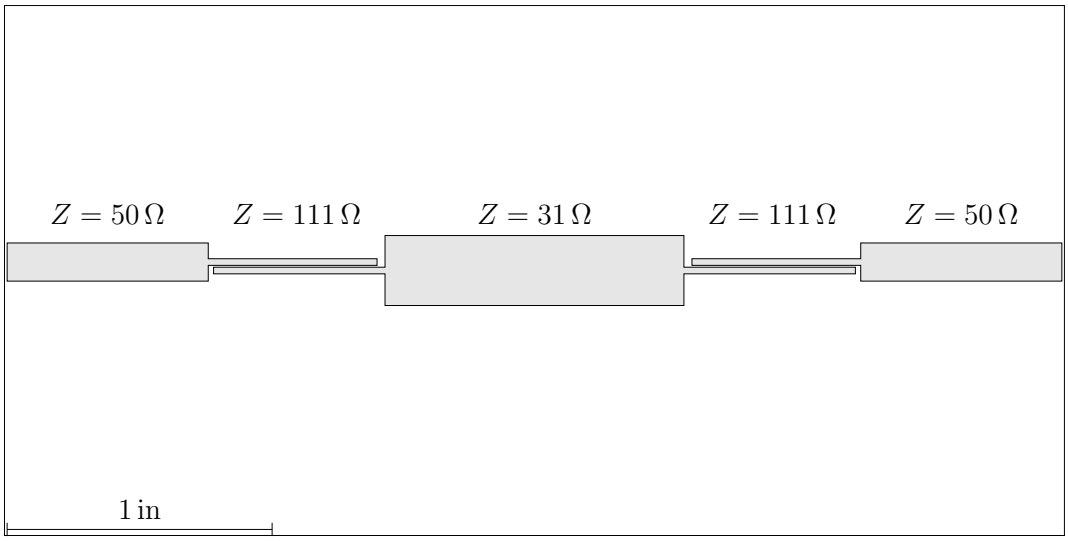

(b)

Figure 9.10: *Stepped-Impedance, Coupled-Line Filters.* The layouts for a pair of 2–4 GHz filters are illustrated in (a) and (b). In both cases, the Rogers 4003 substrate is backed with a ground plane; the boards are sized as indicated by the outlines.

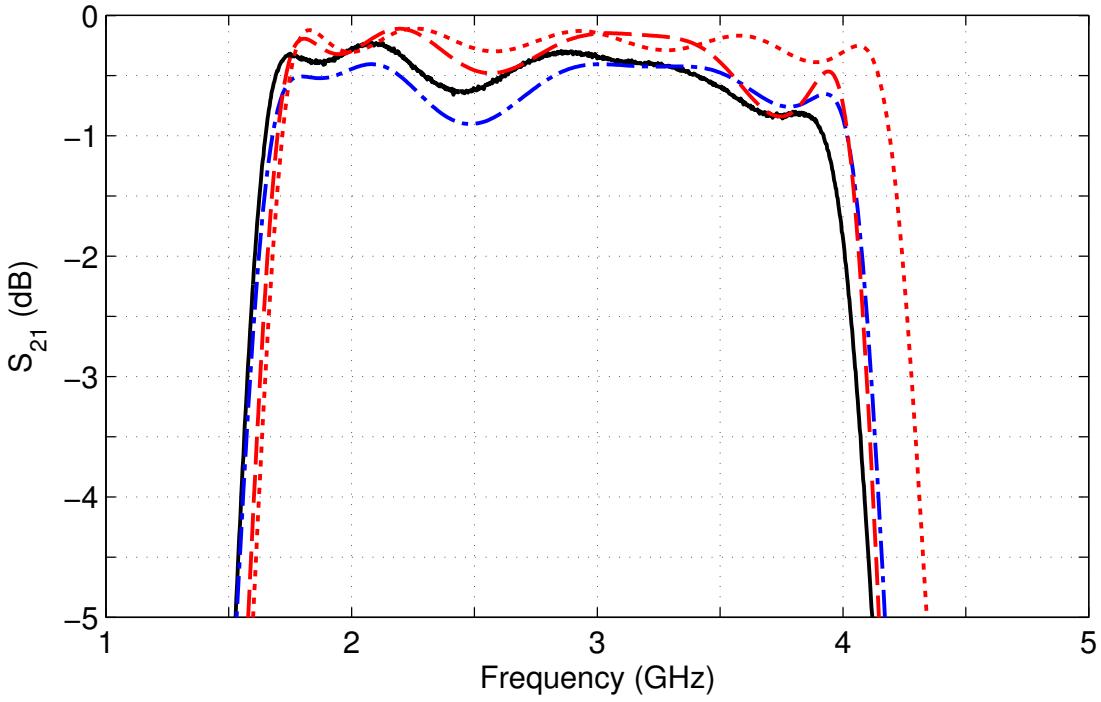

(a)

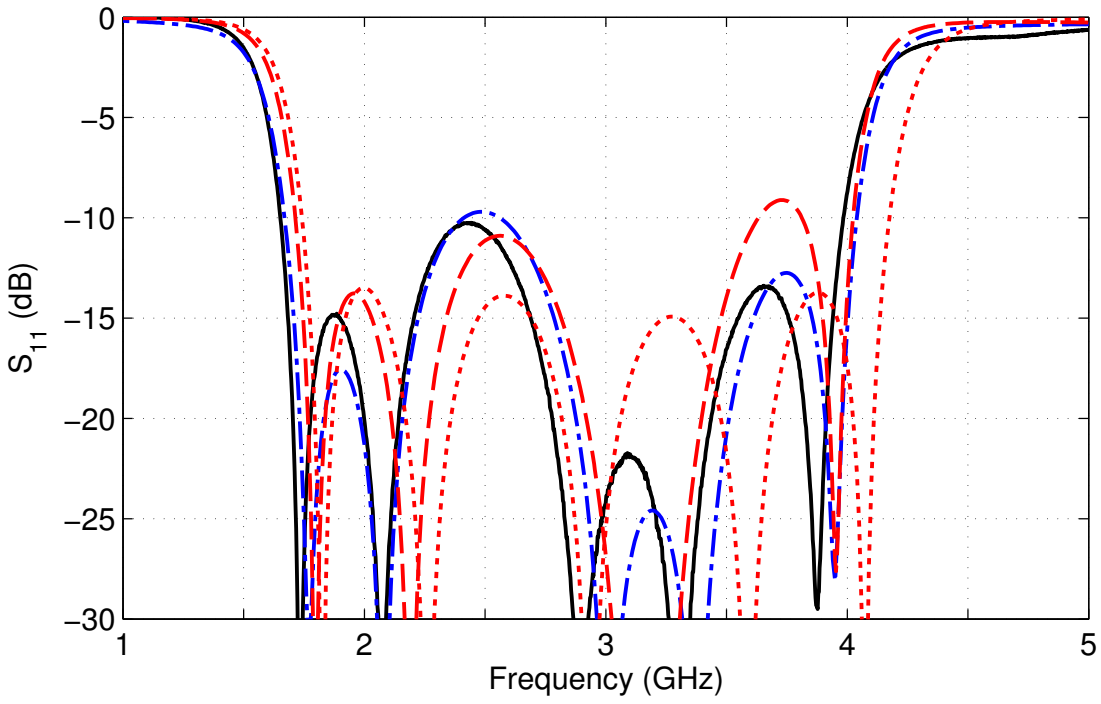

(b)

Figure 9.11: *Stepped-Impedance, Coupled-Line Filter S-Parameters.* The simulated and measured S-parameters for the filter shown in Figure 9.10a are plotted. The measured data is plotted in black solid lines; the HFSS results are plotted in blue, dot-dashed lines; the Momentum results are plotted in red, dashed lines; and the ADS results are plotted in red, dotted lines.

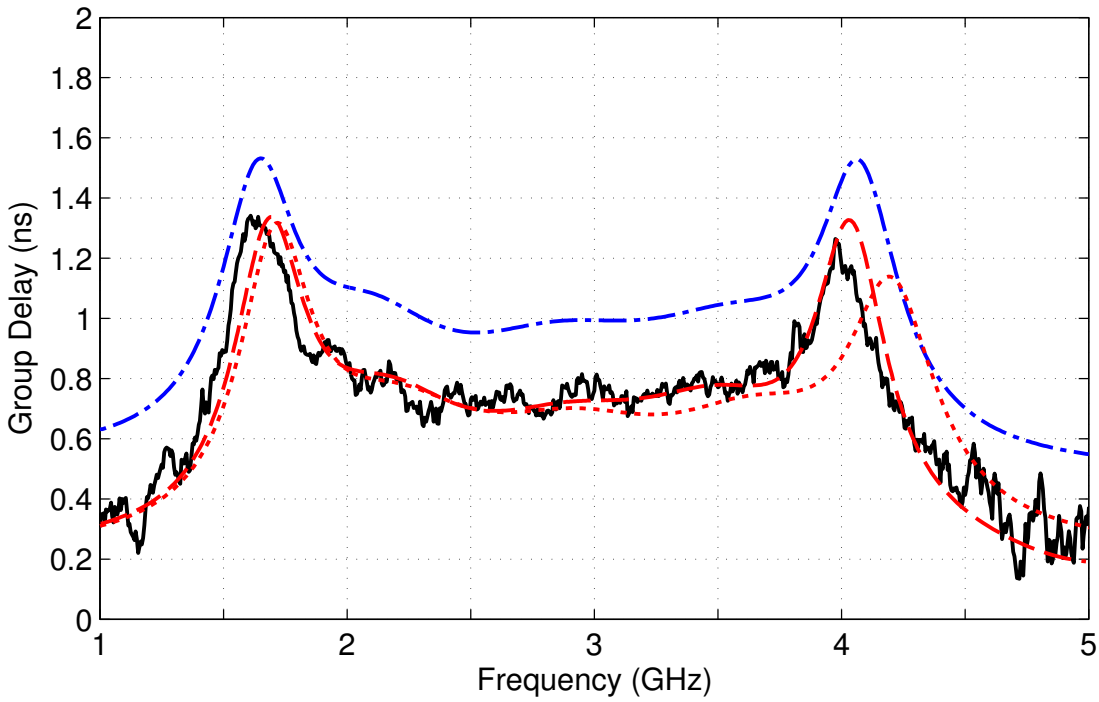

Figure 9.12: *Stepped-Impedance, Coupled-Line Filter Group Delay.* The simulated and measured group delays for the filter shown in Figure 9.10a are plotted. The measured data is plotted with a black solid line; the HFSS results are plotted with a blue, dot-dashed line; the Momentum results are plotted with a red, dashed line; and the ADS results are plotted with a red, dotted line.

9.5.4 Packaging

The radar in this thesis uses metal boxes to isolate the various radar components. For the integrated design, clamshells can be used instead. Due to the smaller footprint of the integrated components, the clamshells are unlikely to suffer from resonances, as occurred with the metal boxes in this work.

9.6 Summary and Contributions

In summary, this thesis presents, for the first time, an implementation of a short-pulse Doppler radar that employs UWB design techniques to detect a target at short range ($R \leq 7$ m). The radar is implemented at S-band with a transmitted

FWHM pulsewidth of 730 ps and 10 dB-bandwidth of 1 GHz. The results of closed-loop testing are summarized in Table 9.3. The specific contributions of this thesis can be summarized as follows:

- A set of desired radar characteristics were analyzed, and subsystem specifications were developed for the transmitter and receiver [191].
- A transmitter architecture was developed, based on a homodyne, pulsed transmitter architecture, that allows subnanosecond pulse generation with an adjustable PRF [191].
- A transmitter architecture was developed that lends itself to an efficient design with low DC power consumption by capitalizing on the unique requirements for a radar that detects targets at short range. Specifically, the bandwidth and single PRF of the transmitter can be exploited.
- A simple, low-component count pulse compression circuit was designed as the pulse generator for the UWB transmitter [191].

Table 9.3: UWB Pulse Doppler Radar Parameters

Parameter	**Symbol**	**Value**
Minimum Detectable SNR (N = 730)	$\mathrm{SNR}_{1,min}^{out}$	0 dB
Maximum Channel Attenuation	L_{max}^{ch}	100–105 dB
Coherent Processing Interval	—	5 ms
Integration Time (N = 730)	—	36.5 µs
Radar Turn-Off Time ($I_{TX/RX}$ = 80 dB)	t_{to}	3.5 ns
Radar Turn-Off Rate ($I_{TX/RX}$ = 80 dB)	R_{to}	11.1 dB/ns
Minimum Range ($I_{TX/RX}$ = 80 dB)	R_{min}	1.3 m + R_{lk}
Range Accuracy (SNR_1^{out} = 0 dB)	δR	±0.03 m
Out-of-Range Ambiguity Rejection Ratio (N = 730)	—	20–40 dB

- The transmitter and receiver architectures were analyzed, and specifications were developed for each component based on the overall transmitter and receiver specifications [191], [192].
- A simple, closed-loop channel model was developed for closed-loop radar testing [192].
- A UWB tapered slot antenna was designed to demonstrate a potential antenna system for the radar under study, as well as to perform preliminary open-loop radar testing.
- The transmitter, channel model, receiver, post processor, and digital control subsystems were carefully integrated and characterized to ensure the desired radar performance [192].
- Closed-loop radar testing was performed to characterize the short-pulse Doppler radar [192].
- A radar system model was developed in Agilent's ADS to simulate the behavior of the full radar system under closed-loop or open-loop test conditions [192]. There is excellent agreement between the simulated and measured results.
- Paths forward for additional radar characterization, simple improvements to the radar subsystems, and the miniaturization of the transmitter and receiver subsystems have been identified.

The primary goal of this work was to demonstrate a pulse Doppler radar architecture capable of detecting targets at short range. UWB design techniques were employed to allow a pulse Doppler radar to operate in a target regime typically reserved for other radar architectures, such as FMCW radar. The

radar demonstrates that UWB design techniques can be used with a pulse Doppler radar architecture to minimize the shortest detectable range of the radar; in addition, the radar provides acceptable sensitivity, even with the short integration time used during radar characterization. That being said, there is still room for improvement and additional research, and it is the hope of the author that this work will be continued. This chapter outlined additional radar testing that should be performed, as well as simple improvements to the radar subsystems. Miniaturization of the transmitter and receiver components will be an important step forward, and the bandwidth and time scales specified for this radar will present unique challenges as the components are integrated using MMIC technology.

Bibliography

[1] W. Mischel, Y. Shoda, and M. L. Rodriguez, "Delay of Gratification in Children," *Science*, vol. 244, pp. 933–938, May 1989. v

[2] M. Skolnik, *Introduction to Radar Systems*, ch. 1: An Introduction to Radar, pp. 1–29. McGraw-Hill, 3rd ed., 2002. 1, 3, 19, 20, 21

[3] D. M. Pozar, *Microwave Engineering*, ch. 1: Electromagnetic Theory, pp. 1–48. Wiley, 3rd ed., 2005. 2, 3

[4] J. D. Taylor and T. E. McEwan, *Ultra-Wideband Radar Technology*, ch. 6: Ultra-Wideband Technology for Intelligent Transportation Systems, pp. 155–164. CRC Press, 2001. 3

[5] T. Fujii and T. Fukuchi, eds., *Laser Remote Sensing*. CRC Press, 2005. 3

[6] M. Skolnik, *Introduction to Radar Systems*, ch. 6: Information from Radar Signals, pp. 313–397. McGraw-Hill, 3rd ed., 2002. 5, 23, 24, 25, 28, 49

[7] R. B. James and J. B. Mendola, *Ultra-Wideband Radar Technology*, ch. 7: Ultra-Wideband Technology for Intelligent Transportation Systems, pp. 165–180. CRC Press, 2001. 5

[8] "First Report and Order 02-48," February 2002. 5, 40, 43

[9] I. I. Immoreev, *Ultra-Wideband Radar Technology*, ch. 1: Main Features of UWB Radars and Differences from Common Narrowband Radars, pp. 1–20. CRC Press, 2001. 5

[10] M. Skolnik, *Introduction to Radar Systems*, ch. 10: Radar Transmitters, pp. 690–726. McGraw-Hill, 3rd ed., 2002. 8, 9

[11] T. A. Weil, *Radar Handbook*, ch. 4: Transmitters, pp. 4.1–4.46. McGraw-Hill Publishing Company, 2nd ed., 1990. 8

[12] C. A. Balanis, *Antenna Theory: Analysis and Design*, ch. 2: Fundamental Parameters of Antennas, pp. 27–106. John Wiley & Sons, 3rd ed., 2005. 10

[13] M. Skolnik, *Introduction to Radar Systems*, ch. 3: MTI and Pulse Doppler Radar, pp. 104–209. McGraw-Hill, 3rd ed., 2002. 10, 11, 20, 26, 27, 28, 33

[14] M. Skolnik, *Introduction to Radar Systems*, ch. 9: The Radar Antenna, pp. 538–689. McGraw-Hill, 3rd ed., 2002. 11

[15] M. E. Yeomans, *Radar Handbook*, ch. 6: Radar Receivers, pp. 6.1–6.51. McGraw-Hill Publishing Company, 3rd ed., 2008. 12

[16] M. Skolnik, *Introduction to Radar Systems*, ch. 2: The Radar Equation, pp. 30–103. McGraw-Hill, 3rd ed., 2002. 13, 16, 17, 66, 130, 168, 181

[17] M. Skolnik, *Radar Handbook*, ch. 1: An Introduction and Overview of Radar, pp. 1.1–1.24. McGraw-Hill Publishing Company, 3rd ed., 2008. 13, 15

[18] D. M. Pozar, *Microwave and RF Design of Wireless Systems*, ch. 10: Receiver Design, pp. 335–356. John Wiley & Sons, 2001. 14, 15

[19] B. R. Mahafza and A. Elsherbeni, *MATLAB Simulations for Radar Systems*

Design, ch. 1: Introduction to Radar Basics, pp. 1–74. Chapman and Hall/CRC, 2003. 15

[20] E. F. Knott, *Radar Handbook*, ch. 14: Radar Cross Section, pp. 14.1–14.46. McGraw-Hill Publishing Company, 3rd ed., 2008. 15, 16, 17, 18

[21] B. R. Mahafza and A. Elsherbeni, *MATLAB Simulations for Radar Systems Design*, ch. 11: Radar Cross Section (RCS), pp. 501–588. Chapman and Hall/CRC, 2003. 17

[22] J. D. Jackson, *Classical Electrodynamics*, ch. 10: Scattering and Diffraction, pp. 456–513. John Wiley & Sons, third ed., 1999. 17

[23] M. Skolnik, *Introduction to Radar Systems*, ch. 11: Radar Receiver, pp. 727–762. McGraw-Hill, 3rd ed., 2002. 18

[24] D. M. Pozar, *Microwave and RF Design of Wireless Systems*, ch. 3: Noise and Distortion in Microwave Systems, pp. 68–109. John Wiley & Sons, 2001. 19

[25] G. Gonzalez, *Microwave Transistor Amplifiers Analysis and Design*, ch. 4: Noise, Broadband, and High-Power Design Methods, pp. 294–383. Prentice Hall, 2nd ed., 1997. 19, 232

[26] G. Gonzalez, *Microwave Transistor Amplifiers Analysis and Design*, ch. 1: Representations of Two-Port Networks, pp. 1–91. Prentice Hall, 2nd ed., 1997. 19

[27] D. M. Pozar, *Microwave Engineering*, ch. 10: Noise and Active RF Components, pp. 486–535. Wiley, 3rd ed., 2005. 19, 134

[28] J. Keeler and R. J. Serafin, *Radar Handbook*, ch. 19: Meteorological Radar, pp. 19.1–19.49. McGraw-Hill Publishing Company, 3rd ed., 2008. 19

[29] R. K. Raney, *Radar Handbook*, ch. 18: Space-Based Remote Sensing Radars, pp. 18.1–18.70. McGraw-Hill Publishing Company, 3rd ed., 2008. 19

[30] R. Sullivan, *Radar Handbook*, ch. 17: Synthetic Aperture Radar, pp. 17.1–17.37. McGraw-Hill Publishing Company, 3rd ed., 2008. 20

[31] D. Daniels, *Radar Handbook*, ch. 21: Ground Penetrating Radar, pp. 21.1–21.41. McGraw-Hill Publishing Company, 3rd ed., 2008. 20

[32] S. Kurt, Şimşek Demir, and A. Hizal, "Zero Crossing Counter for Accuracy Improvement of FMCW Range Detection," *Turkish Journal of Electrical Engineering & Computer Sciences*, vol. 16, no. 2, pp. 125–132, 2008. 26

[33] A. D. Berny, A. M. Niknejad, and R. G. Meyer, "A 1.8-GHz LC VCO With 1.3-GHz Tuning Range and Digital Amplitude Calibration," *IEEE Journal of Solid-State Circuits*, vol. 40, pp. 909–917, April 2005. 27

[34] W. K. Saunders, "Post-War Developments in Continuous-Wave and Frequency-Modulated Radar," *IRE Transactions on Aerospace and Navigational Electronics*, vol. 8, pp. 7–19, 1961. 28

[35] D. D. Howard, *Radar Handbook*, ch. 8: Pulse Compression Radar, pp. 8.1–8.44. McGraw-Hill Publishing Company, 3rd ed., 2008. 30

[36] E. C. Farnett and G. H. Stevens, *Radar Handbook*, ch. 10: Pulse Compression Radar, pp. 10.1–10.39. McGraw-Hill Publishing Company, 2 ed., 1990. 31

[37] G. Morris and L. Harkness, eds., *Airborne Pulsed Doppler Radar*. Artech House, 2nd ed., 1996. 39

[38] J. D. Taylor, ed., *Ultra-Wideband Radar Technology*. CRC Press, 2001. 40, 44

[39] V. A. Mikhnev and P. Vainikainen, "Single-Reference Near-Field Calibration Procedure for Step-Frequency Ground Penetrating Radar," *IEEE Transactions on Geoscience and Remote Sensing*, vol. 41, pp. 75–80, January 2003. 40, 42

[40] J. D. Taylor, *Ultra-Wideband Radar Technology*, ch. 13: Ultra-Wideband Radar Capability Demonstrations, pp. 343–378. CRC Press, 2001. 42

[41] S. Vitebskiy, L. Carin, M. A. Ressler, and F. H.Le, "Ultra-Wideband, Short-Pulse Ground-Penetrating Radar: Simulation and Measurement," *IEEE Transactions of Geoscience and Remote Sensing*, vol. 35, pp. 762–772, May 1997. 42

[42] S. Lukjanov, R. Stepanov, I. Chernyi, and O. Stukach, "Use of the Ground Penetrating Radar Methods for Paleontology on Example of the Mammoth Fauna Investigation," in *Proceedings of the 37th European Microwave Conference*, pp. 1747–1750, 2007. 42

[43] J. S. Lee, C. Nguyen, and T. Scullion, "A Novel, Compact, Low-Cost, Impulse Ground-Penetrating Radar for Nondestructive Evalulation of Pavements," *IEEE Transactions on Instrumentation and Measurement*, vol. 53, pp. 1502–1509, December 2004. 42

[44] V. Utsi, "Design of a GPR for deep investivations," in *4th International Workshop on Advanced Ground Penetrating Radar*, pp. 222–225, 2007. 42

[45] D. Daniels, "Short pulse radar for stratified lossy dielectric layer measurement," *IEE Proceedings of Communications, Radar, and Signal Proceedings*, vol. 127, pp. 384–388, October 1980. 42

[46] K. Langley, S.-E. Hamran, K. A. Høgda, R. Storvold, O. Brandt, J. O. Hagen, and J. Kohler, "Use of C-Band Ground Penetrating Radar to Determine Backscatter Sources Within Glaciers," *IEEE Transactions on Geoscience and Remote Sensing*, vol. 45, pp. 1236–1246, May 2007. 42

[47] Y. Yang and A. Fathy, "Design and Implementation of a Low-Cost Real-Time Ultra-Wide Band See-Through-Wall Imaging Radar System," in *Proceedings of IEEE/MTT-S International Microwave Symposium*, pp. 1467–1470, 2007. 42

[48] G. L. Charvat, L. C. Kempel, E. J. Rothwell, C. M. Coleman, and E. L. Mokole, "A Through-Dielectric Radar Imaging System," *IEEE Transactions on Antennas and Propagation*, vol. 58, p. 8, August 2010. 42

[49] K. E. Browne, R. J. Burkholder, and J. L. Volakis, "A Novel Low-Profile Portable Radar System for High Resolution Through-Wall Radar Imaging," in *Proceedings of IEEE Radar Conference*, pp. 333–338, 2010. 42

[50] M. M. Nikolic, A. Nehorai, and A. R. Djordjevicć, "Estimating Moving Targets Behind Reinforced Walls Using Radar," *IEEE Transactions on Antennas and Propagation*, vol. 57, pp. 3530–3538, November 2009. 42

[51] C. Li, X. Yu, C.-M. Lee, D. Li, L. Ran, and J. Lin, "High-Sensitivity Software-Configurable 5.8-GHz Radar Sensor Receiver Chip in 0.13-μm CMOS for Noncontact Vital Sign Detection," *IEEE Transactions on Microwave Theory and Techniques*, vol. 58, pp. 1410–1419, May 2010. 42, 43

[52] V. M. Lubecke, O. Boric-Lubecke, A. Host-Madsen, and A. E. Fathy, "Through-the-Wall Radar Life Detection and Monitoring," in *IEEE International Microwave Symposium Digest*, pp. 769–772, June 2007. 42, 43, 51

[53] R. M. Narayanan, "Through Wall Radar Imaging Using UWB Noise Waveforms," in *Proceedings of IEEE International Conference on Acoustics, Speech and Signal Processing*, pp. 5185–5188, 2008. 42, 43

[54] I. Gresham, A. Jenkins, R. Egri, C. Eswarappa, N. Kinayman, N. Jain, R. Anderson, F. Kolak, R. Wohlert, S. P. Bawell, J. Bennett, and J.-P. Lanteri, "Ultra-Wideband Radar Sensors for Short-Range Vehicular Applications," *IEEE Transactions on Microwave Theory and Techniques*, vol. 52, pp. 2105–2122, September 2004. 43, 51

[55] M. Klotz and H. Rohling, "A 24 GHz Short Range Radar Network for Automotive Applications," in *Proceedings of 2001 CIE International Conference on Radar*, pp. 115–118, 2001. 43

[56] V. Cojocaru, V. Napijalo, D. Humphrey, and B. Clarke, "24 GHz Low-Cost UWB Front-End Design for Short Range Pulse Radar Applications," in *Proceedings of IEEE Annual Conference Wireless and Microwave Technology*, pp. 1273–1276, 2005. 43

[57] M. R. Mahfouz, C. Zhang, B. C. Merkl, M. J. Kuhn, and A. E. Fathy, "Investigation of High-Accuracy Indoor 3-D Positioning Using UWB Technology," *IEEE Transactions on Microwave Theory and Techniques*, vol. 56, pp. 1316–1330, June 2008. 43

[58] C. Zhang, M. J. Kuhn, B. C. Merkl, A. E. Fathy, and M. R. Mahfouz, "Real-Time Noncoherent UWB Positioning Radar With Milllimeter Range Accuracy: Theory and Experiment," *IEEE Transactions on Microwave Theory and Techniques*, vol. 58, pp. 9–20, January 2010. 43

[59] S. Wehrli, R. Gierlich, J. Hüttner, D. Barras, F. Ellinger, and H. Jäckel, "Integrated Active Pulsed Reflector for an Indoor Local Positioning System," *IEEE Transactions on Microwave Theory and Techniques*, vol. 58, pp. 267–276, February 2010. 43

[60] C. Villien, V. Fleck, E. Ostertag, and P. Raymond, "3-D Short-Range Localization Device By Low-Cost CW-Doppler Radar," in *Proceedings ofIEEE International Radar Conference*, pp. 557–561, 2005. 43

[61] R. J. Fontana, "Recent System Applications of Short-Pulse Ultra-Wideband (UWB) Technology," *IEEE Transactions on Microwave Theory and Techniques*, vol. 52, pp. 2087–2104, September 2004. 43, 44

[62] M. Cavallaro, G. Sapone, G. Giarrizzo, A. Italia, and G. Palmisano, "A 3-5 GHz UWB Front-End for Low-Data Rate WPANs in 90-nm CMOS," *IEEE Transactions on Microwave Theory and Techniques*, vol. 58, pp. 854–865, 2010. 43

[63] G. N. Saddik, R. S. Singh, and E. R. Brown, "Ultra-Wideband Multifunctional Communications/Radar System," *IEEE Transactions on Microwave Theory and Techniques*, vol. 55, pp. 1431–1437, July 2007. 44, 51

[64] U. Megnali and A. N. D'Andrea, *Synchronization Techniques for Digital Receviers*, ch. 1: Introduction, pp. 1–8. Plenum Press, 1997. 53

[65] J. Tsui, *Digital Techniques for Wideband Receivers*, ch. 6: Analog-to-Digital Converters, pp. 155–218. Scitech Publishing, 2nd ed., 2004. 55, 182

[66] J. Tsui, *Digital Techniques for Wideband Receivers*, ch. 4: Discrete Fourier Transform, pp. 77–109. Scitech Publishing, 2nd ed., 2004. 56, 57, 59, 60, 61

[67] J. Tsui, *Digital Techniques for Wideband Receivers*, ch. 5: Fourier Transform-Related Operations, pp. 111–154. Scitech Publishing, 2nd ed., 2004. 58

[68] L. V. Blake, *Radar Range-Performance Analysis*, ch. 7: Clutter, Interference, and Signal Processing, pp. 293–353. Artech House, 1986. 57

[69] J. P. Stralka and W. G. Fedarko, *Radar Handbook*, ch. 4: Pulse Doppler Radar, pp. 4.1–4.53. McGraw-Hill Publishing Company, 3rd ed., 2008. 61

[70] J. L. Kurtz, *Coherent Radar Performance Estimation*, ch. 16: Coherent Radar System Tests: Techniques, Considerations, and Equipment, pp. 399–420. Artech House, 1993. 62

[71] J. Marcum, "A Statistical Theory of Target Detection By Pulsed Radar," Research Memo RM-754, RAND Corp, December 1948. 65

[72] D. Iverson, "Coherent Processing of Ultra-Wideband Radar Signals," in *IEE Proceedings of Radar, Sonar and Navigation*, vol. 141, pp. 171–179, June 1994. 65, 188, 224

[73] W. J. Albersheim, "A Closed-Form Approximation to Robertson's Detection Characteristics," *Proceedings of the IEEE*, vol. 69, p. 839, July 1981. 66

[74] R. G. Lyons, *Understanding Digital Signal Processing*, ch. 8: Signal Averaging, pp. 319–348. Prentice Hall, 3 ed., 2004. 71

[75] A. P. Annan, *Ground Penetrating Radar: Theory and Applications*, ch. 1: Electromagnetic Principles of Ground Penetrating Radar, pp. 4–40. Elsevier, 2009. 73

[76] B. R. Mahafza and A. Elsherbeni, *MATLAB Simulations for Radar Systems Design*, ch. 4: The Radar Ambiguity Function, pp. 187–233. Chapman and Hall/CRC, 2003. 75

[77] B. Lathi and Z. Ding, *Modern Digital and Analog Communication Systems*, ch. 12: Spread Spectrum Communications, pp. 714–766. Oxford University Press, 2009. 75

[78] D. D. Wentzloff, R. Blazquez, F. S. Lee, B. P. Ginsburg, J. Powell, and A. P. Chandrakasan, "System Design Considerations for Ultra-Wideband Communication," *IEEE Communications Magazine*, pp. 114–121, August 2005. 79

[79] "Pulse and Waveform Generation with Step Recovery Diodes," Application Note 918, Hewlett Packard. 79, 80, 94

[80] J. Han and C. Nguyen, "On the Development of a Compact Sub-Nanosecond Tunable Monocycle Pulse Transmitter for UWB Applications," *IEEE Transactions on Microwave Theory and Techniques*, vol. 54, pp. 285–293, January 2006. 81, 82, 94

[81] C. Zhang and A. E. Fathy, "Reconfigurable Pico-Pulse Generator for UWB Applications," *IEEE International Microwave Symposium Digest*, pp. 407–410, June 2006. 82, 94

[82] E. Maxwell, T. Weller, and E. Odu, "Design and Analysis of a Multiport Circuit for Shaping Sub-Nanosecond Pulses," *IEEE Transactions on Microwave Theory and Techniques*, vol. 56, pp. 2764–2770, December 2008. 82, 83, 94

[83] J. Breitbarth, *Design and Characterization of Low Phase Noise Microwave Circuits*. PhD thesis, University of Colorado, 2006. 83, 90, 91, 94, 98

[84] Y. H. Choi, "Gated UWB Pulse Signal Generation," *International Workshop on Ultra Wideband Systems. Joint with Conference on Ultrawideband Systems and Technologies. Joint UWBST & IWUWBS.*, pp. 122–124, May 2004. 84, 85, 94

[85] R. Xu, Y. Jin, and C. Nguyen, "Power-Efficient Switching-Based CMOS UWB Transmitters for UWB Communications and Radar Systems," *IEEE Transactions on Microwave Theory and Techniques*, vol. 54, pp. 3271–3277, August 2006. 84, 94

[86] A. Mollfulleda, P. Miskovsky, and J. Mateu, "Robust Passive Shaping Network for Impulse Radio and UWB Signal Generator," *IEEE International Microwave Symposium Digest*, pp. 1339–1342, June 2005. 85, 94

[87] B. Jung, Y.-H. Tseng, J. Harvey, and R. Harjani, "Pulse Generator Design for UWB IR Communication Systems," *IEEE International Symposium on Circuits and Systems*, pp. 4381–4384, May 2005. 85, 86, 87, 88, 94

[88] M. Miao and C. Nguyen, "On the Development of an Integrated CMOS-Based UWB Tunable-Pulse Transmit Module," *IEEE Transactions on Microwave Theory and Techniques*, vol. 54, pp. 3681–3687, October 2006. 87, 94

[89] D. S. M, M. B. Nejad, H. Tenhunen, and L.-R. Zheng, "Low Power Tunable CMOS I-UWB Transmitter Design," *NORCHIP*, pp. 1–4, November 2007. 87, 94

[90] L. Stoica, A. Rabbachin, H. O. Repo, T. S. Tiuraniemi, and I. Oppermann, "An Ultrawideband System Architecture for Tag Based Wireless Sensor Networks," *IEEE Transactions on Vehicular Technology*, vol. 54, pp. 1632–1645, September 2005. 87, 88, 94

[91] P. K. Datta, X. Fan, and G. Fischer, "A Transceiver Front-End for Ultra-Wide-Band Applications," *IEEE Transactions on Circuits and Systems II: Express Briefs*, vol. 54, pp. 362–366, April 2007. 85, 87, 88, 89, 94

[92] Z. N. Chen and M. Y. W. Chia, *Broadband Planar Antennas*, ch. 5: Planar Monopole Antennas and Ultra-wideband Applications, pp. 179–240. John Wiley & Sons, 2006. 86, 94, 138

[93] T. W. Hertel and G. S. Smith, "On the Dispersive Properties of the Conical Spiral Antenna and Its Use for Pulsed Radiation," *IEEE Transactions on Antennas and Propagation*, vol. 51, pp. 1426–1432, July 2003. 86

[94] A. G. Yarovoy, A. D. Schukin, I. V. Kaploun, and L. P. Ligthart, "The Dielectric Wedge Antenna," *IEEE Transactions on Antennas and Propagation*, vol. 50, pp. 1460–1471, October 2002. 86

[95] J. Ryckaert, C. Desset, A. Fort, M. Badaroglu, V. D. Heyn, P. Wambacq, G. V. der Plas, S. Donnay, B. V. Poucke, and B. Gyselinckx, "Ultra-Wide-Band Transmitter for Low-Power Wireless Body Area Networks: Design and Evaluation," *IEEE Transactions on Circuits and Systems I: Regular Papers*, vol. 52, pp. 2515–2525, December 2005. 89, 90, 94

[96] D. D. Wentzloff and A. P. Chandrakasan, "A 3.1-10.6 GHz Ultra-Wideband Pulse-Shaping Mixer," *Digest of Papers IEEE Radio Frequency Integrated Circuits (RFIC) Symposium*, pp. 83–86, June 2005. 89, 94, 234

[97] C. Fang, C. L. Law, and J. Hwangr, "High-Voltage High-Efficiency Ultra-wideband Pulse Synthesizer," *IEEE Microwave and Wireless Components Letters*, vol. 20, pp. 49–51, January 2010. 90, 93, 94

[98] M. Remoissenet, *Waves Called Solitons*, ch. 3: Solitons in Nonlinear Transmission Lines, pp. 37–64. Springer, 1999. 90, 97

[99] M. Case, *Nonlinear Transmission Lines for Picosecond Pulse, Impulse and Millimeter-Wave Harmonic Generation*. PhD thesis, University of California, Santa Barbara, 1993. 90, 94, 97, 98, 99

[100] T. Tsuboi, "Formation process of solitons in a nonlinear transmission line: Experimental study," *Physical Review A*, vol. 41, pp. 4534–4537, April 1990. 90, 94

[101] D. Salameh and D. Linton, "Microstrip GaAs Nonlinear Transmission-Line (NLTL) Harmonic and Pulse Generators," *IEEE Transactions on Microwave Theory and Techniques*, vol. 47, pp. 1118–1121, July 1999. 90, 94, 229

[102] J.-M. Duchamp, P. Ferrari, M. Fernandez, A. Jrad, X. Mélique, J. Tao, S. Arscott, D. Lippens, and R. G. Harrison, "Comparison of Fully Distributed and Periodically Loaded Nonlinear Transmission Lines," *IEEE Transactions on Microwave Theory and Techniques*, vol. 51, pp. 1105–1116, April 2003. 90, 94

[103] D. S. Ricketts, X. Li, and D. Ham, "Electrical Soliton Oscillator," *IEEE Transactions on Microwave Theory and Techniques*, vol. 54, pp. 373–382, January 2006. 91, 230

[104] M. Pontón, F. Ramírez, A. Suárez, and J. P. Pascual, "Applications of Pulsed-Waveform Oscillators in Different Operation Regimes," *IEEE Transactions on Microwave Theory and Techniques*, vol. 57, pp. 3362–3372, December 2009. 91, 230

[105] M. Remoissenet, *Waves Called Solitons*, ch. 2: Linear Waves in Electrical Transmission Lines, pp. 12–36. Springer, 1999. 95

[106] M. Skolnik, *Introduction to Radar Systems*, ch. 5: Detection of Signals in Noise, pp. 276–312. McGraw-Hill, 3rd ed., 2002. 98, 129

[107] "Varactor Diodes," Application Note 200824 Rev A, Skyworks, August 2008. 98

[108] A. R. Djordjevicć, A. G. Zajić, A. S. Steković, M. M. Nikolić, Z. A. Maricević, and M. F. C. Schemmann, "On a Class of Low-Reflection Transmission-Line Quasi-Gaussian Low-Pass Filters and Their Lumped-Element Approximations," *IEEE Transactions on Microwave Theory and Techniques*, vol. 51, pp. 1871–1877, July 2003. 110, 129

[109] J. Breitbarth and D. Schmelzer, "Absorptive Near-Gaussian Low Pass Filter Design with Applications in the Time and Frequency Domain," in *IEEE Microwave Theory and Techniques Symposium Digest*, pp. 1303–1306, 2004. 110, 129

[110] "LVDS Fundamentals," Application Note AN-5017, Fairchild Semiconductor, 2005. 126

[111] A. M. Abbosh, M. E. Bialkowski, and H. K. Kan, *Printed Antennas for Wireless Communications*, ch. 6: Printed Tapered Slot Antennas, pp. 161–194. John Wiley & Sons, 2007. 137, 138, 149, 151

[112] Z. N. Chen, *Ultra-wideband Antennas and Propagation for Communications, Radar and Imaging*, ch. 8: Antenna Elements for Impulse Radio, pp. 147–162. John Wiley & Sons, 2007. 137, 138, 158

[113] F. Merli, J.-F. Zürcher, A. Freni, and A. K. Skrivervik, "Analysis, Design and Realization of a Novel Directive Ultrawideband Antenna," *IEEE Transactions on Antennas and Propagation*, vol. 57, pp. 3458–3466, November 2009. 138

[114] K. M. K. H. Leong and T. Itoh, *Printed Antennas for Wireless Communications*,

ch. 3: Printed Quasi-Yagi Antennas, pp. 69–102. John Wiley & Sons, 2007. 138

[115] E. E. Ekon, *Ultra-wideband Antennas and Propagation for Communications, Radar and Imaging*, ch. 11: Ultra-Wideband Arrays, pp. 221–240. John Wiley & Sons, 2007. 138

[116] M. Ghavami and K. Heidary, *Ultra-wideband Antennas and Propagation for Communications, Radar and Imaging*, ch. 12: UWB Beamforming, pp. 241–258. John Wiley & Sons, 2007. 138

[117] R. W. Kindt, M. Kragalott, M. G. Parent, and G. C. Tavik, "Preliminary Investigations of a Low-Cost Ultrawideband Array Concept," *IEEE Transactions on Antennas and Propagation*, vol. 57, pp. 3791–3799, December 2009. 138

[118] X. Chen, *Ultra-wideband Antennas and Propagation for Communications, Radar and Imaging*, ch. 7: Theory of UWB Antenna Elements, pp. 111–145. John Wiley & Sons, 2007. 138

[119] P. Massey, *Ultra-wideband Antennas and Propagation for Communications, Radar and Imaging*, ch. 9: Planar Dipole-like Antennas for Consumer Products, pp. 163–196. John Wiley & Sons, 2007. 138

[120] H. Schantz, *The Art and Science of Ultrawideband Antennas*, ch. 6: A Taxonomy of UWB Antennas, pp. 201–274. Artech House, 2005. 138

[121] R. Waterhouse and D. Novak, *Printed Antennas for Wireless Communications*, ch. 5: Printed Folded Beverage Antennas, pp. 133–159. John Wiley & Sons, 2007. 138

[122] Q. Wu, R. Jin, and J. Geng, "A Single-Layer Ultrawideband Microstrip Antenna," *IEEE Transactions on Antennas and Propagation*, vol. 58, pp. 211–214, January 2010. 138

[123] J. Yang, "On Conditions for Constant Radiation Characteristics for Log-Periodic Array Antennas," *IEEE Transactions on Antennas and Propagation*, vol. 58, pp. 1521–1526, May 2010. 138

[124] C. Chen and J. Volakis, *Printed Antennas for Wireless Communications*, ch. 4: Printed Spiral Antennas, pp. 103–132. John Wiley & Sons, 2007. 138

[125] W. S. T. Rowe, *Printed Antennas for Wireless Communications*, ch. 2: Multi-layered Patch Antennas, pp. 39–68. John Wiley & Sons, 2007. 138

[126] Z. N. Chen and M. Y. W. Chia, *Broadband Planar Antennas*, ch. 2: Broadband Microstriip Patch Antennas, pp. 17–46. John Wiley & Sons, 2006. 138

[127] A. K. Amert and K. W. Whites, "Miniaturization of the Biconical Antenna for Ultrawideband Applications," *IEEE Transactions on Antennas and Propagation*, vol. 57, pp. 3728–3735, December 2009. 138

[128] T. P. Montoya and G. S. Smith, "A Study of Pulse Radiation from Several Broad-Band Loaded Monopoles," *IEEE Transactions on Antennas and Propagation*, vol. 44, pp. 1172–1182, August 1996. 139

[129] O. E. Allen, D. A. Hill, and A. R. Ondrejka, "Time-Domain Antenna Characterizations," *IEEE Transactions on Electromagnetic Compatibility*, vol. 35, pp. 339–346, August 1993. 139

[130] B. Scheers, M. Acheroy, and A. V. Vorst, "Time Domain Simulation and Characterization of TEM Horns Using Normalized Impulse Response," *IEE Proceedings of Microwaves, Antennas, and Propagation*, vol. 147, pp. 463–468, 2000. 139, 143, 146

[131] E. G. Farr and C. E. Baum, "Time Domain Characterization of Antennas with TEM Feeds," Sensor and Simulation Notes Note 426, Farr Research Inc. and Air Force Research Laboratory/DEHP, October 1998. 139

[132] E. G. Farr and C. E. Baum, "Extending the Definitions of Antenna Gain and Radiation Pattern Into the Time Domain," Sensor and Simulation Notes Note 350, Farr Research and Phillips Laboratory, November 1992. 139, 143

[133] C. A. Balanis, *Antenna Theory: Analysis and Design*, ch. 4: Linear Wire Antennas, pp. 151–230. John Wiley & Sons, 3rd ed., 2005. 143

[134] S. Zwierzchowski and P. Jazayeri, "A Systems and Network Analysis Approach to Antenna Design for UWB Communications," in *IEEE Antennas and Propagation Society International Symposium*, pp. 826–829, 2003. 144

[135] X. Qing, Z. N. Chen, and M. Y. W. Chia, "Characterization of ultrawideband antennas using transfer functions," *Radio Science*, vol. 41, pp. 1–10, 2006. 146

[136] T. W. Hertel, "Phase Center Measurements Based on the Three-Antenna Method," in *IEEE Antennas and Propagation Society International Symposium*, pp. 816–819, 2003. 146

[137] J. D. McKinney, D. Peroulis, and A. M. Weiner, "Dispersion Limitations of Ultra-Wideband Wireless Links and Their Compensation Via Photonically Enabled Arbitrary Waveform Generation," *IEEE Transactions on Microwave Theory and Techniques*, vol. 56, pp. 710–719, March 2008. 147

[138] E. Hamidi and A. M. Weiner, "Post-Compensation of Ultra-Wideband Antenna Dispersion Using Microwave Photonic Phase Filters and Its Applications to UWB Systems," *IEEE Transactions on Microwave Theory and Techniques*, vol. 57, pp. 890–898, April 2009. 147

[139] M. Armanious and J. S. Tyo, "UWB Self-Compensating Antennas: Numerical Demonstration of the Electromagnetic Working Principle," *IEEE Transactions on Antennas and Propagation*, vol. 57, p. 3736, December 2009. 147

[140] J. R. Andrews, "UWB Signal Sources, Antennas & Propagation," Application Note AN-14a, Picosecond Pulse Labs, August 2003. 147

[141] A. M. Abbosh, H. K. Kan, and M. E. Bialkowski, "Compact Ultra-Wideband Planar Tapered Slot Antenna for Use in a Microwave Imaging System," *Microwave and Optical Technology Letters*, vol. 48, pp. 2212–2216, 2006. 149

[142] G. Brzezina, L. Roy, and L. MacEachern, "Planar Antennas in LTCC Technology With Transceiver Integration Capability for Ultra-Wideband Applications," *IEEE Transactions on Microwave Theory and Techniques*, vol. 54, pp. 2830–2838, June 2006. 158

[143] T.-G. Ma and S.-K. Jeng, "Planar Miniature Tapered-Slot-Fed Annular Slot Antennas for Ultrawide-Band Radios," *IEEE Transactions on Antennas and Propagation*, vol. 53, pp. 1194–1202, March 2005. 158

[144] E. Gazit, "Improved design of the Vivaldi antenna," *IEE Proceedings*, vol. 135, pp. 89–92, April 1988. 158

[145] Z. Wang and H. Zhang, "Improvements in a High Gain UWB Antenna with Corrugated Edges," *Progress in Electromagnetics Research C*, vol. 6, pp. 159–166, 2009. 158

[146] P. Zhang and W.-X. Zhang, "Gain Enhancement of Tapered Slot-line Antenna with Directive Grating," in *Proceedings of Asia-Pacific Microwave Conference*, 2008. 160

[147] A. M. Abbosh, "Directive Antenna for Ultrawideband Medical Imaging Systems," *International Journal of Antennas and Propagation*, vol. 2008, pp. 1–6, January 2008. 160

[148] H. Schantz, *The Art and Science of Ultrawideband Antennas*, ch. 3: Antennas as Transformers, pp. 65–94. Artech House, 2005. 160

[149] H. Loui, J. P. Weem, and Z. Popović, "A Dual-Band Dual-Polarized Nested Vivaldi Slot Array With Multilevel Ground Plane," *IEEE Transactions on Antennas and Propagation*, vol. 51, pp. 2168–2175, September 2003. 160

[150] J. Zhang, E. C. Fear, and R. H. Johnston, "Cross-Vivaldi Antenna for Breast Tumor Detection," *Microwave and Optical Technology Letters*, vol. 51, pp. 275–280, February 2009. 160

[151] E. F. Knott, J. F. Schaeffer, and M. T. Tuley, *Radar Cross Section*, ch. 6: Phemonenological Examples of Radar Cross Section, pp. 225–268. Scitech Publishing, 2nd ed., 2004. 166

[152] D. D'Aloisi, A. D. Vito, and G. Galati, "Sampling Losses in Radar Signal Detection," *Jour of the Institution of Electronic and Rdio Engineers*, vol. 56, pp. 237–242, June/July 1986. 168

[153] J. Nadolny, "EMI Design of Shielded Cable Assemblies," in *Proceedings of IEEE International Symposium on Electromagnetic Compatibility*, 2007. 174

[154] G. T. Ruck, "Ultra-Wideband Radar Receiver," *Proceedings of the SPIE - The International Society for Optical Engineering*, vol. 1631, pp. 174–180, May 1992. 223, 225

[155] M. Y. Frankel, S. Gupta, J. A. Valdmanis, and G. A. Mourou, "Terahertz Attenuation and Dispersion Characteristics of Coplanar Transmission Lines," *IEEE Transactions on Microwave Theory and Techniques*, vol. 39, pp. 910–915, June 1991. 229

[156] M. J. W. Rodwell, M. Kamegawa, R. Y. M. C. E. Carman, and K. S. Giboney, "GaAs Nonlinear Transmission Lines for Picosecond Pulse Generation and Millimeter-Wave Sampling," *IEEE Transactions on Microwave THeory and Techniques*, vol. 39, pp. 1194–1203, July 1991. 229

[157] K. Chang, I. Bahl, and V. Nair, *RF and Microwave Circuit and Component*

Design for Wireless Systems, ch. 7: Switches, pp. 221–270. Wiley Series in Microwave and Optical Engineering, Wiley, 2002. 230, 233

[158] Y. Jin and C. Nguyen, "Ultra-Compact High-Linearity High-Power Fully Integrated DC–20-GHz 0.18-μm CMOS T/R Switch," *IEEE Transactions on Microwave Theory and Techniques*, vol. 55, pp. 30–36, January 2007. 230

[159] Q. Li and Y. P. Zhang, "CMOS T/R Switch Design: Towards Ultra-Wideband and Higher Frequencies," *IEEE Journal of Solid-State Circuits*, vol. 42, pp. 563–570, March 2007. 230

[160] T. M. Hanclock and G. M. Rebeiz, "Design and Analysis of a 70-ps SiGe Differential RF Switch," *IEEE Transactions on Microwave Theory and Techniques*, vol. 53, pp. 2403–2410, July 2005. 230

[161] D. M. Pozar, *Microwave Engineering*, ch. 11: Microwave Amplifier Design, pp. 536–576. Wiley, 3rd ed., 2005. 232

[162] A. Sayed, S. von der Mark, and G. Boeck, "An Ultra Wideband 5 W Power Amplifier Using SiC MESFETs," in *Proceedings of the European Microwave Conference*, pp. 57–60, 2004. 232

[163] A. K. Ezzeddine and H. C. Huang, "Ultra-Broadband GaAs HIFET MMIC PA," in *IEEE MTT-S International Microwave Symposium Digest*, 2006. 232

[164] M. Elsbury, *Broadband Microwave Integrated Circuits for Voltage Standard Applications*. PhD thesis, University of Colorado at Boulder, 2010. 232

[165] J. Hoversten, *Efficient and Linear Microwave Transmitters for High Peak-to-Average Ratio Signals*. PhD thesis, University of Colorado at Boulder, 2010. 232

[166] K. W. Kobayashi, A. K. Oki, D. K. Umemoto, S. K. Z. Claxton, and D. C. Streit,

"Monolithic GaAs HBT p-i-n Diode Variable Gain Amplifiers, Attenuators, and Switches," *IEEE Transactions on Microwave Theoery and Techniques*, vol. 41, pp. 2295–2303, December 1993. 233

[167] X. Guan and C. Nguyen, "Low-Power-Consumption and High-Gain CMOS Distributed Amplifiers Using Cascade of Inductively Coupled Common-Source Gain Cells for UWB Systems," *IEEE Transactions on Microwave Theory and Techniques*, vol. 54, pp. 3278–3283, August 2006. 234

[168] S.-E. Shih, W. R. Deal, D. M. Yamauchi, W. E. Sutton, W.-B. Luo, Y. Chen, I. P. Smorchkova, B. Heying, M. Wojtowicz, and M. Siddiqui, "Design and Analysis of Ultra Wideband GaN Dual-Gate HEMT Low-Noise Amplifiers," *IEEE Transactions on Microwave Theory and Techniques*, vol. 57, pp. 3270–3277, December 2009. 234

[169] J. Lee and J. D. Cressler, "Analysis and Design of an Ultra-Wideband Low-Noise Amplifier Using Resistive Feedback in SiGe HBT Technology," *IEEE Transactions on Microwave Theory and Techniques*, vol. 54, pp. 1262–1268, March 2006. 234

[170] H.-I. Wu, R. Hu, and C. F. Jou, "Complementary UWB LNA Design Using Asymmetrical Inductive Source Degeneration," *IEEE Microwave and Wireless Components Letters*, vol. 20, pp. 402–404, July 2010. 234

[171] K.-P. Ahn, R. Ishikawa, and K. Honjo, "Group Delay Equalized UWB InGaP/GaAs HBT MMIC Amplifier Using Negative Group Delay Circuits," *IEEE Transactions on Microwave Theory and Techniques*, vol. 57, pp. 2139–2147, September 2009. 234

[172] S.-R. Feng, Liao-Huailin, Yan-tao, Hung-Ru, and W.-Y. Yuan, "Design of 3-5 GHz BiFET Mixer for Ultra Wideband Application," in *Proceedings of International Conference on Solid-State and Integrated Circuit Technology*, 2006. 234

[173] W.-J. Choi and Y.-H. L. N.-Y. Kim, "Broadband MMIC Mixer with High

Output Power using InGaP/GaAs HBT Technology," in *Proceedings of the 37th European Microwave Conference*, pp. 1265–1268, 2007.

[174] P. Paliwoda and M. Hella, "An Optimized CMOS Gilbert Mixer Using Inter-Stage Inductance for Ultra Wideband Receivers," in *Proceedings of IEEE International Midwest Symposium on Circuits and Systems*, pp. 362–365, 2006.

[175] P.-Z. Rao, T.-Y. Chang, C.-P. Liang, and S.-J. Chung, "An Ultra-Wideband High-Linearity CMOS Mixer With New Wideband Active Baluns," *IEEE Transactions on Microwave Theory and Techniques*, vol. 57, pp. 2184–2192, September 2009. 234

[176] J. B. Lai and C. G. Christodoulou, "A Fully On-Chip, Single-Ended S-band Image Reject Mixer for High Dynamic Range Applications," in *Proceedings of IEEE Compound Semiconductor Integrated Circuit Symposium*, 2007. 234, 235

[177] T. Chang and J. Lin, "1-11 GHz Ultra-Wideband Resistive Ring Mixer in 0.18-μm CMOS Technology," in *Proceedings of IEEE Radio Frequency Integrated Circuits (RFIC) Symposium*, 2006. 234

[178] S. Sadoshima, S. Fukuda, T. Yammouch, H. Ito, K. Okada, and K. Masu, "Small-Area CMOS RF Distributed Mixer Using Multi-Port Inductors," in *Proceedings of Topical Meeting on Silicon Monolithic Integrated Circuits in RF Systems*, 2007. 235

[179] R. G. Lyons, *Understanding Digital Signal Processing*, ch. 7: Advanced Sampling Techniques, pp. 297–318. Prentice Hall, 3 ed., 2004. 235

[180] L. Zhu, S. Sun, and W. Menzel, "Ultra-Wideband (UWB) Bandpass Filters Using Multiple-Mode Resonator," *IEEE Microwave and Wireless Components Letters*, vol. 15, pp. 796–798, November 2005. 235

[181] L. Han, K. Wu, and X. Zhang, "Development of Packaged Ultra-Wideband Bandpass Filters," *IEEE Transactions on Microwave Theory and Techniques*, vol. 58, pp. 220–228, January 2010.

[182] Z.-C. Hao, J.-S. Hong, J. P. Parry, and D. P. Hand, "Ultra-Wideband Bandpass Filter With Multiple Notch Bands Using Nonuniform Periodical Slotted Ground Structure," *IEEE Transactions on Microwave Theory and Techniques*, vol. 57, pp. 3080–3088, December 2009.

[183] T. H. Duong and I. S. Kim, "New Elliptic Function Type UWB BPF Based on Capacitively Coupled $\lambda/4$ Open T Resonator," *IEEE Transactions on Microwave Theory and Techniques*, vol. 57, pp. 3089–3098, December 2009.

[184] S. Sun and L. Zhu, "Capacitive-Ended Interdigital Coupled Lines for UWB Bandpass Filters With Improved Out-of-Band Performances," *IEEE Microwave and Wireless Components Letters*, vol. 16, pp. 440–442, August 2006. 235

[185] M. Makimoto and S. Yamashita, *Microwave Resonators and Filters for Wireless Communication: Theory, Design, and Application*. Advanced Microelectronics, Springer, 2001. 235

[186] D. Haigh, "Wideband Active Microwave Isolators Using GaAs MMIC Technology," *IEE Proceedings of Microwaves, Antennas, and Propagation*, vol. 143, pp. 179–183, April 1996. 236

[187] R. Pyndiah and F. van den Bogaart, "Novel Multioctave MMIC Active Isolator (1-20 GHz)," *Electronics Letters*, vol. 25, pp. 1420–1422, October 1989.

[188] J. Lee, J. D. Cressler, and A. J. Joseph, "A 5-6 GHz SiGe HBT Monolithic Active Isolator for Improving Reverse Isolation in Wireless Systems," *IEEE Microwave and Wireless Components Letters*, vol. 15, pp. 220–222, April 2005. 236

[189] F. Ali and A. Podell, "A Wide-Band Push-Pull GaAs Monolithic Active Isolator," *IEEE Microwave and Guided Wave Letters*, vol. 1, pp. 26–27, February 1991. 236

[190] M. A. Smith, "GaAs Monolithic Implementation of Active Circulators," in *IEEE MTT-S International Microwave Symposium Digest*, pp. 1015–1016, 1988. 236

[191] N. J. Kinzie, C. T. Rodenbeck, and Z. B. Popović, "An Ultra-Wideband Transmitter for a Short Range Pulse Doppler Radar," *submitted to joint issue of IEEE Transactions on Microwave Theory and Techniques, IEEE Transactions on Antennas and Propagation*. 240, 241

[192] N. J. Kinzie, C. T. Rodenbeck, , J. M. Pankonin, R. E. Heintzleman, and Z. Popović, "A Short-Range, Ultra-Wideband Pulse Doppler Radar," *to be submitted to IEEE Transactions on Microwave Theory and Techniques*. 241

Acronyms and Abbreviations

2D 2-dimensional

3D 3-dimensional

ADC analog-to-digital converter

ADS Advanced Design System

BiCMOS bipolar complementary metal-oxide-semiconductor

BPSK binary phase-shift keying

CMOS complementary metal-oxide-semiconductor

COTS commercial off-the-shelf

CPI coherent processing interval

CPW coplanar waveguide

CW continuous-wave

DC direct current

DSB double sideband

EM electromagnetic

EMC electromagnetic compatibility

EMI electromagnetic interference

FCC Federal Communications Commission

FEM finite element method

FFT fast Fourier transform

FM frequency modulated

FMCW frequency-modulated continuous-wave

FPGA field-programmable gate array

FR4 flame retardant 4

FWHM full-width half-maximum

GaAs gallium arsenide

GaN gallium nitride

GPR ground-penetrating radar

HFSS high frequency structure simulator

HIFET high-voltage, high-impedance FET

HP Hewlett Packard

IC integrated circuit

IF intermediate frequency

ISAR interferometric synthetic aperture radar

ISM industrial, scientific, and medical

JPL Jet Propulsion Laboratory

LIDAR light detection and ranging

LFSR linear feedback shift register

LNA low noise amplifier

LO local oscillator

LPF low-pass filter

LSB least significant bit

LVTTL low-voltage transistor-transistor logic

MMIC monolithic microwave integrated circuit

MTI moving target indicator

NLTL nonlinear transmission line

P1dB 1 dB compression

PA power amplifier

PCC pulse compression circuit

pHEMT pseudomorphic high electron mobility transistor

PLL phase-locked loop

PNA precision network analyzer

PRF pulse repetition frequency

PRI pulse repetition interval

PSD power spectral density

RADAR RAdio Detection And Ranging

RCS radar cross section

RF radio frequency or radar frequency

rms root mean square

RX receiver

SAR synthetic aperture radar

Si silicon

SiC silicon carbide

SiGe silicon germanium

SINAD signal-to-noise-and-distortion ratio

SMA sub-miniature A

SNL Sandia National Laboratories

SNR signal-to-noise ratio

SOIC-8 small-outline integrated circuit (8 pins)

SPDT single-pole, double-throw

SPICE simulation program with integrated circuit emphasis

SRD step recovery diode

SSB single-sideband

TEM transverse electro-magnetic

TX transmitter

UWB ultra-wideband

VCO voltage controlled oscillator

Appendix A: MATLAB Signal Processing Script

```
%-------------------------------------------------------------------------
% process_dig_data() takes a mat file with time, ch_1, and ch_2 vectors
% and generates correlation plots, fft plots, and/or time domain plots
%
% Author:       Nicola Kinzie
% Last Edited:  27 July 2010
%
% Inputs:   pc_ch - channel number (1 or 2) of phase code
%           return_ch - channel number (1 or 2) of return data
%           int_bandwidth - integration bandwidth (10, 20, 30, or 40 for
%           10, 20, 30, or 40 dB bandwidth
%           system_impedance - the impedance of the measurement system
%           range_shift_offset - the number of time shifts by which the
%               phase code and received pulses are offset due to cable
%               lengths
%           ---------------------------------------------------------
%           samples - number of samples to use (0 uses all samples)
%           zero_pad - amount of samples to zero pad with (0 sets the
%               zero padding to the next power of 2 based on "samples")
%           averages - the number of FFTs to average for the final PSD
%               result
%           range_decorr_shift_max - the maximum number of shifts to
%               consider for the decorrelated power and SNR
%               determinations
%           ---------------------------------------------------------
%           auto_search_signal_freq - 1 to search for the signal
%               frequency
%           signal_freq_init - expected signal frequency (ignored if
%               "auto_search_signal_freq" == 1)
%           ---------------------------------------------------------
%           FontSize - font size for figures (30 is recommended)
%           LineWidth - line width for figures (2 is recommended)
%           MarkerSize - marker size for figures (6 is recommended)
```

```
%           ------------------------------------------------------------
%           filter_processed_return_decorr - 1 to LPF the decorrelated
%               data
%           filter_order - order of digital LPF
%           cutoff_freq - cutoff frequency of digital LPF
%           filter_method - 1 for filtfilt() filtering, otherwise
%               filter() will be used
%           ------------------------------------------------------------
%           plot_pc_raw - 1 to plot the raw phase code data
%           plot_pc_processed - 1 to plot the processed phase code data
%           plot_pc_hist - 1 to plot the phase code histogram
%           plot_pc_autocorr - 1 to plot the phase code autocorrelation
%           plot_return_raw - 1 to plot the raw return data
%           plot_return_processed - 1 to plot the processed return data
%           plot_return_pc_corr - 1 to plot the correlation between the
%               processed return and phase code data
%           plot_return_processed_decorrelated - 1 to plot the
%               decorrelated processed return data
%           plot_return_processed_decorrelated_filtered - 1 to plot the
%               filtered decorrelated processed return data
%-------------------------------------------------------------------------

function process_dig_data(pc_ch, return_ch, int_bandwidth, ...
    system_impedance, range_shift_offset, samples, zero_pad, ...
    averages, range_decorr_shift_max, auto_search_signal_freq, ...
    signal_freq_init, FontSize, LineWidth, MarkerSize, ...
    filter_processed_return_decorr, filter_order, cutoff_freq, ...
    filter_method, plot_pc_raw, plot_pc_processed, plot_pc_hist, ...
    plot_pc_autocorr, plot_return_raw, plot_return_processed, ...
    plot_return_pc_corr, plot_return_processed_decorrelated, ...
    plot_return_processed_decorrelated_filtered)

%% Loads data

% Select .mat file
[file_name, path_name] = uigetfile('*.mat', 'Pick a file', ...
    'MultiSelect', 'off');

% Closes all figure windows
close all;

% Loads data
try
    load([path_name file_name]);
catch ME
    fprintf('Couldn''t read %s.\n', [path_name file_name]);
end
```

```
% If averaging is to be performed, checks if the number of samples is
% selected such that the phase is correct on the desired signal
% frequency
if auto_search_signal_freq ~= 1 && averages ~= 1
    if mod(samples, (fs/signal_freq_init - 1)) ~= 0
        fprintf(['\nWARNING: The number of samples was not set to\n' ...
            'ensure the correct phase for a signal with frequency\n' ...
            num2str(signal_freq_init) ' Hz.  \n']);
    end
elseif auto_search_signal_freq == 1 && averages ~= 1
    fprintf(['\nWARNING: It is not advisable to autosearch for the\n' ...
        'signal frequency and use averaging at the same time.\n']);
end

% Checks that enough data exists for the requested processing
if samples > length(ch_1) && averages == 1
    fprinft(['\nWARNING: The number of samples exceeds the number of\n' ...
        'samples in the data set.  The full data set will be used,\n' ...
        'changing the number of samples from ' num2str(samples) ' to ' ...
        num2str(length(ch_1)) '.\n']);
    samples = length(ch_1);
elseif samples*averages > length(ch_1)
    fprintf(['\nWARNING: The number of samples required for ' ...
        num2str(averages) '\nFFTs with ' num2str(samples) ' sample ' ...
        'points exceeds the number of samples in\nthe data set.  ']);
    if floor(length(ch_1)/samples) > 0
        averages = floor(length(ch_1)/samples);
    else
        averages = 1;
        samples = length(ch_1);
    end
    fprintf([num2str(averages) ' FFTs with ' num2str(samples) ...
        'sample points will be used instead.\n']);
end

% Determines length of FFT
if zero_pad == 0
    zero_pad = 2^(nextpow2(samples))-samples;
end
fft_length = samples + zero_pad;

%% Checks that the "system_impedance" matches the recorded measurement
%  impedance
system_impedance_warning = 0;

switch ch1Coupling
```

```
    case 0
        if system_impedance ~= 0 system_impedance_warning = 1; end
    case 1
        if system_impedance ~= 1e6 system_impedance_warning = 1; end
    case 2
        if system_impedance ~= 1e6 system_impedance_warning = 1; end
    case 3
        if system_impedance ~= 50 system_impedance_warning = 1; end
    case 4
        if system_impedance ~= 50 system_impedance_warning = 1; end
end

switch ch2Coupling
    case 0
        if system_impedance ~= 0 system_impedance_warning = 1; end
    case 1
        if system_impedance ~= 1e6 system_impedance_warning = 1; end
    case 2
        if system_impedance ~= 1e6 system_impedance_warning = 1; end
    case 3
        if system_impedance ~= 50 system_impedance_warning = 1; end
    case 4
        if system_impedance ~= 50 system_impedance_warning = 1; end
end

if system_impedance_warning == 1
    fprintf(['\nWARNING: The requested system impedance does not\n' ...
        'match the recorded system impedance.\n']);
end

%% Process Raw Data

% Processes phase code
if pc_ch == 1
    for i = 1:averages
        [processed_phase_code(1:samples, i)] = process_phase_code(ch_1, ...
            time, samples, zero_pad, i, plot_pc_raw, plot_pc_processed, ...
            plot_pc_hist, plot_pc_autocorr, FontSize, LineWidth, ...
            path_name, file_name);
    end
else
    for i = 1:averages
        [processed_phase_code(1:samples, i)] = process_phase_code(ch_2, ...
            time, samples, zero_pad, i, plot_pc_raw, plot_pc_processed, ...
            plot_pc_hist, plot_pc_autocorr, FontSize, LineWidth, ...
            path_name, file_name);
    end
```

```
end

% Processes return data
if return_ch == 1
    for i = 1:averages
        [processed_return(1:samples, i)] = process_return(ch_1, ...
            time, samples, zero_pad, i, plot_return_raw, ...
            plot_return_processed, FontSize, LineWidth, MarkerSize, ...
            path_name, file_name);
    end
else
    for i = 1:averages
        [processed_return(1:samples, i)] = process_return(ch_2, ...
            time, samples, zero_pad, i, plot_return_raw, ...
            plot_return_processed, FontSize, LineWidth, MarkerSize, ...
            path_name, file_name);
    end
end

%% Performs Correlation between phase code and return data

for i = 1:averages
    [processed_corr_result(1:(2*samples-1), i), ...
        processed_corr_result_lags(1:(2*samples-1), i)] = ...
        corr_return_and_pc(processed_phase_code, processed_return, ...
        i, FontSize, LineWidth, plot_return_pc_corr, ...
        path_name, file_name);
end

%% Determines the power and SNR for the decorrelated  "processed_return"
%  using a variety of methods

for i = 1:averages
    for n = 0:range_decorr_shift_max
        processed_return_decorr_temp = processed_return(:, i) .* ...
            circshift(processed_phase_code(:, i), n);

        % Plots the decorrelated return data
        if plot_return_processed_decorrelated == 1 && i == 1 && ...
                n == range_shift_offset
            processed_time(1:samples) = ...
                time((1 + (i - 1)*samples):i*samples);
            [scale_factor, time_units] = set_time_units(samples* ...
                (processed_time(2) - processed_time(1)));
            axes('Parent',figure,'fontsize', FontSize);
            plot(processed_time*scale_factor, ...
                processed_return_decorr_temp, '.', 'LineWidth', ...
```

```
        LineWidth, 'MarkerSize', MarkerSize);
    grid on;
    xlabel(['Time (' time_units ')'], 'fontsize', FontSize);
    ylabel('Correlated Target Return (V)', 'fontsize', FontSize);
    title('Processed Correlated Target Return');

    try
        saveas(gcf, [path_name ...
            file_name(1:(length(file_name)-4)) ...
            '_return_processed_decorr'], 'fig');
        clear('figure_handle');
    catch ME
        fprintf(['There was a problem saving the processed ' ...
            'correlated return figure for %s.\n'], ...
            [path_name file_name]);
    end
end

% Filters the decorrelated return data
if filter_processed_return_decorr == 1  && ...
        n == range_shift_offset && i == 1
    processed_return_decorr_filt_temp = filter_return(...
        filter_order, cutoff_freq, fs, filter_method, ...
        processed_return_decorr_temp, time, samples, ...
        FontSize, LineWidth, MarkerSize, path_name, file_name, ...
        plot_return_processed_decorrelated_filtered);
elseif filter_processed_return_decorr == 1
    processed_return_decorr_filt_temp = filter_return(...
        filter_order, cutoff_freq, fs, filter_method, ...
        processed_return_decorr_temp, time, samples, FontSize, ...
        LineWidth, MarkerSize, path_name, file_name, 0);
end

% Sets the return_signal
if filter_processed_return_decorr == 1
    return_signal = processed_return_decorr_filt_temp;
else
    return_signal = processed_return_decorr_temp;
end

% Plots the PSD if it corresponds to the correct range bin; this is
% determined based on "range_shift_offset".  It also saves the
% "processed_return_decorr_temp" and
% "processed_return_decorr_filt_temp" vectors.
if n == range_shift_offset && i == 1
    plot_PSD = 1;
    processed_return_decorr(1:samples, i) = ...
```

```
                processed_return_decorr_temp;
            if filter_processed_return_decorr == 1
                processed_return_decorr_filt(1:samples, i) = ...
                    processed_return_decorr_filt_temp;
            end
        else
            plot_PSD = 0;
        end

        % Performs signal calculations using a periodogram
        [signal_power_dBm_temp, total_power_dBm_temp, SNR_dB_temp, ...
            signal_freq_temp, scale_factor_temp, freq_units_temp, ...
            PSD_temp, frequency_temp] = power_periodogram(...
            return_signal, fs, samples, zero_pad, ...
            auto_search_signal_freq, signal_freq_init, ...
            int_bandwidth, system_impedance, FontSize, LineWidth, ...
            path_name, file_name, plot_PSD, 'corr');

        signal_power_dBm_periodogram_decorr((n + 1), i) = ...
            signal_power_dBm_temp;
        total_power_dBm_periodogram_decorr((n + 1), i) = ...
            total_power_dBm_temp;
        SNR_dB_periodogram_decorr((n + 1), i) = SNR_dB_temp;
        signal_freq_periodogram_decorr((n + 1), i) = signal_freq_temp;
        if n == range_shift_offset
            scale_factor_periodogram_decorr(1, i) = scale_factor_temp;
            freq_units_periodogram_decorr(1:3, i) = freq_units_temp;
            PSD_periodogram(1:fft_length, i) = PSD_temp;
            frequency_periodogram(1:fft_length, i) = frequency_temp;
        end
    end
end

% Calculates average SNR
if averages > 1
    [signal_power_dBm_averaged_periodogram_decorr, ...
        total_power_dBm_averaged_periodogram_decorr, ...
        SNR_dB_averaged_periodogram_decorr] = average_PSD(...
        PSD_periodogram, frequency_periodogram, averages, ...
        signal_freq_periodogram_decorr((range_shift_offset+1), 1), ...
        scale_factor_periodogram_decorr(1, 1), ...
        freq_units_periodogram_decorr(1:3, 1), ...
        int_bw_scale_factor_periodogram*(rf_bandwidth/samples), ...
        system_impedance, FontSize, LineWidth, path_name, ...
        file_name, plot_PSD_periodogram, 'Averaged Periodogram');

    clear PSD_periodogram frequency_periodogram;
```

```
end

%% Plots results from the decorrelated SNR calculations

plot_decorr_SNR_results(SNR_dB_periodogram_decorr(:, 1), FontSize, ...
    LineWidth, 'Periodogram', path_name, file_name);

%% Prints data for decorrelated "processed_return"

% Prints the signal frequency
fprintf(['\nCORRELATED PROCESSED RETURN:\nSIGNAL FREQUENCY:\n']);

fprintf('\tPeriodogram: %g %s\n', ...
    signal_freq_periodogram_decorr((range_shift_offset + 1), 1)* ...
    scale_factor_periodogram_decorr(1, 1), ...
    freq_units_periodogram_decorr(1:3, 1));

% Prints the calculated SNRs for the processed returns
fprintf(['\nSNR FOR CORRELATED PROCESSED RETURN:\n']);

fprintf('\tPeriodogram: %g dB\n', ...
    SNR_dB_periodogram_decorr((range_shift_offset + 1), 1));
if max(SNR_dB_periodogram_decorr(:, 1)) > ...
        SNR_dB_periodogram_decorr((range_shift_offset + 1), 1)
    fprintf(['\tWARNING: This is not the maximum correlated ' ...
        'SNR value.  Consider adjusting "Range Bin Offset".\n']);
end
if averages > 1
    fprintf('\tAveraged Periodogram: %g dB\n', ...
        SNR_dB_averaged_periodogram_decorr);
end

% Prints the calculated signal and noise power for the processed returns
fprintf(['\nSIGNAL AND NOISE POWER, NOISE STD FOR CORRELATED ' ...
    'PROCESSED RETURN:\n']);

fprintf('\tPeriodogram: %g dBm, %g dBm\n', ...
    signal_power_dBm_periodogram_decorr((range_shift_offset+1), 1), ...
    (signal_power_dBm_periodogram_decorr((range_shift_offset+1), 1) ...
    - SNR_dB_periodogram_decorr((range_shift_offset + 1), 1)));
if averages > 1
    fprintf('\tAveraged Periodogram: %g dB, %g dB\n', ...
        signal_power_dBm_averaged_periodogram_decorr, ...
        (signal_power_dBm_averaged_periodogram_decorr - ...
        SNR_dB_averaged_periodogram_decorr));
end
```

```
fprintf('\n');
```

```
%-------------------------------------------------------------------------
% process_phase_code takes a digitized phase code array, truncates it,
% and applies zero padding.  It also plots the processed phase code, a
% histogram of the phase code values, and the correlation of the phase
% code with itself, if desired.
%
% Author:       Nicola Kinzie
% Last Edited:  27 July 2010
%
% Inputs:   raw_phase_code - the raw phase code data
%           raw_time - the raw time vector
%           samples - the number of samples to be used
%           zero_pad - the number of zero pads to use (0 to set
%               automatically to the next power of 2 based on
%               "samples")
%           sample_set - indicates which set of samples to use.  for
%               example if i = n, then
%               raw_phase_code(1 + (n-1)*samples:n*samples) is used
%           ---------------------------------------------------------
%           plot_pc_raw - 1 to plot the raw phase code data
%           plot_pc_processed - 1 to plot the processed phase code data
%           plot_pc_hist - 1 to plot the phase code histogram
%           plot_pc_autocorr - 1 to plot the phase code autocorrelation
%           ---------------------------------------------------------
%           FontSize - font size for figures
%           LineWidth - line width for figures
%           ---------------------------------------------------------
%           path_name - path to save files to
%           file_name - the filename for the .mat file the data is taken
%               from
%
% Outputs:  processed_phase_code - the processed, truncated phase code
%           data
%-------------------------------------------------------------------------

function [processed_phase_code] = process_phase_code(raw_phase_code, ...
    raw_time, samples, zero_pad, sample_set, plot_pc_raw, ...
    plot_pc_processed, plot_pc_hist, plot_pc_autocorr, FontSize, ...
    LineWidth, path_name, file_name)

% Plots the raw phase code
if plot_pc_raw == 1 && sample_set == 1
    [scale_factor, time_units] = set_time_units(...
        length(raw_phase_code)*(raw_time(2) - raw_time(1)));
    axes('Parent',figure,'fontsize', FontSize);
    plot(raw_time*scale_factor, raw_phase_code, ...
        'LineWidth', LineWidth);
```

```
    grid on;
    xlabel(['Time (' time_units ')'], 'fontsize', FontSize);
    ylabel('Phase Code', 'fontsize', FontSize);
    title('Raw Phase Code');

    try
        saveas(gcf, [path_name ...
            file_name(1:(length(file_name)-4)) '_phase_code_raw'], ...
            'fig');
        clear('figure_handle');
    catch ME
        fprintf(['There was a problem saving the raw phase code ' ...
            'figure for %s.\n'], [path_name file_name]);
    end
end

% Sets phase code values to -1, 0, or 1
raw_phase_code = raw_phase_code - mean(raw_phase_code);
raw_phase_code = sign(raw_phase_code);

% Prints the total samples, the number of 1's and -1's, and the
% difference
if sample_set == 1
    fprintf(['\nTotal Samples: ' num2str(length(raw_phase_code)) ...
        '\n1''s: ' num2str(sum(raw_phase_code == 1)) '\n-1''s: ' ...
        num2str(sum(raw_phase_code == -1)) '\nDifference: ' ...
        num2str(sum(raw_phase_code == 1) - ...
        sum(raw_phase_code == -1)) '\n']);
end

% Truncates array and applies zero padding
if zero_pad == 0
    zero_pad = 2^(nextpow2(samples))-samples;
end
processed_phase_code = zeros((samples + zero_pad), 1);
processed_phase_code(1:samples) = ...
    raw_phase_code((1 + (sample_set - 1)*samples):sample_set*samples);

% Truncates time array
processed_time = zeros((samples + zero_pad), 1);
processed_time(1:samples) = ...
    raw_time((1 + (sample_set - 1)*samples):sample_set*samples);

% Plots the processed phase code
if plot_pc_processed == 1 && sample_set == 1
    [scale_factor, time_units] = set_time_units(...
        samples*(processed_time(2) ...
```

```
        - processed_time(1)));
    axes('Parent',figure,'fontsize', FontSize);
    plot(processed_time(1:samples)*scale_factor, ...
        processed_phase_code(1:samples), 'LineWidth', LineWidth);
    grid on;
    xlabel(['Time (' time_units ')'], 'fontsize', FontSize);
    ylabel('Phase Code', 'fontsize', FontSize);
    title('Processed Phase Code');

    try
        saveas(gcf, [path_name ...
            file_name(1:(length(file_name)-4)) ...
            '_phase_code_processed'], 'fig');
        clear('figure_handle');
    catch ME
        fprintf(['There was a problem saving the processed ' ...
        'phase code figure for %s.\n'], [path_name file_name]);
    end
end

% Plots a histogram of the phase code values
if plot_pc_hist == 1
    [histCounts, histBinLocations] = ...
        hist(processed_phase_code(1:samples), 2);
    axes('Parent',figure,'fontsize', FontSize);
    bar(histBinLocations, histCounts);
    xlabel('Phase Code Value', 'fontsize', FontSize);
    ylabel('Count', 'fontsize', FontSize);
    title('Histogram of Phase Code Values');
    text(-0.9, samples*11/12, ['Samples: ' num2str(samples)], ...
    'FontSize', FontSize);
    text(-0.9, samples*10/12, ['1''s: ' num2str(histCounts(2))], ...
        'FontSize', FontSize);
    text(-0.9, samples*9/12, ['-1''s: ' num2str(histCounts(1))], ...
        'FontSize', FontSize);
    text(-0.9, samples*8/12, ['Difference: ' num2str(abs(...
    histCounts(2) - histCounts(1)))], 'FontSize', FontSize);
    ylim([0 samples]);

    if sample_set == 1
        try
            saveas(gcf, [path_name ...
                file_name(1:(length(file_name)-4)) ...
                '_phase_code_histogram'], 'fig');
            clear('figure_handle');
        catch ME
            fprintf(['There was a problem saving the phase code ' ...
```

```
            'histogram figure for %s.\n'], [path_name file_name]);
        end
    end
end

% Plots the correlation of the phase code with itself
if plot_pc_autocorr == 1 && sample_set == 1
    [phase_code_autocorrelation, x_lags] = ...
        xcorr(processed_phase_code, 'coeff');

    phase_code_autocorrelation = ...
        20*log10(abs(phase_code_autocorrelation));

    axes('Parent',figure,'fontsize', FontSize);
    plot(x_lags, phase_code_autocorrelation, 'LineWidth', LineWidth);
    xlabel('t/T', 'fontsize', FontSize);
    ylabel('Ratio (dB)', 'fontsize', FontSize);
    ylim([-50 0]);
    title('Phase Code Autocorrelation');

    try
        saveas(gcf, [path_name ...
            file_name(1:(length(file_name)-4)) ...
            '_phase_code_autocorrelation'], 'fig');
        clear('figure_handle');
    catch ME
        fprintf(['There was a problem saving the phase code ' ...
            'autocorrelation figure for %s.\n'], [path_name file_name]);
    end
end

% Removes the zero padding
processed_phase_code = processed_phase_code(1:samples);
```

```
%-------------------------------------------------------------------------
% process_return takes a digitized data array, trancates it, and applies
% zero padding.  It also plots the processed return data, if desired.
%
% Author:       Nicola Kinzie
% Last Edited:  27 July 2010
%
% Inputs:   raw_return - the raw return data
%           raw_time - sample time vector
%           samples - the number of samples to be used
%           zero_pad - the number of zero pads to use (0 to set
%               automatically to the next power of 2 based on "samples")
%           sample_set - indicates which set of samples to use.  for
%               example if i = n, then
%               raw_phase_code(1 + (n-1)*samples:n*samples) is used
%           ---------------------------------------------------------
%           plot_return_raw - 1 to plot the raw return data
%           plot_return_processed - 1 to plot the processed return data
%           ---------------------------------------------------------
%           FontSize - font size for figures
%           LineWidth - line width for figures
%           MarkerSize - marker size for figures
%           ---------------------------------------------------------
%           path_name - path to save files to
%           file_name - the filename for the .mat file the data is taken
%               from
%
% Outputs:  processed_return - the processed, truncated return data
%-------------------------------------------------------------------------

function [processed_return] = process_return(raw_return, raw_time, ...
    samples, zero_pad, sample_set, plot_return_raw, ...
    plot_return_processed, FontSize, LineWidth, MarkerSize, ...
    path_name, file_name)

% Subtracts out the DC offset
raw_return = raw_return - mean(raw_return);

% Truncates array and applies zero padding
if zero_pad == 0
    zero_pad = 2^(nextpow2(samples)) - samples;
end
processed_return = zeros((samples + zero_pad), 1);
processed_return(1:samples) = ...
    raw_return((1 + (sample_set - 1)*samples):sample_set*samples);

% Truncates time array
```

```
processed_time = zeros((samples + zero_pad), 1);
processed_time(1:samples) = ...
    raw_time((1 + (sample_set - 1)*samples):sample_set*samples);

% Plots the raw return
if plot_return_raw == 1 && sample_set == 1
    [scale_factor, time_units] = set_time_units(...
        length(raw_return)*(raw_time(2) - raw_time(1)));
    axes('Parent',figure,'fontsize', FontSize);
    plot(raw_time*scale_factor, raw_return, '.', 'LineWidth', ...
        LineWidth, 'MarkerSize', MarkerSize);
    grid on;
    xlabel(['Time (' time_units ')'], 'fontsize', FontSize);
    ylabel('Target Return (V)', 'fontsize', FontSize);
    title('Raw Target Return');

    try
        saveas(gcf, [path_name ...
            file_name(1:(length(file_name)-4)) '_return_raw'], ...
            'fig');
        clear('figure_handle');
    catch ME
        fprintf(['There was a problem saving the raw return ' ...
            'figure for %s.\n'], [path_name file_name]);
    end
end

% Plots the processed return
if plot_return_processed == 1 && sample_set == 1
    [scale_factor, time_units] = set_time_units(samples* ...
        (processed_time(2) - processed_time(1)));
    axes('Parent',figure,'fontsize', FontSize);
    plot(processed_time(1:samples)*scale_factor, ...
        processed_return(1:samples), '.', 'LineWidth', ...
        LineWidth, 'MarkerSize', MarkerSize);
    grid on;
    xlabel(['Time (' time_units ')'], 'fontsize', FontSize);
    ylabel('Target Return (V)', 'fontsize', FontSize);
    title('Processed Target Return');

    try
        saveas(gcf, [path_name ...
            file_name(1:(length(file_name)-4)) '_return_processed'], ...
            'fig');
        clear('figure_handle');
    catch ME
        fprintf(['There was a problem saving the processed return ' ...
```

```
            'figure for %s.\n'], [path_name file_name]);
    end
end

% Removes the zero padding
processed_return = processed_return(1:samples);
```

```
%-------------------------------------------------------------------------
% corr_return_and_pc correlates the return signal with the phase code
% signal.  It also plots the correlation result, if desired.
%
% Author:       Nicola Kinzie
% Last Edited:  27 July 2010
%
% Inputs:   processed_phase_code - the processed phase code date
%               (truncated and zero padded)
%           processed_return - the processed return data (truncated and
%               zero padded)
%           sample_set - indicates which set of samples to use
%           ---------------------------------------------------------
%           FontSize - font size for figures (30 is recommended)
%           LineWidth - font size for figures (2 is recommended)
%           ---------------------------------------------------------
%           plot_return_pc_corr - 1 to plot the correlation between
%               "processed_phase_code" and "processed_return"
%           ---------------------------------------------------------
%           path_name - path to save files to
%           file_name - the filename for the .mat file the data is taken
%               from
%
% Outputs:  processed_corr_result - the correlation vector for
%               "processed_phase_code" and "processed_return"
%           processed_corr_result_lags - the shift vector for
%               "processed_corr_result"
%-------------------------------------------------------------------------

function [processed_corr_result, processed_corr_result_lags] = ...
    corr_return_and_pc(processed_phase_code, processed_return, ...
    sample_set, FontSize, LineWidth, plot_return_pc_corr, path_name, ...
    file_name)

[processed_corr_result, processed_corr_result_lags] = ...
    xcorr(processed_phase_code(:, sample_set), ...
    processed_return(:, sample_set), 'coeff');

% Plots the correlation of the phase code with the return
if plot_return_pc_corr == 1 && sample_set == 1
    processed_corr_result = 20*log10(abs(processed_corr_result));

    axes('Parent',figure,'fontsize', FontSize);
    plot(processed_corr_result_lags, processed_corr_result, ...
        'LineWidth', LineWidth);
    xlabel('\tau/T', 'fontsize', FontSize);
    ylabel('Ratio (dB)', 'fontsize', FontSize);
```

```
    ylim([-50 0]);
    title('Correlation Result');

    try
        saveas(gcf, [path_name ...
            file_name(1:(length(file_name)-4)) '_corr_result'], 'fig');
        clear('figure_handle');
    catch ME
        fprintf(['There was a problem saving the ' ...
            'correlation result figure for %s.\n'], ...
            [path_name file_name]);
    end
end
```

```
%-------------------------------------------------------------------------
% filter_return takes a digitized data array and applies a fir filter to
% it.
%
% Author:       Nicola Kinzie
% Last Edited:  27 July 2010
%
% Inputs:   filter_order - order of fir filter
%           cutoff_freq - desired cutoff frequency
%           sample_freq - sample frequency
%           filter_method - 1 for filtfilt(), otherwise filter() is used
%           ------------------------------------------------------------
%           data - vector to be filtered
%           time - corresponding time vector
%           samples - number of samples used
%           ------------------------------------------------------------
%           FontSize - font size for figure
%           LineWidth - line width for figure
%           MarkerSize - marker size for figure
%           ------------------------------------------------------------
%           path_name - path to save files to
%           file_name - the filename for the .mat file the data is taken
%               from
%           ------------------------------------------------------------
%           plot_return_processed_decorrelated_filtered - 1 to plot the
%           filtered data
%
% Outputs:  processed_return_decorr_filtered - filtered vector
%-------------------------------------------------------------------------

function processed_return_decorr_filtered = filter_return(...
    filter_order, cutoff_freq, sample_freq, filter_method, data, ...
    time, samples, FontSize, LineWidth, MarkerSize, path_name, ...
    file_name, plot_return_processed_decorrelated_filtered)

%% Performs Filtering
h = fir1(filter_order, cutoff_freq/(sample_freq/2));
if filter_method == 1
    b = filtfilt(h, 1, data);
else
    b = filter(h, 1, data);
end
processed_return_decorr_filtered = b;

%% Plots the filtered data

if plot_return_processed_decorrelated_filtered == 1
```

```
    processed_time(1:samples) = time(1:samples);
    [scale_factor, time_units] = set_time_units(samples* ...
        (processed_time(2) - processed_time(1)));
    axes('Parent',figure,'fontsize', FontSize);
    plot(processed_time(1:samples)*scale_factor, ...
        b(1:samples), '.', 'LineWidth', LineWidth, 'MarkerSize', ...
        MarkerSize);
    grid on;
    xlabel(['Time (' time_units ')'], 'fontsize', FontSize);
    ylabel('Filtered Correlated Target Return (V)', 'fontsize', ...
        FontSize);
    title('Filtered Processed Correlated Target Return');

    try
        saveas(gcf, [path_name ...
            file_name(1:(length(file_name)-4)) '_return_processed' ...
            '_decorr_filt'], 'fig');
        clear('figure_handle');
    catch ME
        fprintf(['There was a problem saving the processed ' ...
            'correlated filtered return figure for %s.\n'], ...
            [path_name file_name]);
    end
end
```

```
%-------------------------------------------------------------------------
% power_periodogram calculates the signal power, total power, and SNR of
% a signal using a periodogram to calculate the PSD.  The power
% calculationis performed using that sampling only occurs during the on
% time of the received pulses.  As such, the calculated powers are peak
% power measurements rather than average power measurements.
%
% The periodogram uses a Hamming window that matches the length of
% "processed_return".
%
% Author:       Nicola Kinzie
% Last Edited:  27 July 2010
%
%
% Inputs:   processed_return - the truncated and zero-padded signal of
%               interest
%           fs - the sample frequency
%           samples - the number of samples being processed
%           zero_pad - the number of zero pads to add (0 for the next
%               power of 2)
%           ---------------------------------------------------------
%           auto_search_signal_freq - 1 to auto search for the signal
%               frequency
%           signal_freq_init - the signal frequency to integrate about;
%               this input is ignored if "auto_search_signal_freq" == 1
%           ---------------------------------------------------------
%           int_bandwidth - the integration bandwidth of the PSD (10,
%               20, 30, or 40 for 10, 20, 30, or 40 dB bandwidth)
%           system_impedance - the system impedance
%           ---------------------------------------------------------
%           FontSize - font size for plot
%           LineWidth - line width for plot
%           ---------------------------------------------------------
%           path_name - path name to data file
%           file_name - file name of data file
%           ---------------------------------------------------------
%           plot_PSD_periodogram - 1 to plot the PSD calculated using
%               the periodogram method
%           ---------------------------------------------------------
%           descriptor - string with a descriptor for the filename
%
% Outputs:  signal_power_dBm - the integrated signal power
%           total_power_dBm - the total integrated power
%           SNR_dB - the SNR for the measurement
%           signal_freq - the signal frequency that corresponds to
%               "signal_power_dBm"
%           scale_factor - scale factor for "signal_freq"
```

```
%           freq_units - units for "signal_freq"
%           PSD - the calculated PSD
%           frequency - the frequency vector for the PSD
%--------------------------------------------------------------------------

function [signal_power_dBm, total_power_dBm, SNR_dB, ...
    signal_freq, scale_factor, freq_units, PSD, frequency] = ...
    power_periodogram(processed_return, fs, samples, zero_pad, ...
    auto_search_signal_freq, signal_freq_init, int_bandwidth, ...
    system_impedance, FontSize, LineWidth, path_name, file_name, ...
    plot_PSD_periodogram, descriptor)

%% Initialization

% Signal frequency initialization
signal_freq = signal_freq_init;

% [] specifies a rectangular window, which is used for a standard
% periodogram
window = hamming(samples);

% Sets the integration bandwidth
if int_bandwidth == 10
    processed_bandwidth = fs/samples*2.3; % 10dB lobewidth for hamming
elseif int_bandwidth == 20
    processed_bandwidth = fs/samples*3.1; % 20dB lobewidth for hamming
elseif int_bandwidth == 30
    processed_bandwidth = fs/samples*3.6; % 30dB lobewidth for hamming
else
    processed_bandwidth = fs/samples*4; % 40dB lobewidth for hamming
end

% Determines the amount of zero-padding that will be used
if zero_pad == 0
    zero_pad = 2^(nextpow2(samples))-samples;
end

%% Computes and adjusts PSD

% Computes the two-sided periodogram
[PSD, frequency] = periodogram(processed_return, window, ...
    (samples + zero_pad), fs, 'twosided');

% Adjust "frequency"
frequency_spacing = frequency(2) - frequency(1);
frequency = frequency - max(frequency)/2 - frequency_spacing/2;
```

```
% Adjust "PSD"
PSD = PSD/system_impedance;
PSD = fftshift(PSD);

%% Integrates PSD to obtain power and SNR calculations

% Find the peak signal power
if auto_search_signal_freq == 1
    index_freq_zero = find_index(frequency, 0);
    [peak_pwr, index_peak_pwr] = max(PSD(index_freq_zero:end));
    signal_freq = frequency(index_freq_zero + index_peak_pwr - 1);
end

% Integrates "PSD" around "signal_frequency" with a bandwidth of
% "processed_bandwidth"
[signal_power_dBm, total_power_dBm, SNR_dB] = ...
    integrate_PSD(PSD, frequency, signal_freq, processed_bandwidth);

%% Plots the PSD

[scale_factor, freq_units] = set_freq_units(max(frequency));

if plot_PSD_periodogram == 1
    axes('Parent',figure,'fontsize', FontSize);
    plot(frequency*scale_factor, 10*log10(PSD/max(PSD)), ...
        'LineWidth', LineWidth);
    grid on;
    xlabel(['Frequency (' freq_units ')'], 'fontsize', FontSize);
    ylabel('PSD (dB)', 'fontsize', FontSize);
    if signal_freq ~= 0
        xlim([-signal_freq*10*scale_factor ...
            signal_freq*10*scale_factor]);
    end
    title('Power Spectral Density: Periodogram');

    try
        if strcmp(descriptor, '')
            saveas(gcf, [path_name ...
                file_name(1:(length(file_name)-4)) ...
                '_psd_periodogram'], 'fig');
        else
            saveas(gcf, [path_name ...
                file_name(1:(length(file_name)-4)) ...
                '_psd_periodogram' '_' descriptor], 'fig');
        end
        clear('figure_handle');
    catch ME
```

```
        fprintf(['There was a problem saving the periodogram PSD ' ...
            'figure for %s.\n'], [path_name file_name]);
    end
end
```

```
%-------------------------------------------------------------------------
% integrate_PSD integrates "PSD" around +/-"signal_frequency" with a
% bandwidth of "processed_bandwidth".  It calculates the signal power,
% the total power, and the SNR.
%
% Author:       Nicola Kinzie
% Last Edited:  27 July 2010
%
% Inputs:   PSD - the two-sided power spectral density
%           frequency - the frequency vector associated with "PSD"
%           signal_frequency - the frequency to integrate about
%           processed_bandwidth - the bandwidth over which to integrate
%
% Outputs:  signal_power_dBm - the signal power in dBm
%           total_power_dBm - the total power in dBm
%           SNR_dB - the signal to noise ratio in dB
%-------------------------------------------------------------------------

function [signal_power_dBm, total_power_dBm, SNR_dB] = ...
    integrate_PSD(PSD, frequency, signal_frequency, processed_bandwidth)

%% Calculates signal power

if signal_frequency > processed_bandwidth
    % Find integration indices
    index_pos_freq_low = find_index(frequency, (signal_frequency - ...
        processed_bandwidth/2));
    index_pos_freq_high = find_index(frequency, (signal_frequency + ...
        processed_bandwidth/2));
    index_neg_freq_low = find_index(frequency, (-signal_frequency - ...
        processed_bandwidth/2));
    index_neg_freq_high = find_index(frequency, (-signal_frequency + ...
        processed_bandwidth/2));

    % Integrate the positive and negative frequency contributions
    signal_power_pos = trapz(...
        frequency(index_pos_freq_low:index_pos_freq_high), ...
        PSD(index_pos_freq_low:index_pos_freq_high));
    signal_power_neg = trapz(...
        frequency(index_neg_freq_low:index_neg_freq_high), ...
        PSD(index_neg_freq_low:index_neg_freq_high));
    signal_power = signal_power_pos + signal_power_neg;
else
    index_freq_low = find_index(frequency, -signal_frequency - ...
        processed_bandwidth/2);
    index_freq_high = find_index(frequency, signal_frequency + ...
        processed_bandwidth/2);
```

```
    signal_power = trapz(frequency(index_freq_low:index_freq_high), ...
        PSD(index_freq_low:index_freq_high));
end

signal_power_dBm = 10*log10(signal_power/1e-3);

%% Calculates total power

total_power = trapz(frequency, PSD);
total_power_dBm = 10*log10(total_power/1e-3);

%% Calculates SNR

SNR = signal_power/(total_power - signal_power);
SNR_dB = 10*log10(SNR);
```

```
%-------------------------------------------------------------------------
% average_PSD averages a set of PSD results.  The averaged PSD is
% plotted and the SNR, total power, and signal power are calculated.
%
% Author:       Nicola Kinzie
% Last Edited:  27 July 2010
%
% Inputs:   PSD - a matrix containing the PSD results from multiple
%               sample sets.  each column is a new set of data.
%           frequency - a matrix containing the frequency vectors for
%               the PSDs.  each column is a new set of data.
%           averages - the number of FFTs to be averaged
%           ---------------------------------------------------------
%           signal_freq - the signal frequency that corresponds to
%               "signal_power_dBm"
%           scale_factor - scale factor for "signal_freq"
%           freq_units - units for "signal_freq"
%           ---------------------------------------------------------
%           processed_bandwidth - the integration bandwidth
%           system_impedance - the system impedance
%           ---------------------------------------------------------
%           FontSize - font size for plot
%           LineWidth - line width for plot
%           ---------------------------------------------------------
%           path_name - path name to data file
%           file_name - file name of data file
%           ---------------------------------------------------------
%           plot_PSD - 1 to plot the PSD calculated using the
%               periodogram method
%           ---------------------------------------------------------
%           descriptor - string with a descriptor for the filename
%
% Outputs:  signal_power_dBm - the integrated signal power
%           total_power_dBm - the total integrated power
%           SNR_dB - the SNR for the measurement
%-------------------------------------------------------------------------

function [signal_power_dBm, total_power_dBm, SNR_dB] = average_PSD(...
    PSD, frequency, averages, signal_freq, scale_factor, freq_units, ...
    processed_bandwidth, system_impedance, FontSize, LineWidth, ...
    path_name, file_name, plot_PSD, descriptor)

%% Calculates average PSD

PSD_average = 0;
for i = 1:averages
    PSD_average = PSD_average + PSD(:, i)/averages;
```

```
end

frequency_average = frequency(:, 1);

%% Integrates PSD to obtain power and SNR calculations

% Integrates "PSD" around "signal_frequency" with a bandwidth of
% "processed_bandwidth"
[signal_power_dBm, total_power_dBm, SNR_dB] = ...
    integrate_PSD(PSD_average, frequency_average, signal_freq, ...
    processed_bandwidth);

%% Plots the PSD

[scale_factor, freq_units] = set_freq_units(max(frequency));

if plot_PSD == 1
    axes('Parent',figure,'fontsize', FontSize);
    plot(frequency_average*scale_factor, ...
        10*log10(PSD_average/max(PSD_average)), 'LineWidth', LineWidth);
    grid on;
    xlabel(['Frequency (' freq_units ')'], 'fontsize', FontSize);
    ylabel('Averaged PSD (dB)', 'fontsize', FontSize);
    if signal_freq ~= 0
        xlim([-signal_freq*10*scale_factor ...
            signal_freq*10*scale_factor]);
    end
    title(['Averaged Power Spectral Density: ' descriptor]);

    try
        if strcmp(descriptor, '')
            saveas(gcf, [path_name ...
                file_name(1:(length(file_name)-4)) ...
                '_psd_averaged'], 'fig');
        else
            saveas(gcf, [path_name ...
                file_name(1:(length(file_name)-4)) ...
                '_psd_averaged_' strrep(lower(descriptor), ' ', ...
                '_')], 'fig');
        end
        clear('figure_handle');
    catch ME
        fprintf(['There was a problem saving the averaged ' ...
            descriptor 'PSD figure for %s.\n'], [path_name file_name]);
    end
end
```